Université de Montréal

La translecture traductionnelle dans la sénescence et le cancer

Par

Jacob Bouchard

Département de Biochimie et Médecine Moléculaire,

Faculté de Médecine

Mémoire présenté en vue de l'obtention du grade de maîtrise en sciences (M. Sc.)

En biochimie, option générale

Janvier 2022

Université de Montréal

Unité académique : Département de biochimie et médecine moléculaire, Faculté de Médecine

---

Ce mémoire intitulé

La translecture traductionnelle dans la sénescence et le cancer

Présenté par

Jacob Bouchard

A été évalué par un jury composé des personnes suivantes

Sylvie Mader
Présidente-rapporteur

Gerardo Ferbeyre
Directeur

Luis Rokeach
Membre du jury

Résumé

La cellule est en permanence sujette à des attaques et soumise à des évènements stressants. D'un point de vue évolutif, l'organisme doit s'adapter à son environnement et faire face aux atteintes dont il peut être victime. Pour survivre, celui-ci doit répondre aux dommages reçus de manière la plus optimale possible tout en limitant l'occurrence de mutations pouvant mener à l'apparition de cancer. Afin d'y parvenir, l'organisme a développé les suppresseurs de tumeurs, gérant des voies de signalisation cellulaire complexes, limitant l'apparition de mutations à l'ADN, stimulant sa réparation et, en dernier recours, activant l'arrêt permanent du cycle cellulaire, la sénescence, ou la mort cellulaire, l'apoptose. Le défaut de fonctionnement de ces mécanismes entraîne l'accumulation de mutations favorisant l'initiation et la progression de la tumorigenèse. Les erreurs traductionnelles, en contribuant à l'expansion du protéome, ont elles aussi été reconnues comme faisant partie d'un mécanisme pouvant être utilisé pour répondre au stress de sélection. Cependant, chez les organismes plus développés ainsi que dans la tumorigenèse, leur rôle reste peu compris à ce jour. En revanche, si ce phénomène peut contribuer à l'oncogenèse, les mécanismes suppresseurs de tumeurs devraient, en théorie, les prévenir.

Les travaux présentés dans ce mémoire ont été entrepris dans le but d'étudier les erreurs traductionnelles survenant à la terminaison, la translecture du codon d'arrêt (TR), en contexte de sénescence. En utilisant une construction double luciférase séparée par des contextes de terminaison normale ou de TR programmé, nos résultats montrent que l'induction de la sénescence par l'activation d'oncogène, l'activation de suppresseurs de tumeurs et des agents chimiothérapeutiques, est associée avec une diminution significative du TR. De surcroît, nous avons observé que les cellules échappant à la sénescence montrent un niveau de TR augmenté. Nous avons également démontré ces effets en utilisant AGO1x un isoforme dépendant du TR impliqué dans la progression du cancer du sein.

D'autre part, nos travaux ont visé à établir un lien mécanistique entre les suppresseurs de tumeurs impliqués dans la sénescence et la régulation du TR. Dans un premier temps, en déplétant p53 et RB nous avons montré une régulation majoritairement médiée par la voie RB. Les résultats ont été confirmés en ciblant de diverses manières la voie RB. Quant à l'implication de p53, nous

avons montré en utilisant des cellules p53-null que la réduction de TR dans la sénescence était indépendante de cette voie.

Les données présentées dans ce mémoire contribuent à une meilleure compréhension des mécanismes par lesquels les voies de signalisation des suppresseurs de tumeurs pourraient limiter la carcinogenèse. Ainsi, à la lumière de nos observations, nous proposons que l'amélioration de l'efficacité de terminaison observée en sénescence puisse être un nouveau mécanisme antitumoral médié par la voie RB.

Mots-clés : Translecture traductionnelle, Terminaison traductionnelle, Sénescence, Suppresseur tumoral rétinoblastome (RB)

Abstract

The cell is constantly victim of attacks and stressful events. From an evolutionary perspective, the organism must be able to adapt to its environment and respond to the harm it may suffer. To survive, it must respond to damage received in the most optimal way possible, by limiting the appearance of mutations that can lead to cancer. To achieve this, tumor suppressors evolved, managing complex cellular signaling pathways limiting DNA mutations, stimulating DNA repair and, in the worst case, activating a permanent cell cycle arrest, namely senescence, or cell death(apoptosis). Defects in these mechanisms may lead to the accumulation of mutations favoring the initiation of tumorigenesis. Translational errors, by contributing to the expansion of cellular proteome, have also been associated as a mechanism that can be used to respond to selection stress. However, their role in more developed organisms, as well as in tumorigenesis, is still poorly understood. On the other hand, if this phenomenon can contribute to oncogenesis, tumor suppressor mechanisms should theoretically prevent them to occur.

The work presented in this thesis was undertaken with the aim of studying translational errors occurring at the termination, the translational readthrough (TR), in the context of senescence. Using a dual luciferase construct with normal termination or programmed TR context, our results show that induction of senescence by oncogene activation, activation of tumor suppressors and chemotherapeutic drugs is associated with significant decrease in TR. In addition, we observed that cells escaping senescence show an increased level of TR. We have also demonstrated these effects using AGO1x a TR-dependent isoform implicated in the breast cancer progression.

Furthermore, our work aimed to establish a mechanistic link between tumor suppressors involved in senescence and in the regulation of TR. Firstly, by depleting p53 and RB, we showed that the reduction of TR seen in senescence is mainly mediated by the RB pathway. These results were confirmed by targeting the RB pathway in various ways. As for the implication of p53, we showed by using p53-null cells that the reduction of TR in senescence was independent of this pathway.

The data presented in this thesis contribute to a better understanding of the mechanisms by which tumor suppressor signaling pathways could limit carcinogenesis. Thus, in light of our

findings, we propose that the improved termination efficiency observed in senescence may be a novel RB pathway-mediated antitumor mechanism.

Keywords : Translational readthrough, Translational termination, Senescence, Retinoblastoma (RB) tumor suppressor

Table des matières

Liste des tableaux

Liste des figures

Liste des abréviations

3’UTR : Région non traduite 3’

53BP1 : p53-binding protein 1

5’UTR : Région non traduite 5’

9-1-1 : Complexe RAD1-RAD1-HUS1

AA : Acide aminé

AA-ARNt : l’ARN de transfert aminoacylé

ABCE1/Rli1 : ATP Binding Cassette Subfamily E Member 1

ADN : Acide désoxyribonucléique

AGO1 : Argonaute 1

AGO1x : Forme allongé en C-terminal d’argonaute 1

AMPK : AMP-activated protein kinase

APC : Adenomatous polyposis coli

ARF : Alternate-reading-frame protein

ARN : Acide ribonucléique

ARNm : Acide ribonucléique messager

ARNr : Acide ribonucléique ribosomal

ARNt : Acide ribonucléique transférase

ASPH : Aspartate beta hydroxylase

ATM : Ataxia telangiectasia mutated

ATP : Adenosine triphosphate

ATR : Ataxia telangiectasia and Rad3-related protein

ATRIP: ATR-interacting protein

AQP4 : Aquaporine 4

AQP4x : Forme allongée en C-terminal d’aquaporine 4

BRCA1/2 : breast-ovarian cancer susceptibility 1/2

Cdc25 : Cell division cycle 25

CDKs : Kinases dépendantes des cyclines

CDK1 : Kinase dépendante des cyclines 1

CDK2 : Kinase dépendante des cyclines 2

CDK4 : Kinase dépendante des cyclines 4

CDK6 : kinase dépendante des cyclines 6

CHK1 : Checkpoint kinase 1

CHK2 : Checkpoint kinase 2

CDKi : Inhibiteur de kinases dépendantes des cyclines

CIP/KIP : Famille des protéines interagissant avec les CDK/protéines inhibitrices de kinases

DDB2 : DNA damage-binding protein 2

DDR : Réponse aux dommages à l’ADN

DRAM : Damage-regulated autophagy modulator

DDX: Helicase d'ARN à domaine DEAD-Box

E2F : facteur E2

E.coli : Escherichia coli

eIF : Facteur d'initiation de la traduction eucaryote

eEF : Facteur d'élongation eucaryote

eRF : Facteur de relâche/terminaison de la traduction eucaryote

GAPDH : Glycéraldéhyde-3'— phosphate déshydrogénase

H2AX : Histone H2A

H2AXɣ : Forme phosphorylé d'histone H2A

H2AX : Histone H2A

HPN : Hepsin

HR : Recombinaison homologue

INK : Famille des inhibiteurs de CDK

LDHB : Lactate déhydrogénase bêta

LDHBx : Forme allongé en C-terminal de lactate déhydrogénase bêta

MAPK : Mitogen-activated protein kinase

MDC1 : Mediator of DNA-damage checkpoint 1

MDH1 : Malate déhydrogénase 1

MDH1x : Forme allongée en C-terminal de malate déhydrogénase 1

MDM2 : Mouse double minute 2 Homolog

MLH1 : MutL Homolog 1

MMR : Mismatch repair/réparation de non-correspondance

MMuLV : Moloney Murine Leukemia Virus

MRN : Complexe MRE11-RAD50-NBS1

MSH2 : MutS Homolog 2

mTOR : Mammalian target of rapamycin

NAD : Dicotinamide adénine dinucleotide

NADP : Nicotinamide adénine dinucléotide phosphate

Nc-ARNt : ARNt semblable au codon d'arrêt

NHEJ : Non-homologous end joining/ jonction d'embout non homologue

NMD : Nonsens mediated mRNA decay

NOXA : Phobol-12-Myristate-13-Acetate-Induced Protein

TP53 : Tumor protein p53

P107 : Retinoblastoma-like protein 1

P130 : Rétinoblastoma-like protein 2

PGK : 3’— phosphoglycerate kinase

Phase G1 : Phase de croissance

Phase G2 : Phase de croissance 2

Phase M : Phase mitotique

Phase S : Phase de réplication de l’ADN

PML : protéine promyelocytic leukemia

PNPT1 : Polyribonucleotide nucleotidyltransférase 1

Pol I : ARN polymérase I

Pol II : ARN polymérase II

Pol II : ARN polymérase III

Pré-ARNr : ARNr précurseur

PRC : Polycomb protein

PTC : Codon d’arrêt prématuré

PTS1 : Signal de localisation peroxisomal type 1

PUMA : p53-upregulated modulator of apoptosis

OAZ : Antizyme ornithine décarboxylase

ODC : Enzyme ornithine décarboxylase

OPRK1 : Récepteur à opioïde Kappa 1

OPRL1 : Opioid Related Nociceptin Receptor 1

ORF : Open reading frame

RAS : Rat sarcoma viral oncogene homolog

RB : Protéine associée au rétinoblastome

pRB : Protéine du rétinoblastome

ROS/DRO : Reactive oxygen species /dérivés réactifs de l’oxygène

RPA : Replication protein A

RPL: Protéines ribosomales de la grande sous-unité

RPS: Protéines ribosomales de la petite sous-unité

RSL1D1 : Ribosomal L1 domain-containing protein 1

TIGAR : TP53 Induced Glycolysis Regulatory Phosphatase

SA-β-Gal : Senescence-accociated-beta-galactosidase

SAPD : Senescence-associated protein degradation

SARD : Senescence-associated ribosome biogenesis defect

SASP : Senescence-associated secretory phenotype

SESN1/2 : Sestrine 1 et 2

SET7/9 : SET domain containing lysine methyltransferase 7

snoRNA: Petits ARN nucléolaire

snoRNP: Petite ribonucléoprotéine nucléolaire

T-ALL : Leucémie aiguë lymphoblastique à cellules T

TFIIIB : Transcription factor IIIB

TR : Translecture du codon d'arrêt/Translecture traductionnelle/translational readhtrough

UBF : Upstream Binding Transcription Factor

VASP : Vasodilator stimulated phosphoprotein

VEGFA : Facteur de croissance endothéliale vasculaire A

VEGFAx : Forme allongée en C-terminal du facteur de croissance endothéliale vasculaire A

Je dédicace ce mémoire à tous ceux et celles qui comme moi ont une lueur dans les yeux, un désir de faire de ce monde un endroit plus juste et humain, qui disent oui à la vie et surtout s'accrochent aux rêves guidant leurs pas

« Tout est possible à qui rêve, ose, travaille et n'abandonne jamais»

Xavier Dolan

« Croyez en vos rêves et ils se réaliseront peut-être. Croyez en vous et ils se réaliseront sûrement »

Martin Luther King

« Les obstacles sont ces choses effrayantes que vous apercevez lorsque vous détournez les yeux de vos objectifs »

Henry Ford.

« Il faut viser la lune, parce qu'au moins, si vous échouez, vous finirez dans les étoiles »

Oscar Wilde

Remerciements

Bien que de courte durée, mon temps passé au département de Biochimie et Médecine Moléculaire fut des plus enrichissant, et ce, fort probablement dû à tous ces gens que j'ai eu la chance de côtoyer. Bien que minime comparé à ce que vous m'avez apporté, ces quelques lignes sont là pour vous remercier.

Je souhaite tout d'abord remercier mon directeur de recherche Dr. Gerardo Ferbeyre sans qui rien de tout cela n'aurait été possible. En effet, il m'a accueilli au sein de son laboratoire sachant fort bien mes perspectives personnelles. Gerardo est un scientifique passionné dont le savoir et l'expertise ne sont certainement pas à prendre à la légère. Il n'en est pas moins une personne accessible et présente pour les membres de son laboratoire. Une chose que j'ai rapidement comprise est que sa pensée est sans fin et est en mesure de générer d'innombrables idées/projets/expériences tous plus stimulants les uns que les autres. Je suis particulièrement reconnaissant de son support et de ses encouragements qui ont su me guider afin de les mener à bien. Je le remercie également pour l'autonomie à laquelle j'ai eu droit. Lors de mon temps passé au laboratoire, j'ai appris à apprécier la beauté et l'importance de la recherche fondamentale. Bien que mes projets futurs ne soient pas encore établis, je sais vouloir incorporer, si possible, cet intérêt pour la recherche ayant grandi en moi et mettre en pratique cet esprit critique et scientifique développer dans ce laboratoire.

Je voudrais également remercier tous les membres du laboratoire qui m'ont aidé par leur conseil et leur support au courant de ces années. Merci à Sebastian, Frédéric, Véronique, Neylen, Guillaume Camille, Tony, Stéphane, Paloma, Ana, Lian, Marie-Camille, Rose et Bianca.

Sebastian, je me souviendrais toujours de la déstabilisation que j'ai ressentie lors de notre première rencontre. Je n'étais encore qu'un étudiant au baccalauréat ne sachant pas trop comment manipuler en laboratoire. Je me rappelle à quel point j'étais initialement intimidé par tes vastes connaissances et à quel point je pouvais être perdu suivant tes questions « quiz ». Tu trouves le moyen d'aller chercher chez les gens le meilleur qu'ils peuvent offrir. En effet, dans cette incertitude que j'ai ressentie initialement résidait un défi. Un défi d'apprendre, de me dépasser et de montrer ma valeur. Tu as été un vrai mentor pour moi et je ne pourrai te remercier assez pour ce que tu m'as appris. Toi et Gérardo avez sans doute su me faire, non seulement, dépasser mes

limites, mais aussi m'en faire prendre conscience. Ne lâche pas ta passion et tes objectifs. Tu es travaillant et excellent dans ce que tu fais. Je suis certains que s'investir dans les choses à fond finit toujours par payer. Je souhaite à toi et ta famille le meilleur que l'avenir a à offrir.

Une autre « légende » du laboratoire est sans nul doute Frédéric. Fred est la personne-ressource en cas de problèmes. Que ce soit pour support moral ou encore une expérience qui ne fonctionne pas, il a toujours été présent pour écouter et apporter des idées, et ce, même après avoir quitté le laboratoire.

Véronique, merci pour tes conseils et tes idées éclairantes. Que ce soit en clonage ou en culture cellulaire, tes connaissances et astuces ont toujours été d'une grande aide. Tu es un maillon central de l'équipe. Merci aussi pour toutes les fois où tu m'as rappelé l'importance de manger et dormir et à quel point une diète « bonbon et café de 15 h » n'était pas optimal.

Neylen, bien que nous n'ayons pas eu beaucoup de temps à travailler ensemble, je tiens à te remercier pour ta disponibilité lorsque j'avais des questions sur le TR et les luciférases. Merci de m'avoir fait confiance dans la poursuite de ton projet.

J'en profite aussi pour remercier les membres du laboratoire DesGroseillers qui ont su endurer mon énergie et avec qui il a toujours été agréable de discuter. Merci à Yulémi et Florence qui était toujours prêtent à aider lorsque j'avais un manque de réactif. Je tiens aussi à mentionner Bellastrid avec qui j'ai pu apprécier les luciférases. Je remercie aussi Lionel sans qui les nuits au laboratoire à travailler n'auraient pas été les mêmes. Je suis convaincu qu'une grande carrière en science t'attend.

J'oublie certainement certaines personnes, mais je souhaite tous vous remercier. Merci à vous d'avoir créé et contribué à cet environnement de collaboration et d'apprentissage ! Merci d'avoir fait de ces jours passés au laboratoire une expérience agréable ! Et surtout, merci pour ce bagage d'expériences et de connaissances dont je tâcherai de me souvenir et que j'utiliserai très certainement dans le futur.

Dans cette lancée, je souhaite garder quelques lignes à ma famille. Je veux remercier particulièrement mes parents, Valérie et Janic, ainsi que mon grand-père, Yvon, sans qui je ne serais pas là où je suis aujourd'hui. À ma conjointe, Azéa, qui est là pour moi et me supporte au

quotidien. Vous m'encouragez sans cesse dans tout ce que j'entreprends et pour cela je vous en suis reconnaissant.

Chapitre 1 : Introduction

1.1. Renouvellement cellulaire

Le corps humain est composé d'environ $3*10^{13}$ cellules (1), dont plusieurs d'entre elles devront subir un renouvèlement au cours de leur vie. D'ailleurs, on estime qu'au courant de la durée de vie moyenne d'un humain, le corps comptera environ $1*10^{16}$ divisions cellulaires (BNID100379). En effet, dans le cas de certains tissus subissant beaucoup d'insultes externes (radiation solaire, alimentation, etc.) telles que la peau ou encore les muqueuses du tractus gastro-intestinale, ceux-ci pourraient atteindre des taux de renouvellement allant jusqu'à $7*10^{8}$ et $56*10^{9}$ respectivement (BNID113419).

Afin d'assurer le bon déroulement des multiples évènements de division cellulaire prenant place chaque jour dans l'organisme, le cycle cellulaire s'est constitué, au fil de l'évolution, de quatre phases : la première phase de croissance (G1), la phase de réplication de l'ADN (S), la deuxième phase de croissance 2 (G2) et la phase mitotique (M) (2). On y note aussi une cinquième phase, cette fois-ci en dehors du cycle cellulaire, la phase G0, aussi connue sous le nom de quiescence, qui correspond à un état de repos cellulaire réversible. On retrouve la majorité des cellules composant le corps humain dans cet état. En présence de signaux mitotiques, les cellules quiescentes feront leur entrée dans la phase G1 et entament ainsi leur division cellulaire (3, 4).

Chez la cellule humaine, le cycle cellulaire nécessite l'expression de plus de 850 gènes (5). La gestion d'expression d'une si grande quantité de gènes nécessite une régulation étroite afin de limiter les erreurs pouvant survenir lors de la division cellulaire. C'est pourquoi la progression à travers le cycle cellulaire est coordonnée par différentes protéines régulatrices. L'une des familles de protéines clefs de cette régulation est la famille des kinases dépendantes des cyclines (CDKs). Celles-ci sont activées à certains moments précis du cycle cellulaire par leurs partenaires, les cyclines (2, 6). En effet, bien que les CDKs soient présentes en quantité similaire tout au long du cycle cellulaire, la progression dans ce cycle dépend de la synthèse des cyclines (7). Selon le modèle classique présenté à la figure 1, la kinase dépendante des cyclines 4 (CDK4) et la kinase dépendante des cyclines 6 (CDK6), toutes deux associées à la cycline D régulent les événements

initiaux en G1, alors que la kinase dépendante des cyclines 2 (CDK2) couplée à cycline E active l'entrée en phase S. Par la suite, CDK2 et la kinase dépendante des cyclines 1 (CDK1), toutes deux activées par la cycline A, régulent le bon déroulement des phases S et G2 jusqu'à leur complétion menant à la mitose qui est orchestrée par CDK1-Cyclin B (2, 7). Lorsqu'activés, ces complexes induisent des processus en aval via la phosphorylation de protéines spécifiques nécessaires à la complétion d'une phase et au passage des points de contrôle (*checkpoint*). Ces derniers sont présents à trois endroits dans le cycle. On retrouve le premier à la fin de G1. Le point de contrôle G1/S, aussi nommé point de restriction, est le moment après lequel la cellule est dite commise à la division cellulaire et progresse indépendamment de la présence de signaux mitotiques (8). Un inhibiteur empêchant la cellule de s'engager dans le cycle cellulaire est la protéine du rétinoblastome (RB), pour laquelle une discussion détaillée sera tenue plus loin dans ce mémoire, initialement liée à des protéines de la famille de facteurs liant au promoteur E2 (E2F). La phosphorylation de RB par CDK4/6-cyline D, permettra le relâchement d'E2F menant à l'expression des gènes nécessaires à la phase S (8). Le second point de contrôle, *checkpoint G2-M,* à la fin de la phase G2. C'est à ce moment que les mécanismes de régulation s'assurent qu'aucune cellule ne débute la mitose avec de l'ADN endommagé ou encore incomplet. Le franchissement de ce contrôle nécessite l'accumulation progressive de CDK1 et cycline B lors de la phase G2, et ce, jusqu'à l'atteinte d'un seuil activant une boucle de régulation positive via l'activation de la phosphatase *cell division cycle 25* (Cdc25) (9). Finalement, le dernier point de contrôle du cycle cellulaire a lieu lors de la métaphase. Il assure que la séparation cellulaire se produise quand tous les chromosomes sont correctement alignés et attachés au fuseau mitotique. La résolution de cette étape dépend de plusieurs facteurs, notamment de la dégradation progressive de cycline B et donc de l'inactivation de CDK1 (10).

Un autre facteur déterminant du déroulement du cycle cellulaire est l'expression d'inhibiteurs de kinases dépendantes des cyclines (CDKi). À l'inverse des cyclines, ces effecteur antagonisent l'activité des CDK, empêchant la progression dans le cycle. On retrouve deux familles classiques de CDKi : la famille des inhibiteurs de CDK (INK) et la famille des protéines interagissant avec les CDK/protéines inhibitrices de kinases (CIP/KIP). La famille INK est composée de quatre protéines structurellement semblables (p15, p16, p18 et p19). Celles-ci, en se liant à CDK4 et CDK6,empêchent spécifiquement la formation du complexe CDK4/6-CyclinD et leur activation (11). La famille CIP/KIP, quant à elle, comporte trois protéines (p21, p27 et p57).

Ces dernières effectuent leur rôle en se liant au complexe CDK-Cyclin, ce qui les rend capables de se lier et d'inactiver toutes les CDKs du cycle cellulaire (11-15). Ensemble, les interactions entre CDKs, cyclines et CDKis gèrent en majeure partie la progression à travers le cycle cellulaire.

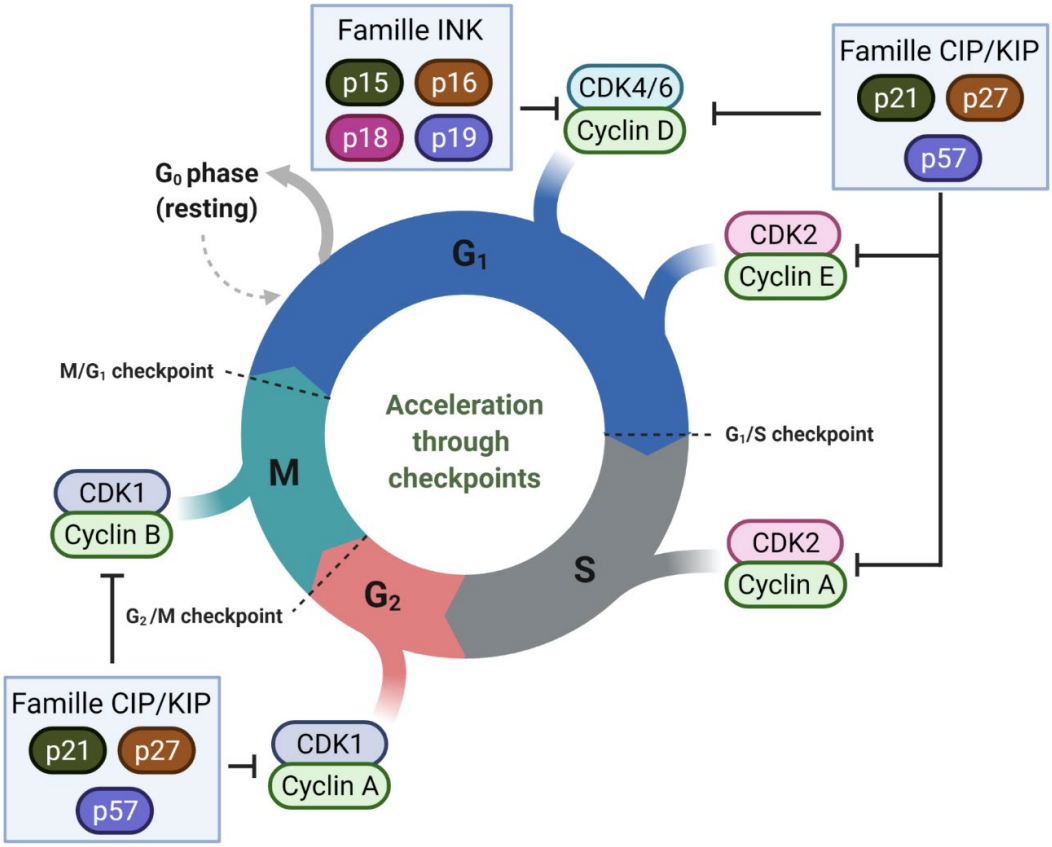

Figure 1. – Phases du cycle cellulaire et leurs régulations

Le niveau d'une cycline varie au cours du cycle cellulaire et l'interaction avec sa CDK correspondante permettant ainsi l'activation de la kinase et la phosphorylation de ses cibles. Les cellules débutent en G1 où l'accumulation de CDK4/6-CyclineD permet la phosphorylation de RB et le passage du point de contrôle G1/S. CDK2-Cycline E débute son accumulation vers la fin de la phase G1 et permet l'entrée en phase S. Le complexe CDK2-CyclineA suivi de CDK1-CyclineA régule le bon déroulement des phases S et G2 jusqu'à leur complétion. Le point de contrôle G2/M s'assure de l'intégrité de l'ADN répliqué avant de poursuivre vers la mitose orchestrée par CDK1-CyclineB. L'effet inhibiteur des familles des CDKis INK et CIP/KIP est mentionné en marge. Cette figure a été basée sur un modèle BioRender et complétée avec des informations provenant des références (2, 7)

1.2. Suppresseurs de tumeurs

Les atteintes au fonctionnement normal de la cellule peuvent être de cause multiple. Que ce soit de nature environnementale, physique, mais aussi génétique, comme lors de l'activation anormale d'oncogènes, des dommages à l'ADN et d'apparition de mutations, l'accumulation de ce genre de défauts peut mener à l'apparition de conséquences délétères pour l'organisme (16, 17). L'une des conséquences possibles et redoutées est la transformation cellulaire, soit transition d'une cellule normale vers un état tumorigénique. Cette transformation s'effectue par l'acquisition de traits spécifiques, les « *hallmarks of cancer* » (figure 2) pouvant ultimement mener au développement d'une tumeur maligne (18).

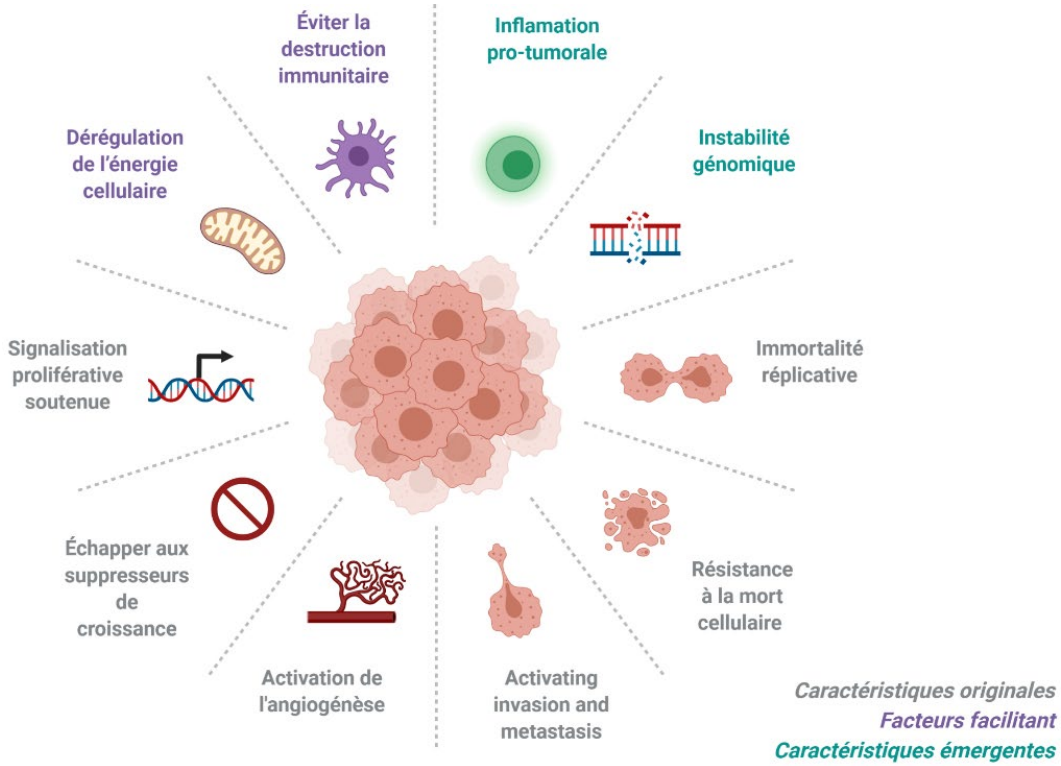

Figure 2. – Caractéristiques du cancer

Cette figure est une adaptation de (18) utilisant un modèle de BioRender. Elle présente les dix caractéristiques du cancer proposées. Dans cette version on retrouve les 8 caractéristiques

initiales, dont deux facilitant l'implantation tumorale, ainsi que deux caractéristiques ayant émergées récemment.

Afin d'empêcher la division des cellules dont le génome a été altéré et ainsi empêcher l'établissement tumoral, on retrouve dans la cellule les suppresseurs de tumeurs. Ceux-ci activent des processus visant la sauvegarde de la cellule via l'arrêt de la prolifération et la réparation des défauts acquis. Il s'agit de mécanismes très efficaces, dans la majorité des cas, bloquant la propagation d'informations génétiques corrompues et l'acquisition de traits favorisant le cancer (19). Dû à l'importance de leur rôle dans l'inhibition de la carcinogenèse, l'inactivation ou encore la mutation délétère d'un ou plusieurs suppresseurs de tumeurs est souvent présente, pour ne pas dire toujours, dans les tumeurs malignes (19, 20).

Les suppresseurs de tumeurs peuvent être classés en trois familles : les gènes de paysagement (*landscapers*), les gènes de stabilisation/réparation de l'ADN (*caretaker*) et finalement les gènes garde-barrières (*gatekeeper)*. Cependant, ces classes ne sont pas indépendantes. En effet, certains gènes peuvent faire partie de plus d'une famille à la fois (21, 22).

1.2.1 Landscapers

L'hypothèse des *landscapers* a d'abord été proposée par Vogelstein et W.Kinzler suite à l'analyse d'études sur le syndrome de polype juvénile, où l'environnement anormal en cellules stromales peut affecter le développement des cellules adjacentes et favoriser le changement néoplasique(23). Aujourd'hui, il est bien connu que l'environnement dans lequel les cellules évoluent a un impact sur la tumorigénicité de celles-ci. En effet, l'établissement d'un contexte inflammatoire pro-prolifératif, ou encore d'un environnement « immunosupprimé » sont certains des facteurs pouvant promouvoir la malignité d'une tumeur (24). Les gènes faisant partie de cette famille de suppresseurs de tumeurs sont impliqués dans des processus tels que la régulation de la matrice extracellulaire, la sécrétion de facteurs de croissance et de survie, l'adhésion cellulaire ou encore les interactions avec le système immun (24).

Les résultats d'études démontrant que la perte de PTEN mènerait à des dommages hépatiques suggèrent ce phénomène. L'apparition chronique de ces dommages causerait un remodelage de l'environnement hépatique, favorisant l'infiltration de cellules inflammatoires. La

sécrétion de cytokines et de chimiokines provenant de cette dernière favoriserait l'hépato carcinogenèse (25, 26). Un autre exemple a démontré que la perte ou la mutation dominante négative de cadhérine épithéliale (E-CAD), une protéine d'adhésion épithéliale, coïncide avec la carcinogenèse des cellules pancréatiques bêta (27).

Par conséquent, comparativement aux autres familles de suppresseurs de tumeurs, qui agissent directement ou indirectement dans la régulation de la prolifération cellulaire, l'effet de la perte ou de la mutation des *landscapers* résulterait en une modulation des interactions entre les cellules et l'environnement créant un espace favorable à la croissance tumorale.

1.2.2 Caretakers

Les suppresseurs de tumeurs inclus dans cette famille agissent indirectement pour supprimer la croissance cellulaire en prévenant l'instabilité génomique. En effet, ils s'assurent de l'intégrité et de la fidélité du génome via la résolution des erreurs de correspondance (MMR), survenant dans la réplication. Ils s'assurent aussi de la réparation des dommages à l'ADN, en passant par la recombinaison homologue (HR) ou la jonction d'embouts non-homologues (NHEJ) (22, 28).

En ce qui concerne les exemples de caretakers jouant un rôle dans la réparation de l'ADN, on retrouve *breast-ovarian cancer susceptibility 1/2* (BRCA 1/2), ainsi que les protéines impliquées médiant la réponse aux dommages à l'ADN (DDR) comme les protéines kinases *ataxia telangiectasia and Rad3-related* (ATR) et *ataxia telangiectasia mutated* (ATM) *(28, 29).* On retrouve aussi MutS Homolog 2 (MSH2) et MutL Homolog 1 (MLH1), deux caretakers bien étudiés, jouant un rôle dans la MMR.

Dû à leur rôle dans l'évitement d'altérations génomiques, l'inactivation ou la mutation de ces gènes n'a pas d'effet initiateur direct sur la tumorigenèse. Cependant, il en résulte une augmentation de la vitesse d'acquisition de mutations favorisant la tumorigenèse, notamment la mutation de suppresseurs de tumeurs garde-barrières (21, 28). Par exemple, la mutation de BRCA 1/2 compte pour près du deux tiers des causes de cancers héréditaires du sein ou de l'ovaire (30). De plus, les mutations germinales des gènes nécessaires au MMR, MLH1 et MSH2, sont associées à un risque augmenté de cancer colorectal, endométrial et plusieurs autres (31).

1.2.3 Gatekeepers

Les gènes garde-barrières sont la troisième et dernière famille de suppresseurs de tumeurs. Par définition, il s'agit de tout gène inhibant directement la prolifération cellulaire. En effet, l'action de ceux-ci peut viser l'arrêt du cycle de prolifération cellulaire, l'induction de la mort cellulaire programmée ou apoptose, ainsi que la promotion de la différenciation cellulaire (21, 22).

Faisant partie de cette famille on retrouve notamment le gène *adenomatous polyposis coli* (APC), connu pour son rôle, lorsque muté, dans l'initiation de la tumorigenèse colorectale (32). Plus importants dans le cadre de ce mémoire, p53 et RB sont deux autres membres de ce groupe.

P53

P53 est un facteur de transcription pléiotropique pouvant être classifié, à la fois, en tant que *gatekeeper* et *caretaker* (22). Il agit en aval de multiples signaux de stress, tels qu'en réponse au DDR, à l'expression oncogénique, au stress endoplasmique, à la perturbation ribosomale et plus encore. Il agit donc comme un senseur central à la situation intracellulaire (33).

En réponse aux signaux de stress subit par la cellule, p53 est activé par sa stabilisation et/ou par modification post-traductionnelle. Dans un contexte normal, p53 subit une dégradation par la E3 ubiquitine ligase *mouse double minute 2 homologue* (MDM2) empêchant son activité (34). Cependant, dans le cas d'un dommage à l'ADN, par exemple, le p53 sera phosphorylé sur sa Ser^{15} suivant l'induction du DDR. Cette modification limite l'effet de MDM2 et stabilise p53 (34, 35).

Comme pour ses activateurs, les fonctions suppressives de tumeurs associées à l'activité de p53 sont étendues et de nouvelles fonctions sont constamment découvertes. À la suite de son activation, p53 peut induire l'apoptose par la transcription de *p53-upregulated modulator of apoptosis* (PUMA) et *Phobol-12-Myristate-13-Acetate-Induced Protein* (NOXA) ou l'arrêt du cycle cellulaire par la transcription de p21 (33, 36). L'induction d'un processus ou de l'autre dépend de l'importance du dommage et de sa durée (36). De plus, p53 est impliqué dans la prévention de l'instabilité génomique. En effet, plusieurs gènes de réparation de l'ADN contiennent des éléments de réponse à p53. Par conséquent, en plus de faciliter les mécanismes de réparation de l'ADN par l'arrêt du cycle cellulaire, l'activation de p53 stimule directement la transcription de gènes de réparation de l'ADN comme MSH1, MLH1 et *DNA damage-binding protein 2* (DDB2) (33, 37). D'autres rôles connus de p53 comprennent par exemple son action sur métabolisme par

la transcription de gènes comme Sestrine 1 et 2 (SESN1/2) et *TP53 Induced Glycolysis Regulatory Phosphatase* (TIGAR) (38) et sur l'autophagie par via *AMP-activated protein kinase* (AMPK) et *damage-regulated autophagy modulator* (DRAM) (33, 39).

Les multiples rôles que joue p53 font de cette protéine un élément fondamental dans la suppression tumorale. Cette importance est d'ailleurs observable lorsque l'on analyse l'impact de son absence/malfonction. En effet, 50 % des cancers vus chez l'homme comportent une mutation du gène TP53 codant pour p53. Cette affirmation est aussi vraie lorsque l'on observe l'amplification MDM2, menant à une réduction du niveau de p53, qui est présente dans 17 % des cancers (33, 34).

RB

Comme pour le cas de p53, l'activité du suppresseur de tumeurs RB est étroitement régulée par une multitude de mécanismes, et ce, principalement par la modification post-traductionnelle de celui-ci (40). Comme mentionné plus haut, RB médie la transition entre la phase G1 et S du cycle cellulaire. En effet, la protéine RB (pRB) ainsi que les membres de sa famille, les *pocket proteins* p107 (*retinoblastoma-like protein 1*) et p130 (*retinoblastoma-like protein 2)*, sont initialement liées aux facteurs de transcription de la famille E2F. Elles répriment ainsi l'expression des gènes nécessaires à cette transition. Suite à l'inactivation par la phosphorylation des protéines de la famille RB, il s'en suit une libération de E2F, qui active la transcription de ces gènes, permettant ainsi l'entrée dans la phase S (8).

D'un autre côté, l'interaction entre RB-E2F peut être stabilisée, renforçant la répression de la transcription. En effet, des sites de méthylation et d'acétylation de pRB ont été identifiés comme induisant une hypophosphorylation de pRB. En réponse à la différenciation ou l'arrêt stable du cycle cellulaire, comme pour la sénescence, pRB serait méthylée au résidu K873 par *SET domain containing lysine methyltransferase 7*(SET7/9) (41). De plus, dans le cadre de la réponse au dommage à l'ADN (DDR), qui sera détaillé plus loin, le site de phosphorylation de pRB est entravé par l'acétylation de K873/874 retenant ainsi pRB sous sa forme active (42). *Checkpoint Kinase 1*(CHK1) et *Checkpoint Kinase 2*(CHK2), aussi activées lors du DDR, phosphorylent pRB au résidu S612 favorisant un complexe entre pRB et E2F-1 (43).

En plus de séquestrer physiquement E2F, le suppresseur de tumeurs RB est aussi impliqué dans la formation d'hétérochromatine au niveau des promoteurs cibles de E2F(44) ,au maintien de

la stabilité génomique, en participant aux mécanismes de réparation génomique (45, 46), et la séquestration d'*Upstream Binding Transcription Factor* (UBF) et *transcription factor IIIB* (TFIIIB), réprimant ainsi l'activité des polymérases I et III (47).

Ces rôles font du suppresseur de tumeurs RB un élément fondamental dans la gouvernance de la prolifération cellulaire. La perte ou encore la mutation de RB fait partie d'un mécanisme majeur dans la tumorigenèse permettant aux cellules cancéreuses d'acquérir un avantage. Par conséquent, la mutation de RB est souvent retrouvée dans le cancer. En effet, l'altération de l'activité de RB est impliquée dans la pathogenèse, la progression, l'invasion métastatique et, par conséquent, à un mauvais prognostique clinique de plusieurs cancers comme l'ostéosarcome, le cancer du sein, des poumons ou encore le rétinoblastome pédiatrique (48).

En résumé, les gènes suppresseurs de tumeurs s'assurent du bon fonctionnement de la cellule en empêchant l'accumulation d'altérations qui mèneraient à une transformation cellulaire et ultimement à une tumeur. L'activation de ces mécanismes antitumoraux, à la suite d'une insulte compromettant la cellule, mènera à un arrêt transitoire de son cycle cellulaire dans le but de permettre le rétablissement cellulaire. Dans le cas où il y aurait une altération trop importante, empêchant ce rétablissement , les mécanismes régulés par les gènes garde-barrières mèneront soit à l'apoptose ou bien à l'arrêt permanent de la prolifération correspondant à la définition de la sénescence (49).

1.3. La Sénescence : un mécanisme antitumoral

À ne pas confondre avec la quiescence, qui a été abordée plus haut, la sénescence cellulaire est un autre mécanisme par lequel la cellule sort du cycle cellulaire. Dans ce cas, comparativement à la quiescence qui elle était un arrêt de prolifération réversible, la sénescence est définie comme un arrêt stable et « permanent » de la réplication en phase G1 du cycle cellulaire, où la cellule reste viable et métaboliquement active (3, 4, 50). Dû à son rôle bénéfique dans plusieurs processus physiologiques, la sénescence cellulaire a reçu beaucoup d'attention dans les dernières années. En

effet, on retrouve son implication dans le développement embryologique (51, 52), la guérison des plaies (53, 54), la réduction des dommages tissulaires (55), sans oublier son rôle central dans la défense contre le cancer, laissant place à son potentiel d'utilisation comme thérapie anticancer (56-58).

Le processus de sénescence a d'abord été décrit par les études de Hayflick et Moorhead en 1961 suivant leurs observations de l'arrêt de prolifération irréversible chez des cellules fibroblastiques cultivé *in vitro (59)*. Cette observation a suggéré l'existence d'une minuterie cellulaire chez les cellules dites normales (non transformées). La découverte des télomères et de leurs érosions à la suite de chaque cycle de réplication de l'ADN a apporté l'explication nécessaire pour confirmer cette hypothèse (60, 61). Aujourd'hui cet arrêt cellulaire survenant lors de l'atteinte du nombre de divisions maximales est connu sous le nom de la sénescence réplicative. Hayflick et ses collègues ont ouvert la porte à un tout nouveau domaine. Les recherches qui ont suivi ont permis d'approfondir nos connaissances des mécanismes régulant la sénescence. En effet, nous savons aujourd'hui que divers stress pouvant affecter la cellule, tels que ceux mentionnés plus haut ou encore le stress oxydatif, les stress chimiques, le dysfonctionnement mitochondrial et d'autres (62, 63), ont tous été associés avec une réponse cellulaire pouvant mener à un phénotype semblable à celui retrouvé dans les expériences d'Hayflick.

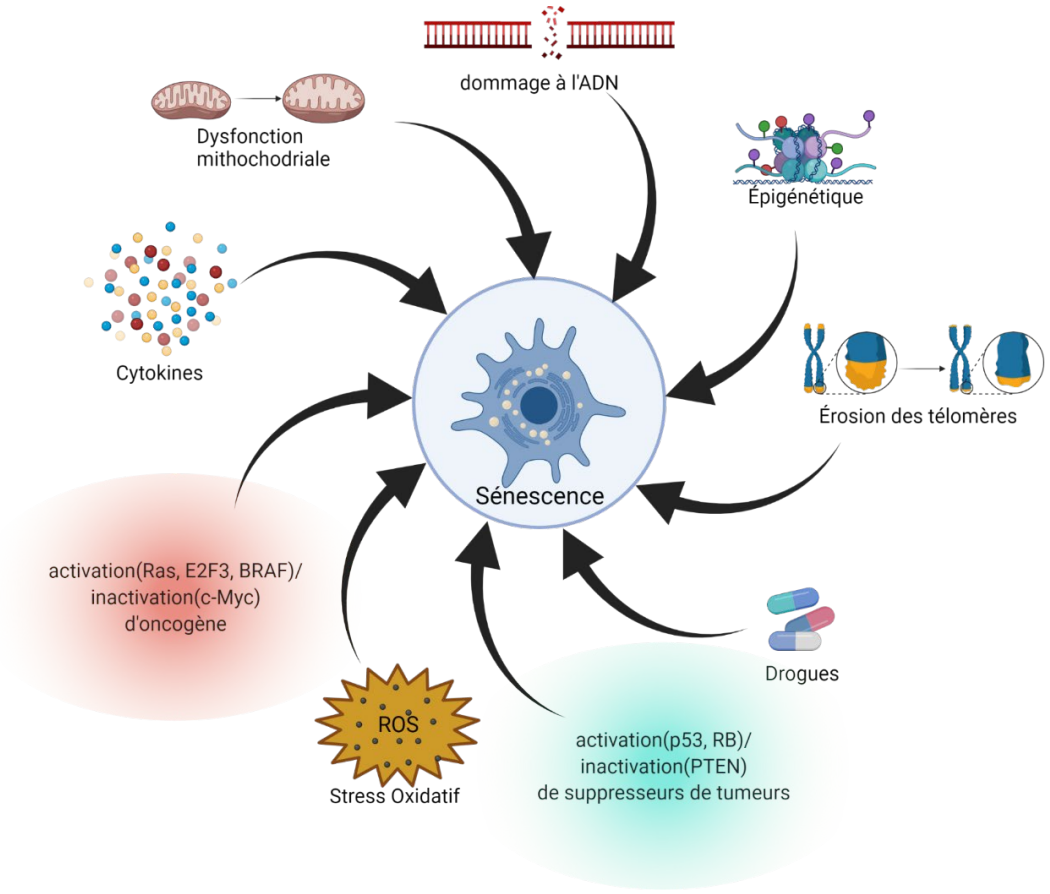

Figure 3. – Causes pouvant mener à la sénescence cellulaire

La sénescence cellulaire peut être la conséquence de plusieurs inducteurs. Ici sont illustrées certaines des causes de la sénescence cellulaire. Cette figure a été confectionnée à l'aide de BioRender avec les informations provenant des références (62, 63).

Chez la cellule, l'activation de la sénescence est accompagnée par plusieurs altérations phénotypiques majoritairement médiées par des changements de l'expression génique. En effet, les cellules sénescentes tendent à démontrer des changements drastiques tels qu'une morphologie large et aplatie, un remodelage extensif de la chromatine, une reprogrammation métabolique et une augmentation de l'autophagie (63-65). On mentionne aussi souvent l'apparition d'un sécrétome spécifique, le phénotype sécrétoire associé à la sénescence (SASP), qui, si présente chroniquement, pourrait entrainer des effets délétères sur l'organisme (66-68). Le manque de données a porté à croire pendant longtemps que tous les types de sénescence cellulaire, peu importe leur voie d'induction, présentaient un mécanisme commun et homogène. Cependant, son étude plus ample a permis de reconnaitre une grande hétérogénéité quant aux voies effectrices modulant la

sénescence et par conséquent aux phénotypes que peuvent présenter ces cellules. Aujourd'hui, on parle plutôt d'un spectre de sénescence. Le type cellulaire, la cause de stress/insulte à la cellule, les conditions extracellulaires, les facteurs génétiques et d'autres contextes cellulaires, régulent ensemble la présentation phénotypique de la sénescence cellulaire complexifiant ce phénomène (69). En effet, l'analyse transcriptionnelle montre un schéma d'expression d'ARNm variant selon la lignée cellulaire, avec peu de superposition (70). Malgré cette variation, il en résulte certaines présentations récurrentes pouvant être résumées dans la figure 4 ci-dessous.

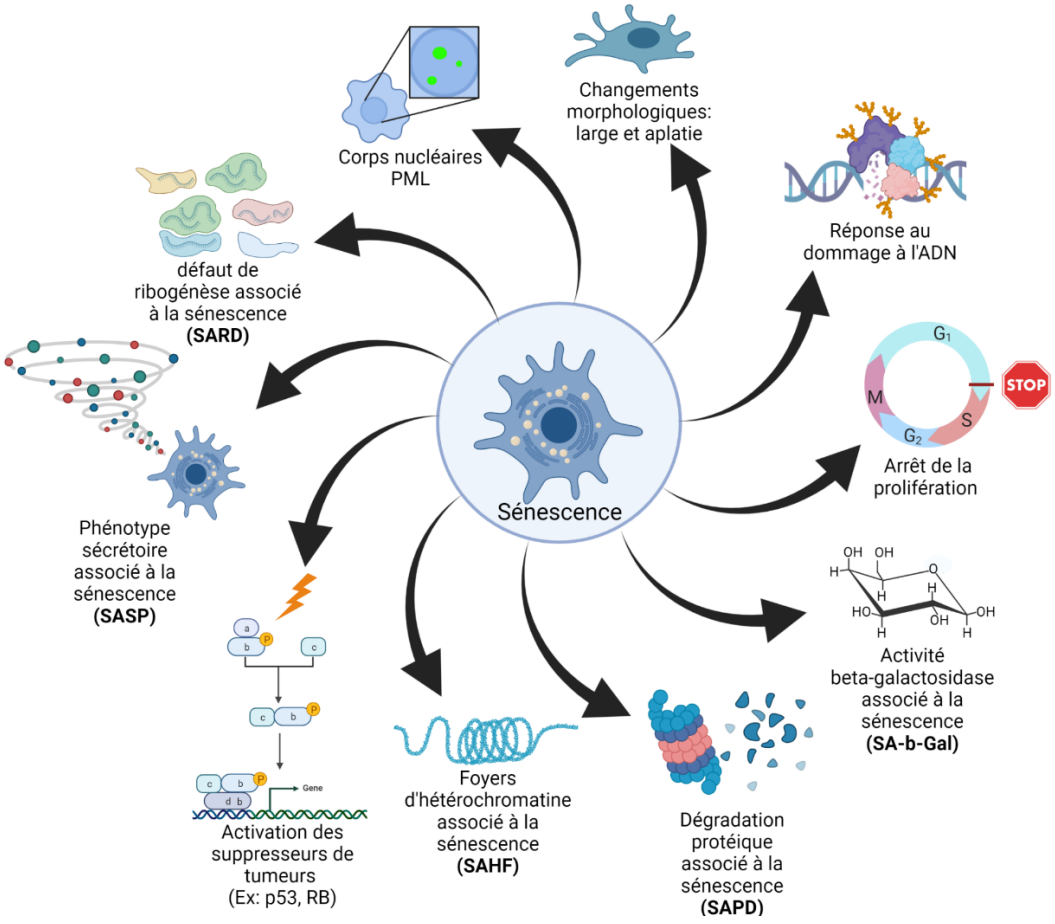

Figure 4. – Caractéristiques des cellules sénescentes

La sénescence cellulaire est un mécanisme antitumoral complexe ayant plusieurs conséquences moléculaires. Cette image souligne certaines de ces caractéristiques connues. Il est cependant pertinent de mentionner que la cellule sénescente peut présenter une combinaison de ces marqueurs sans nécessairement tous les avoir. Cette figure a été confectionnée utilisant BioRender selon les informations provenant des références (62, 65, 71-73)

1.2.1. Mécanisme d'activation de la sénescence

L'arrêt de la prolifération observé dans la sénescence est principalement médié et maintenu par les voies des suppresseurs de tumeurs p53 et p16-RB, celles-ci agissant en réponse à divers stimulus. Elles peuvent exercer leur action de manière conjointe ou encore indépendamment l'une de l'autre (63).

Comme mentionné ci-haut, la sénescence peut résulter de plusieurs types d'altérations. Par exemple, elle peut être le produit d'un épuisement réplicatif menant à l'érosion des télomères, ou encore de l'induction aberrante de mécanisme de réplication causée par l'activation d'oncogène. Un point commun de ces deux phénomènes est la forte et persistante activation du *DNA dammage response* (DDR) (Figure 5) ayant été montrée comme à la fois un mécanisme de causalité et de maintien de la sénescence (65, 74-76). Le DDR résulte en une réponse majoritairement médiée par la voie p53. Cependant la voie p16-RB est elle aussi induite de manière secondaire.

Un moyen par lequel la voie p16-RB est activée est via l'induction du locus INK4/ARF. Celui-ci est généralement réprimé par les complexes de répression *Polycomb*(PRC). Cependant, lors de l'induction de la sénescence, moins de PRCs seraient produits, générant une activation du locus INK4/ARF. En conséquence, p16 et l'*alternate-reading-frame protein* (ARF) sont transcrits. ARF médie l'inhibition de MDM2, affectant le niveau cellulaire de p53, et p16 inhibe l'activité de CDK4/6 (Figure 5) (62).

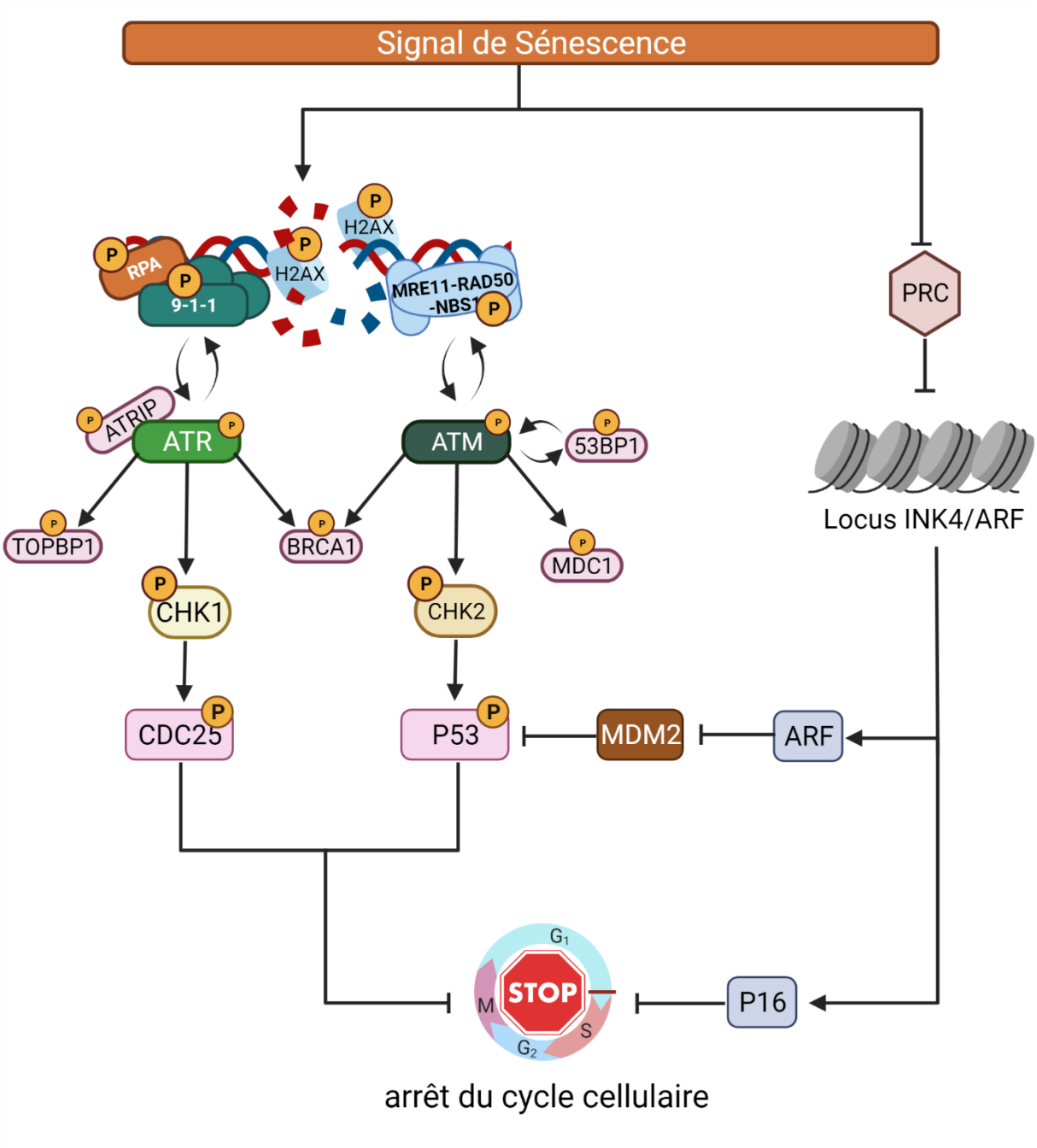

Figure 5. – Cascade d'induction de la sénescence

L'arrêt du cycle cellulaire dans la sénescence est régulé par deux voies majeures : la voie p16-RB et la voie p53. Section de droite : Le locus INK4/ARF, initialement réprimé par PRC, est activé suivant un signal de sénescence. Il résulte en l'expression de ARF et p16 convergeant vers l'arrêt du cycle cellulaire. Section de gauche : La sénescence induit une réponse aux dommages à l'ADN (DDR), dont la cascade est présentée dans cette image. Il en résulte en l'activation de CDC25 et

p53 menant à l'arrêt du cycle cellulaire. Cette figure a été confectionnée utilisant BioRender en adaptant les informations présentes dans les références (62, 63, 76)

1.2.2. Dégradation protéique associée à la sénescence

Outre les modifications transcriptionnelles qui ont été mentionnées brièvement plus haut, il est intéressant d'évoquer que la régulation des niveaux protéiques semble avoir une toute aussi grande contribution dans le contrôle et le maintien du phénotype de sénescence (71, 73, 77).

Dans le cas de la sénescence induite par l'activation de l'oncogène *rat sarcoma viral oncogene homolog* (Ras), notre laboratoire a montré que l'activation continue de la voie *Extracellular signal-Regulated Kinase* (ERK)/*Mitogen-Activated Protein Kinase* (MAPK) conduit à la dégradation dépendante du protéasome de protéines spécifiques. Ce phénomène, que nous avons nommé *senescence-associated protein degradation* (SAPD) ciblerait plus de 1000 protéines dont plusieurs favorisent la sénescence et inhibent la transformation cellulaire (73). Les fonctions cellulaires dans lesquelles participent les protéines identifiées sont vastes, mais comprennent principalement la régulation du cycle cellulaire, la biogenèse des ribosomes, la fonction mitochondriale, la gestion du stress protéotoxique, ainsi que la modification cytosquelettique, la motilité et l'adhésion cellulaire (71, 73). Dû aux protéines ciblées et à leurs fréquentes implications dans la sénescence, il a été proposé que le SAPD aiderait l'établissement et le maintien de la sénescence (71).

1.2.3. Déficience de la biogenèse des ribosomes dans la sénescence

Le ribosome est constitué d'environ 80 protéines ribosomales assemblées sur 4 ARN ribosomaux (ARNr). Il est divisé en 2 sous-unités, la petite sous-unité 40S, comportant l'ARNr 18S ainsi que 33 protéines ribosomales de la petite sous-unité (RPS), et la grande sous-unité 60S, comportant l'ARNr 5S, 5,8 S et 25S ainsi que 46 protéines ribosomales de la grande sous-unité (RPL) (78). Comme anticipé et à cause de la quantité de particules nécessaires pour le former, sa biogenèse est un procédé complexe se déroulant en majorité dans le nucléole, un sous-compartiment non membraneux du noyau cellulaire, mettant en action près de 200 protéines et requérant la participation de chacune des trois polymérases (79).

La biogenèse du ribosome débute dans le nucléole par la transcription du pré-ARNr 35S par l'ARN polymérase I (pol I). Ce transcrit donnera naissance à l'ARNr 18S, 25S et 5,8 S. Le 4^{e} ARNr, le 5S, est quant à lui transcrit par l'ARN polymérase III (pol III). L'ARNr précurseur (pré-ARNr) initialement synthétisé doit être soumis à un processus de maturation. Ces étapes de maturation comprennent le clivage d'ARN excédentaire, la 2'-O-méthylation et la pseudouridylation (79). L'implication de facteurs guidant la biogenèse est constante. Par exemple, le bon repliement des composants du ribosome est médié par des chaperonnes, alors que de petits ARN nucléolaires (snoRNA) et ribonucléoprotéines (snoRNP) orchestrent les modifications des pré-ARNr (79). Finalement, les ARNr sont assemblés à leurs protéines destinées et exportées vers le cytosol donnant naissance aux deux sous-unités ribosomales 40S et 60S (79).

De façon intéressante, les protéines impliquées dans la biogenèse du ribosome ont été impliquées dans le mécanisme de sénescence. Notamment la *Ribosomal L1 domain-containing protein 1* (RSL1D1) a été observée comme un régulateur important dans la sénescence réplicative *(80).*Également, l'activation de p53 aurait été démontrée comme inhibant le transport des ARNr et des protéines ribosomales, ainsi que la traduction des ARNr (81, 82). D'un autre côté, les cibles du SAPD présentent plusieurs protéines nucléolaires ou associées à la biogenèse du ribosome (Tableau 1) et supportent ainsi l'importance de ce processus dans la sénescence. Un article récent de notre laboratoire a renforcé cette idée en démontrant que l'induction de la sénescence menait à une réduction de la biogenèse du ribosome et à l'accumulation de précurseurs d'ARNr et de protéines ribosomales. De plus, l'accumulation de ces facteurs (p. ex. RPS14) par *Senescence-associated ribosome biogenesis defect* (SARD) contribuait à l'arrêt du cycle cellulaire (72). Outre une ribogenèse perturbée, la traduction chez la cellule sénescente est à la fois diminuée et augmentée en ciblant la synthèse d'un bassin de protéines précis, notamment celles impliquées dans le SASP (83). Ce paradoxe s'explique probablement par l'activation de la voie de *mammalian target of rapamycin*(mTOR) dans la sénescence (65).

Tableau 1. – Protéines nucléolaires ou associées à la biogenèse du ribosome ciblé par le SAPD

Protéine	*Fonction associée*
CCDC86	*Maturation de l'ARNr de la large sous-unité 60S (5,8 S et 25S)(84)*
DDX21	*Hélicase à ARN, maturation du pré-ARNr(85, 86)*
DDX24	*Hélicase à ARN, maturation de pré-ARNr(87)*
DDX42	*Hélicase à ARN, maturation de pré-ARNr(87)*
DDX51	*Hélicase à ARN, maturation de l'ARNr 28S(88)*
NCL	*Implication dans chaque étape de la biogenèse du ribosome : la transcription, la maturation d'ARNr, le transport nucléoplasmic et l'assemblage(89)*
NOC2L/NIR	*Maturation de l'ARNr 18S, 28S et 5,8 S(90)*
NOLC1	*Régulateur transcriptionnel de l'ARN pol I, organisation spatiale du nucléole(91)*
NOL6/NRAP	*Maturation de l'ARNr 18S(92)*
NOP56	*Composant de la boite SnoRNPs C/D(93)*
NOP58	*Composant de la boite SnoRNPs C/D(93)*
NPM1	*Assemblage et transport du ribosome, duplication des centrosomes, activité chaperonne, activité endonucléase, régulation de la voie ARF-p53, réparation de l'ADN (94)*
RPLP1	*Protéine ribosomale, sa surexpression permet le contournement de la sénescence réplicative(95)*
RPL23	*Protéine ribosomale, régulateur négatif de l'apoptose(96)*
RSL1D1	*Impliquée dans la maturation d'ARNr(87), contrôle la localisation de nucléostémine(97), inhibé en sénescence(80)*

Tableau adapté de (73) et (71)

Malgré la lumière apportée par ces découvertes, l'ampleur des conséquences que peut avoir le SARD sur les mécanismes cellulaires en sénescence est encore à découvrir. Cependant, nous pouvons nous demander quel est l'impact sur la machinerie traductionnelle? En effet, la constitution du ribosome pourrait-elle être changée ? Menant le ribosome à acquérir des fonctionnalités pouvant différer, tel que le suggère l'idée de l'hétérogénéité ribosomale (98).

Finalement et plus pertinemment à ce mémoire, est-ce que le défaut de la ribogenèse pourrait avoir un impact sur la qualité de la traduction en sénescence ?

1.4. La traduction : d'ARNm à la protéine

La traduction génétique est l'étape permettant de transformer l'information comprise dans le génome cellulaire en protéine active et fonctionnelle pouvant contribuer aux mécanismes cellulaires. En plus d'être un phénomène virtuellement indispensable au fonctionnement de la cellule, la traduction est aussi l'une des activités cellulaires les plus couteuses énergétiquement (99, 100). En effet, elle consommerait près de 20 % de l'énergie produite par la cellule via la chaîne respiratoire (99).

La synthèse protéique est divisée en 4 étapes : l'initiation, l'élongation, la terminaison et le recyclage. Afin d'empêcher les effets néfastes potentiels que pourraient avoir des erreurs de la traduction, ces étapes sont régulées et orchestrées par divers facteurs assurant le bon fonctionnement du processus (101, 102). Dans le cadre de ce mémoire, les prochaines pages aborderont les étapes et acteurs participant à la terminaison de la traduction.

1.4.3 Terminaison et recyclage

La terminaison survient lorsque l'un des trois codons d'arrêt (UGA, UAG, UAA) entre au sein du site A du ribosome et est reconnu par le facteur de terminaison 1 (eRF1) lié au facteur de terminaison 3 (eRF3) (103). La structure générale d'eRF1 ressemble à celle d'un ARN de transfet (ARNt) et comporte 3 domaines (N, C et M). Le domaine « N » est responsable l'interaction avec la séquence de terminaison, alors que le domaine « C » est celui permettant la liaison d'eRF3. Le domaine « M », quant à lui, comporte le motif GGQ et est l'élément catalytique d'eRF1(104, 105). Ce motif hautement conservé, permet d'induire l'hydrolyse du lien ester entre l'ARNt du site P du ribosome et la chaine peptidique naissante, relâchant celle-ci (103). L'insertion d'eRF1-eRF3 ; GTP au site A du ribosome, avec la présence d'appariement spécifique, stimule l'activité GTPase d'eRF3 et cause hydrolysation du GTP en GDP. La résultante est un changement conformationnel du complexe de terminaison menant à l'accommodation d'eRF1 dans le site A et le placement du motif GGQ près de son site d'action (103, 104). La relâche du peptide marque la fin de la synthèse protéique et l'initiation du recyclage de la machinerie.

Remarquablement, la structure induite au centre de décodage par l'interaction entre eRF1 et le codon d'arrêt cause une compaction de l'ARNm permettant le nucléotide en position +1, selon le site de terminaison, d'être accommodé dans le site A (104). Une interaction médiée par le 4^{e} nucléotide envers les facteurs de relâche supporte l'existence d'un rôle de ce dernier dans la régulation de l'efficacité de terminaison (104, 106). Il a donc été proposé que les facteurs de relâche reconnaissent un tétranucléotide plutôt qu'une séquence trinucléotidique (106). Malgré la complexité déjà apparente du processus terminaison de la traduction, plusieurs études proposent même une implication dans l'efficacité de la terminaison des 6 nucléotides suivant le codon-stop (+9) ainsi que de ceux précédents le codon d'arrêt (107-109).

La synthèse de protéines est un processus cyclique où les complexes initiant la traduction dérivent du recyclage de la machinerie traductionnelle suivant la terminaison d'un autre évènement traductionnel (110). Afin de permettre ce recyclage, *l'ATP Binding Cassette Subfamily E Member 1* (ABCE1), une ATPase aussi connue sous le nom de RLI1, prend la place d'eRF3 et se lie au complexe post-traductionnel (103, 104). L'hydrolyse d'ATP et le relâchement d'ADP génèrent l'énergie nécessaire pour induire le changement structural nécessaire à la dissociation des deux sous-unités ribosomales (103). L'ARNt dé-acylé restant ancré sur la sous-unité 40S sera dissocié lors de l'initiation d'une traduction suivante par les facteurs d'initiation eIF3, eIF1 et eIF1A (103, 110). De surcroit, plus qu'uniquement impliqué dans le recyclage, des études ont montré que l'absence d'ABCE1 avait un impact sur l'efficacité de la terminaison, suggérant un rôle de celui-ci dans l'entièreté du mécanisme (111, 112). La figure 6 résume les étapes de la terminaison de la traduction et du recyclage de la machinerie traductionnelle.

Il est clair que la régulation de la terminaison est complexe et implique divers facteurs autant externes (trans-acting) qu'internes (cis-acting) à la séquence ARNm (103). De manière intéressante, l'action modulatrice d'efficacité de la terminaison de ces facteurs a été rarement suspectée jusqu'à leurs découvertes. Par exemple, certaines études ont fait le lien entre les facteurs d'initiation, comme eIF3 et eIF5A, et la translecture du codon d'arrêt, phénomène qui sera discuté en profondeur prochainement (113-115). En effet, eIF3 interfèrerait avec l'eRF1 favorisant l'insertion d'un AA-ARNt au site du codon d'arrêt permettant la poursuite de la traduction en 3'UTR (113). Dans le cas de eIF5A, il aiderait à l'hydrolyse du lien peptidyl-ARNt et sa déplétion

causerait une forte diminution de l'efficacité de la terminaison (114, 115). Finalement, certaines hélicases d'ARN à domaine DEAD-box(DDX), comme DDX19 pourraient stimuler une terminaison adéquate (116).

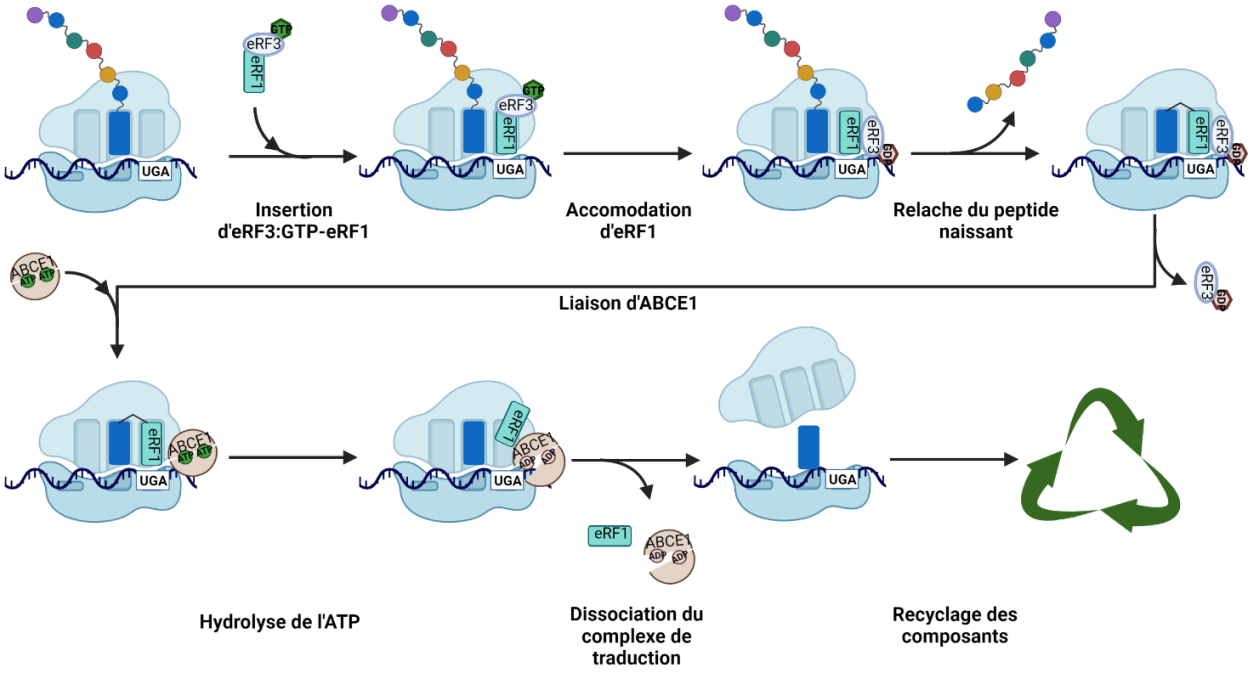

Figure 6. – Terminaison de la traduction et recyclage de la machinerie traductionnelle

La partie du haut présente la terminaison de la traduction. La protéine eRF3 : GTP-eRF1 lie le site A où eRF1 reconnait le codon d'arrêt. L'hydrolyse du GTP par eRF3 permet l'accommodation d'eRF1 au centre de peptidyl-transférase du ribosome. Cette accommodation positionne le motif GGQ d'eRF1 de façon à induire le relâchement du peptide naissant. La section du bas présente le mécanisme de recyclage de la machinerie traductionnelle. ABCE1 lie eRF1 suivant la terminaison de la traduction. L'hydrolyse de l'ATP donne l'énergie nécessaire pour dissocier les deux sous-unités ribosomales. Cette figure est adaptée de (103) utilisant BioRender.

1.4.4 Erreurs traductionnelles

Afin d'obtenir une protéine dite fonctionnelle, la traduction doit être fidèle. Cependant, les erreurs ne sont pas inévitables et mènent à l'apparition de changements dans la séquence d'acides

aminés de la protéine synthétisée. Dans la littérature, ces erreurs sont appelées des mutations phénotypiques et sont plutôt fréquentes chez les organismes vivants. En effet, chez *Escherichia coli,* le taux d'erreurs survenant lors de la synthèse d'une protéine est estimé à environ 10^{-3} à 10^{-4} erreurs de lecture par codon (117). Ce genre de mutations survient principalement à la suite d'une sélection inexacte de l'ARNt. Par contre, le changement du cadre de lecture (*frameshift*), dont l'occurrence est estimée à 10^{-5} par codon (118), et la mauvaise synthèse de l'ARNt, survenant à environs 10^{-4} par synthèse (119), peuvent résulter en l'apparition d'erreurs de la traduction. Les recherches chez la bactérie et la souris ont su montrer les conséquences néfastes qu'ont les erreurs lors de la synthèse des protéines sur la viabilité de l'organisme (118, 120). En effet, dans la majorité des cas, les peptides résultants de ces erreurs survenant de manière aléatoire seront non-fonctionnels (118).

Malgré les effets délétères que peuvent avoir les erreurs de traduction à court terme, une grande proportion d'organismes, virus comme mammifère, ont su évoluer de sorte à tirer parti de ces erreurs (118). Le *frameshift* programmé, par exemple, est l'un du mécanisme le plus largement utilisé pour générer la synthèse de gènes dépendants des erreurs de traduction (118, 121). Le *frameshift* consiste en un « glissement » du ribosome d'un seul nucléotide vers l'extrémité 5' (-1) ou l'extrémité 3' (+1) lors de l'élongation (118, 121). Comparativement aux évènements non programmés survenant de manière randomisée, la présence d'une séquence « glissante » heptaédrique suivie d'une structure pseudo-noeud ou tige-boucle permet de favoriser l'occurrence d'un *frameshift* à un endroit désiré, programmant celui-ci (121). Les sous-unités τ et γ de l'ADN polymérase III d'E.Coli, l'antizyme ornithine décarboxylase (OAZ) inhibant l'enzyme ornithine décarboxylase (ODC) chez les eucaryotes, ainsi que certaines protéines de réplications (p. ex. la polyprotéine GAG-Pol) chez les virus notamment le VIH-1 et le SARS-CoV2, sont quelques exemples de l'utilisation du *frameshift* (122-125).

Outre la production de protéines en dépendant, les erreurs traductionnelles ont le potentiel de révéler des séquences cryptiques, présentes au sein du génome, causant une modification de la fonction ou de la localisation d'une protéine (118, 126-130). De plus, s'il s'agit de nouveaux phénotypes, ceux-ci peuvent être bénéfiques pour la lignée les développant (118, 131). D'un autre côté, les erreurs de synthèse peuvent « supprimer » des mutations délétères (118). Il s'agit d'ailleurs de la raison pour laquelle une importance a été attribuée à certains composés favorisant l'infidélité

traductionnelle pour le traitement de maladies comportant un codon d'arrêt prématuré (mutation non-sens), comme la fibrose kystique ou la dystrophie musculaire de Duchenne (132, 133).

1.4.5 Translecture du codon d'arrêt

Comme abordé ci-haut, la traduction n'est pas un processus fiable à 100% et, comme discuté précédemment, l'efficacité de terminaison peut elle aussi être modulée et laisser place à des erreurs. Plusieurs mécanismes naturels existent pour supprimer la terminaison traductionnelle et permettent de poursuivre la traduction au-delà de la région *open reading frame* (ORF). Le *frameshift* en est un exemple (134).

Un autre mécanisme permettant la suppression de la terminaison survient lorsque le codon d'arrêt est lu comme un codon sens, codant pour un acide aminé (AA), et un AA-ARNt est inséré au site A du ribosome. Ce phénomène est communément appelé « translecture du codon d'arrêt » ou « *translational readthrough* » (TR) et est un autre exemple d'erreur traductionnelle (134). Il s'agit d'un mécanisme biologique qui surviendrait spontanément dans 0,02% à 1,4% des synthèses de protéines (135). Cependant, d'abord observé chez les virus, le *readthrough*, comme pour le *frameshift*, permet d'utiliser les erreurs traductionnelles pour optimiser le potentiel codant de leur petit génome et semblerait survenir de manière programmée (134, 136). Par exemple, le rétrovirus *Moloney Murine Leukemia Virus* (MMuLV) utilise une structure pseudo-nœud en aval de la région du codon d'arrêt du gène GAG afin d'induire le TR dans environ 5% des traductions (137). D'ailleurs, plusieurs études ont aujourd'hui montré l'occurrence du TR chez les procaryotes et les eucaryotes tels que *E.coli, Saccharomyces cerevisiae* ainsi que chez l'humain (134, 138).

Conséquence et prévalence de la translecture du codon d'arrêt

Dans le cadre du TR, le codon de terminaison initial est interprété comme un codon sens, permettant ainsi la continuation de la traduction et la production d'une protéine comportant une extension à l'extrémité C-terminale. Cette extension peut apporter des modifications du fonctionnement, par l'ajout de domaines permettant de nouvelles interactions protéine-protéine, et de la localisation, en ajoutant un signal de localisation cellulaire à un compartiment (134). Un exemple réside chez les champignons où la Glycéraldéhyde-3'-phosphate déshydrogénase (GAPDH) et la 3'- phosphoglycerate kinase (PGK), des enzymes glycolytiques, encodent un signal de localisation peroxisomal type 1 (PTS1) dans leur région cryptique 3'UTR (139). La translecture du codon d'arrêt chez ces enzymes leur permet donc d'être localisées au sein du peroxysome, un

organite cellulaire impliqué dans la métabolisation des acides gras, acides aminés et dans la réduction des dérivés réactifs de l'oxygène (ROS ou DRO) (139, 140). À l'opposé , les mutants n'ayant pas la forme proximale auraient montré une diminution quant à leur virulence (139). Chez les organismes plus développés, le rôle du TR n'est cependant pas encore clair. En revanche, la fréquence de TR n'en est pas moins importante, puisque l'utilisation d'approches systématiques, comme une approche phylogénique, chez *Drosophila melanogaster* a montré 283 gènes candidats au TR. D'un autre côté, le profilage de ribosome chez le même modèle a identifié 350 gènes candidats dont 43 concordent avec les résultats phylogéniques. En utilisant ces mêmes approches, plusieurs candidats de TR chez l'humain ont été proposés et plusieurs furent confirmés (138). Comme mentionné plus haut, on estime à environ 0.02% à 1.4 % la fréquence du *readthrough* spontané (135). Cependant, chez l'humain 4 gènes, codant pour l'Aquaporine 4 (AQP4), le récepteur à opioïde Kappa 1 (OPRK1), l'*Opioid Related Nociceptin Receptor 1* (OPRL1) et le *Mitogen-Activated Protein Kinase 10*(MAPK10), ont démontré une efficacité de TR allant jusqu'à 31% du niveau total de leur traduction (141). D'autres exemples de gènes humains ayant une grande efficacité de TR seraient l'Argonaute 1 (AGO1), la malate déshydrogénase 1 (MDH1), le facteur de croissance endothéliale vasculaire A (VEGFA) et la lactate déshydrogénase bêta (LDHB) (126, 142-144).

Également, les formes étendues de ces derniers, ainsi que d'AQP4, ont été observées comme étant fonctionnelles, signifiant que leur extension C-terminale leur confère une fonction additionnelle. Dans le cas AQP4x, l'isomère allongé d'AQP4, l'enzyme permet de moduler la formation de groupes supramoléculaires et est nécessaire pour l'ancrage d'AQP4 chez les astrocytes du système nerveux central (129, 145). Semblables aux observations de GAPDH et PGK chez les champignons, MDH1x et LDHBx, eux, exprimeraient un signal PTS1, permettant la localisation d'une portion de ces enzymes au peroxysome (126, 142). AGO1x, contrairement aux autres membres la famille argonaute agissant au cytosol, se localiserait au nucléole et interagirait avec le Polyribonucleotide nucleotidyltransférase 1(PNPT1). De cette façon il peut prévenir les signaux interférons induits par le bris du double brin d'ADN (143). Finalement, l'extension de VEGFA changerait sa fonction le faisant passer de proangiogénique à antiangiogénique (144). Cette observation est toutefois controversée puisqu'une étude aurait montré un effet proangiogénique de VEGFAx (146).

Facteurs influençant la translecture du codon d'arrêt

Comme mentionné précédemment, les facteurs influençant l'efficacité de terminaison ont la capacité d'induire ou de limiter l'occurrence de TR. Le TR peut survenir spontanément à la suite de chacun des trois codons d'arrêt, cependant l'occurrence basale varie en fonction de la nature de la séquence trinucléotidique ainsi que selon le contexte de terminaison qui l'entoure (107-109, 134). En effet, l'expérience sur des lignées cellulaires a produit une échelle de fidélité de terminaison où UAA correspond au moins susceptible au *readthrough* alors que UGA serait le plus permissif (UAA<UAG<UGA) (134). Comme mentionné, la conformation spatiale que prend l'ARNm permet l'insertion d'un 4^{e} nucléotide au sein du site A (104). La présence d'une cytidine suivant le codon d'arrêt aurait le plus de chance d'induire le TR, suivi de l'uracile, la guanine et l'adénine (C>U>G>A) (134). Cela expliquerait en partie la prévalence élevée chez les mammifères de certaines de séquence UNN-N par rapport à d'autres (106). En accord avec la proposition suggérant que les nucléotides suivant la position +4 auraient un impact sur l'efficacité de terminaison (107), des motifs stimulants le *readthrough* ont été proposés (134). Chez les virus, UAG-CAAUYA, UGA-GGG/UGA-CUA et UGA-G suivie d'une structure pseudo-nœud sont 3 types de motifs rencontrés (134). Chez les eucaryotes des motifs semblables ont été retrouvés notamment UNN-CA(A/G)N(U/C/G)A, CAAUUA étant le plus efficace, chez la levure (147) et UGA-CUAG chez la lignée HEK-293T provenant de cellules épithéliales rénales humaines (141). Le TR implique une compétition entre le facteur de relâche eRF1 et les ARNt dont l'anticodon est semblable au codon d'arrêt, *near-cognate tRNA* (nc-ARNt), dit d'ARNt suppresseurs (134). Ces nc-ARNts se baseraient sur un pairage de bases alternatif afin de permettre leur incorporation (148). De plus, d'une manière semblable à l'association ARNt-codon sens, UAA serait sensible au TR avec l'ARNt^{tyr}, l'ARNt^{Gln}, l'ARNt^{Arg} et l'ARNt^{Lys}. UAG, quant à lui, est sensible au *readthrough* par l'incorporation de l'ARNt^{Tyr} et l'ARNt^{Arg}, alors que le TR de UGA peut être facilité par l'incorporation de l'ARNt^{Gln}, l'ARNt^{Lys}, l'ARNt^{Cys} et l'ARNt^{Trp} (149, 150). Par conséquent, l'abondance de ces derniers, comme pour l'abondance des facteurs de relâche, peut grandement impacter l'occurrence de TR (134).

Translecture du codon d'arrêt et implication du pathologique

Il est clair qu'il existe un paradoxe quant à l'utilité de la translecture du codon d'arrêt. D'un côté, tel que mentionné plus haut, un taux élevé d'erreurs traductionnelles s'est montré délétère dans plusieurs cas. Nonobstant, il s'agit aussi d'un moyen d'optimiser la capacité génique (p. ex. les virus) et certaines bactéries surent profiter du *readthrough* pour répondre à des conditions de stress et s'adapter à leur habitat (131). Chez l'humain, les observations obtenues jusqu'à présent ne permettent pas de juger de ce mécanisme conservé au fil de l'évolution et son rôle reste encore controversé.

Les mutations non-sens, ajoutant un codon d'arrêt prématuré (PTC), comptent pour approximativement 11% des désordres génétiques chez l'humain (151). Ces ARNm comportant un PTC ne peuvent pas être traduits en protéine et seront la cible du *nonsense mediated mRNA decay* (NMD) (152). Dans cette situation, le TR s'avère un moyen pour les cellules d'exprimer ces gènes en contournant le PTC. C'est ce qu'a proposé Jia et ses collègues ayant observé un modèle de PTC *readthrough* prenant place dans ce qu'ils qualifient de « *readthrough bodies»* en présence d'UPF (153), une famille de protéines au centre du mécanisme du NMD (152).De plus, l'utilisation du TR pour produire des isoformes comme AQP4x, dont la présence semble nécessaire au bon fonctionnement du système nerveux central (129, 145), supporterait le rôle avantageux de ce mécanisme biologique.

En contrepartie, l'effet adaptatif observé chez certaines bactéries pourrait avoir lieu dans des pathologies malignes comme le cancer. Une observation supportant cette idée provient des études sur LDHBx et MDH1x ayant montré un niveau particulièrement élevé de TR dans certaines lignées cancéreuses, notamment les cellules de glioblastome U118 (126, 142). Une augmentation du métabolisme du peroxysome pourrait s'avérer un avantage pour le cancer (154). De plus, AGO1x, par son action sur les signaux interférons, favorise la prolifération cellulaire et son expression augmentée a été observée dans des cellules provenant de cancer du sein (143).

D'un autre côté, des observations montrant une dérégulation des facteurs impliqués dans la traduction amènent à croire que les cellules cancéreuses génèrent une plasticité traductionnelle afin de potentialiser leur progression et leur résistance (155). L'altération de l'expression et de la synthèse des ARNt, positivement régulés par les oncogènes, retrouvée dans le cancer en serait un exemple (156). La reprogrammation traductionnelle chez le cancer semble aussi mener à des

niveaux anormaux de facteurs de traduction comme eIF4F, eIF2 ou encore eEF1Ba, ce dernier ayant été associé avec un mauvais pronostique lors de cancer gastrique (155, 157). Finalement, la composition des ribosomes s'est avérée elle aussi modifiée acquérant des fonctions avantageuses pour la cellule cancéreuse, d'où le concept d'«onco-ribosome» (158). En effet, chez les patients pédiatriques atteints de leucémie aiguë lymphoblastique à cellules T(T-ALL), la mutation RPL10-R98S induit la formation de ribosomes défectueux ayant une fidélité traductionnelle réduite (159).

1.5. Problématique et hypothèse de travail

La perturbation de la biogenèse du ribosome, par la dégradation ciblée de protéines du nucléole dans la cellule sénescente, a mené notre laboratoire à se questionner sur les conséquences traductionnelles en résultant. Parmi les conséquences possibles touchant la traduction, notre équipe s'est arrêtée sur celles affectant la fidélité traductionnelle, notamment l'efficacité de la terminaison dont le rôle s'est montré controversé dans le passé. Ainsi, nous avons porté comme hypothèse que la perturbation de la biogenèse du ribosome dans le contexte de sénescence cause une altération de la fidélité traductionnelle, notamment au niveau de la terminaison. Afin d'explorer cette hypothèse, le laboratoire a élaboré des expériences d'étude du TR basé sur la technique d'essai double-luciférase en contexte de sénescence ou non. Les résultats initiaux ont montré une diminution significative de la translecture du codon d'arrêt dans la sénescence.

D'un autre côté, la transformation cellulaire dans un contexte de cellules cancéreuses nécessite l'augmentation de la synthèse protéique. Pour favoriser cet effet, la biogenèse de la machinerie de traduction, soit les ribosomes, est augmentée dans la tumorigenèse. De plus, l'altération des effecteurs de la traduction s'est avérée jusqu'à présent être un avantage évolutif pour le cancer. En nous basant sur nos résultats en sénescence, nous avons exploré l'efficacité de la terminaison à la suite de l'échappement de la sénescence en suggérant qu'il s'agisse d'un processus avantageant la carcinogenèse.

Par conséquent, ces informations nous ont conduits à approfondir l'étude du TR dans le contexte de la sénescence, et ce, en proposant un nouveau moyen pour la sénescence d'empêcher la progression tumorale.

1.5.1 Contribution supplémentaire

Dans le cadre de cette maitrise, j'ai également contribué à l'étude des altérations du métabolisme cellulaire en particulier le métabolisme de la nicotinamide adénine dinucléotide (NAD) et l'homéostasie mitochondriale dans le contexte de sénescence. Dans cet article, présenté dans l'annexe 1, nous avons caractérisé un nouveau complexe multienzymatique ayant la capacité de reprogrammer le métabolisme cellulaire et de contourner la sénescence. Ce complexe a été nommé HTC pour complexe de transfert hydrure permettant le transfert de l'ion hydrure du NADH vers le NADPH.

Chapitre 2: La sénescence cellulaire limite la translecture traductionnel

2.1. Contribution à l'article

Ce projet a été débuté initialement par une étudiante au PhD du laboratoire. À mon arrivée à la maitrise, j'ai repris le projet en question afin de le terminer. J'ai, dans un premier temps, participé à la validation et reproduction des données de l'article qui avaient été acquises initialement (figure 1G, Figure 2A et Figure 3). J'ai aussi participé à l'investigation supplémentaire des données manquantes qui ont mené à la publication de l'article. Notamment dans la recherche du marqueur endogène TR, dans l'application de notre modèle dans des lignées cellulaires cancéreuses et finalement dans l'implication des protéines du ribosome dans la réduction de TR. Mon implication a, en outre, permis l'élaboration des figures suivantes : figure 5 G-J et figure 6 A-C. J'ai aussi participé à la confection de la méthode, à l'acquisition des données et à leur analyse. J'ai aussi apporté mon aide dans la méthode, l'acquisition et l'analyse des données ayant permis l'élaboration de la figure 6 D-G. Bien que non présenté dans l'article, j'ai participé aux tentatives initiales d'acquisition de données, utilisant une autre méthode (Western blot), pour la confection de la figure 7. J'ai aussi participé au processus de publication de cet article, soit à la confection des figures, à l'édition, à la révision ainsi qu'en partie à son écriture. Cet article auquel je suis 3^{e} auteur est maintenant publié dans la revue *Biology Open.*

2.2. Article 1

Cellular senescence limits translational readthrough

(160)

Neylen Del Toro [1], Frédéric Lessard [1], Jacob Bouchard [1], Nasrin Mobasheri [1], Jordan Guillon [2], Sebastian Igelmann [1 2], Sarah Tardif [1], Tony Buffard [1], Véronique Bourdeau [1], Léa Brakier-Gingras [1], Gerardo Ferbeyre [1 2]

Affiliations :

[1]Département de Biochimie et Médecine Moléculaire, Université de Montréal C.P. 6128, Succ. Centre-Ville, Montréal, Québec, H3C 3J7, Canada.

[2]CRCHUM-Université de Montréal, 900 Saint-Denis, bureau R10.432, Montréal, Québec, H2X 0A9, Canada.

KEYWORDS : Retinoblastoma (RB) tumor suppressor; Senescence; Translation termination; Translational readthrough.

2.2.1. Summary

The origin and evolution of cancer cells is considered to be mainly fueled by DNA mutations. Although translation errors could also expand the cellular proteome, their role in cancer biology remains poorly understood. Tumor suppressors called caretakers block cancer initiation and progression by preventing DNA mutations and/or stimulating DNA repair. If translational errors contribute to tumorigenesis, then caretaker genes should prevent such errors in normal cells in response to oncogenic stimuli. Here, we show that in the process of cellular senescence induced by oncogenes, tumor suppressors or chemotherapeutic drugs are associated with a reduction in translational readthrough (TR) measured using reporters containing termination codons withing the context of both normal translation termination or programmed TR. Senescence reduced both basal TR and TR stimulated by aminoglycosides. Mechanistically, the reduction of TR during senescence is controlled by the RB tumor suppressor pathway. Cells that escape from cellular senescence either induced by oncogenes or chemotherapy have an increased TR. Also, breast cancer cells that escape from therapy-induced senescence express high levels of AGO1x, a TR isoform of AGO1 linked to breast cancer progression. We propose that senescence and the RB pathway reduce TR, limiting proteome diversity and the expression of TR proteins required for cancer cell proliferation.

2.2.2. Introduction

Cellular senescence is a tumor suppressor mechanism that prevents proliferation in cells bearing oncogenic stimuli (Collado and Serrano, 2010). Senescent cells can efficiently halt tumor progression by remaining out of the cell cycle permanently as benign lesions (Collado and Serrano, 2010; Vernier and Ferbeyre, 2014). Ideally, they also activate their elimination through immune mediated clearance (Kang et al., 2011; Xue et al., 2007). However, if not cleared, some senescent cells can occasionally escape from their dormancy and progress into malignant tumors (Milanovic et al., 2018; Romanov et al., 2001). There is a great heterogeneity in the senescence response depending on the inducer, tissue type and genetic background (Hernandez-Segura et al., 2017). Nevertheless, most senescent cells activate the p53 and retinoblastoma (RB) tumor suppressor pathways that block cell cycle progression (Collado and Serrano, 2010; Vernier et al., 2011; Vernier and Ferbeyre, 2014). In epithelial cells, reactive oxygen species, defective DNA repair and DNA damage were linked to senescence bypass and malignant progression (Gosselin et al., 2009; Nassour et al., 2016). It is commonly accepted that DNA damage and mutations fuel tumor initiation and progression (Harfe and Jinks-Robertson, 2000; Kandoth et al., 2013) by generating both oncogenic drivers and genetic diversity (Bielas et al., 2006). However, little is known about the contribution of translational errors in tumorigenesis.In normal cells, translational errors in the form of aminoacid misincorporation are estimated to occur at a reduced frequency and to be unlikely to significantly affect the proteome (Drummond and Wilke, 2009). In microorganisms, mistranslation contributes to adaptive evolution by purging deleterious mutations and inducing stress adaptation (Bratulic et al., 2017; Ribas de Pouplana et al., 2014; True et al., 2004). Moreover, translational recoding is often used by viruses to increase the coding potential of their small genomes (Bidou et al., 2010). For example, retroviruses use frameshifting to control the synthesis of viral replication proteins (Charbonneau et al., 2012). Overall, translational readthrough (TR), originally discovered in viruses and now extended to metazoans, can add a new C-terminal signal to proteins that may change their function and localization (Jungreis et al., 2011; Schueren et al., 2014; Schueren and Thoms, 2016; Singh et al., 2019). The extensions usually contain potential signals to target proteins to the nucleus, peroxisomes or the membrane (Schueren et al., 2014; Schueren and Thoms, 2016; Singh et al., 2019). Taken together, the available evidence suggests that

tumor cells could use such recoding mechanisms to generate new protein variants and evolve. Therefore, tumor suppressor pathways could counteract TR as part of their mechanism of action. TR results from the recognition of stop codons (UAA, UAG and UGA) by near cognate tRNAs instead of the release factors (RFs) that can also recognize the termination codons to end translation (Tate et al., 2018). The efficiency of translation termination depends on the identity of the stop codon (Firth et al., 2011; Grentzmann et al., 1998; Loughran et al., 2014) and is modulated by metabolic stress in bacteria (Zhang et al., 2020) or oxidative stress in yeast (Gerashchenko et al., 2012). However, little is known about the processes controlling TR in mammalian cells. Here, we report that TR is significantly reduced during oncogene-induced senescence (OIS) or therapy-induced senescence (TIS), which are anticancer responses controlled by the tumor suppressors RB, p53 and PML. Using defined genetic tools, we also show that senescence-associated readthrough suppression is mostly mediated by the RB tumor suppressor pathway. In addition, we show that cells that escape from senescence increase the expression of AGO1x, an endogenous TR isoform of AGO1 that suppresses the interferon pathway, stimulating cell proliferation in breast cancer cells (Ghosh et al., 2020). Hence, like DNA mutations, TR can both increase the expression of specific cancer drivers and generate proteome diversity fueling cancer cell evolution.

2.2.3. Materials and Methods

Cell culture and materials

IMR-90 human diploid fibroblasts were obtained from Coriell Institute for Medical Research (New Jersey, NY). Prostate Cancer cells (PC-3) and MDA.MB.231 breast cancer cells were obtained from ATCC. A certificate of authentication was obtained from Coriell for IMR90 cells and from ATCC for PC-3 and MDA.MB.231 cells. All cells were mycoplasma free after testing that was performed once a month for all cell lines by immunofluorescence. IMR-90 containing human telomerase reverse transcriptase (hTERT) were generated in our laboratory by transducing cells with the FG12-hTERT lentiviral vector (Voghel et al., 2010). Phoenix ampho packaging cells used for retroviral infections were given by S.W. Lowe

(Memorial Sloan Kettering Cancer Center, New York, NY). IMR90 and MDA.MB.231 were cultured in Dulbecco's modified Eagle medium (DMEM; Wisent) supplemented with 10% fetal bovine serum (FBS; Wisent), 1% penicillin G/streptomycin sulfate (Wisent) and2 mmol/L L-glutamine (Wisent). PC-3 were cultured in Roswell Park Memorial Institute Medium (RPMI 1640; Wisent) supplemented with 10% fetal bovine serum (FBS; Wisent), 1% penicillin G/streptomycin sulfate (Wisent) and 2 mmol/L L-glutamine (Wisent). The translation elongation inhibitor cycloheximide and the aminoglycoside gentamicin sulfate were purchased from Sigma-Aldrich (Oakville, ON). The CDK4/6 inhibitor palbociclib (PD-0332991) was purchased from Chemietek. Camptothecin and 4-hydroxy-tamoxifen werepurchased from Sigma-Aldrich (Oakville, ON). A phthalamide derivative named CDX5-1 was donated by M. Roberge (University of British Columbia, Vancouver, BC, Canada).

Plasmids and cloning

Retroviral vectors pBabe/pBabe-ER, pBabe-H-RasV12, pWZL/pWZL-H-RasV12 were described in (Ferbeyre et al., 2000), pBabe-PML-IV-ER in (Vernier et al., 2011), pLXSN, pLXSN-E6, pLXSN-E7, pLXSN-E6/E7 and pLXSN-E7 Δ 21-24 in (Mallette et al., 2004), pBABE-RPL22(WT)-Myc in (Del Toro et al., 2019), pBABE-RPS14(WT)-Myc in (Lessard et al., 2018). pBABE-CDK4(WT) was a gift from Scott W. Lowe (Memorial Sloan-Kettering Cancer Center, New-York, NY). The genes coding for Renilla luciferase (Rluc) and Firefly luciferase (Fluc) were linked by an intercistronic region in order to obtain a 96 kDa bifunctional protein (Gendron et al., 2005). These reporters were PCR-amplified and subcloned in NotI/NsiI restriction sites to obtain pMSCV-Rluc-Fluc variants. A UGA stop codon, created by site-directed mutagenesis using PfuUltra II fusion HS DNA polymerase (Agilent, Canada), was inserted in the intercistronic sequence. Primers for PCR are provided in Supplementary Table 1. The readthrough region from Moloney Murine Leukemia Virus (MMuLV) as well as sequences flanking the stop codon from the readthrough sequence of Aquaporin 4 (AQP4, NM_001650.4) (Loughran et al., 2014) were chemically synthesized (Biocorp, Canada) and subcloned in XhoI/ApaI restriction sites between Rluc and Fluc genes. The readthrough region sequences are provided in Supplementary Table 2. The non-readthrough control was performed by mutating the stop codon TGA to CGA.

Identification of readthrough candidates in mammalian cells using bioinformatic analysis

In order to look for endogenous readthrough candidates, we looked in silico for peptides encoded after termination codons detected in proteomics experiments. We first built a database of peptide sequences located between the first arginine/lysine after the canonical stop codon and the next stop codon, always in the same reading frame using sequences deposited in RefSeq hg38.2. We discarded sequences shorter than 5 aminoacids. Candidate readthrough peptides were then matched to the data set of peptides identified by trypsin digestion of human proteins and mass spectrometry published in (Rosenberger et al., 2014). We found 278 candidates for endogenous readthrough above the false discovery rate (FDR) threshold (Supplementary Table 3). Following a readthrough propensity predictor algorithm (Schueren et al., 2014), four candidates showing the highest readthrough propensity values were chosen. This algorithm assigns regression coefficients to the stop codon and all possible nucleotides in the stop codon context based on experimental data. The stop codon context comprises the nucleotide sequences from -6 to +9 positions surrounding the stop codon. The new readthrough candidates are: Vasodilator-stimulated phosphoprotein (VASP, NM_003370.3), Aspartate beta hydroxylase (ASPH, NM_004318.3), Hepsin (HPN, NM_182983.2) and Fibrillarin (FBL, NM_001436.3). Oligonucleotides containing 30 up-stream and 30 down-stream nucleotides flanking the stop codon, as well as the stop codon of those readthrough candidates were chemically synthesized (Biocorp, Canada) and subcloned in XhoI/ApaI restriction sites between Rluc and Fluc genes of our pMSCV-Rluc-Fluc reporter construct. The sequences of all new readthrough candidates region are provided in Supplementary Table 2.

Polysome fractionation

The protocol was performed as previously described (Gandin et al., 2014). Briefly, 60% (w/v) sucrose stock solution was used to make sucrose gradients (5 to 50%) in a buffer containing 200 mM Tris-HCl (pH 7.6), 1 M KCl, 50 mM MgCl2, 100 µg/ml cycloheximide, 1X cOmplete EDTA-free protease inhibitor cocktail (Roche) and 200 units/ml of RNase inhibitor (abm-Applied Biological Materials, BC). After 12 days post-infection, proliferating and

senescent fibroblasts at 80-90% confluence were treated with cycloheximide at a final concentration of 100 µg/ml for 5 min at 37°C. Cells were washed with ice-cold 1X PBS - 100 µg/ml cycloheximide, scratched and lysed in a hypotonic buffer (5 mM Tris-HCl pH 7.5, 2.5 mM MgCl2, 1.5 mM KCl, 1X complete EDTA-free protease inhibitor cocktail, 100 µg/mL cycloheximide, 1 mM DTT, 100 units of RNAse inhibitor, followed by addition of 25 µl of 10% Triton X-100 (final concentration of 0.5%) and 25 µl of 10% sodium deoxycholate (final concentration of 0.5%). Cells were vortexed and then centrifuged at low speed (140 x g) for 15 min at 4°C. Sample supernatants were adjusted so that they contain the same OD (10-20 OD at 260 nm). The lysate was loaded onto the ultracentrifuge tubes containing sucrose gradients, then centrifuged at 22,223 x g (36,000 rpm) for two hours at 4°C using SW41Ti rotor Beckman Coulter (Optima L80 XP ultracentrifuge). After ultracentrifugation, the samples were placed in the UV detector (Brandel #IV-22-117140) and fraction collector (Retriever 500, Teledyne Isco). Each fraction was collected and monitored from the top to the bottom of the ultracentrifuge tube.

Dual-luciferase Assays

IMR-90 transduced cells were washed with 1X PBS, scratched and lysed in 1X Passive lysis buffer supplied in the Dual Luciferase Stop & Glo® Reporter Assay System (Promega). A 20 µl cell lysate sample was used for luminescence measurements with Lumin Triathler-Hidex. After adding 50 µl of the Fluc reagent (Substrate + Buffer) to the samples, luminescence was measured for 10 seconds. Addition of 50 µl of the Rluc reagent-Fluc quenching (Stop & Glo®) preceded another 10 seconds measurement. The efficiencies of readthrough (% Readthrough) were determined by averaging the relative Fluc activities (Fluc/Rluc ratio) from luciferase reporters UGA or AQP4, divided by the relative luciferase activities of their non-readthrough controls. We also compared the readthrough fold-changes, relative Fluc activities (Fluc/Rluc) of each condition were normalized to the relative Fluc activities from non-senescent cells:

$$Normalized\,\frac{Fluc}{Rluc} = \left(\frac{\frac{Fluc}{Rluc(x\ condition)}}{\frac{Fluc}{Rluc(non-senescent\ cells)}} \right)$$

To measure readthrough after therapy-induced senescence, PC3 and MDA.MB.231 cells were retrovirally transduced with luciferase reporter AQP4 or UGA. Transduced cells were treated 24h using 100 nM of camptothecin, or vehicle (DMSO), to induce senescence. Following the treatment, cells were washed with 1X PBS and fresh medium was added.Luciferase activities were measured at day 7 post-treatment. All assays were performed in technical triplicates. Normalized relative Fluc fold changes and Fluc/Rluc ratios are provided in Supplementary Table 4 as well as all biological replicates.

Immunoblotting and Immunofluorescence

To prepare total cell extracts, cells were washed with 1X PBS containing 1X protease and phosphatase Inhibitor cocktails (Roche), scratched and collected by centrifugation at low speed (140 x g) for 5 min, lysed in 200 µl of SDS sample buffer (62.5 mM Tris-HCl, pH 6.8, 10% glycerol, 2% SDS and 5% 2-mercaptoethanol), and boiled for 5 min. Fifteen µg of total cell proteins were separated on SDS-PAGE and transferred to nitrocellulose membranes (Millipore). The primary antibodies used wereanti-Renilla Luciferase rabbit polyclonal (1:3000, Code No. PM047, MBL), anti-H-Ras mouse monoclonal (1:250, clone F235, sc-29, Santa Cruz Biotechnology), anti-phospho-H3S10 rabbit polyclonal (1:1000, #06–570, Millipore, Billerica, MA), anti-phospho-RBS795 rabbit polyclonal (1:500, #9301, lot: 13, Cell Signaling), anti-RB mouse monoclonal (1:1000, clone 4H1, #9309, Cell Signaling), anti-MCM6 rabbit polyclonal (1:1000, A300-194A, Bethyl Laboratories), anti-p53 mouse monoclonal (1:1000, clone DO-1, sc-126, Santa Cruz Biotechnology), anti-p21 (1:500, 556431, BD Pharmingen), anti-RNR (1:500, sc-398294, Santa Cruz Biotechnology), anti-phospho-γH2A.XS139 mouse monoclonal (1:500, JBW-301, lot: 2552645, Millipore, Billerica, MA), anti-c-Myc rabbit polyclonal (1:1000, clone A-14, sc-789, Santa Cruz Biotechnology) and anti-α-tubulin mouse monoclonal (B-5-1-2, 1:20000, Sigma). Signals were revealed after incubation with goat anti-mouse IgG (1:3000, #170-6516, Bio-Rad, Mississauga, ON) or goat anti-rabbit IgG (1:3000, #170-6515, Bio-Rad, Mississauga, ON) secondary antibodies, and by using enhanced chemiluminescence (ECL, Amersham) or Lumi-LightPLUS (Roche). Immunofluorescence were done as described (Igelmann et al., 2021) with the following modifications for the AGO1x staining. For blocking 10% goat serum (#16210072, Life Technologies), and 1% BSA (BioShop Canada)

in PBS for 30 min. Primary antibodies were AGO1x (1:50, #RBP 1510, Lucerna-Chem.) and KI67 (1:200, Cat# RM9106, ThermoFisher Scientific). Cells were analyzed using upright microscope Zen Imager with 20X air objective. Images were processed using Image J and quantification was done using region of interest (ROI) mean intensity staining. To determine ROI, DAPI staining was used

Cell proliferation assay and Senescence-associated β-galactosidase assay

Relative density of cells was assessed from estimations of cell number according to crystal violet retention assay (Vernier et al., 2011). The senescence associated β-galactosidase (SA-β-Gal) activity was measured at day 7, 12 or 35 post-infection as previously described (Vernier et al., 2011). All assays were performed in technical triplicates.

RT-qPCR

Senescent and non-senescent IMR-90s were collected at 12- or 35-days post-infection, with either pBabe-H-RasV12 or pBabe control vector in TRIzol reagent (Invitrogen) and total RNA was extracted following manufacturer's instructions. Two µg of total RNA were then used for the RT-qPCR reactions as described in (Igelmann et al., 2021). Primers for qPCR were designed using the Universal Probe Library Assay Design Center (https://www.roche-applied-science.com/sis/rtpcr/upl/index/jsp) and are provided in Supplementary Table 5. Analysis for indicated genes were done using the ΔΔCT method. HMBS and TBP were used as reference genes (Vernier et al., 2011). All assays were performed in technical triplicates.

Statistics and reproducibility

Statistical analysis (One-way ANOVA with post-hoc Tukey HSD (Honestly Significant Difference)) was done using the One-way ANOVA test calculator at: http://astatsa.com/OneWay_Anova_with_TukeyHSD/. Two-tailed Student's t-tests were performed using GraphPad Prism version 6.0c software. A $p<0.05$ was considered statistically significant. Each experiment was repeated at least three times, except for those in Figures: 2C-D;

3B (UGA), and Supplementary Figure S1C-E and S2D, which were done twice. SA-β-Gal assays were quantified from many fields within one experiment to represent the entire petri dish and confirmed as described in Figures 5F, 6A, 7A and S1A.

2.2.4. Results

Translation termination is improved in oncogene-induced senescence

To investigate the effect of cellular senescence on TR efficiency, we first used a model of oncogene-induced senescence (OIS) in human primary cells. Primary fibroblasts were retrovirally transduced with H-RasV12 oncogene (senescence inducer) or the control empty vector. They were also transduced with luciferase reporter plasmids containing either: 1) a TGA within an artificial intercistronic region (UGA readthrough); 2) the stop codon context from AQP4, a well-known mammalian readthrough candidate (Loughran et al., 2014); or 3) the non-readthrough control (TGA mutated to CGA) between Rluc and Fluc fusion protein gene (Figure 1A). Immunoblotting shows a band at 35 kDa corresponding to Renilla luciferase, as well as a weak band at 100 kDa indicating the fusion protein Renilla-Firefly luciferase produced after a ribosomal readthrough in cells transduced with the AQP4 readthrough reporter (Figure 1B, right panel, left lane). For the UGA reporter, the fusion protein is not detectable. On the other hand, in cells transduced with the non-readthrough control, only the fusion protein can be detected (Figure 1B, left). At early stages of H-RasV12 oncogene expression, cells present a cancer-like behavior characterized by a hyperproliferation phase. However, around 6 days after introduction of oncogenic ras, cells stop proliferation and enter a well-characterized and stable cell cycle arrest (Serrano et al., 1997). We confirmed this senescent cell cycle arrest at day 12 post-infection, using an assay for the senescence-associated β-galactosidase activity that allowed visualizing characteristically large and flat cells that stained positive for this biomarker (Figure S1A). RT-qPCRs were carried out to evaluate the decrease of Ki67 expression, indicating the proliferation arrest, and the activation of p53 targets (CDKN1A/p21, GADD45A) and RB pathway (CDKN2A/p16INK4a, MCM6) in senescent cells (Figure S1B). Global translation was not affected in senescent cells since their polysome profiles were similar to control growing cells (Figure 1C). This is consistent with previous reports and with the fact that senescent cells are actively secreting multiple pro-inflammatory mediators

(Young et al., 2009). In addition, the non-readthrough (CGA) controls presented similar relative Fluc activities both in senescent and proliferating cells (Figure S1C). Cap-dependent Rluc expression increased with time (Figure 1D). Readthrough-dependent translation of the firefly luciferase reporter increased early after introduction of oncogenic ras in normal human fibroblasts when cells proliferate rapidly, but it decreased when the cells underwent OIS as measured at days 12 or 20 after H-Ras-introduction (Figure 1E). The relative efficiency of TR was calculated by dividing Fluc by Rluc values, then normalizing to the Fluc/Rluc ratio obtained in the same cells using the non-readthrough (CGA) control. The results clearly show that the senescent program reduced TR efficiency at UGA codons without any particular context and in the sequence flanking the AQP4 translation termination signal (Figure 1F). Similar results can be seen after plotting the Fluc/Rluc ratio of senescent Ras-expressing cells relative to cells with empty vectors (Fig 1G). In contrast, control cells did not change TR efficiency during the same time in culture (Figure S1D). To discard the possibility that TR efficiency might be decreased due to a cell-cycle arrest independent from the senescent phenotype, proliferating cells were starved for a week to induce quiescence. Starved normal cells compared to cells supplied with fetal bovine serum (FBS) showed no differences in the efficiency of TR. Besides, starved and FBS-supplied senescent cells showed similar TR values (Figure S1E). These observations lead us to conclude that the decrease of TR efficiency is senescence-specific. Immunoblots showed the gradual reduction of phosphorylated RB, the absence of the E2F target MCM6 and the reduction of the mitotic marker H3(pS10) in H-Ras cells, confirming the establishment of senescence. P53 accumulates in senescent cells but decreases after 20 days post-infection in H-Ras cells (Figure 1H).

The aminoglycoside gentamicin disrupts prokaryotic protein synthesis by binding to 16S ribosomal RNA, but also affects eukaryotic ribosome proofreading, inducing a conformational change in the ribosome-mRNA complex stimulating the efficiency of TR (Manuvakhova et al., 2000). We sought to investigate whether OIS can decrease TR stimulated by gentamicin. We added 900 μg/ml of gentamicin sulfate to OIS cells 24 hours before luciferase assays. The non-readthrough controls were unaffected by gentamicin stimulation (Figure S2A). Gentamicin increased TR efficiency and this effect was reduced in senescent cells both at UGA stop codons and the natural readthrough sequence of AQP4 (Figure 2A and S2B-C). Of note, for the UGA reporter the TR efficiency was very small (0.1%) but

increased more than 50-fold for the AQP4 reporter (6.9%). In both cases, the levels of TR were reduced by about a factor of 2 in senescent cells and we obtained similar results after gentamicin treatment (Figure S2B and C). Strikingly, TR levels were the same in senescent and proliferating cells with the reporter containing the programmed readthrough region from Moloney Murine Leukemia Virus (MMuLV) (Figure 2A). This region contains a UAG stop codon followed by a pseudo-knot structure (Houck-Loomis et al., 2011) and it allows up to 10% of ribosomes to suppress translation termination in order to synthesize the Gag-Pol polyprotein in cells infected with the virus (Yoshinaka et al., 1985). Also, the aminoglycoside gentamicin did not affect MMuLV TR efficiency.

We also treated cells 72-hours before cell lysis with 600 µg/ml of gentamicin and 25 µM of CDX5-1, a novel small molecule that potentiates TR efficiency when combined with aminoglycosides although it has by itself no effect (Baradaran-Heravi et al., 2016). We observed that while single gentamicin treatment increased UGA TR efficiency up to 6.6-fold in control cells, the combination increased it up to 16.5-fold. Surprisingly, the TR efficiency was still limited in senescent cells after the combination, which improved the efficiency only 1.7-fold over gentamicin treatment alone (Figure S2D). Together, these results indicate that senescence engages a significantbarrier for TR.

To investigate more broadly whether senescence affects natural readthrough signals, we made luciferase reporters using the stop codon context of several mRNAs, which we predicted in silico as candidates for readthrough (see Material and Methods). We tested both their basal and gentamicin-stimulated TR. We found that the TR of VASP and HPN were significantly reduced during OIS while the TR of FBL showed a tendency to be reduced (Figure S2E). ASPH TR was undetectable either in proliferating or in senescent fibroblasts. Nevertheless, after gentamicin stimulation, we could observe the TR decrease in senescent cells (Figure S2F).

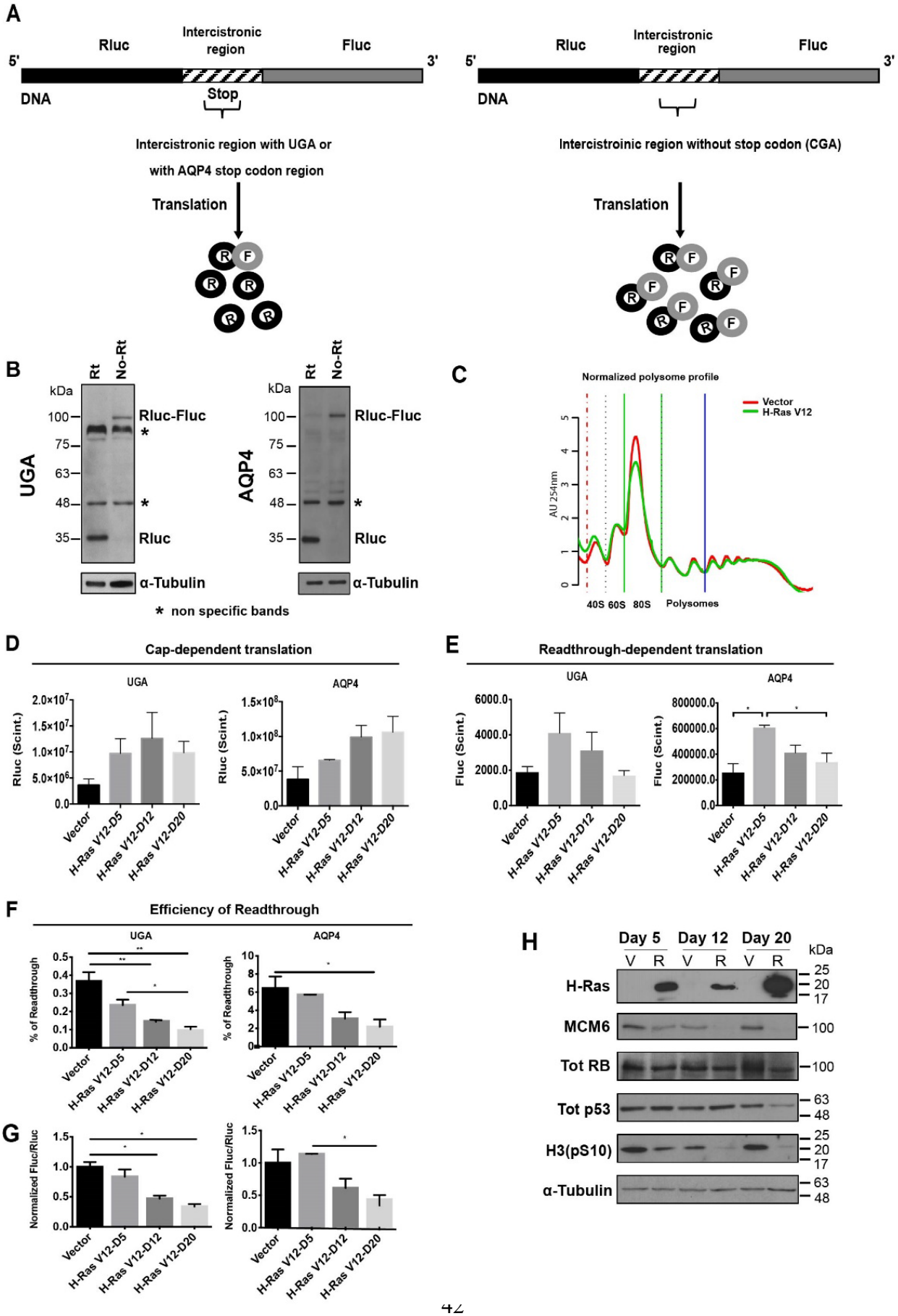
A
Rluc
Intercistronic region
Fluc
5'
3'
DNA
Stop
Intercistronic region with UGA or with AQP4 stop codon region
Translation
Intercistroinic region without stop codon (CGA)
B
Rt
No-Rt
kDa
100
75
63
48
35
Rluc-Fluc
Rluc
α-Tubulin
UGA
AQP4
* non specific bands
C
Normalized polysome profile
Vector
H-Ras V12
AU 254nm
40S
60S
80S
Polysomes
D
Cap-dependent translation
UGA
AQP4
Rluc (Scint.)
Vector
H-Ras V12-D5
H-Ras V12-D12
H-Ras V12-D20
E
Readthrough-dependent translation
Fluc (Scint.)
F
Efficiency of Readthrough
% of Readthrough
G
Normalized Fluc/Rluc
H
Day 5
Day 12
Day 20
V
R
kDa
H-Ras
MCM6
Tot RB
Tot p53
H3(pS10)
α-Tubulin

Figure 7. – Figure 1; Readthrough is reduced in OIS.

A. Rluc (Renilla luciferase) in black is linked to Fluc (Firefly luciferase) in gray, by an intercistronic region in stripes. Rluc is the internal control of the gene, while Fluc is the readthrough sensor. A UGA codon within an artificial context or the AQP4 stop codon region is inserted in the intercistronic region (left). The expression of Fluc indicates the efficiency of readthrough. The intercistronic region from the non-readthrough control lacks the stop codon (TGA mutated by CGA) (right). **B.** Immunoblots for Rluc in IMR-90 cells transduced with UGA and AQP4 reporters (Rt) or with the non-readthrough controls (No Rt), 12 days post-infection. Alpha-Tubulin was used as a loading control. *: non-specific bands at 48 and 90 kDa, n=3. **C.** Polysome profiles were performed 12 days post-infection with an empty vector (Vector) or H-Ras V12 oncogene (H-RasV12) showing that global translation is similar in senescent and non-senescent IMR-90 cells, n=1. **D.** Rluc plots indicate cap-dependent translation in IMR-90 cells with an empty vector (Vector) or with the oncogene H-Ras V12 (H-RasV12) at day 5 (D5, still proliferating), 12 (D12, senescent cells) or 20 (D20, senescent cells).Error bars indicate SD of three independent experiments, n=3. **E.** Fluc plots indicate the decrease of readthrough dependent-translation of cells as in (D). Error bars indicate SD of three independent experiments, n=3. **F.** The percent of readthrough was calculated in cells as in (D) by dividing the Fluc/Rluc ratio from UGA or AQP4 luciferase reporters by the Fluc/Rluc ratio from non-readthrough controls multiplied by 100, n=3. **G.** Fluc/Rluc ratios with data as in (F) but normalized relative to empty vector-infected cells n=3. **H.** Immunoblots of H-Ras, total RB (Tot RB), total p53 (Tot p53), MCM6, phosphorylated Histone H3 on serine 10 (H3(pS10)) and tubulin at day 5, 12 and 20 post-infection with an empty vector (V) or H-RasV12 oncogene (R), n=3, representative blot is shown. For panels E, F & G: significance was tested with one-way ANOVA with post-hoc Tukey HSD (Honestly Significant Difference) tests were performed.Error bars indicate SD of three independent experiments. Tukey HSD p-values indicate that * = $p<0.05$ and ** $p<0.01$.

Translation termination is improved in PML-induced senescence

The tumor suppressor PML controls p53 and RB which are central for the establishment of OIS response (Vernier et al., 2011). Also, PML plays a role in antiviral responses (El Asmi et al., 2014;

Regad et al., 2001) and, since many viruses use readthrough, we wanted to investigate whether PML modulates this process. Normal human fibroblasts IMR-90 cells were retrovirally transduced with a vector that allows expression of a conditionally inactive PML (pBabe-PML-IV-Estrogen Receptor) as well as with UGA, MMuLV and AQP4 luciferase reporters, in order to analyze TR efficiency in this model. Transduced cells were stimulated with 100 nM of the estrogen antagonist 4-hydroxy-tamoxifen (4-OHT), to induce PML-IV nuclear translocation and senescence (Acevedo et al., 2016). We found that induction of PML reduced basal or gentamicin-induced TR at UGA stop codons (Figure 2B). Intriguingly, the effect of PML on gentamicin-induced readthrough was much more important than the effect of OIS, suggesting that PML could be one important regulator of TR efficiency. TR was also reduced after PML induction with 4-OHT, with or without gentamicin, in AQP4 and MMuLV transduced cells (Figure 2 C-D). The decrease of TR efficiency in MMuLV reporter further suggests an antiviral role of PML-IV.

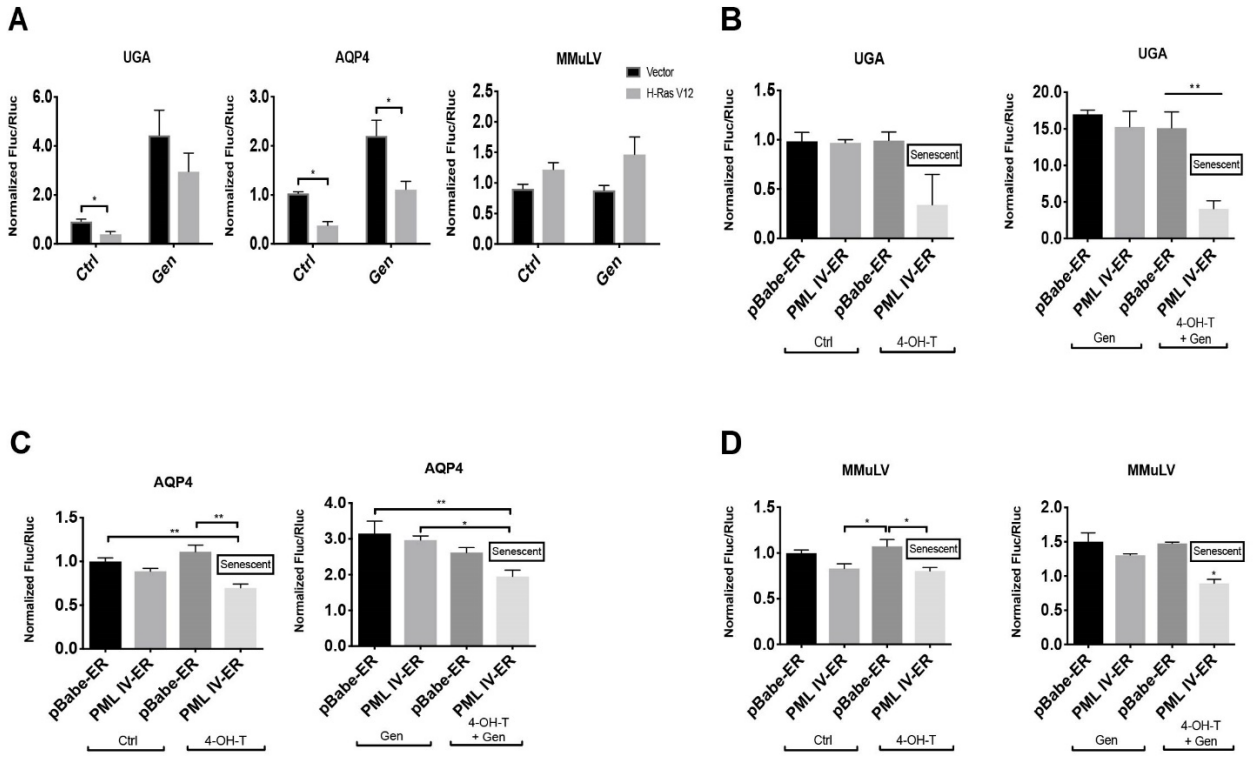

Figure 8. – Figure 2; Gentamicin-dependent translation errors are reduced in OIS and PML-induced senescence.

A. IMR-90 cells were transduced with either an empty vector (Vector) or H-RasV12 oncogene (H-RasV12), to induce OIS, and with a luciferase reporter containing either: a UGA within an artificial context, a stop codon within the natural context from AQP4 or a MMuLV programmed readthrough region for gag-pol proteins inserted in the intercistronic region of the reporter. Cells were treated with vehicle (Ctrl) or 900 μg/ml of gentamicin sulfate (Gen) for 24 hours before measuring luciferase activities at day 12 post-infection. Unpaired Student's t-testwith equal SD were performed. Error bars indicate SD of biological triplicates. * = $p<0.05$ is significantly different, using two-tailed Student's t-test, n=3. **B-D.** IMR-90 cells were transduced with pBabe-ER empty vector (pBabe-ER) or pBabe-PML-IV-ER (PML IV-ER), and with luciferase reporters UGA (B), AQP4 (C) or MMuLV (D). Cells were treated with vehicle (Ctrl) or 100 nM 4-hydroxy-tamoxifen (4-OHT), inducing or not PML-IV nuclear translocation to induce senescence. Moreover, cells were treated with vehicle or 900 μg/ml of gentamicin sulfate (Gen) for 24 hours before measuring luciferase activities at day 12 post PML-IV induction. Normalized Fluc/Rluc ratios indicate the efficiency of readthrough. Normalizations are presented as means relative to empty vector-infected cells from three independent experiments with technical triplicates for each experiment, except for (C, D), which are representative of 2 independent experiments with similar results. **B-D:** One-way ANOVA with post-hoc Tukey HSD were performed. Error bars indicate SD of biological triplicates (B) or technical triplicates (C, D). Tukey HSD p-values indicate that * = $p<0.05$, ** = $p<0.01$ are significantly different.

Circumventing senescence decreases the fidelity of translation termination

Although senescence in response to oncogenes includes a very stable cell cycle arrest, some cells escape from the process and progress towards malignant transformation. Cells that circumvent OIS display a gene expression profile typical of malignant cells and chromosomal aberrations (Deschenes-Simard et al., 2016). We sought to determine whether these cells also lose their tight control over TR. We obtained cell populations that bypassed OIS from long-term cultures (35 days) of IMR-90 cells expressing oncogenic ras. Cells that escaped senescence revert their morphology to that of normal growing cells (not shown) and expressed lower levels of oncogenic ras (Figure 3A), indicating a mechanism that allow them to prevent pro-senescence

ras/ERK signaling. This is consistent with our previous observation that decreasing ERK signaling accelerates senescence bypass in H-Ras-expressing cells (Deschenes-Simard et al., 2013; Deschenes-Simard et al., 2016). Cells that bypassed senescence also had lower levels of the CDK inhibitor p16INK4a and higher levels of the proliferation marker KI67 (Figure 3A). We next measured TR in these cells using the UGA stop codon or the natural signals for AQP4 (Loughran et al., 2014), VASP and HPN. In all cases, the cells that bypassed senescence displayed an increased TR even higher than control non-senescent cells (Figure 3B).

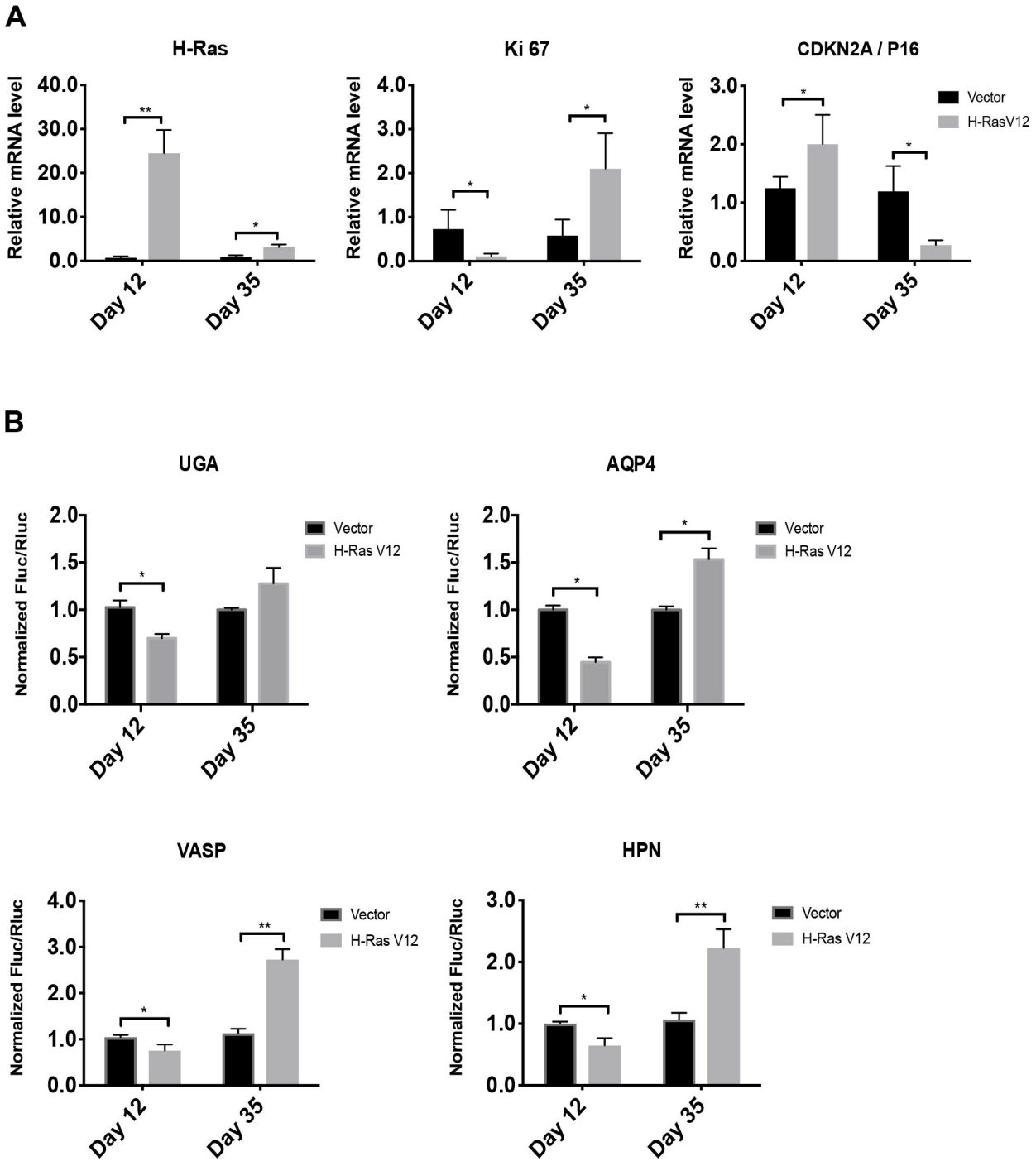

Figure 9. – Figure 3; Cells that bypassed-OIS show increased readthrough.

A. RT-qPCR for H-RAS and senescent marker mRNAs were performed in IMR-90 cells at day 12 and 35 post-infection with an empty vector (Vector) or H-RasV12 oncogene (H-RasV12). Data are normalized over TBP and HMBS, and presented as means relative to vector infected cells, n=3. **B.** Luciferase activities in non-senescent and senescent cells measured at day 12 and 35

post-infection in cells having the indicated reporters. Normalizations are presented as means relative to vector-infected cells from three independent experiments with technical triplicates for each experiment, except for UGA reporter, which are representative of 2 independent experiments with similar results. Error bars indicate SD of biological triplicates (AQP4, HPN, VASP) or technical triplicates (UGA). * = $p<0.05$, ** = $p<0.01$ are significantly different, using two-tailed Student's t-test.

E7 Oncoprotein increases TR

Since low translation fidelity and increased TR are associated with escape from senescence and with malignant transformation (Marcel et al., 2013), we next investigated which tumor suppressor pathways activated in senescent cells could modulate TR. To investigate whether p53 and/or RB pathways are implicated in translation termination efficiency, we used E6 (inhibits p53) and E7 (inhibits RB) oncoproteins from HPV-16 virus. Transduction of E6 did not affect the TR levels in senescent cells. However, RAS-senescent cells infected with E7 oncoprotein or with both E6 and E7, showed a significant increase in TR at UGA stop codons and the natural readthrough signals from AQP4 and VASP (Figure 4A-C). These results indicate that E7 targets, likely the pocket proteins family including RB, p107 and p130, mediate the readthrough decrease in senescent cells. We also knocked-down RB mRNAs' expression with shRNAs in H-Ras cells but we failed to see the increase of TR levels (data not shown) we observed in E7 expressing cells, suggesting that RB in coordination with p107 and p130 must influence the reduction in TR.

To further implicate the RB pathway in the control of TR in senescent cells, we used an in-frame deletion mutant of E7 whose interactions with RB, P107 and p130 are disrupted (E7 Δ21-24) (Helt and Galloway, 2001). As expected, H-Ras cells transduced with wild type E7 showed a two-fold increase in TR compared to senescent cells but the mutant E7 Δ21-24 failed to do so (Figure 4D). Besides, the proliferating cells transduced with E7 presented a tendency to increase TR, while the TR was not affected in proliferating cells transduced with the mutant E7 Δ21-24 (Figure S3A). In addition, RT-qPCRs were carried out to evaluate the expression of E2Fs target genes in cells transduced with E7 or the E7Δ21-24 mutant. As expected E7 but not E7 Δ21-24 increased E2F target genes expression (Figure S3B). Next, we used a retroviral vector

for CDK4 overexpression to block pocket proteins activity in senescent cells (Sherr et al., 2016) and, as expected, we observed an increase in TR (Figure 4E). Relative cell growth and RT-qPCRs show that CDK4 overexpression does not affect proliferation arrest markers at day 12 post-infection in senescent IMR-90 cells (Figure S3C-D). Taken together, these results indicate that the observed reduction in TR is not a simple consequence of the growth arrest of senescent cells and strongly suggest that the activation of the RB tumor suppressor pathway increases the fidelity of translation termination during OIS.

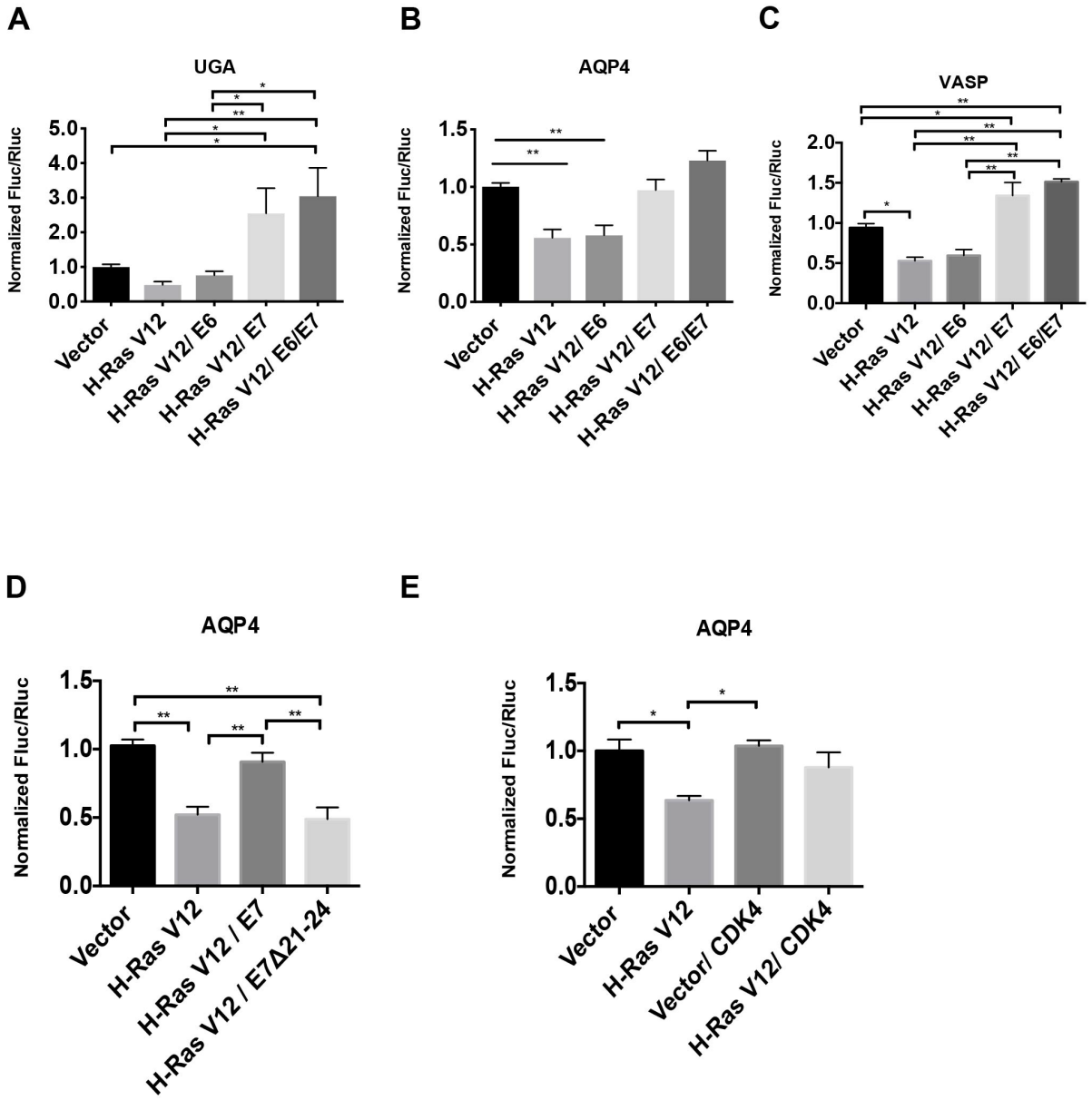

Figure 10. – Figure 4; RB pathway disruption increases readthrough.

A-C. Readthrough efficiencies expressed as normalized Fluc/Rluc obtained from the luciferase reporters bearing a UGA stop codon within an artificial context (A) or astop codon within natural contexts from either AQP4 (B) or VASP (B) that were expressed in IMR-90 cells. These cells also expressed HTERT, an empty vector (Vector) or H-RasV12 and an empty control vector (pLXSN), E6, E7 or E6/E7 oncogenes to study the readthrough efficiency in proliferating vs senescent vs transformed-like cells, n=3. **D.** Relative readthrough luciferase values from IMR-90 cells transduced with the AQP4 readthrough reporter, with an empty vector (Vector) or H-RasV12 and an empty control vector (pLXSN), wild-type E7 or E7 Δ21-24 mutant oncogene. **E.** IMR-90 cells were transduced with an empty vector or H-RasV12 or CDK4 and AQP4 luciferase reporters to study the readthrough efficiency variations in proliferating vs senescent vs. cells overexpressing CDK4, n=3. **A-E.** Luciferase activities were measured in non-senescent and senescent cells at day 12 post-infection. Normalizations are presented as means relative to vector-infected cells, n=3 with technical triplicates for each experiment. One-way ANOVA with post-hoc Tukey HSD were performed. Error bars indicate SD of biological triplicates. Tukey HSD p-values indicate that * = $p<0.05$, ** = $p<0.01$ are significantly different.

RB pathway activation reduces TR

Having demonstrated that RB pathway inhibition increased TR we next investigated whether activation of the RB pathway would inhibit TR. First, we used the CDK inhibitor palbociclib (Law et al., 2015). Treatment of proliferating fibroblasts with palbociclib reduced TR of the AQP4 reporter and gentamicin-stimulated TR at the UGA stop codon (Figure 5A-B). Interestingly, palbociclib also reduces TR in cells that spontaneously escaped from senescence (Figure 5C). As expected, palbociclib also inhibits cell proliferation and strongly activates the RB pathway in proliferating and H-Ras-escaped IMR-90 cells (Figure 5D and S4) restoring their senescent phenotype (Figure 5E-F).

We recently demonstrated that extra-ribosomal functions of RPS14/uS11 and RPL22/eL22 were linked to the regulation of the cell cycle and senescence. We found that these two proteins interact with the CDK4-Cyclin D1 complex inhibiting its activity and consequently activating the RB pathway (Bury et al., 2021; Del Toro et al., 2019; Lessard et al., 2019; Lessard

et al., 2018). These results suggest that RPS14/uS11 and RPL22/eL22 could, as palbociclib, affect TR. We transduced IMR-90 cells with Myc tagged RPL22/eL22 or RPS14/uS11 as well as with the AQP4 readthrough reporter and measured TR efficiency at day 7, 12 and 14 after transduction. The expression of RPL22/eL22 or RPS14/uS11 was confirmed by immunoblots against the Myc tag (Figure 5G). We also measured biomarkers of senescence such as RB, the E2F target MCM6 and the mitosis marker phospho-H3 (Figure 5G). Cells bearing RPS14/uS11 showed a 15% decrease of TR at days 7 and 12 after transduction, and 30% decrease of TR 14 days after transduction compared to control cells (Figure 5H). In contrast, RPL22/eL22-transduced cells showed a peak of TR reduction at day 7 post-infection, and a progressive recovery 12- and 14-days post-infection (Figure 5I). We already reported that RPS14/uS11 is more efficient than RPL22/eL22 for inhibition of CDK4 and induction of senescence (Del Toro et al., 2019), explaining this difference. These results suggest that RPS14/uS11 haploinsufficiency in the 5q-syndrome (Ebert et al., 2008) and frequent RPL22/eL22 hemizygous gene deletions found in cancer (Ajore et al., 2017) could play a role in proteome diversity and tumorigenesis. Taken together, our results suggest that the RB pathway is implicated in translation termination accuracy (Figure 5J).

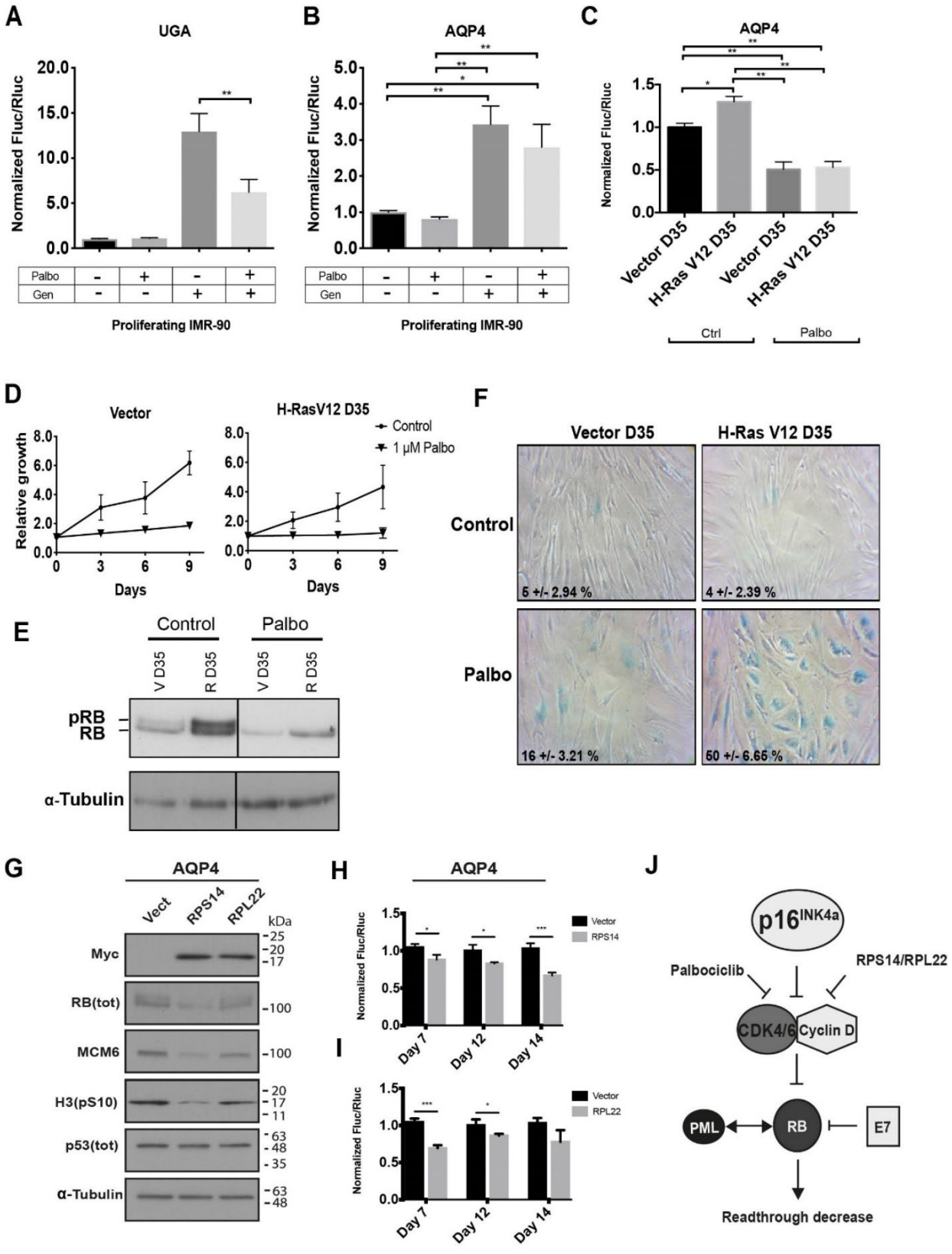

Figure 11. – Figure 5; RB pathway activation reduces readthrough.

A-B. Normalized Fluc/Rluc ratios ofIMR-90 cells transduced with luciferase reporters UGA (A) or AQP4 (B) and treated with vehicle and/or 1 μM of palbociclib (Palbo) and/or 900 μg/ml of gentamicin sulfate (Gen) for 5 days before luciferase measurements. Error bars indicate SD of three independent experiments, n=3. **C.** Normalized Fluc/Rluc ratios of IMR-90fibroblasts transduced with an empty vector (Vector) or H-RasV12 oncogene (H-RasV12) to induce OIS but cultured for 35 days until they bypassed the phenotype (D35) and with AQP4 luciferase reporter. Cells were treated with vehicle (Ctrl) or 1 μM of palbociclib (Palbo) for 5 days before measuring luciferase activities at day 35 post-infection. Normalizations are presented as means relative to vector-infected cells, n=3 with technical triplicates for each experiment. One-way ANOVA with post-hoc Tukey HSD. Error bars indicate SD of biological triplicates. Tukey HSD p-values indicate that * = $p<0.05$, ** = $p<0.01$ are significantly different. **D.** Growth curves of proliferating (Vector) and ras bypassed (H-RasV12 D35) IMR-90 cells treated with vehicle (Control) or 1 μM of palbociclib (Palbo) for 5 days are shown. Data are presented as means normalized to day 0 of each condition and error bars indicate SD of three independent experiments, n = 3. **E.** Immunoblots for total RB (Tot RB) (note: upper band represents phosphorylated RB: pRB) and alpha-tubulin from non-senescent (V D35) and ras by-passed cells (R D35) following treatments with vehicle (Ctrl) or 1 μM of palbociclib (Palbo) for 5 days. Blots are representative of 3 independent experiments with similar results. **F.** SA-β-gal of proliferating (Vector D35) IMR-90 cells and IMR-90 cells that have by-passed the senescent stage (H-RasV12 D35) treated for 5 days with vehicle (Ctrl) or 1 μM of palbociclib (Palbo) and fixed at day 35 (D35) post-infection. Data were quantified from many fields within one experiment to represent the entire petri dish. Three independent cell counts up to a total of at least 100 cells are presented as the mean and SD of positive cells. **G.** Immunoblots for indicated proteins at day 7 post-infection with an empty vector (Vect), pBABE-RPS14(WT)-Myc (RPS14) or pBABE-RPL22(WT)-Myc (RPL22): Myc (Myc-tag), total RB (RB [tot]), MCM6, phosphorylated H3 on serine 10 (H3(pS10)), total p53 (p53(tot)) and alpha-tubulin.Blots are representative of 3 independent experiments with similar results. **H-I.** Normalized Fluc/Rluc ratios ofIMR-90 cells transduced with an empty vector (Vector), or pBABE-RPS14(WT)-Myc (RPS14, H), or pBABE-RPL22(WT)-Myc (RPL22, I), and with the luciferase reporter AQP4. Luciferase activities were measured at days 7, 12 and 14 post-infection. Normalizations are presented as means relative to vector-infected cells, n=3 with technical triplicates for each

experiment Unpaired t tests with equal SD were performed. Error bars indicate SD of biological triplicates. * = $p<0.05$, ** = $p<0.01$, *** = $p<0.001$ are significantly different, using two-tailed Student's t-test. **J.** Schema showing the RB activation/inhibition factors that modulate readthrough.

Therapy-induced senescence and TR

To investigate whether a reduction in readthrough also applies to the senescent response induced by chemotherapeutic drugs in cancer cells (therapy-induced senescence: TIS) we treated PC3 prostate cancer cells with camptothecin for 24 hours and confirmed that most of the cell population was senescent using the SA-β-Gal assay and western blots for phospho-RB, MCM6 and pH3(S10) (Figure 6A-B). As found for OIS, TIS also reduced TR on both the UGA and the AQP4 reporters (Figure 6C) and a similar results were found in MDA.MB.231 breast cancer cells (Figure 6D-E). TIS is not a stable phenotype (Guillon et al., 2019; Milanovic et al., 2018; Saleh et al., 2020). After 20 days in culture, a population of growing cells emerged from the TIS population and continued to grow without signs of senescence. These cells that bypass TIS are known to be more malignant (Milanovic et al., 2018; Saleh et al., 2020) and they have an increased TR (Figure 6F) along with higher phosphorylation of RB (Fig 6G).

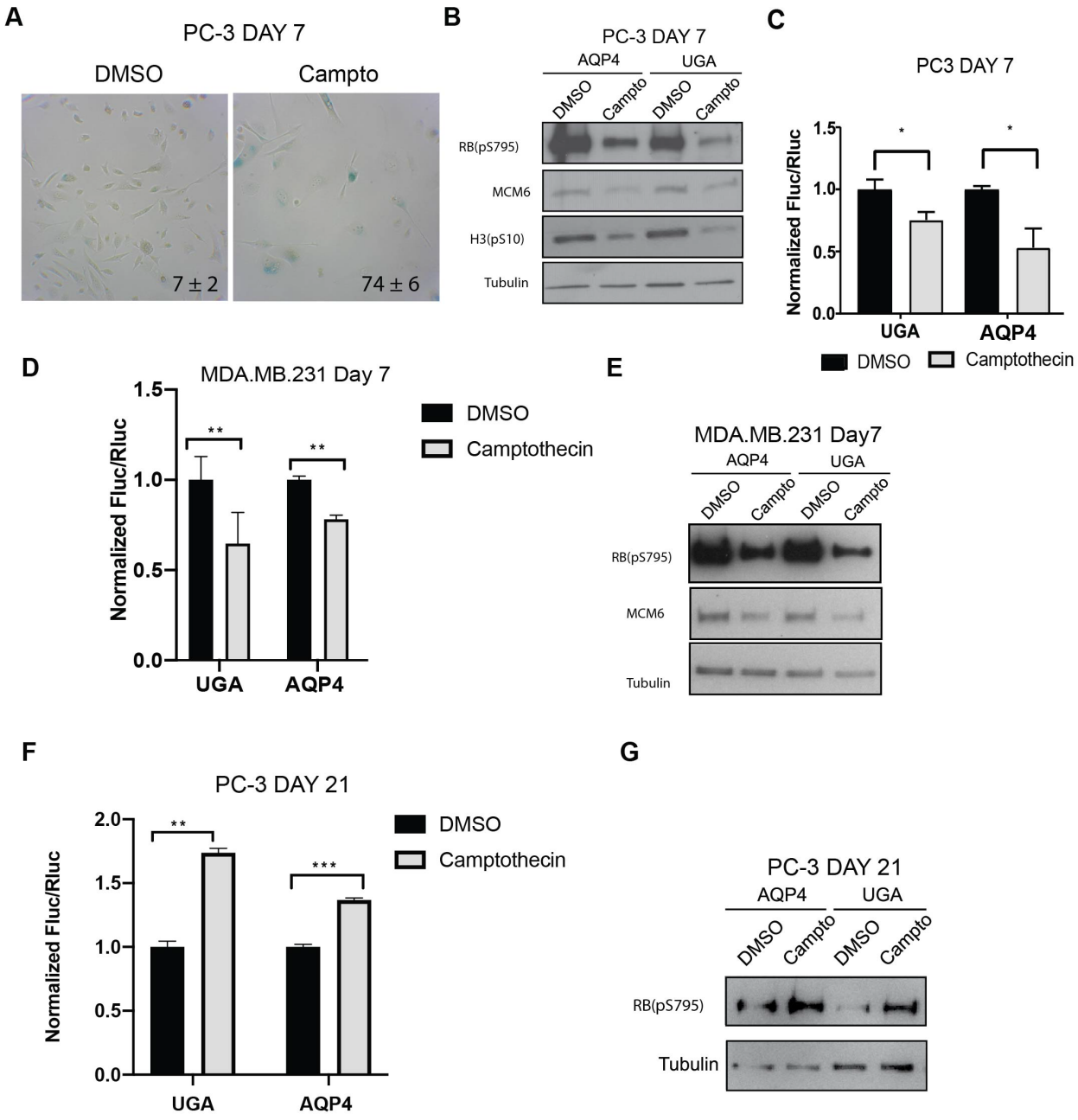

Figure 12. – Figure 6; Therapy-induced senescence reduces readthrough in cancer cells.

A. SA-β-gal staining of PC-3 cells treated 24h with vehicle and/or 100nM of camptothecin and fixed seven days later (day 7), the percent positive cells ± SD is shown in lower corner, n=3. **B.** Immunoblots in PC-3 cells transduced with luciferase reporter (AQP4, UGA) and treated as in (A) for the proteins: RB(pS795) [phosphorylated RB on serine 795], MCM6, H3(pS10) [phosphorylated H3 on serine 10] and tubulin. Blots are representative of 3 independent experiments with similar results. **C.** Normalized Fluc/Rluc ratios of indicated readthrough

reporters in cells as in (A). Normalizations are presented as means relative to vehicle treated cells from (UGA) n=4 and (AQP4) n=5 independent experiments each with technical triplicates. **D.** Normalized Fluc/Rluc ratios in ofMDA.MB.231 cells transduced with the luciferase reporters (UGA, AQP4) and treated as in (A). Normalizations are presented as means relative to vehicle treated cells, n=3. **E.** Normalized Fluc/Rluc ratios of indicated readthrough reporters in PC-3 cells as in (A) 21 days post-treatment when the cell population bypassed senescence. For all luciferase assays, n=3, error bars indicate SD of technical triplicates of each experiment. * = $p<0.05$, ** = $p<0.01$, *** = $p<0.001$ using two-tailed Student's t-test. **F.** Immunoblots for phosphorylated RB at serine 795 (RB[pS795]) and tubulin in cells as in (E), n=3.

Senescence suppresses the expression of AGO1x, an AGO1 isoform generated by TR.

AGO1x is an isoform of AGO1 that is expressed by TR of the AGO1 mRNA (Eswarappa et al., 2014; Ghosh et al., 2020; Singh et al., 2019). AGO1x acts as an inhibitor of the miRNA pathway (Singh et al., 2019) and in breast cancer cells it is required to maintain cell proliferation through inhibition of interferon genes expression (Ghosh et al., 2020). Senescent cells upregulate interferon gene expression (Fridman and Tainsky, 2008; Frisch and MacFawn, 2020; Moiseeva et al., 2006) suggesting that a reduced TR of AGO1 mRNA may lead to low levels of AGO1x and high levels of interferon genes in these cells. To test this idea, we triggered therapy induced senescence (TIS) in MDA.MB.231 breast cancer cells with Camptothecin (Figure 7A and B). As expected, the expression of AGO1x was reduced in these TIS cells (Figure 7C) but was dramatically induced after cells escaped from senescence (Figure 7C-D). Senescence and the escape from senescence was characterized using KI67 (Figure 7E-F) and immunoblots for RNR (a repression target of p53), p21 (an activation target of p53), MCM6 (a repression target of RB), phospho-H3(a marker of cell proliferation) and γH2AX (a marker of DNA damage) (Figure 7G). These results demonstrate that senescence can lead to repression of cancer driver proteins like AGO1x by reducing TR.

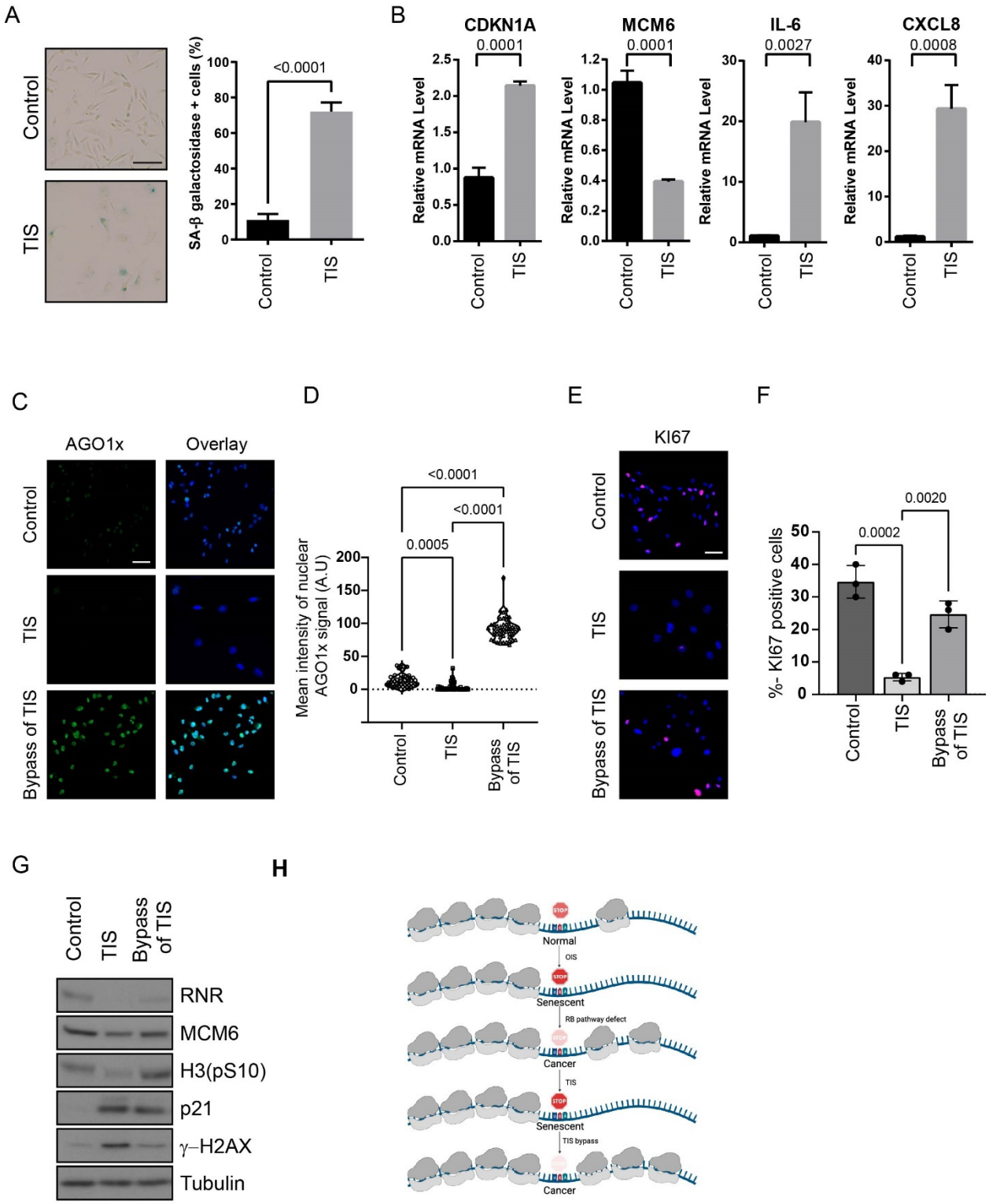

Figure 13. – Figure 7; Senescence affects endogenous TR target AGO1x.

A. Images of senescence-associated β galactosidase assay and its quantification in MDA.MB.231 treated with 40 nM of camptothecin (therapy-induced senescence (TIS)) or Vehicle (Control)

for 96h. Data shows mean of three biological replicates and error bars show SD. Student's-T-test was performed and p value is indicated. **B.** Relative mRNA levels of indicated mRNA in cells as in (A). Data shows mean of three biological replicates and error bars show SD. Student's-T-test was performed and p value is indicated. **C.** Immunofluorescence of AGO1x in MDA.MB.231 cells that were treated with 40 nM of camptothecin (TIS) or Vehicle (Control) or cells that were treated with camptothecin and left to recover for 14 days to allow bypass of senescence (Bypass of TIS). Scale bar = 50 μm. A representative image of three biological replicates is shown. **D.** Quantification of results in (C). A minimum of 50 cells were scored for nuclear staining intensity using Image J. Statistical analysis was performed by ANOVA with Tukey post-test. A.U.= arbitrary units. **E.** Immunofluorescence of KI67 from MDA.MB.231 cells treated as in (C). Scale bar = 50μm. A representative image of three biological replicates is shown. **F.** Quantification of the percentage of cells expressing Ki67 shown in (E). Statistical analysis was performed by ANOVA with Tukey post-test. **G.** Immunoblot against the indicated proteins in MDA.MB.231 cells treated as in (C). H3(pS10): phosphorylated Histone H3 at serine 10, and γH2AX: phosphorylated at serine 139 of histone H2AX variant. **H.** Regulation of readthrough in senescent cells.

2.2.5. Discussion

We show here that cellular senescence induced by oncogenic ras, the tumor suppressor PML, CDK4 inhibitors or chemotherapy reduces TR. Conversely, we also report that cells that bypass senescence have an increase in translational TR (Figure 7H). The effect of senescence was demonstrated in a variety of reporters containing stop codons in a common context, within regions that stimulate endogenous TR and on an endogenous RT target, AGO1x. We propose a novel caretaker tumor suppressor activity for cellular senescence controlled mainly by the RB pathway in preventing TR and the generation of C-terminally extended proteins (Schueren et al., 2014; Stiebler et al., 2014). The potential for TR to confer advantages to cells in stress was previously reported in yeast cells expressing the prion PSI that enhances both TR and resistance to several stresses (True et al., 2004).

Senescence also reduced the stimulatory effect of aminoglycosides and the enhancer effect of CDX5-1 on TR (Manuvakhova et al., 2000). It has been reported that CDX5-1

potentiates G418-induced TR up to 180-fold compared to the aminoglycoside G418 alone (Baradaran-Heravi et al., 2016). Here, we show a clear resistance of senescent cells to induce C-terminal extended proteins. Green and Goff reported that aminoglycosides can increase TR of the MMuLV gag-pol junction in HEK-293 cells (Green and Goff, 2015). However, using normal fibroblasts, we found that the same drugs did not have such effect. HEK-293 cells have an inactivation of the RB and PML tumor suppressor pathways due to expression of adenovirus E1A oncoprotein. In our normal cells, disruption of these pathways increases TR. It is thus plausible that in the context of an altered control in HEK293 cells, the MMuLV gag-pol junction TR is stimulated by aminoglycosides. In addition, Green and Goff used several aminoglycosides in their studies, gentamicin being the less active and its effects were reported as dose-independent and not consistent. Since gentamicin does increase TR in other stop codon contexts, we suggest that the pseudoknot structure of the viral signal may interfere with the binding or the action of gentamicin on the ribosome.

Our results indicate that translation termination tends to be inaccurate in cancer-like cells where the RB pathway is dysfunctional but is particularly efficient in senescent cells. Early work by Stanners and colleagues showed that SV40-mediated transformation increased mistranslation in mammalian cells (Pollard et al., 1982). SV40 encodes for the large T antigen that binds and inactivates the RB family of tumor suppressors (DeCaprio et al., 1988) like the E7 oncoprotein we used in this study. Recently, Ruggero et al found that loss of SNORA24, a small nucleolar RNA that mediates pseudouridylation of rRNA, leads to bypass of RAS-induced senescence in the liver promoting hepatocellular carcinoma. Intriguingly, cells lacking SNORA24 had an increase in TR and mistranslations (McMahon et al., 2019). Also Diaz and colleagues found that translational fidelity is decreased in the most aggressive breast cancer cell lines (Belin et al., 2009). They also reported that the p53 tumor suppressor controls translational fidelity and in particular the translation of oncogenic proteins from IRES (Marcel et al., 2013). In our experimental system, the RB pathway was more important to control TR levels in OIS. Consistent with this notion, we show that TR was reduced after TIS in p53 mutant PC-3 and MDA.MB.231 cells. However, we did notice that inactivation of p53 in cells where RB is also inactivated further increased TR, suggesting also an important role for p53 (Figure 4A-C). Taken together, the evidence indicates that preventing translational errors and TR is a tumor suppressor mechanism.

The RB tumor suppressor pathway may repress genes that modulate TR. TR occurs when near cognate tRNAs outcompete the translation termination factors eRF1/eRF3 (Beissel et al., 2019; Cassan and Rousset, 2001). RB represses tRNA expression (Gjidoda and Henry, 2013) and this could prevent TR by near cognate suppressor tRNAs. Also, the translation initiation factor eIF3 interacts with post-initiation ribosomes and controls TR (Beznoskova et al., 2013; Beznoskova et al., 2015). RB could repress the expression of eIF3 subunits or sequester them in PML bodies (Vernier et al., 2011). Consistent with the latter mechanism the eIF3 subunits EIF3K and EIF3E (Int-6) localize to PML bodies (Morris-Desbois et al., 1999; Salsman et al., 2013). Viral proteins such as HTLV-I Tax can delocalize EIF3E from PML bodies (Desbois et al., 1996), an event that could facilitate TR.

Of special interest for a plausible pharmacological modulation of readthrough levels, we found that the CDK4 inhibitor palbociclib was able to reduce TR and re-induce a stable cell cycle arrest in cells that bypassed senescence. If the phenotypic plasticity conferred by C-terminal extended proteins plays a causal role in the origin of human cancers or their resistance to chemotherapy, palbociclib could be used to halt the progression of these lesions.

2.2.6. Funding

This work was supported by a NSERC grants to L. B.-G. and G.F. and a CCSRI (Canadian Cancer Society Research Institute) grant [704223 to G.F.]. N.D.T. acknowledges a studentship support from the GRUM (Université de Montréal), F.L. acknowledges support from the FRQS and CRS (Cancer Research Society), S.T. acknowledges a summer NSERC studentship. G.F. is the recipient of a CIBC chair for breast cancer research at the CR-CHUM.

2.2.7. Acknowledgements

We are grateful to I. Topisirovic, K. Tandook, and M. Leibovitch at the Lady Davis Institute, Department of Oncology, McGill University, for their help and advices in polysome fractionation assays, M. Roberg at the University of British Columbia for CDX5-1 and X. Roucoux, J-F. Lucier and F-M. Boisvert at the Université de Sherbrooke, Département de Biochimie, for their help in the identification of readthrough events by bioinformatic analysis.This paper is dedicated to the memory of Dr Léa Brakier-Gingras

(1940-2021) who committed her life to study the ribosome and the signals that increase proteome diversity.

2.2.7. References

Acevedo, M., Vernier, M., Mignacca, L., Lessard, F., Huot, G., Moiseeva, O., Bourdeau, V. and Ferbeyre, G. (2016). A CDK4/6-Dependent Epigenetic Mechanism Protects Cancer Cells from PML-induced Senescence. *Cancer Res* **76**, 3252-64.

Ajore, R., Raiser, D., McConkey, M., Joud, M., Boidol, B., Mar, B., Saksena, G., Weinstock, D. M., Armstrong, S., Ellis, S. R. et al. (2017). Deletion of ribosomal protein genes is a common vulnerability in human cancer, especially in concert with TP53 mutations. *EMBO Mol Med* **9**, 498-507.

Baradaran-Heravi, A., Balgi, A. D., Zimmerman, C., Choi, K., Shidmoossavee, F. S., Tan, J. S., Bergeaud, C., Krause, A., Flibotte, S., Shimizu, Y. et al. (2016). Novel small molecules potentiate premature termination codon readthrough by aminoglycosides. *Nucleic Acids Res* **44**, 6583-98.

Beissel, C., Neumann, B., Uhse, S., Hampe, I., Karki, P. and Krebber, H. (2019). Translation termination depends on the sequential ribosomal entry of eRF1 and eRF3. *Nucleic Acids Res* **47**, 4798-4813.

Belin, S., Beghin, A., Solano-Gonzalez, E., Bezin, L., Brunet-Manquat, S., Textoris, J., Prats, A. C., Mertani, H. C., Dumontet, C. and Diaz, J. J. (2009). Dysregulation of ribosome biogenesis and translational capacity is associated with tumor progression of human breast cancer cells. *PLoS One* **4**, e7147.

Beznoskova, P., Cuchalova, L., Wagner, S., Shoemaker, C. J., Gunisova, S., von der Haar, T. and Valasek, L. S. (2013). Translation initiation factors eIF3 and HCR1 control translation termination and stop codon read-through in yeast cells. *PLoS Genet* **9**, e1003962.

Beznoskova, P., Wagner, S., Jansen, M. E., von der Haar, T. and Valasek, L. S. (2015). Translation initiation factor eIF3 promotes programmed stop codon readthrough. *Nucleic Acids Res* **43**, 5099-111.

Bidou, L., Rousset, J. P. and Namy, O. (2010). Translational errors: from yeast to new therapeutic targets. *FEMS Yeast Res* **10**, 1070-82.

Bielas, J. H., Loeb, K. R., Rubin, B. P., True, L. D. and Loeb, L. A. (2006). Human cancers express a mutator phenotype. *Proc Natl Acad Sci U S A* **103**, 18238-42.

Bratulic, S., Toll-Riera, M. and Wagner, A. (2017). Mistranslation can enhance fitness through purging of deleterious mutations. *Nat Commun* **8**, 15410.

Bury, M., Le Calvé, B., Ferbeyre, G., Blank, V. and Lessard, F. (2021). New Insights into CDK Regulators: Novel Opportunities for Cancer Therapy. *Trends in Cell Biology*.

Cassan, M. and Rousset, J. P. (2001). UAG readthrough in mammalian cells: effect of upstream and downstream stop codon contexts reveal different signals. *BMC Mol Biol* **2**, 3.

Charbonneau, J., Gendron, K., Ferbeyre, G. and Brakier-Gingras, L. (2012). The 5' UTR of HIV-1 full-length mRNA and the Tat viral protein modulate the programmed -1 ribosomal frameshift that generates HIV-1 enzymes. *Rna* **18**, 519-29.

Collado, M. and Serrano, M. (2010). Senescence in tumours: evidence from mice and humans. *Nat Rev Cancer* **10**, 51-7.

DeCaprio, J. A., Ludlow, J. W., Figge, J., Shew, J. Y., Huang, C. M., Lee, W. H., Marsilio, E., Paucha, E. and Livingston, D. M. (1988). SV40 large tumor antigen forms a specific complex with the product of the retinoblastoma susceptibility gene. *Cell* **54**, 275-283.

Del Toro, N., Fernandez-Ruiz, A., Mignacca, L., Kalegari, P., Rowell, M. C., Igelmann, S., Saint-Germain, E., Benfdil, M., Lopes-Paciencia, S., Brakier-Gingras, L. et al. (2019). Ribosomal protein RPL22/eL22 regulates the cell cycle by acting as an inhibitor of the CDK4-cyclin D complex. *Cell Cycle* **18**, 759-770.

Desbois, C., Rousset, R., Bantignies, F. and Jalinot, P. (1996). Exclusion of Int-6 from PML nuclear bodies by binding to the HTLV-I Tax oncoprotein. *Science* **273**, 951-3.

Deschenes-Simard, X., Gaumont-Leclerc, M. F., Bourdeau, V., Lessard, F., Moiseeva, O., Forest, V., Igelmann, S., Mallette, F. A., Saba-El-Leil, M. K., Meloche, S. et al. (2013). Tumor suppressor activity of the ERK/MAPK pathway by promoting selective protein degradation. *Genes Dev* **27**, 900-15.

Deschenes-Simard, X., Roy, S. and Ferbeyre, G. (2016). Genome reprogramming in cells that escape from senescence. *Bionatura* **1**, 54-61.

Drummond, D. A. and Wilke, C. O. (2009). The evolutionary consequences of erroneous protein synthesis. *Nat Rev Genet* **10**, 715-24.

Ebert, B. L., Pretz, J., Bosco, J., Chang, C. Y., Tamayo, P., Galili, N., Raza, A., Root, D. E., Attar, E., Ellis, S. R. et al. (2008). Identification of RPS14 as a 5q— syndrome gene by RNA interference screen. *Nature* **451**, 335-9.

El Asmi, F., Maroui, M. A., Dutrieux, J., Blondel, D., Nisole, S. and Chelbi-Alix, M. K. (2014). Implication of PMLIV in both intrinsic and innate immunity. *PLoS Pathog* **10**, e1003975.

Eswarappa, S. M., Potdar, A. A., Koch, W. J., Fan, Y., Vasu, K., Lindner, D., Willard, B., Graham, L. M., DiCorleto, P. E. and Fox, P. L. (2014). Programmed translational readthrough generates antiangiogenic VEGF-Ax. *Cell* **157**, 1605-18.

Ferbeyre, G., de Stanchina, E., Querido, E., Baptiste, N., Prives, C. and Lowe, S. W. (2000). PML is induced by oncogenic ras and promotes premature senescence. *Genes Dev* **14**, 2015-27.

Firth, A. E., Wills, N. M., Gesteland, R. F. and Atkins, J. F. (2011). Stimulation of stop codon readthrough: frequent presence of an extended 3' RNA structural element. *Nucleic Acids Res* **39**, 6679-91.

Fridman, A. L. and Tainsky, M. A. (2008). Critical pathways in cellular senescence and immortalization revealed by gene expression profiling. *Oncogene* **27**, 5975-87.

Frisch, S. M. and MacFawn, I. P. (2020). Type I interferons and related pathways in cell senescence. *Aging Cell* **19**, e13234.

Gandin, V., Sikstrom, K., Alain, T., Morita, M., McLaughlan, S., Larsson, O. and Topisirovic, I. (2014). Polysome fractionation and analysis of mammalian translatomes on a genome-wide scale. *J Vis Exp*.

Gendron, K., Dulude, D., Lemay, G., Ferbeyre, G. and Brakier-Gingras, L. (2005). The virion-associated Gag-Pol is decreased in chimeric Moloney murine leukemia viruses in which the readthrough region is replaced by the frameshift region of the human immunodeficiency virus type 1. *Virology* **334**, 342-52.

Gerashchenko, M. V., Lobanov, A. V. and Gladyshev, V. N. (2012). Genome-wide ribosome profiling reveals complex translational regulation in response to oxidative stress. *Proc Natl Acad Sci U S A* **109**, 17394-9.

Ghosh, S., Guimaraes, J. C., Lanzafame, M., Schmidt, A., Syed, A. P., Dimitriades, B., Borsch, A., Ghosh, S., Mittal, N., Montavon, T. et al. (2020). Prevention of dsRNA-induced interferon signaling by AGO1x is linked to breast cancer cell proliferation. *Embo J* **39**, e103922.

Gjidoda, A. and Henry, R. W. (2013). RNA polymerase III repression by the retinoblastoma tumor suppressor protein. *Biochim Biophys Acta* **1829**, 385-92.

Gosselin, K., Martien, S., Pourtier, A., Vercamer, C., Ostoich, P., Morat, L., Sabatier, L., Duprez, L., T'Kint de Roodenbeke, C., Gilson, E. et al. (2009). Senescence-associated oxidative DNA damage promotes the generation of neoplastic cells. *Cancer Res* **69**, 7917-25.

Green, L. and Goff, S. P. (2015). Translational readthrough-promoting drugs enhance pseudoknot-mediated suppression of the stop codon at the Moloney murine leukemia virus gag-pol junction. *J Gen Virol* **96**, 3411-21.

Grentzmann, G., Ingram, J. A., Kelly, P. J., Gesteland, R. F. and Atkins, J. F. (1998). A dual-luciferase reporter system for studying recoding signals. *Rna* **4**, 479-86.

Guillon, J., Petit, C., Moreau, M., Toutain, B., Henry, C., Roche, H., Bonichon-Lamichhane, N., Salmon, J. P., Lemonnier, J., Campone, M. et al. (2019). Regulation of senescence escape by TSP1 and CD47 following chemotherapy treatment. *Cell Death Dis* **10**, 199.

Harfe, B. D. and Jinks-Robertson, S. (2000). DNA mismatch repair and genetic instability. *Annu Rev Genet* **34**, 359-399.

Helt, A. M. and Galloway, D. A. (2001). Destabilization of the retinoblastoma tumor suppressor by human papillomavirus type 16 E7 is not sufficient to overcome cell cycle arrest in human keratinocytes. *J Virol* **75**, 6737-47.

Hernandez-Segura, A., de Jong, T. V., Melov, S., Guryev, V., Campisi, J. and Demaria, M. (2017). Unmasking Transcriptional Heterogeneity in Senescent Cells. *Curr Biol* **27**, 2652-2660 e4.

Houck-Loomis, B., Durney, M. A., Salguero, C., Shankar, N., Nagle, J. M., Goff, S. P. and D'Souza, V. M. (2011). An equilibrium-dependent retroviral mRNA switch regulates translational recoding. *Nature* **480**, 561-4.

Igelmann, S., Lessard, F., Uchenunu, O., Bouchard, J., Fernandez-Ruiz, A., Rowell, M. C., Lopes-Paciencia, S., Papadopoli, D., Fouillen, A., Ponce, K. J. et al. (2021). A hydride transfer complex reprograms NAD metabolism and bypasses senescence. *Mol Cell* **81**, 3848-3865 e19.

Jungreis, I., Lin, M. F., Spokony, R., Chan, C. S., Negre, N., Victorsen, A., White, K. P. and Kellis, M. (2011). Evidence of abundant stop codon readthrough in Drosophila and other metazoa. *Genome Res* **21**, 2096-113.

Kandoth, C., McLellan, M. D., Vandin, F., Ye, K., Niu, B., Lu, C., Xie, M., Zhang, Q., McMichael, J. F., Wyczalkowski, M. A. et al. (2013). Mutational landscape and significance across 12 major cancer types. *Nature* **502**, 333-339.

Kang, T. W., Yevsa, T., Woller, N., Hoenicke, L., Wuestefeld, T., Dauch, D., Hohmeyer, A., Gereke, M., Rudalska, R., Potapova, A. et al. (2011). Senescence surveillance of pre-malignant hepatocytes limits liver cancer development. *Nature* **479**, 547-51.

Law, M. E., Corsino, P. E., Narayan, S. and Law, B. K. (2015). Cyclin-Dependent Kinase Inhibitors as Anticancer Therapeutics. *Mol Pharmacol*.

Lessard, F., Brakier-Gingras, L. and Ferbeyre, G. (2019). Ribosomal Proteins Control Tumor Suppressor Pathways in Response to Nucleolar Stress. *Bioessays* **41**, e1800183.

Lessard, F., Igelmann, S., Trahan, C., Huot, G., Saint-Germain, E., Mignacca, L., Del Toro, N., Lopes-Paciencia, S., Le Calve, B., Montero, M. et al. (2018). Senescence-associated ribosome biogenesis defects contributes to cell cycle arrest through the Rb pathway. *Nat Cell Biol* **20**, 789-799.

Loughran, G., Chou, M. Y., Ivanov, I. P., Jungreis, I., Kellis, M., Kiran, A. M., Baranov, P. V. and Atkins, J. F. (2014). Evidence of efficient stop codon readthrough in four mammalian genes. *Nucleic Acids Res* **42**, 8928-38.

Mallette, F. A., Goumard, S., Gaumont-Leclerc, M. F., Moiseeva, O. and Ferbeyre, G. (2004). Human fibroblasts require the Rb family of tumor suppressors, but not p53, for PML-induced senescence. *Oncogene* **23**, 91-9.

Manuvakhova, M., Keeling, K. and Bedwell, D. M. (2000). Aminoglycoside antibiotics mediate context-dependent suppression of termination codons in a mammalian translation system. *Rna* **6**, 1044-55.

Marcel, V., Ghayad, S. E., Belin, S., Therizols, G., Morel, A. P., Solano-Gonzalez, E., Vendrell, J. A., Hacot, S., Mertani, H. C., Albaret, M. A. et al. (2013). p53 acts as a safeguard of translational control by regulating fibrillarin and rRNA methylation in cancer. *Cancer Cell* **24**, 318-30.

McMahon, M., Contreras, A., Holm, M., Uechi, T., Forester, C. M., Pang, X., Jackson, C., Calvert, M. E., Chen, B., Quigley, D. A. et al. (2019). A single H/ACA small nucleolar RNA mediates tumor suppression downstream of oncogenic RAS. *Elife* **8**.

Milanovic, M., Fan, D. N. Y., Belenki, D., Dabritz, J. H. M., Zhao, Z., Yu, Y., Dorr, J. R., Dimitrova, L., Lenze, D., Monteiro Barbosa, I. A. et al. (2018). Senescence-associated reprogramming promotes cancer stemness. *Nature* **553**, 96-100.

Moiseeva, O., Mallette, F. A., Mukhopadhyay, U. K., Moores, A. and Ferbeyre, G. (2006). DNA Damage Signaling and p53-dependent Senescence after Prolonged beta-Interferon Stimulation. *Mol Biol Cell* **17**, 1583-92.

Morris-Desbois, C., Bochard, V., Reynaud, C. and Jalinot, P. (1999). Interaction between the Ret finger protein and the Int-6 gene product and co-localisation into nuclear bodies. *J Cell Sci* **112 (Pt 19)**, 3331-42.

Nassour, J., Martien, S., Martin, N., Deruy, E., Tomellini, E., Malaquin, N., Bouali, F., Sabatier, L., Wernert, N., Pinte, S. et al. (2016). Defective DNA single-strand break repair is responsible for senescence and neoplastic escape of epithelial cells. *Nat Commun* **7**, 10399.

Pollard, J. W., Harley, C. B., Chamberlain, J. W., Goldstein, S. and Stanners, C. P. (1982). Is transformation associated with an increased error frequency in mammalian cells? *J Biol Chem* **257**, 5977-9.

Regad, T., Saib, A., Lallemand-Breitenbach, V., Pandolfi, P. P., de The, H. and Chelbi-Alix, M. K. (2001). PML mediates the interferon-induced antiviral state against a complex retrovirus via its association with the viral transactivator. *Embo J* **20**, 3495-505.

Ribas de Pouplana, L., Santos, M. A., Zhu, J. H., Farabaugh, P. J. and Javid, B. (2014). Protein mistranslation: friend or foe? *Trends Biochem Sci* **39**, 355-62.

Romanov, S. R., Kozakiewicz, B. K., Holst, C. R., Stampfer, M. R., Haupt, L. M. and Tlsty, T. D. (2001). Normal human mammary epithelial cells spontaneously escape senescence and acquire genomic changes. *Nature* **409**, 633-7.

Rosenberger, G., Koh, C. C., Guo, T., Rost, H. L., Kouvonen, P., Collins, B. C., Heusel, M., Liu, Y., Caron, E., Vichalkovski, A. et al. (2014). A repository of assays to quantify 10,000 human proteins by SWATH-MS. *Sci Data* **1**, 140031.

Saleh, T., Bloukh, S., Carpenter, V. J., Alwohoush, E., Bakeer, J., Darwish, S., Azab, B. and Gewirtz, D. A. (2020). Therapy-Induced Senescence: An "Old" Friend Becomes the Enemy. *Cancers (Basel)* **12**.

Salsman, J., Pinder, J., Tse, B., Corkery, D. and Dellaire, G. (2013). The translation initiation factor 3 subunit eIF3K interacts with PML and associates with PML nuclear bodies. *Exp Cell Res* **319**, 2554-65.

Schueren, F., Lingner, T., George, R., Hofhuis, J., Dickel, C., Gartner, J. and Thoms, S. (2014). Peroxisomal lactate dehydrogenase is generated by translational readthrough in mammals. *Elife* **3**, e03640.

Schueren, F. and Thoms, S. (2016). Functional Translational Readthrough: A Systems Biology Perspective. *PLoS Genet* **12**, e1006196.

Serrano, M., Lin, A. W., McCurrach, M. E., Beach, D. and Lowe, S. W. (1997). Oncogenic ras provokes premature cell senescence associated with accumulation of p53 and p16INK4a. *Cell* **88**, 593-602.

Sherr, C. J., Beach, D. and Shapiro, G. I. (2016). Targeting CDK4 and CDK6: From Discovery to Therapy. *Cancer Discov* **6**, 353-67.

Singh, A., Manjunath, L. E., Kundu, P., Sahoo, S., Das, A., Suma, H. R., Fox, P. L. and Eswarappa, S. M. (2019). Let-7a-regulated translational readthrough of mammalian AGO1 generates a microRNA pathway inhibitor. *Embo J* **38**, e100727.

Stiebler, A. C., Freitag, J., Schink, K. O., Stehlik, T., Tillmann, B. A., Ast, J. and Bolker, M. (2014). Ribosomal readthrough at a short UGA stop codon context triggers dual localization of metabolic enzymes in Fungi and animals. *PLoS Genet* **10**, e1004685.

Tate, W. P., Cridge, A. G. and Brown, C. M. (2018). 'Stop' in protein synthesis is modulated with exquisite subtlety by an extended RNA translation signal. *Biochem Soc Trans* **46**, 1615-1625.

True, H. L., Berlin, I. and Lindquist, S. L. (2004). Epigenetic regulation of translation reveals hidden genetic variation to produce complex traits. *Nature* **431**, 184-7.

Vernier, M., Bourdeau, V., Gaumont-Leclerc, M. F., Moiseeva, O., Begin, V., Saad, F., Mes-Masson, A. M. and Ferbeyre, G. (2011). Regulation of E2Fs and senescence by PML nuclear bodies. *Genes Dev* **25**, 41-50.

Vernier, M. and Ferbeyre, G. (2014). Complete senescence: RB and PML share the task. *Cell Cycle* **13**, 696.

Voghel, G., Thorin-Trescases, N., Mamarbachi, A. M., Villeneuve, L., Mallette, F. A., Ferbeyre, G., Farhat, N., Perrault, L. P., Carrier, M. and Thorin, E. (2010). Endogenous oxidative stress prevents telomerase-dependent immortalization of human endothelial cells. *Mech Ageing Dev* **131**, 354-63.

Xue, W., Zender, L., Miething, C., Dickins, R. A., Hernando, E., Krizhanovsky, V., Cordon-Cardo, C. and Lowe, S. W. (2007). Senescence and tumour clearance is triggered by p53 restoration in murine liver carcinomas. *Nature* **445**, 656-60.

Yoshinaka, Y., Katoh, I., Copeland, T. D. and Oroszlan, S. (1985). Murine leukemia virus protease is encoded by the gag-pol gene and is synthesized through suppression of an amber termination codon. *Proc Natl Acad Sci U S A* **82**, 1618-22.

Young, A. R., Narita, M., Ferreira, M., Kirschner, K., Sadaie, M., Darot, J. F., Tavare, S., Arakawa, S., Shimizu, S., Watt, F. M. et al. (2009). Autophagy mediates the mitotic senescence transition. *Genes Dev* **23**, 798-803.

Zhang, H., Lyu, Z., Fan, Y., Evans, C. R., Barber, K. W., Banerjee, K., Igoshin, O. A., Rinehart, J. and Ling, J. (2020). Metabolic stress promotes stop-codon readthrough and phenotypic heterogeneity. *Proc Natl Acad Sci U S A* **117**, 22167-22172.

2.2.7. Supplementary material

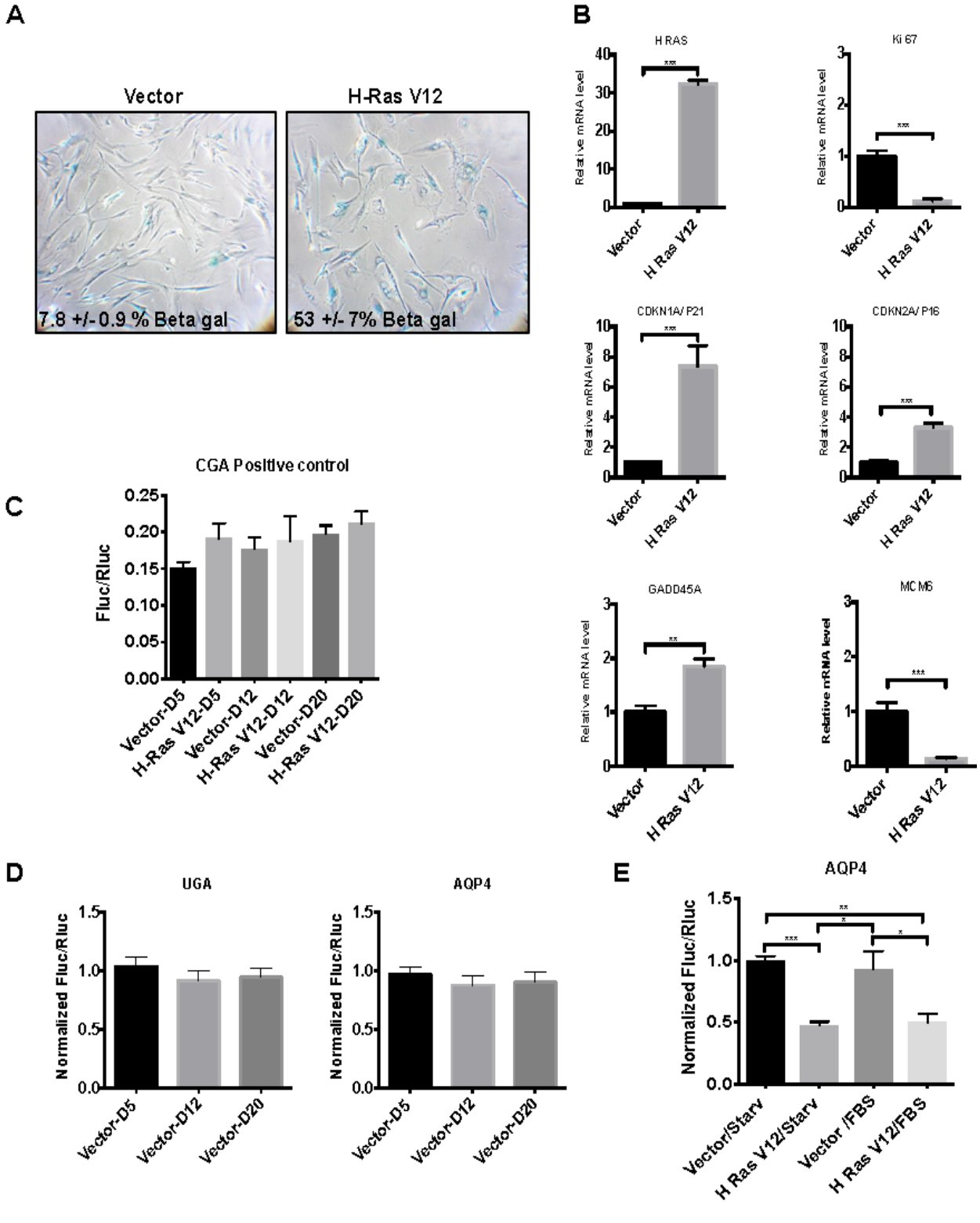

Figure 14. – Figure S1; Readthrough isreduced in OIS

A. SA-β-gal of proliferating (Vector) and senescent IMR90 (H-RasV12 oncogene) cells, fixed at day 12 post-infection. Datawere quantified from many fields within one experiment to represent the entire petri dish.Threeindependent cell counts up to a total of at least 100 cells are presented as the mean and SD of positive cells. **B.** RT-qPCRs for senescent marker mRNAs were performedin IMR-90 cells at day 12 post-infection for cells as in (A). Data are normalized over TBPand HMBS, and presented as means relative to vector infected cells. Errorbars indicate SD of technical triplicates. ** = $p<0.01$, *** = $p<0.001$ are significantly different, using two-tailed Student's t-test. **C.** Luciferase activities from non-readthrough control (CGA-Positive control) in proliferating (Vector) and H-RasV12 senescent cells measured at days 5 (D5), 12 (D12) and 20 (D20) post-infection. Assays are representative of 2 independent experiments with similar results with technical triplicates for each experiment. One-way ANOVA with post-hoc Tukey HSD were performed. Error bars indicate SD of technical triplicates. **D.** Normalized Fluc/Rluc ratios indicate that readthrough leveldoes not change in non-senescent cells (Vector) at day 5 (D5), 12 (D12) or 20 (D20) post-infection. Error bars indicate SD of biological triplicates. **E.** Luciferase activities from AQP4 reporter were measured at day 12 post-infection. Normalized Fluc/Rluc ratios from non-senescent (Vector) and senescent cells (H-RasV12), starved (Starv) or supplied with fetal bovine serum (FBS) are represented. Starvation was performed for a week to induce quiescence. Data are presented as means relative to empty vector-infected cells, which are representative of 2 independent experiments with similar results with technical triplicates for each experiment. One-way ANOVA with post-hoc Tukey HSD were performed. Error bars indicate SD of technical triplicates. Tukey HSD p-values indicate that * = $p<0.05$, ** = $p<0.01$, *** = $p<0.001$ are significantly different

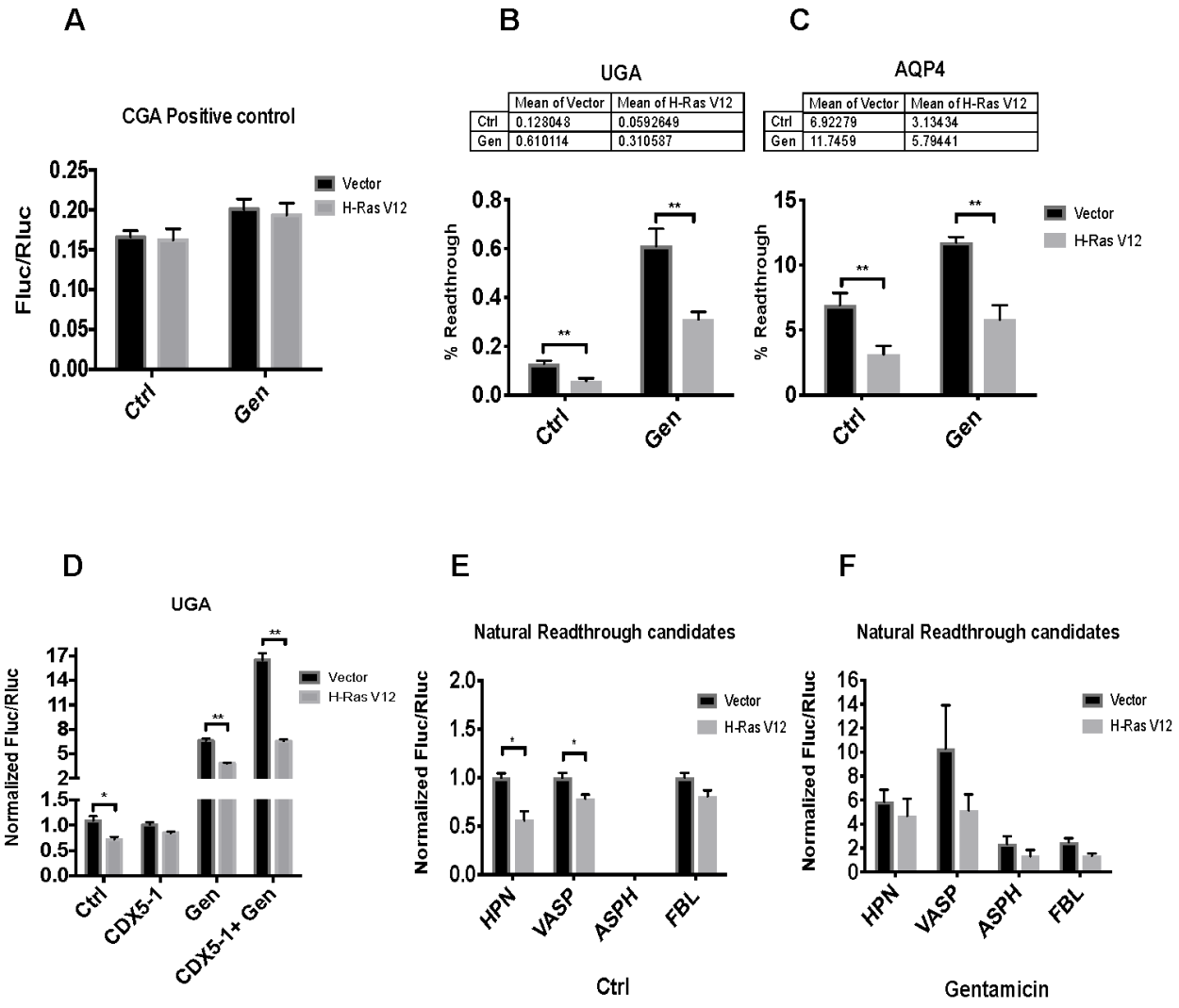

Figure 15. – Figure S2 ; Senescent cells are resistant to gentamicin-induced readthrough.

A. IMR-90 cells were transduced with an empty vector (Vector) or H-RasV12 oncogene to induce OIS and with indicated non-readthrough control luciferase reporter. Cells were treated with vehicle (Ctrl) or with 900 µg/ml of gentamicin sulfate (Gen) 24 hours before measuring luciferase activities at day 12 post-infection. Error bars indicate SD of biological triplicates. **B-C.** The percent of readthrough was determined by dividing Fluc/Rluc ratio from UGA or AQP4 luciferase reporters by Fluc/Rluc ratio from non-readthrough controls multiplied by 100. Error bars indicate SD of biological triplicates. ** = $p<0.01$ is significantly different, using two-tailed Student's t-test. **D.** IMR-90 cells were transduced with an empty vector (Vector) or H-RasV12 oncogene to induce OIS and with a UGA luciferase reporter. Cells were treated with vehicle (Ctrl) and/or 600 µg/ml of gentamicin sulfate (Gen) and/or 25 µM of CDX5-1 72 hours before measuring luciferase

activities at day 12 post-infection. Error bars indicate SD of biological triplicates. * = $p<0.05$, ** = $p<0.01$ are significantly different, using two-tailed Student's t-test. **E.** A stop codon within natural contexts from VASP, ASPH, HPN and FBL, was inserted in the intercistronic region of Rluc-Fluc luciferase reporter. IMR-90 cells were transduced with an empty vector (Vector) or H-RasV12 oncogene to induce OIS and with luciferase reporters. Luciferase activities were measured in non-senescent and senescent cells at day 12 post-infection. Error bars indicate SD of biological triplicates. * = $p<0.05$ is significantly different, using two-tailed Student's t-test. **F.** Cells as in (E) were treated with 900 μg/ml of gentamicin sulfate (Gen) 24 hours before measuring luciferase activities at day 12 post-infection. Normalized Fluc/Rluc ratios indicate the efficiency of readthrough. Normalizations are presented as means relative to vector-infected cells from three independent experiments with technical triplicates for each experiment. Unpaired Student's t-test with equal SD were performed. Error bars indicate SD of biological triplicates.

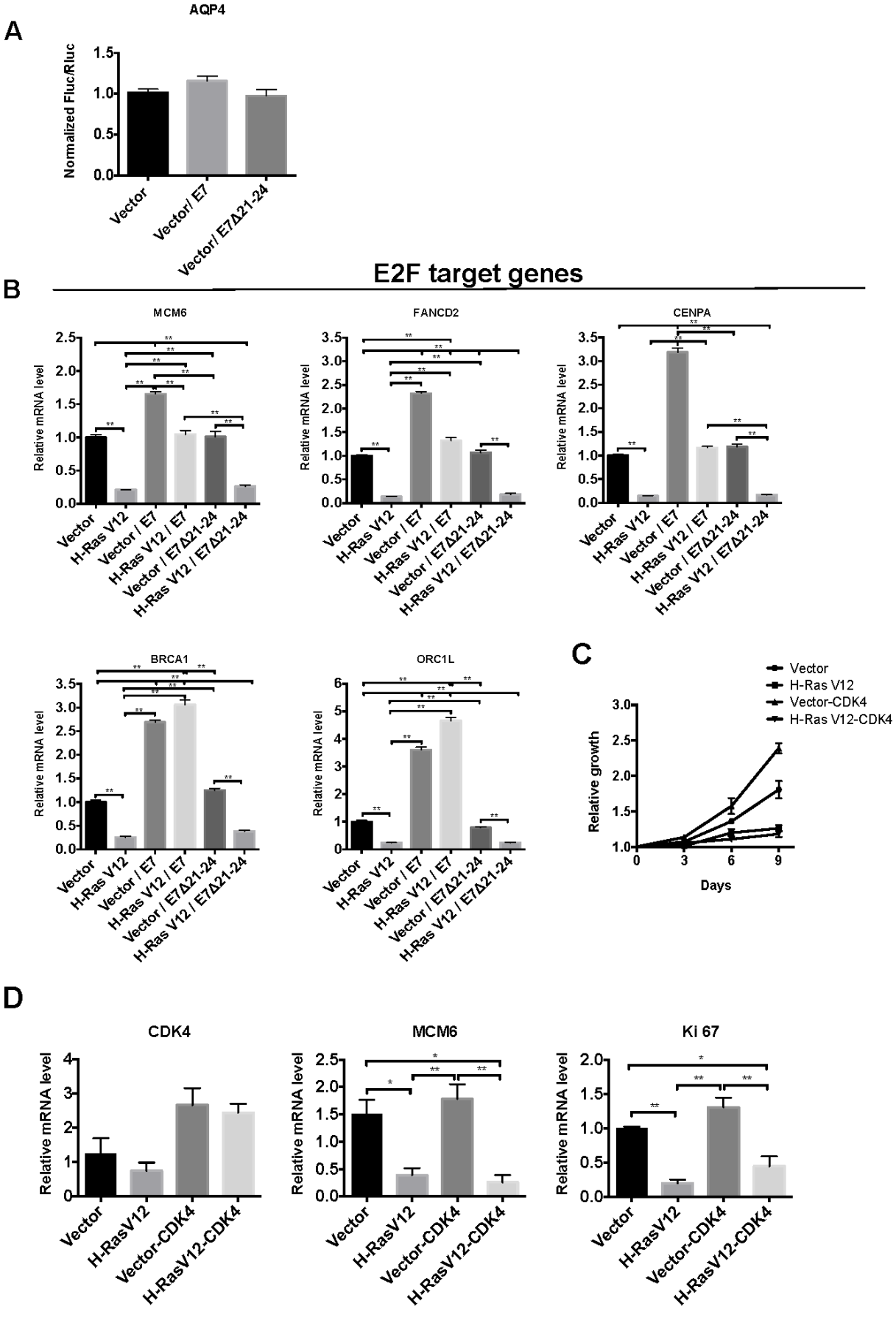
A
AQP4
Normalized Fluc/Rluc
Vector
Vector/ E7
Vector/ E7Δ21-24
B
E2F target genes
MCM6
FANCD2
CENPA
BRCA1
ORC1L
Relative mRNA level
Vector
H-Ras V12
Vector / E7
H-Ras V12 / E7
Vector / E7Δ21-24
H-Ras V12 / E7Δ21-24
C
Vector
H-Ras V12
Vector-CDK4
H-Ras V12-CDK4
Relative growth
Days
D
CDK4
MCM6
Ki 67
Relative mRNA level
Vector
H-RasV12
Vector-CDK4
H-RasV12-CDK4

Figure 16. – Figure S3; RB pathway disruption affects the efficiency of readthrough.

A. IMR-90 cells were transduced with luciferase reporter AQP4and an empty vector (Vector), wild-type E7 or E7 Δ21-24 mutant oncogene. Luciferase activities were measured at day 12 post-infection. Normalized Fluc/Rluc ratios indicate the efficiency of readthrough. Normalizations are presented as means relative to vector-infected cells from three independent experiments with technical triplicates for each experiment. Error bars indicate SD of biological triplicates. **B.** Representative RT-qPCR from E2Fs' target mRNAs were performed in IMR-90 cells transduced with an empty control vector (pLXSN), wild-type E7 or E7 Δ21-24 mutant oncogene, and with an empty vector (Vector) or with H-RasV12 oncogene to induce OIS at day 12 post-infection. Data are normalized over TBP and HMBS, and presented as means relative to vector infected cells. Experiments were done three times with technical triplicates for each experiment. Error bars indicate SD of technical triplicates. Tukey HSD p-values indicate that ** = $p<0.01$ is significantly different. **C.** Growth curves of non-senescent (Vector) and H-RasV12 senescent IMR-90s overexpressing or not CDK4. Data are presented as means normalized to day 0 of each condition. Assays are representative of 2 independent experiments with similar results with technical triplicates for each experiment. Error bars indicate SD of technical triplicates. **D.** RT-qPCRs for CDK4, MCM6 and KI67 mRNAs were performed in IMR-90 cells as in (C) and at day 12 post-infection. Data are normalized over TBP and HMBS, and presented as means relative to vector infected cells from three independent experiments with technical triplicates for each experiment. One-way ANOVA with post-hoc Tukey HSD were performed in (A, B, D) and Unpaired Student's t-test with equal SD was performed in (C). Error bars indicate SD of biological triplicates. Tukey HSD p-values indicate that * = $p<0.05$, ** = $p<0.01$ are significantly different.

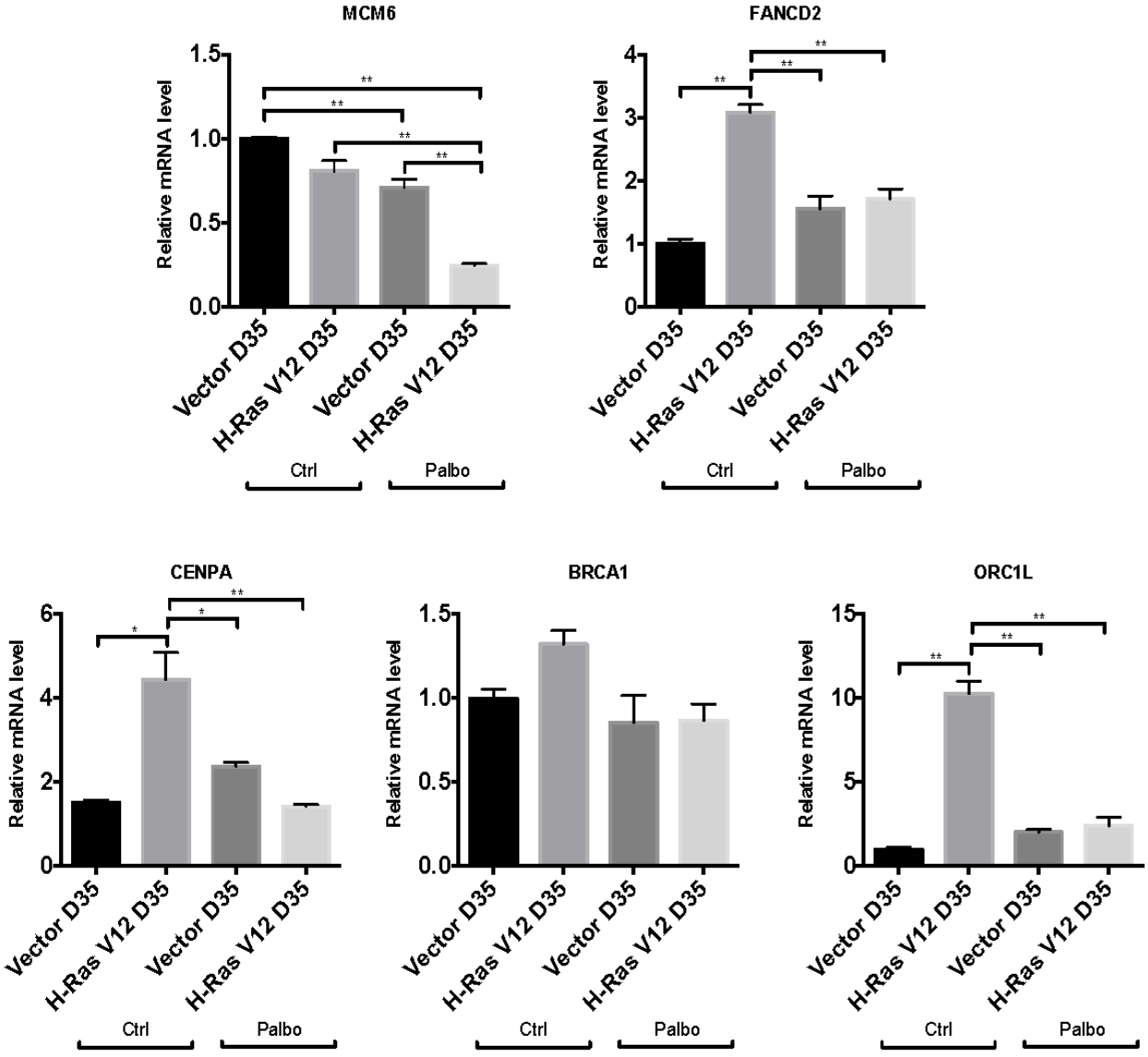

Figure 17. – Figure S4; E2Fs target genes.

A. RT-qPCR for E2Fs' target mRNAs were performed inIMR-90 at day 35 post-infection with an empty vector (Vector D35) or with the oncogene H-RasV12 (H-RasV12 D35) and treated with vehicle (Ctrl) or with 1 μM of palbociclib (Palbo) for 5 days before cell lysis. Data are normalized over TBP and HMBS, and presented as means relative to vector infected cells from three independent experiments with technical triplicates for each experiment. One-way ANOVA with post-hoc Tukey HSD were performed. Error bars indicate SD of technical triplicates. Tukey HSD p-values indicate that * = $p<0.05$, ** =$p<0.01$ are significantly different.

Tableau 2. – Table S1; PCR cloning primers

Name	5' forwad primer (5'-3')	3' reverse primer (5'-3')
pMSCV-RLUC-FLUC	GGAAGAAAGCGGCCGCTTCAGATCCGCTAGAGCC	TGGATGCATGAATTTCGTCATCGCTGAATAC
UGA STOP CODON	CCAAGCTTGCACCAGTGACCAGCAAGGTGTACG	CGTACACCTTGCTGGTCACTGGTGCAAGCTTGG

Tableau 3. – Table S2; Readthrough region

Gene name			Readthrough context
AQP4	Aquaporin 4	NM_001650.4	ATCTGGAGAGGTATTGTCTTCAGTA**TGA**CTAGAAGATCGCACTGAAAGCAGACAAGACTCCTTAGAA
ASPH	Aspartate beta hydroxylase	NM_004318.3	AGAACAGCAGGAAGTACCACCAGATACT**TAA**AGCTTCAAAAAGACTGCCCCTACCACCGGGCC
FBL	Fibrillarin	NM_001436.3	GTACAGGCCACCCCCCAAGGTGAAGAAC**TGA**AGTTCAGCGCTGTCAGGATTGCGAGAGATGGG
HPN	Hepsin	NM_182983.2	TCGAGGCCAGCGGCATGGTGACCCAGCTC**TGA**CCGGTGGCTTCTCGCTGCGCAGCCTCCAGGG
MMuLV	Moloney Murine Leukemia Virus		C**TAG**GGAGGTCAGGGTCAGGAGCCCCCCCCTGAACCCAGGATAACCCTCAAAGTCGGGGGGCC
VASP	Vasodilator-stimulated phosphoprotein	NM_003370.3	GGAGCTGAGGAAGCGGGGTTCTCCC**TGA**CCACAGGGACCCAGAAGACCCGCTTCTGGGCCCCA

Tableau 4. – Table S3; Readthrough candidates

Readthrough code	Gene name	peptides found by MS analysis			peptides « confi stop- DNA 3’UTR	RTP (readthough propensity)(Ref 22)	RTP Linfs3 (Ref 22)
RT_012331.1	FAM19A5 family with sequence similarity 19 (chemokine (C-C motif)	APSEDGLRLR	NP_001076436	3608	TGAcaaacacagcccctgaggggccccgggagtggccttggctccctggagagcccacgtctcagccacagttctccact cgcctcggacttcacccgttctctgccgcccgcccactccgtttccctgtggtccgtgaaggacggcctcaggccttggcatcctgagcttcggtctgtccagccgacccgaggaggccggactcagacacataggcggggggcggcacctggcatcagcaatacgcagtctgtgggagcccggccgcgc	0.309	0.646
RT_006854.1	ZNF182 zinc finger protein 182	YGSKFSLSSFHLSHNPK	NP_001171570.1, NP_00	3732	TAGagagctaatcagcagtatctattatggacactgaaagaaagttgtgtcaattttactcacattttaaaagtatattttgacttgtggtttaaatatgggagtaaattcagcctttcttcttttcatctcagtcataacccaaaagctacgggagaaaaagcagaagtgtaa	0.143	0.215
RT_020801.1	ACADS acyl-CoA dehydrogenase, C-2 to C-3 short chain	LGGPAGAPWGPQMGSVLPPR	NP_000008.1,	8117	TGAgcccgcggcggactgccccaggactgcgggaaggcgcgggagccaggggcctccaccccaaccccggctcagagactgggcggcccggcggggctccctggggaccccagatgggctcagtgctgccacccagatcagatcacatgggaatgaggc cctccgaccattggcagctccgcctctgggcctttccgcctcctcaccactgtgcctcaagttcctcatctaagtggccctggcctcctgggggcggggttgtggggggctgagcgacactcagggacacctcagttgtcctcccgcgggccctggtgccctggcatga	-0.077	0.066
RT_017649.1	ACSL5 acyl-CoA synthetase long-chain family member 5	VLKYLPAHCALLVR	NP_976313.1, NP_97631	690	TAGgataaggtacttaagtacctgccggcccactgtgcactgcttgtgagaaaatggattaaaaactattcttacatttgttttgcctttcctcctattttttttaa	-0.08	-0.226
RT_009441.1	ADCK2 aarF domain containing kinase 2	AGGHSQEPLLWQLGR	NP_443085.2 XP_01151	464	TGAtggggcagtggcctctgtgggcccttgtcaagagctggaggccactcccaagagcctctcctatggcagctgggacg tttaaaattgggaaccaatttcaaatgtaaccctccagtggtggaaggcacaccatggcttcctctgcttggtttga TGAgg[illegible]ccctt	0.237	0.065
RT_013024.1	ADCY7 adenylate cyclase 7	GLLLDSEK	NP_001105.1 XP_01152	9511	TGAgggctcctgctggattccgaaaaggccgggaagccagtctccttccctgaagcaagcccaggagaagactctccgcc ccacgccaatcccaaaggcatgcagatggctgtgcatgttggcttctttggacctgcactggaggatttctcagacacat TAGcagg[illegible]aatgtttagcacaagacacagcggagctcgggattggctaaactcccatagtatttatggtggccgccggcgggggccccagcccagcttgc gcaccagattctggctcgaagcagccactgagccataa	-0.029	0.028
RT_024040.1	AGAP2 ArfGAP with GTPase domain, ankyrin repeat and PH domain 2	EGLVHGR	NP_055585.1, XP_00526	6563	TAGttgcccagcgggagagacacccccatccccacgcgggccgggcacgaccacaccgggcggaccgctggacagacgcacccactcacctctccgatccgcaccccgccccacgggagcacttcctacccccacgagggcacagcccccacgccttcca gaagacacaaactcacctccctctccccaacgaggcatggagaccccagctcaacacgccccctctccattgtttccacactcggattgctctgggtctacccgctcggggttcgcggaaggggaggtccccagcggtacgggctcctaggcgcttggacatgcccgcttgtgccccctaggggcggaaag	0.059	0.072
RT_009047.1	AK1 adenylate kinase 1	QRWSRFPSSEPRPTPS	NP_000467.1, XP_01151	5273	TAGcaacgctggagccgcttccccagctcagagccccgccccaccccgtcctga	0.054	0.424
RT_002208.1	AKAP8L A kinase (PRKA) anchor protein 8-like	PELGAGGAR	NP_001278407 XP_00525	924	TGAcccgagctcggggcgggcggagcccgcgtggccgaagctggaaaccaaacctaa	0.42	0.432
RT_017612.1|	alpha-(1,3)-fucosyltransferase 9	NFSSLAHLINILMR	NP_006572.2 XP_01153	652	TAAaatttttcatcacttgcacacttgataaatattttgatgagatatcatccaagtattgaggataagaagagatgcaacatactacttttgtgtcacaatttatttttatcaccctctctagggtaa	-0.081	-0.089
RT_022128.1	AMOT angiomotin	SRAADYQQK	NP_573572.1, XP_01152	3141	TAAacggccaaatcaagagctgcagattatcagcaaaaatgcttttaa	0.051	-0.11
RT_021756.1	ANKLE2 ankyrin repeat and LEM domain containing 2	EGRVICLLLNCQK	NP_055929.1, XP_00526	2085	TAGgcttggcgctgggctctcggtttgttcttcatttttaaagaaggaagggtcatatgtttattgctaaactgtcaaaaaggaatatattctgattaa	-0.028	-0.215
RT_002681.1	ANKRD13D ankyrin repeat domain 13 family, member D	AIAPGGLARPLPAR	NP_997237.2, XP_01154	10572	TGAgccatagccccgggagggctggccaggccactccctgcccgcttttgtaatttatttatttataaactctctgctgctgagcttggggcctggagccccaggaatgagcaggcaggggagactgagatggaaataaagagactgtcgcagcagggctgct ctgctcactgggctggagcggtggggaccctgaaggtggggcgctgtggagaggcactgtggatggcggcctcagacctg ggcttgaatcctggtcatggtccccttagcctatctgagcctcagtttcttcagttgtaa	0.041	0.066
RT_001281.1	ANO10 anoctamin 10	GLCLCHTCHGGRGGTRGSIVAPEPR	NP_001191762 XP_01153	7239	TGAgtgcccagcgtgcccagctgccctgttggcagaggcctgtgtctgtgccacacctgccacggtggcaggggggtacccggggcagcatcgtggctcctgaacccagacccaatgcttag	0.236	0.257
RT_005833.1	APLP1 amyloid beta (A4) precursor-like protein 1	AQTSPLPGAPEPQLPA	NP_001019978.1, NP_00	2785	TGAcccggccccttcacccttcagccgagcccagacctcccctcttcctggagccccagaaccccaactcccagcctag	0.271	0.432
RT_021610.1	APPL2 adaptor protein, phosphotyrosine interaction, PH domain and	LTCACGGR	NP_060641.2, XP_00671	20075	TAActcacttgcgcctgtgggggaagagcaaacaggaaggagagctacctcctaagggttttaacgtctctgacatacaggcacactgacctgatttccgaaggctgacaatcgtttgtggaatgtaa	0.027	0.147
RT_023876.1	AQP12B aquaporin 12B	ALGSSKAAARSPVAR	XP_01150	9755	TGAgccctggggagctccaaggctgcagccaggagccccgtagccagggatggtcctggctgtgctgctgcaccagggcc gccttccccaccttttccagaggaacctgttctacggccagaagaacaagtaccGAGCACCCCGAGGGAAGCCGGCCCCGGCCTCAGGGGACACCCAGACCCCTGCAAAGGGGTCCAGTGTCCGGGAGCCTGGGCGCAGTGGTGTTGA (alternative spl	0.214	0.066
RT_007575.1	ARHGAP17 Rho GTPase activating protein 17	RTWRPPLK	NP_060524.4, XP_01154	3300	TGAagaaagccctttcccagccctccaccacttccaccctggcgagtggagcaggggcaggcgaacctctttcttttgcagaccgaacagtgaaaagctttcagtggaggacaaaggagggcctcactgtgcgggacctggccttctgcacggcccaaggagaacctggaggccaccactaaagctga	0.319	0.437
RT_018159.1	ARHGEF1 Rho guanine nucleotide exchange factor 1	IGGLFFNIYYLR	XP_00525	8679	TGAattggaggtttattttttaatatatattatctaagaagagatctgtgtgtgtga	0.186	0.382
RT_023604.1	ARPP21 cAMP-regulated phosphoprotein 21kDa	KLQMERNSK	NP_001254545 XP_00671	4165	TGAaaactgcaaatggaaaggaattcaaaagaatttagattaaaagttaaataa	0.28	0.373
RT_026723.1	ASB14 ankyrin repeat and SOCS box containing 14, predicted transcri	SSSAWEAEAGGLLHLGRSR	XP_00526	2744	TAAtcaaaccattctaatggaaaaggtataatttttgcagctgtattccttaaaatttcacttatgtatgattcatatttttttgctttacccaccaactaaaatctcaatgcagtctaagtccttttaaaaagtagctctgcttgggaggctgaggcaggaggattgcttcaccttgggaggtcaaggctgcagtga	0.161	0.151
RT_011768.1	ASPH aspartate beta-hydroxylase	KTAPTTTGGPA	NP_001158227.1, NP_00	5997	TAAagcttcaaaaagactgcccctaccaccacaggaggaccagcctaac	0.123	0.033
RT_021372.1	ASTN2 astrotactin 2	GRVLPSVSTETLHGR	NP_054729.3,	235	TGAgggagggtattgccctccgtgagcacagagactctccatgggagggggagcagtattctcctggatcctggggcctg ggtgggctgggggacagctgaggatgggcctagcagatga	0.001	0.028
RT_013285.1	ATG9A autophagy related 9A	DSSLIPR	NP_076990.4, NP_00107	11636	TAGacaaggctgagcagggttcctgtggcccaggatggaggccaccgctgccctgccatcccgtctgcctgccatgggacggctcctctgagtgttccctggccccacgtgtgtggtgtttgtgtgtctgtgcctggccaagggaggtgccaacactgggcttgccacagccccaggagaggaatttgggg	0.105	0.162
RT_006517.1	ATP10D ATPase, class V, type 10D	DFEEVSLQAR	NP_065186.3, XP_00524	2260	TAGataccctccttggagttgcaagtattctttcaaggttggaagagggattttgaagaggtatctctccaagcaagaatgacttgtttttccataagggacatgagcattttactaggcttggaagagctgacatga	0.203	0.444
RT_003127.1	ATP11C ATPase, class VI, type 11C	QNPNLELPMLLSYK	NP_775965.2 XP_01152	3127	TAAcagaatccgaatcttgaactgcctatgttattgtcctacaagcatactgacagtggttacagctaa	0.129	0.152
RT_007887.1	ATP13A1 ATPase type 13A1	CLPEMAVLVPTAHPGCR	XP_01152	666	TGAaagtgccttcctgagatggcagtgctggtacccactgcccaccctggctgccgctgggcgggaaccccaacagggcc ccgggagggaaccctgcccccaacccccacagcaaggctgtacagtctcgcccttggaagactgagctgggaccccccac agccatccgctggcttggccagcagaaccagccccaagccagcacctttggtaaataaagcagcatctgagattttaaaa aaaaaaaaaaaaaaaaa…	-0.032	0.056
RT_027025.1	ATP6V0B ATPase, H+ transporting, lysosomal 21kDa, V0 subunit b	LGVQGPPCTPLLLR	NP_004038.1, NP_00103	2970	TAGatgatatgtgtgggtggggccgtgcctcacttttatttattgctggttttcctgggacagctggagctgtgtcccttagcctttcagaggcttggtgttcagggccctccctgcactcccctcttgctgcgtgttgatttggaggcactgcagtccaggccgagtcctcagtgcggggagcaggctgctgctgc	0.123	0.127
RT_025167.1	BCORL1 BCL6 corepressor-like 1	LQNEAIIR	NP_068765.3 XP_00526	6940	TGAccgggaaaacagcccctcctctctttctccttccgagttcgcccttcccccacctccttgtctttccccgaccgag caccagactgcagaatgaggcaataatacggaccaacaagaagccgccttatcaatgccagcattag	0.176	0.341
RT_020389.1	C10orf105 chromosome 10 open reading frame 105	WGVHKHAPTSP	NP_001161862 XP_01153	9533	TAAtggggtgtccacaaacatgcccccacatcccctag	0.056	-0.113
RT_023564.1	C1GALT1 core 1 synthase, glycoprotein-N-acetylgalactosamine 3-bet	KKIMNEQR	NP_064541.1 XP_00524	1008	TGAaagaaaatcatgaatgaacaaaggtaa	0.112	0.056
RT_024012.1	C1orf186 chromosome 1 open reading frame 186	IPNIFNGVQFSMDSYI	NP_001007545 XP_00527	10908	TGAattccaaatatttttaatggggtccagttctctatggattcttacatttaa	0.197	0.382
RT_021492.1	C1S complement component 1, s subcomponent	YIPPASPR	NP_958850.1, XP_00525	4939	TAAtccagatacatcccaccagcctctccaagggtggtgaccaatgcattaccttctgttccttatgatattctcattatttcatcatga	0.001	-0.075
RT_007816.1	C22orf15 chromosome 22 open reading frame 15	GDGLHTVVR	NP_872326.2, XP_00526	8506	TAAggggatggattgcacactgtagtgagacatccatcctgac	0.116	-0.15
RT_019768.1	C22orf23 chromosome 22 open reading frame 23	LTAPSAEK; QSPSIPTRTCV	NP_001193991 XP_00526	1593	TAAtctgtctccagagacgggcagggtagcccaagctcgaccactggagtccactcctctgccaggcagggccatcctcaggccagcccatcctaccagccttctgccacgtcaggtggtggcatagcactgccctgcagtaccccaaggcatactcagcagcctagcccctgccccggaatgcagatg	0.131	-0.134
RT_013060.1	C5orf60 chromosome 5 open reading frame 60	VTGITGLCHR	XP_01153	7069	TAGggagaccccacatgcaggcaggtggaggcaggggtcccgctttcctcagcctggatgtgccaacgctgctggacgcataagacaccaaaatcccagacactcccatggacaccgaatatccgacatccacgaacaattgggaatctcctgaggacaacttggagatggagtctcactctgttgctc	0.364	0.122
RT_024351.1	CACNA1A calcium channel, voltage-dependent, P/Q type, alpha 1A s	THPTRGAAQRPR	NP_001120694.1, NP_07	2949	TAAgcccgggcgaggtggcgcccgcccggcccccacgcaccccacgcacacaccccacccgaggagccgcgcagaggccgcgggggcccagcacagagggcccgggagagggccagccgggagaccccagactctggagaggccagggctgggccacaagggtgtcccgcagagaccctc	-0.086	-0.112
RT_018787.1	CAPN1 calpain 1, (mu/l) large subunit	QPRPPVPSPPSHHR	NP_001185797 XP_00671	1683	TGAggcagggactcggtccccttgccgtgctcccctccctcctcgtctgccaagcctcgcctcctaccacaccacacca ggccaccccagctgcaagtgccttccttggagcagagaggcagcctcgtcctcctgtcccctctcctcccagccaccatc gttcatctgctccgggcagaactgtgtggccccctgcctgtgccagccatgggctcgggatggactccctgggccccaccc attgccaagccaggaaggcagctttcgcttgttcctgcctcgggacagccccgggtttccccagcatcctga	0.169	0.119
RT_005409.1	CASK calcium/calmodulin-dependent serine protein kinase (MAGUK f	ASLLSALCQQVMVPR	NP_001119527 XP_00672	1200	TAGgcctctccccagatatctgagcataactgggagcacctcatttgtggaaaagcctctttgttatcggccttgtgtca gcaggtcatggtccctagagactacctagttgtagtgtga	-0.161	-0.156
RT_010840.1	CCDC58 coiled-coil domain containing 58	REILFFFFFFFFLRTGSSHK	NP_001017928 XP_00524	3768	TAAagagagattcttttttttttttttttttttttttttaaggactgggtcatctcataagagctaa2	0.285	0.259
RT_004671.1	CCL3 chemokine (C-C motif) ligand 3	GVQKLR	NP_002974.1,	287	TGAggggtccagaagcttcgaggcccagcgacctcagtgggcccagtggggaggagcaggagcctgagccttgggaacat gcgtgtgacctccacagctacctcttctatggactggttattgccaaacagccacactgtgggactcttcttaacttaa	0.291	0.028
RT_012415.1	CCNH cyclin H	PFEVDFSMLTNQEK	NP_001230.1, NP_00118	7561	TAAccatttgaagttgatttctcaatgctaactaatcaagagaagtag	0.402	0.48
RT_004395.1	CD72 molecule	NWTVPGK	XP_00671	1058	TGAaactggactgttcctgggaaaagggtgaagccacctctagaagggactttggcctccccccaagaacttcccatggt agaatggggtgggggaggagggcgcacgggctga	0.231	0.147
RT_016795.1	CD82 molecule	TLLPILTESRGLSGA	NP_002222.1, XP_00671	4030	TGAggcagctgctatccccatctccctgcctggcccccaacctcagggctcccagggggtctccctggctccctcctccag gcctgcctcccacttcactgcgaagaccctcttgcccatcctgactgaaagtagggggctttctggggcctag	0.065	0.119
RT_006924.1	CDH23 cadherin-related 23	FILEGGK	NP_001165402 XP_01153	7762	TAGgtgggggcaggtgagggtggaaaagaggtcagggctctactgttgggctttagcctctggtggtgcctcccgaggatttgctcctggctcttcccaagggctttgcagctggatcactctggactggctccctggggacctcctgaacctgttggttgcagggacggggagcatctaccaaggttcattc	0.136	0.035
RT_019066.1	CDK2AP2 cyclin-dependent kinase 2 associated protein 2	LDLSGHCRAPASPWPSSR	NP_005842.1,	4819	TAAcaggaagcgcctcggcctcagcgtctggacctatccggccactgcagagcacccgcttctccctggccttcatcccg agttgcactaaccatcctgggcttcctgtcctgtgtcccttggtgggtcccctccaggaaccaaggagtggccctccagg tggcagcactaaggacaccccccacaacaagagttag	0.153	0.152
RT_008545.1	CEACAM4 carcinoembryonic antigen-related cell adhesion molecule	KEGALWLFWTHLG	XP_01152	3977	TAAaaggaaggagccttgtggttattttggacgcacctgggataa	-0.015	-0.122
RT_022767.1	CEP57L1 centrosomal protein 57kDa-like 1	QNSKTVTLMNFVSETLNCLKWF	NP_001077004 XP_00526	8129	TAAcaaaacagcaaaactgtcaccttaatgaactttgtcagtgagaccttgaattgtctaaagtggttttaa	0.29	0.468
RT_002593.1	CFAP54 cilia and flagella associated 54	ISYTRDDKTEK	XP_01153	1470	TGAatatcctatacacgggatgataaaactgagaaataa	0.333	0.666
RT_023936.1	CFHR3 complement factor H-related 3	GSIVTLNVCPTSTFPLLTLMVSK	NP_066303.2, NP_00116	9546	TAAggcagcattgttaccctaaatgtatgtccaacttccacttttccacttctcactcttatggtctcaaagcttgcaaagatagcttctgatattgttgtaatttctactttatttcaaagaaaattaatataa	0.059	-0.059
RT_003463.1	CHRNA1 cholinergic receptor, nicotinic, alpha 1	AENELSLALPWNLPEQRRAGEEDLS	NP_000070.1,	15187	TGAgcagaaaatgagctgagcttagctctgccctggaacctaccagagcagagaagggcaggagaggaagatttgtctac ttgctccactcgcacttatcaaacgtgttatattccatacttattattgatgataagatttacctttatgtaa	0.219	0.292
RT_021669.1	CLEC12A C-type lectin domain family 12, member A	SVGGGGSRL	NP_001193939 XP_01151	2968	TGAggcatcaatcaaatacatttaaggagtgtagggggtgggggttctaggctatag	0.238	0.119
RT_010570.1	COG3 component of oligomeric golgi complex 3	SLAVCRTPR	NP_113619.2, XP_01153	3531	gaggaatcgtatgtgggaacgtccccgagaaccacacgagcgtgctgctcagtgctga	0.213	0.114
RT_016946.1	COL1A1 collagen, type I, alpha 1	TPSIPTWLPPTQPTFPPTR	NP_000079.2 XP_01152	3390	TAAgcaggccagccgggctgtgcacctaaatgtctgtctgggaggagcaggctgagaagtcttgcagtctgcaggacacc TAAactccctccatcccaacctggctccctcccacccaaccaactttcccccaacccggaaacagacaagcaacccaaa ctga	0.046	-0.078
RT_004138.1	COL4A4 collagen, type IV, alpha 4	RMRNSPTR	NP_000083.3, XP_00524	886	TAGagaatgcgaaattcaccaacacgtggccaagagaaacttcctagggggctaagacttcctagactgtgctaag	0.2	0.215
RT_014034.1	CORO2A coronin, actin binding protein, 2A	AETSALLTLR	NP_438171.1, XP_01151	20475	TGAgcagagacctctgccctcctcaccctcagggacaccactcggctccatggggaggtttag	0.259	0.292
RT_024782.1	CPS1 carbamoyl-phosphate synthase 1, mitochondrial	HPSPIIK	NP_001116105 XP_01150	5966	TAGagatgcagacaccccagccccattattaaatcaacctga	0.222	0.215
RT_011692.1	CREB3L4 cAMP responsive element binding protein 3-like 4	AGTDLPGPLPDHK	NP_570968.1, XP_00671	671	TGAgctggaacagaccttcctggcccacttcctgatcacaaggaatcctgggcttccttatggctttgcttcccactgggattcctacttaggtgtctgccctcaggggtccaaatcacttcaggacaccccaagagatgtcctttagtctctgcctga	0.075	0.008
RT_021761.1	CUX1 cut-like homeobox 1	GAAALGRAAR	NP_001189472 XP_01151	2074	TGAggggccgcggccctggggcgggcagccaggctgggccgcaagggcctggacggggtcggacggggcaggcgctgcggacaccgtggcctgggcttggcccgcggcctgcaccgaccccgggccggacctgagcccgcagcccagacccccctccacggtccgcggcctgcaccgacccgag cagggcaaaatcgccatag	0.237	0.028
RT_013213.1	CYB561 cytochrome b561	RLQDCRLR	NP_001906.3, XP_00525	12262	TGAtgcgcccggccggccctgggggttcgcggggtgtcttcttgcctgcccctgctgaggcgtcttcaggactgcaggct ccggagagtggctctggcagcaggcgggcgcgtgggtgcagctgcatctgtttga	0.292	0.156
RT_019282.1	CYB5D2 cytochrome b5 domain containing 2	AVASSVNNTQRALPST	NP_001241685 XP_01152	4632	TAAgccgtagcctcttctgttaataacacacagagagctctgccaagcacctga	0.057	-0.112
RT_011989.1	CYGB cytoglobin	APVNQKHMAQVPQHAARPALPTLP	XP_01152	12296	TGAccacactggccccgggctggctcctgctcccctccccctctcccgtcagcaccaccccaagagagtggagtcctcgggaactgctggctggagccaagccaactccagatgtgcacagctgggccctggcctgcctgagacctgggagtcaatgggaaacaagcagatgttggcccaccagagg	0.393	0.658
RT_016292.1	DAAM2 dishevelled associated activator of morphogenesis 2	PGELATQEAGRQGLVR	NP_001188356 XP_00671	12479	TGAcctggggaactagccacacaggaggccgggagacagggactggtgagaatggggctgagtggaggaggtggtgatat ttaa	0.226	0.373
RT_018283.1	DACH1 dachshund family transcription factor 1	VLLRELPEFCVLMFFK	NP_004383.4, XP_01153	5689	TGAatctttcctgttgaagaaatccatgttatagaaaagaactttgcagtcagacattcgtcatgggaaagttcagaaaa aaataaagtccttttaagggaacttcctgaattttgtgtattaatgttctttaaaagtttaagtattctacaaaaaaaaaaaaaagttttctccattgattttcacctgtggttcataccagagacctgagaatgtttgtaaatgtacaagtatcaaagttcttacagttaattactgcaacttgctgctggacaattgta	0.121	0.44
RT_013666.1	DENND2A DENN/MADD domain containing 2A	LGSSLDEDLGAAWEDSPRKGAR	NP_056504.3 XP_00525	6495	TAActctcagcctcaagggaaaacttcctcctagtgcagccctatgctttaaaaacagttcctggtggcctttctgaaag gctgggtcccaggttgtcacggtgcggaactggaggccgcggtggcttctggccgaggctgggctcttccctggatgagg acctgggagccgcctgggaggacagccccagaaagggagcccgagaccaggcgtgtcgccgacatgcaaatgggttgttt tggtggttgggtttttttttttatcttagatattaa	0.12	0.536
RT_013306.1	DGKD diacylglycerol kinase, delta 130kDa	RLASWALLAWPR	NP_690618.2, XP_01151	2001	TAGcctctgtcctctcagcctgtggcctccacatccccgccgccgaggcctagcctccgccctctcagcctgtggcctctgcgcctcctgccactgaggccctgggcagatgctgcagcccgccccccttctcatggtgctacttcctctgtcagctacagaaagcctccgtgacaccgtccaccagagctctgg	0.227	0.151
RT_022377.1	DHODH dihydroorotate dehydrogenase (quinone)	LSSVPWSDHK	NP_001352.2, XP_00525	13137	TGAggacagcgtctgacgggaagcctgatctggaaccttcccaaggactcaggcaagcctttgtggctggatcatgagaggagggactccatcttgagccatgtcccccagccatggcatggctgcactgtaaacgccaatcggggggtcaccaggatcaaccgcaggctttcttcagtcccttggtcag	0.035	0.345
RT_007395.1	DOCK11 dedicator of cytokinesis 11	GNADVRDNETDLSQEYLELCK	NP_653259.3 XP_00526	4740	TGAggaaatgcagatgtacgtgacaatgagactgacctttctcaggaatatttggagctgtgcaaatgttaa	0.306	0.345
RT_023489.1	DOCK4 dedicator of cytokinesis 4	TFSVGTLITYSAPSMNGIK	NP_055520.3, XP_01151	786	TAAgtcacttttctatgtacctgcgatgcattctttgcccgtttacaaaataagaagtatgatgagaagacatttagtgtaggcactttaataacttactcagctccttcgatgaatggaattaaaacttgcttattaaatatcatgttgcacaatattaaaagttgctga	0.054	0.17
RT_013182.1	DOCK8 dedicator of cytokinesis 8	EKPSSFVETVALQPWR	NP_982272.2, XP_01151	2611	TAAgaaaagccatcttcattcgtggagactgtggccctgcaaccctggagaaggacttgctggtacttaaaaaatgggac atttgccacccaggactga	0.054	0.103
RT_017352.1	DOHH deoxyhypusine hydroxylase/monooxygenase	SSPAELWR	NP_001138637 XP_01152	1607	TAGggccccaccctcacccggagctcccggaggactcttgagggccgctcctcccccgcagagctttggcgtctaaaccg ggtgtgtgtaaatcggtgtcatcgcttgtgtcttgctgggcgcatggttgctgtcccctcctccgtctgggaccgagga gctgccgttgtgctgtgactccctga	0.047	-0.103
RT_009530.1	DPPA4 developmental pluripotency associated 4	ATSMVINGRK	NP_060659.3 XP_01151	23756	TAGaatatcaggaaaaaggccacatctatggtaattaatggcagaaaagctggagagttggattctgcggtgctgctgac aggtgaactctggtcctctgcacctgtttatgggccatgcagactggtggggtggcagatgttagcctaa	0.046	-0.134
RT_024102.1	DRAM1 DNA-damage regulated autophagy modulator 1	NSVSLSECR	NP_060840.2, XP_00526	626	TGAagaaagaagaattcagtctcactcagtgaatgtcgcaggccatttctaaaagtgctacagaggacagacagggtttt gaggccaccctga	0.267	0.437
RT_014648.1	DUSP18 dual specificity phosphatase 18	AIPRAPALESEVQIYC	NP_689724.3, XP_00672	4973	TGAgccatcccacgagcccctgcattggagtcagaggtacagatctattgttga	0.109	0.066
RT_024715.1	DUSP22 dual specificity phosphatase 22	LGRGAVVVADEDR	NP_001273484 XP_01151	3721	TAAcgcaagcgacctgctgccttccttcccactgcttgtcttcagtgtgcccggctgggcaggggtgcggtggtggtggc cgatgaggacaggaaagggagatag	0.23	0.307
RT_006993.1	EDN3 endothelin 3	FPPLYRQEVNLPGAEHPPK	NP_996917.1, XP_01152	11113	TAGgaggacaggcctgcagcatcctggtctcgggaggcttctgtcattgctcacacacagttcagatttccacctcttta tagacaagaagtgaatttgcctggggcagaacacccacccaaagagtccccacttaacaatacccccccccacggcaag aatgcccaaatccgaatgaccccagttttcctaatgagtaa	0.153	-0.258

RT_023670.1	EFCAB6 EF-hand calcium binding domain 6	TPLLCAQRDDSHR	NP_942153.1,	XP_00526	10512	TAGacacccctgctgtgtgcccagcgggacgacagccacagggcctgtttcaaggctaataaaatcctataa	-0.017	0.162
RT_001248.1	EPHA1 EPH receptor A1	TLLCTPENLFVLK	NP_005223.4	XP_00671	5193	TGAtccctcctctcaccccatgcccaatcagggtgcaaggagcaaggacggggccaaggtcgctcatggtcactccctgc gccccttcccacaacctgccagactaggctatcggtgctgcttctgcccactttcaggagaaccctgctctgcaccccag aaaacctctttgttttaaaagggaggtgggggtag	0.158	0.103
RT_026532.1	ERCC4 excision repair cross-complementation group 4	TVMAVFLSHACTFQRLLAR	NP_005227.1,	XP_01152	10931	TGAacagtgatggctgttttcttatcccatgcctgtacttttcagcggctccttgccagacatcataggtcattattaattattggtttgctatttcattcttttccaatgctcttaatgattgtacggtggaccagaagccaggattcctctctgaactctgcagttaggcatcacttgaacttgcctgtgcctgctctttt	0.218	0.384
RT_003934.1	ESRP1 epithelial splicing regulatory protein 1	MYGDLETSR	NP_001116297		8815	TGAaagatgtatggtgatcttgaaacctccagacacaagaaaacttctagcaaattcaggggaagtttgtctacactcag gctgcagtattttcagcaaacttga	0.122	0.056
RT_002612.1	EVPL envoplakin	TPLASEQPHPR	NP_001979.2	XP_01152	9163	TGAcacgggccaaggagccagtggggaagtgcgtgtgttgggccaggtaggatacgtacacctcttgcctcagagcagcc tcatcccaggcagtgggtcttccctctgtccaaccactgttttattattttactaacatggtga	0.216	0.421
RT_018437.1	FAM192A family with sequence similarity 192, member A	TVHAAYR	NP_079222.1,	XP_00525	8802	TAGtttctccgtccctacacagggagctcctccccaagggtagatcggaccgttcatgctgcctataggcattatgtccc tcaaaaaaaaactcctttgcctgcatcctgtgtacaacatgacatttttaaccaatccaatctaaaaatgtgccagaatc cacctgtggcccgaatcgtgtttggttcctctttctactccactgcagatgaccaaacctgtcccgctgccactttcctc actgatattgggaggagggcaaggcccagccgaagttccactaaaaatgccccaggagaatag	0.236	0.104
RT_011736.1	FAM213B family with sequence similarity 213, member B	AEMGLIPPGGVGGPWRLSGDGPA	NP_001182667	XP_01153	21033	TGAcagagaggtgtgagggaggcgaaggccctggcctccgaggatctgggtggcgtctgctgccctaggtgtgctggaag tccacttggaagaactgttccggaggcgctgggtcgggatgccgaacctctcctgatccgccggcagcaacgagccatta aaactgcagttcctgaccacgcactgcttcgcaggctccgagccctgcatcctccacagcccccgccttgctcactgttg ggccctcagggcgggcagggtggctgtgagtcccaggtgtcatcttcctgctctgcgactttctctggagaccttgggcc tttggcctgtggggcactggggatggtaacctcactgccccgtcactcccttcaaaggcgacagacccaagcccacgtca ggagaggagcgtggggtcagctccagcagggtcggggtcagtgcctgtgtctggtgggggccactcaggagagttgggtt ttcagggcagagatgggcttgattccacctggtggggtgggtggaccctggagactctcaggtgatgggccagcctgccc caaggctctttactga	0.316	0.33
RT_012764.1	FANCE Fanconi anemia complementation group E	GPPSWCSITSFLK	NP_068741.1,	XP_00524	4680	TGAccatccaccaagggaccaccctcttggtgctccatcaccagcttcctgaagggcatttctttcttcaccaccttgtcttga	0.371	0.658
RT_025932.1	FBL fibrillarin	SSALSGLR	NP_001427.2,	XP_00525	120	TGAagttcagcgctgtcaggattgcgagagatgtgtgttgatactgttgcacgtgtgtttttctattaa	-0.004	0.153
RT_026099.1	FBXO10 F-box protein 10	GHRPASGPSLDGCSEELRWK	NP_036298.2,	XP_01151	4883	TGAggacacagacctgcttcagggccaagcctggatgggtgctcagaggagctaaggtggaaatactgcctgaaaagact ccgcccctcccccctcccctcgaacaaatgggtcccgggcctccaaaacacggtacctccagaacacttcagctccacag cccatagcaagaagaaagtgggcaatgtttttcagggagaagggatagaagctggtgggtttccagtcactcgaagtctataa	0.195	0.345
RT_024737.1	FBXO21 F-box protein 21	LHGALGTCCTRK	NP_055817.1,		2900	TAAagtctagagaggacattgcacctttgctgctgctgctatcttccaagagaacgggactccggaagaagacgtctcca cggagccctcgggacctgctgcaccaggaaagccactccaccagtagtgctggttgcctcctactaa	0.081	-0.025
RT_011219.1	FGFRL1 fibroblast growth factor receptor-like 1	GPMARRNGQHPR	NP_001004356	XP_01151	7158	TAGacggcaccgtatctgcagtgggcacgggggggccggccagacaggcagactgggaggatggaggacggagctgcagacgaaggcaggggacccatggcgaggaggaatggccagcaccccaggcagtctgtgtgtgaggcatag	-0.033	-0.155
RT_007474.1	FMNL2 formin-like 2	TCVLLMVPK		XP_01150	2309	TGAggagaagcgtcaggcggcgctttgatgatcagaacttgcgttctgttaatggtgccgaaataa	0.136	0.345
RT_020024.1	FRK fyn-related Src family tyrosine kinase	TLEKNIK	NP_002022.1	XP_01153	386	TGAacactggagaagaatatcaaataa	0.046	0.384
RT_019443.1	FRMD4B FERM domain containing 4B	SHTSVPCKLYLSSERMFVLET	NP_055938.1,	XP_00671	6767	TGAactgcagttggacctcctgaccaagcactgcgttctcacactagtgtgccttgcaaattgtatttgtcttccgagag gatgttcgttttagaaacctaa	0.206	0.1
RT_026450.1	GDF9 growth differentiation factor 9	QMVLLKP	NP_001275753	XP_01154	7924	TAAcaaatggtcctcttaaaaccttga	0.24	0.468
RT_014494.1	GGT5 gamma-glutamyltransferase 5	TVARTRPR	NP_001289393	XP_01152	6149	TAAgactgtaggaggtgcagaggggactccaagaccgtggccagaaccagacccagaggcccttcttcctga	-0.034	-0.123
RT_003442.1	GLB1L2 galactosidase beta 1-like 2	SISLSSNLR	NP_612351.2,	XP_00671	5181	TGAgcggtggcacccccctcctgctggtgccagtgggagactgccgcctcctcttgacctgaagcctggtggctgctgccc cacccctcactgcaaaagcatctccttaagtagcaacctcagggactgggggctacagtctgcccctgtctcagctcaaa accctaagcctgcagggaaaggtgggatggctctgggcctggctttgttgatgatggctttcctacagccctgctcttgt gccgaggctgtcgggctgtctctagggtgggagcagctaatcagatcgcccagcctttggccctcagaaaaagtgctgaa acgtgcccttgcactggacgtcacagccctgcgagcatctgctggactcaggcgtgctctttgctggttcctgggaggct tggccacatccctcatggccccattttatccccgaaatcctgggtgtgtcaccagtgtagagggtggggaaggggtgtct cacctgagctga	0.044	-0.025
RT_007096.1	GLYATL3 glycine-N-acyltransferase-like 3	PSKKLQWFYYFP	NP_001010904	XP_01151	11307	TAGcccagtaaaaaactgcagtggttttattactttccctga	0.129	0.21
RT_024798.1	GPR17 G protein-coupled receptor 17	AGGAVQAER	NP_001154887		1128	TGAgcgggggggcgccgtccaggccgagcgcagactgtttaggactcagcagacccagcaagaggcatctgccctttcccc agccacctccccagcaagcaacctgaaatctcagcagatgcccaccatttctctagatcgcctagtctcaacccataaaa aggaagaactgacaaaggggatccatcggccacccctctgcaggggcttgtga	0.133	-0.025
RT_023626.1	GRID2 glutamate receptor, ionotropic, delta 2	SLHCFFFR	NP_001501.2,	XP_01153	5438	TGAgcatcaaacaaatctcttcactgtttcttttttaggactccctttgcaaggagcaactgtaatattgtgggactaac atggatgtaa	0.19	0.292
RT_000656.1	GRIK3 glutamate receptor, ionotropic, kainate 3	AQLGWGPQAWGLGRGK	NP_000822.2,	XP_01153	865	TAGgcacagctggggtggggacctcaggcctgggggctgggcagaggaaagcaaaggagattggaaggaacgtcccctgt ccccgcactgggcttggggaccagagctgccacctgcctgttgggccaggagcctcctgcccttacctgccaggaagcca gcaggctctcaggccagctgcttgggcttcatcctcctcagatcttctgtgggtttctaaagctgccagccgagatagcc aaggccaaaggaagcacatgcctctctcaggccaaactcacctgcccctcaactctcctccagagtcagaagtttctgcc gcagccctgcagagggcacagaaaatggaagacagctcttatattgccatttcttccacaagagcccaggcctcctacag cttga	0.122	0.07
RT_006083.1	GRK6 G protein-coupled receptor kinase 6	APFTVLHSDLPHCPLK	NP_002073.2,	XP_00671	3763	TAGcagctactccgagcgccgtttacagttttgcacagtgatcttccccattgtccactcaagtcgtggcctggggaaca cagacggagctgtccccagtgtcctccgtccctcagcccctggcctggctga	0.05	0.107
RT_002849.1	H2AFV H2A histone family, member V	RDALTNPLPPR	NP_958844.1,		14036	TAGagggatgctttaaccaaccctcttcctccccgtcattgtactgtaactgggacagaagaaataatggggatatgtgg aatttttaacaacagttaa	0.214	-0.102
RT_012910.1	HAGH hydroxyacylglutathione hydrolase	GRPAPSADLGIR	NP_005317.2,	NP_00103	2154	TGAggccgccctgcaccttcagcggatttggggattaggctcttttag	0.028	0.119
RT_012805.1	HAUS2 HAUS augmin like complex subunit 2	SSTLFLLNYV	NP_060567.1,	XP_00672	7221	TAGtcatcaactttatttttgcttaattatgtgtag	0.019	0.106
RT_006180.1	HEATR9 HEAT repeat containing 9	QSILIFR	NP_689994.2	XP_00527	5817	TAAgtcaattctttgggcctactccccgactccctccctgaagatgcttctcaggctcccatgagaaaacaatctatact tatcttccgtgaataa	0.115	0.17
RT_023343.1	HOXB8 homeobox B8	ASAGTARAAAAR	NP_076921.1	XP_00525	1334	TAGgcttcagctgggactgccagggccgcggccgcccgcacgtccgcgggtcccggccgcgccgccgccgcgcgccccctg cccgagagagctctggccccgctag	-0.2	-0.215
RT_007294.1	HPN hepsin	STGPRTPSLQGPLFHSGGPTQPRDH	NP_892028.1,	XP_00672	1019	TGAccggtggcttctcgctgcgcagcctccagggcccgaggtgatcccggtggtgggatccacgctgggcctaggatggg acgtttttcttcttgggcccggtccacaggtccaaggacaccctccctccagggtcctctcttccacagtggcgggccca ctcagccccgagaccacccaacctcaccctcctgac	0.314	0.341
RT_010197.1	HSPA12B heat shock 70kD protein 12B	VGAGETIVLQSAPFHALQPR	NP_443202.3,	XP_00526	3550	TGAgggcgcgccggcgcggtgccagcgccgtctgcccggccccgccctctttcggttcaggggcctgcggagcgggttgg ggcgggggaaacgatagttctgcagtctgcgcctttccacgccctccagccccgggggagataa	0.142	0.028
RT_012273.1	IDS iduronate 2-sulfatase	VLPTMDGK	NP_001160022.1,	NP_00	3218	TGAgttttgccaaccatggatggcaaatgtgatgtgctcccttccagctggtga	0.075	0.289
RT_004577.1	IFFO1 intermediate filament family orphan 1	GRGWGCTEGNISCSSAPGR	NP_542768.2,	XP_00671	3036	TAGagacctgcctccccccttgcacccgaggccctcgcagcagggagctcagcgaggcagagggtggggctgcacagaggg gaacatcagctgcagctctgcaccaggccggtccctggggactggggcgctcctccctcaggctttctccctcagtcttg gcttctccagggctctggggtgtctggagctaggcttggccctaccattctggggccatttccaccacagttggggctct cctgccttcacgcgtgggtgtctgctacttccccatctttaa	-0.066	0.215
RT_016397.1	IGHMBP2 immunoglobulin mu binding protein 2	WQTMLRLHQGHRGAEGPMGEER	NP_002171.2,	XP_00527	4725	TGAccggccgcatccttgcacgccccgcggagctctctccatggtagcccagggcgctggcagaccatgctccgcctcca ccagggccacagaggagcggaggggcctatgggggaggagcggagggccctgttggggaaggttgggtttttggaccccca gggataagcttttccgatgtcacaatgtggaggaaagcacctgggggacaacagtgctcgtgcaggtggggcttgggaaa tgcacgtcccttcccccttactccccgccaaaacccacatcccagcctctggatcctggggaaggttccagtccctggaga atacccagggcctcaaacttga	0.278	0.341
RT_011586.1	IKZF1 IKAROS family zinc finger 1 (Ikaros)	KSTRTAAFSLPPAA	NP_001278768	XP_01151	10190	TAAagccctcccgcgcccccacccccagaccccgagccaccccaggaaaagcacaaggactgccgccttctcgctcccgcc agcagcatag	-0.107	0.033
RT_023045.1	IL17RE interleukin 17 receptor E	IPCLTGRKSQPSPR	NP_705616.2,	XP_00671	1412	TGAgcagagctccaccgcagtcccgggtgtctgcggccgcaacgcaacggacactggctggaaccccggaatgagccttc gaccctgaaatccttggggtgcctcgaggacgactggccgaaaagccgcattccctgcctcacaggccggaagtcccagc ccagtccccgcgcgcgtccctcttcctcctcatactttcccttgactgagagctcctctaacccctgttctgatgggga gggcggtcttcccacttcctctccagaactccagaaagagcagtgtgcttatgcttcagtccaggctggagaggttgggg ccggggtagggaggcaggagccatgtcagttctgaaggagggtgaggcggtgggggattgcagggggcggctgagagaaa acctccttgggggccagggattccctttcccactctga	0.154	0.292
RT_008965.1	IL33 interleukin 33	RELGLPDPLK	NP_254274.1,	XP_00525	770	not found		
RT_025506.1	IL5RA interleukin 5 receptor, alpha	LTSSCIYFWLCPFGCLSCQL	NP_783853.1,	XP_01153	4995	TGActgtcactttggcatcctctgatgaactcacacatgcctcagtgcctcagtgaaaagaacagggatgctggctcttg gctaagaggtgttcagaatttaggcaacactcaatttacctgcgaagcaatacacccagacacaccagtcttgtatctct taaaagtatggatgcttcatccaaatcgcctcacctacagcagggaagttgactcatccaagcattttgccatgtttttt ctccccatgccgtacagggtagcacctcctcacctgccaatctttgcaatttgcttgactcacctcagacttttcattca caacagacagcttttaaggctaacgtccagctgtatttacttctggctgtgcccgtttggctgtttaagctgccaattgt ag	0.208	0.623
RT_020939.1	JMJD8 jumonji domain containing 8	GGQEHKLCIGAGGFCPGLPWTR	NP_001005920	XP_00525	7736	TAGccaaaacagctggcaggactgccggtcacacaccagcacgtcccacctcgtgctcacggattttattacacagatag tggcggcaatggcctcagcccagcccaccctcacctgcttttccagcccacaaagggggacgatcacggcccagcaaaag cgatgctgagaggggaaacagtccagagtccaacagcagaacttgggggaagcggtcggggtggccaggaacataaacta tgtataggggccgggggcttctgcccagggctcccctggaccaggacgccaggtagggcagggaacctcagtagtcctcc acccagccattctcagagatgaatgcgtcaataacctccttcatagccaagttggggatga	0.182	0.435
RT_010302.1	JUND jun D proto-oncogene	ARPPGIPPPRGCPGLDK	NP_005345.3,		752	TGAgtccgcgcgcggggcgcatgcgcggcccaccctccccaaggggcgggctcgcggggggtgtcgtgggcgccccggacttggagagggtgcggccctggggacccccccctccccgagtgtgcccaggaactcagagagggcgcggcccccggggattc cccccccccgagggtgcccaggactcgacaagctggacccctgctcccgggggggcgagcgcatgaccccccgccctc gcgctgcctctttcccccgcgcggccgccccgtgttgcacaaacccgcgcgtctcggctgccccctttgtacaccgcgccgcggaagggggctccgagggggcgcagcctcaaaccctgcctttcctttacttttacttttttttttttttttctttggaagagagaagaacagagtgttcgattctgccctatttatgtttc	0.187	0.348
RT_009378.1	KCNG2 potassium channel, voltage gated modifier subfamily G, mem	RPHGDPLPPPAAASGPPR		XP_01152	16826	TGAcgcctgcgccgcccacacggagaccccctgcccccctccagctgcagcgtcgggaccccgaggtgcgccaaggggtg gggggcgtctggcctgggggagcggctcctgccggccgcgtcctcggccctcgtgcgtgagcagccccagaacttggcggggccctgcctgactccccgtggcagcgctgggcaaagtcactggcctttgtcctcctgccccaccccttttccttggatttttaattttctacgcctag	0.195	0.485
RT_000486.1	KCNU1 potassium channel, subfamily U, member 1	KILPTFTLLNSLVDWK		XP_01154	14563	TGAaaaatccttccaacattcactttattgaacagcttggtggactggaagggtccctccaagaaacaaatctgcatctc agcactgcctttt	0.108	0.373
RT_003017.1	KIAA0513	RTEAMCHSPGPSARPSPHPMTCM	NP_001273495	XP_00525	10909	TAGgccccagaggtcgcactccgcaggaggactgaggccatgtgccattctcccgggcccagcgcccggccgtcacccca cccgatgacctgcatgaagccagcagcacccagagccactcctgctgccctagaactagcggttagaagaatccgctgtt cctccctcatctcctctgcctgtgtctgcgacccccatccatgtgccaaagtgtcccttgggtcacacagctaa	-0.046	-0.156
RT_021510.1	KIAA1191	SPLSRDSGK	NP_001274264	XP_00526	8368	TAGagccctctttccagggattctggtaaaggtggtttcttgcatcccactccccttttaccttggctttga	0.014	-0.011
RT_003800.1	KIAA1683	DPGSLQWGLRGR	NP_079525.1,	XP_00526	3408	TAGgaccctggctccctgcagtggggacttcgtgggaggcactcatggctctctgggtctaatgaataa	-0.065	-0.167
RT_010079.1	KMT2D lysine (K)-specific methyltransferase 2D	RGSSQSQDPGLGLPAD	NP_003473.3,	XP_00526	6602	TAAgaagctttgaggctaccaggcaggggagtcccctacccacaacctcttccctgaaagggatgagggggaagagagg tagcagccagagccaggacccagggttggggctgccggctgacccggagcccctggagcaggaggctggggcagagggcc ctaggccaagcccaccctgggcaccagggacaatcctcttccccaccaccggccctcaggctggcatctctgcccccagc tccaggaggggccagacagaagcagccattgggcatctcaggtttgaggggatatgggccgggaactacccagaagcat ctgggaggcagcagggtgggggaagaggatgtgtggccgggcctcacagccctgctgctcccactga	0.021	0.103
RT_005240.1	LAMTOR2 late endosomal/lysosomal adaptor, MAPK and MTOR acti	NDHLEGR	NP_054736.1,	NP_00113	2906	TAAcggcattggtggaagctggggtcagaaaagagaaatgaccatttggaggggcggggcctcctagaagaaccttcttag	0.198	0.216
RT_017114.1	LIPG lipase, endothelial	TSCYPSPWRKVTAEDPPNGR	NP_006024.1,	XP_00525	5528	TGAgggtgcccgggcaagtcttgccagcaaggcagcaagacttcctgctatccaagcccatggaggaaagttactgctga ggacccacccaatggaaggattcttctcagccttgaccctggagcactgggaacaactggtctcctgtga	0.063	0.028
RT_023299.1	LMTK2 lemur tyrosine kinase 2	VAANAHARVRGCSPGAAPLRPQPE	NP_055731.2	XP_01151	13730	TAGgtggctgccaacgcgcacgctcgggtccgaggctgctcccctggagcggcgcccctgcgccctcagcccgagcagcg acatccactcgccatttgctga	0.16	0.035
RT_001154.1	LOC102723730 adhesive plaque matrix protein-like	SPWPTGLR		XP_01150	17842	TAAttccctatttctcagcctctgctggtgaagtttctgcctcttacttcagaagtccaagtggtgaagagcccttggcccacaggtctcagggtggtaggaacgaaaaggccgctctga	-0.025	0.207
						TGActggtccacgcacggccaaagcatgaggaagctcatcgtgggattcattttcttacattttggacttacacagtaa		

RT_013953.1	LOC105373926 putative HERV-K_Xq28 provirus ancestral Pol protein	GIHFSYILDLHSKGFN		XP_01151	8461	gggcttcaactga	0.399	0.623
RT_000939.1	LOC643355 uncharacterized LOC643355	KMPRPK	NP_001257874	XP_00527	8225	TGAcggctcaccataaaagccaaaatggggacctgtcaaaaatgttttagccaaactatggcttggctcaggaagatgcc aagaccaaaggctgctgaactttaa	0.209	0.394
RT_024143.1	LRIT2 leucine-rich repeat, immunoglobulin-like and transmembrane	TTQAMGWK	NP_001017924		801	TGAacaacccaggccatggggtggaaacggcttgggcttcaagcctctgaaaccaaccctctgcagcagctccatccatt tatccagcaagtatatattgagcacccactgtgttccaagcactga	0.205	0.384
RT_007580.1	LRRC4B leucine rich repeat containing 4B	GGGAGRARGVEPPTQVPAR	NP_001073926	XP_00672	1548	TGAggcggcggggccgggcgggcgaggggcgtggagcccccccacccaggtcccagcccgggcgcagcctgaccgggacccctccctcccacagcccagcccaccttctgggaccacgcagggaattggggagaggtggcttccagccccatctggggctc ggacccccagtaaggacagggtggggctccaggagcggagtctctgggatcctcgcctcacccccgccaatccccggtga	0.16	0.119
RT_026848.1	LRRFIP1 leucine rich repeat (in FLII) interacting protein 1	TVASLALR	NP_001131022	XP_01151	10123	TAAattccagctctgatcaggcaactggttggtgactggagagcattgtttcataggcttttctctgtcctatctgggag cgctgcttcttcccctgccttccgagagacgaagaccgtggcgagcttggcgcttaggggctcccgtgccatggctcacc ccagggagccccagcagccaccaggtgcctctgtctgcagaccccctggcccgggctggcgccgacgctcagaacctgcag gtacttcataagcacacaggggcctcgagggagctctgtgtctga	-0.019	0.204
RT_006265.1	MAOB monoamine oxidase B	RERVSVITLSSYCIWDMSLGK	NP_000889.3,	XP_01154	6600	TAAagagagagggtgtctgtaatcacactctcttcttactgtatttgggatatgagtttggggaaagagttgcagtaa	0.26	0.259
RT_023252.1	MAP3K6 mitogen-activated protein kinase kinase kinase 6	ELNEGIIGQTGPR	NP_001284538		5739	TGAgagctgaatgagggcatcataggccagacaggcccaaggatggatgaatggagaggacaaaggcagcttctgacacaccagccccaggacctggggcgactggaggaagccaggcgagtggggcccaggactggttccagtgagagaaaccaaccacaggcacccaagcactaccagac gtgggaggggtatcctgggaagagccccctaggtctttttaaaaatttttttgttggccgggcatggtggctcatgcctgtaatcccagcactttgggaggccaaggtgggcagatcacgaggtcaggagatcaagactatcctggctaa	0.059	-0.036
RT_013519.1	MAP7D1 MAP7 domain containing 1	EGLPWIR	NP_060537.3,	XP_00671	2843	TAAgagggtttgccttggatccgggcacagttgtga	-0.005	-0.214
RT_011694.1	MAPK9 mitogen-activated protein kinase 9	VATPLLLSLHR	NP_620707.1,		3409	TAAgtagcaacgccactccttctcagtcttcatcgatcaatgacatttcatccatgtccactgagcagacgctggcctca gacacagacagcagtcttgatgcctcgacgggacccccttgaaggctgtcgatgataggttagaaatagcaaacctgtcag cattgaaggaactctcacctccgtgggcctga	0.151	0.396
RT_022686.1	MARK2 MAP/microtubule affinity-regulating kinase 2	QAARSGGGGGGPAGR	NP_001034558	XP_01154	659	TAAcaggctgccaggagcgggggcggcgggggcgggccagctggacgggctgccggccgctgcgccgccccacctgggcgagactgcagcgatggattggtgtgtctcccctgctggcacttctcccctccctggcccttctcagttttctcttacatgtttgtggggggtgggagattgttctccagcacc	0.181	0.152
RT_022228.1	MCAT malonyl-CoA-acyl carrier protein transacylase	LQGAQMR	NP_775738.3	XP_01152	10785	TGActgcagggggctcaaatgcgatga	0.257	0.623
RT_027052.1	MED1 mediator complex subunit 1	EPYFLKETGPEEK	NP_004765.2	XP_00525	10723	TAGgaaccttatttcctaaaagaaacagggccagaggaaaaaaaactattgataagtttatag	-0.112	0.058
RT_014431.1	MED12L mediator complex subunit 12-like	RHDVLCLH	NP_443728.3	XP_00671	5306	TGAatctgcaagaggagaagacatgacgttttatgtttgcactga	0.257	0.44
RT_022201.1	MEI1 meiotic double-stranded break formation protein 1	SSGLEGPEVER	NP_689726.3,	XP_01152	9595	TGAtcctcaggacttgaaggcccagaagtggagagagaatga	-0.087	0.103
RT_017809.1	MGAT5 mannosyl (alpha-1,6-)-glycoprotein beta-1,6-N-acetyl-glucos	SHAGTLARA	NP_002401.1	XP_00526	2131	TAGcagctacctgctcagccctgcaccatgctgctggggaagacagtggccccagccccgtcaggcagggccagggacag aagtcatgcagggactctggcaagagcctga	0.125	0.107
RT_013659.1	MID1IP1 MID1 interacting protein 1	KMVAGDGR	NP_067065.1,	NP_00109	1487	TGAggcgtggcgcccgtggctgcccagcaccttcttcgacccatctcaccctctctcattcctcaaagcttttttttttttcctggctgggggcgggaagggcagactgcaaactggggggctgcgtacgtgcaggaggcgcggtggggctgcgtggaggagggggccacgtgtgagagagaagaaaa	0.154	0.119
RT_001122.1	MIS12 MIS12 kinetochore complex component	LLSSQKEEPVK	NP_001245146	XP_00525	2641	TAAttgctcagtagtcaaaaggaggagcctgtcaaaaagtag	0.066	0.116
RT_019879.1	MITF microphthalmia-associated transcription factor	RILPALHSHK	NP_937802.1,	XP_01153	3922	TAGcgaatcctccctgcactgcattcgcacaaactgcttcctttcttgattcgtagatttaataacttacctgaagggt tttcttgataattttcctttaa	0.278	0.488
RT_021866.1	MPV17L MPV17 mitochondrial membrane protein-like	EVKDSLK	NP_001121895	XP_01152	10879	TGAgaagtcaaggactctcttaaagggaccacattttttacctaa	0.219	0.281
RT_021358.1	MSL3 male-specific lethal 3 homolog (Drosophila)	NVVGSVR; ATALSSLALWVPGE	NP_523353.2,	XP_00527	1444	TAAaatgttgttggttctgtaagagcaactgctctgtctagtttggcgctctgggttccaggtgaataa	-0.003	-0.089
RT_010471.1	MTR methionine synthase	FAVLGTMVMK	NP_000245.2,	XP_00527	10332	not found		
RT_020347.1	MTSS1 metastasis suppressor 1	VHKKCAGGE	NP_055566.3,	XP_00671	4627	TAGgttcacaagaaatgcgccggtggggaatga	0.134	0.067
RT_025500.1	MYO9B myosin IXB	LKSDVRWAPAPSAESR	NP_004136.2	XP_01152	1548	TGAgagccacagctgacaaagtctgcatgtccgaggacggcccctgcactggagctgggcgccagagctgcagagctagt gttcggccctcagagaaggatccagaatcaaaagctcaagagtgacgtgaggtgggcaccggccccaagtgcagagtcaa ggcagggagaggccggctggagccaggccccctcgcacgcagccccaaatcatggacgcacctgtggggagcaccacat ctccacctgcggcctcacatctccccactcccctttttgtacgtttaa	0.079	-0.036
RT_006029.1	NCAM2 neural cell adhesion molecule 2	QQYYRGLNNTTK	NP_004531.2,	XP_01152	14703	TAAcaacaatattacaggggcttgaacaacactacgaagagtatttggattgcgtga	0.29	0.468
RT_009713.1	NCAPH2 non-SMC condensin II complex, subunit H2	LNAARLMMGPR	NP_001171940		1370	TGAgtggggagcaccgaggcaggggtgggggaatgtgtactgaggagccgtgtgtctgctcctggctggcccggcctaat aaagcagtgttgccatctcatcttccccctaaaaaccctttttatgtacacctgcgcagagaagagggctgcctggcctccctgggccgctggtacagatcacacacacacacagattaaacgcagcccgtttaatgatggggcccagactgcagtggctcaagacaggacactgcggaaagccgccatgt taatccgtga	0.233	0.257
RT_014759.1	NCKAP5L NCK-associated protein 5-like	LSSCPAPGDGDPSLK	NP_001032895	XP_00671	3669	TGAggggctgcgccacgccacggccccgctggagctggggaccacagactggaccggctctcttcatgcccagcccccgg agacggggaccccctccctgaagggaccaaggaggcaggtggatagaaggtgaaaagggggtccctggcacaccccaccacccactgcttcggcggatga	0.164	0.028
RT_015970.1	NCOR2 nuclear receptor corepressor 2	HPCLSKALTK	NP_001070729		13497	TGActcagaacagggcgggggggggggcggtgtcaggtcccagcgagccacaggaacggccctgcaggagcagggcggctgccgactcccccaaccaaggaaggagcccctgagtccgcctgcgcctccatccatctgtccgtccagagccggcatcctt gcctgtctaaagccttaactaagactcccgccccgggctggccctgtgcagaccttactcaggggatgtttacctggtgctcgggaagggaggggaagggggccggggagggggcacggcaggcgtgtggcagccacacgcaggcggccaggcggccagg gacccaaagcaggatgaccacgcacctccacgccactgcctcccccgaatgcatttggaacaaagtctaaactga	0.265	0.714
RT_006054.1	NEB nebulin	AFQSITLVCR	NP_004534.2,	XP_01150	727	TAGgcatttcaaagcatcacacttgtctgcaggacttacagatcctgcagtcaatgtttcggtttagactctccactgtt acctaagttctcaagctgcctatggtttttctgtgtcaatgtgatttatggtagtaccatcctttctcctttgggtttta aaataagttgcagaacagacactttaaaagcttctgcaatattatttctgtgcctagagtctttctccattataaacatg ttttaa	0.092	0.07
RT_001896.1	NEFM neurofilament, medium polypeptide	VLPWGLQTLYFTLCNMR	NP_005373.2,		19012	TAAgatttgagtccattgcaaaaggttaagccatatgacaatttcaaaatgcatgtgattggcagcttcaaaacagaacg ggttctcccatgggggctccagacattgtattttactttgtgcaatatgaggggactgcatgcaagctcagggtgctccc tcctcagtctttgggggattcaaatgcatgatattgtatgtacctgggaaatttgccgatttcctaagctgttggaaggg ggtcacttaagggggatgtcttgagatgtattatgcaaagtaccaactga	-0.018	-0.182
RT_019335.1	NFASC neurofascin	QWPGAVPRAVPAVK	NP_001005389	XP_00524	284	TGAccagccccacccccctccccagcagccagagaagcagtggcccggggcagttccgagggcagtgcctgcagtcaagtg gccgggtcaggcgtggtga	0.407	0.658
RT_016847.1	NFIC nuclear factor I/C (CCAAT-binding transcription factor)	LPKLFISSPPAAR	NP_995315.1,	NP_00123	2713	TAGcaaaggtcttcttccctcgccccttctccatcgtcccaggaatcccagggggcagcacagccggcccccggcccacgttttcggtggaaaattagagtgaacaagaacacccctgccgactcccagcccggccaaaaagacaaaacacatagacgcacacactcaggaggaaaagaaaaaca	0.104	0.424
RT_008486.1	NLRC5 NLR family, CARD domain containing 5	WPPQDLWNPAK	NP_115582.4,	XP_00672	274	TGAtggccccctcaagacctttggaatccagccaagtga	0.086	0.065
RT_015312.1	NPL N-acetylneuraminate pyruvate lyase (dihydrodipicolinate syntha	EDCLSRRTLNY	NP_001186985.1,	NP_00	6156	TGAgaagactgtctctcccgcaggaccctgaattattga	0.22	0.281
RT_016124.1	NPLOC4 NPL4 homolog, ubiquitin recognition factor	GACPLLARTGPSPALPEAR	NP_060391.2,	XP_01152	846	TAGggcgcctgccctctgctggctaggaccgggcccagcccagccctcctgaagccagaagcgttgctgagtgtgttcc ctgtaactgccccatagtgggcagccctggaggaacaaggggctggctgtcctgggctccctga	0.029	-0.103
RT_009589.1	NUDT18 nudix (nucleoside diphosphate linked moiety X)-type motif 1	APSSADLSPSEGGKR	NP_079091.3	XP_01154	600	TAGagaggtgggggaggtgacagggagctaggcagccgtgctccctccagtgcggacttgtctccctctgagggaggcaa gaggctggcgatcagggatcttgttgcattgggagcaggggcggctctcctggtccccaggagagatgctttgaggagca ttcctctagattgcacaagggacagtgcctttaaccaagcgaggagtccaaagctcaggacctga	0.128	0.215
RT_003245.1	NXN nucleoredoxin	GCMAFAKSLAFGEGSARVSWAE	NP_071908.2,	XP_00525	391	TAGcgtggctccggcctcctgagacgttatttaaaactcagccttctcctctcccccctccttccttccgcccttggacttacccagcgtgccccgaatcccacccacccaagtgtccagcctctctgtggtgccttgtttctgcagtaaactcctcagccagcaccctggggtgtggaatcagcagcggcagagtc	0.25	0.203
RT_016280.1	OLFML1 olfactomedin-like 1	CITAVR	NP_940876.2,	XP_00525	2996	TAAtgcattacagctgtgagaaagagcactgtggctttggcagctgttctacaggacagtgaggctatagccccttcaca atatagtatccctctaatcacacacaggaagagtgtgtag	-0.12	-0.022
RT_014428.1	OLFML2A olfactomedin-like 2A	VETCAPRRGAAVR	NP_872293.2,	XP_00671	974	TGAgtggagacctgtgctccccggagaggggcagcagtgcgggaggggctttgcacagcagctcctgcaactgacccagt ccgcaaatatttattgggggccagcccaggctggactgggcatgaggtggtcaccaggattgagcttcctcagcaccc agtgggtaatacttgcttccacttgcagagcaccgtgccaagcacttcccacacacttacccgtttga	0.315	0.257
RT_010142.1	OPA1 optic atrophy 1 (autosomal dominant)	IVLIISSAYI	NP_570850.2,		1229	TAAattaaaatcgtactcataatcagctctgcatacatctgaagaacaaaaacatcaacgtcttttgtccagcctctttt tcttctgctgttccacctttctaa	0.054	0.204
RT_015055.1	PAQR7 progestin and adipoQ receptor family member VII	WEQGLVK	NP_848509.1	XP_01153	3864	TGAagggggatggcatctggtagggagggaggtatagttgggggacaggggtctgggtttggctccaggtgggaacaagg cctggtaaagttgtttgtgtctggcccacagtga	0.138	0.12
RT_005430.1	PARP10 poly(ADP-ribose) polymerase family member 10	APEGGVGDGGQQRPR	NP_116178.2,	XP_01151	3568	TAAccgaaggggccaccctctggcctcctgcttcccaggctcccagctccgcacaggctgatgctccccgcccccaactgtggccgcctgagctgtccccggggacgcccctgcctccctctgcgggctccagaaggcggtgtgggggatggcggtcagcagcggccgagggggggccgggctaggtcc	0.177	0.163
RT_017560.1	PAX2 paired box 2	VGQDGWSRGR	NP_001291498		7788	TAGttaccgcggggaccacatcaagcttcaggccgacagcttcggcctccacatcgtccccgtctgaccccaccccggag ggagggaggaccgacgcgacgcgatgcctcccggccaccgccccagcctcaccccatcccacgacccccgcaacccttca catcaccccccctcgaaggtcggacaggacgggtggagccgtggcgggaccctcaggcccgggcccgccgcccccagccc cgcctgccgcccctccccgcctgcctggactgcgcggcgccgtga	0.08	0.388
RT_014634.1	PCBP2 poly(rC) binding protein 2	NNADSSIIPFCCSPPPMIHLCSF	NP_005007.2,	NP_00112	4813	TAGaacaatgcagattcatccataatccctttctgctgttcaccaccacccatgatccatctgtgtagtttctga	-0.054	-0.075
RT_026547.1	PEBP4 phosphatidylethanolamine-binding protein 4	IAGFAIR	NP_659399.2	XP_01154	6085	TGAtagccggctttgccatccgggcatgtggccacactgcccaccaccgacgatgtgggtatggaaccccctctggata cagaacccttcttttccaaataaaaaaaaaatcatccagggcttggtgctttgtatcctagcttgtattcctttgaaaagcaacaggaggaaattggccaatatccagcactggggactgaggctttcctgtaaatgcaaggggttgggtggggagtgg ggggaatag	0.365	0.444
RT_014747.1	PHF14 PHD finger protein 14	FAAYVIADKISNCKMLNCK		XP_01151	10015	TAAaagattttctgtagtgtttttgaaaagtttgcagcttatgtaatagcagataaaatttctaattgtaaaatgttaaa ttgtaaaatctaa	-0.055	-0.122
RT_013650.1	PIAS2 protein inhibitor of activated STAT, 2	NMTALLLLVPYCQVR	NP_775298.1	XP_00672	3105	TGAatacaaaataaaacaaataatttgtatttatggagtggaaaacagcttatttcaaggaaaaatatgactgccttatt attgctagtgccatattgtcaggtgcgaatggtgctcaaaagttgtatcattaaaatttga	0.22	0.666
RT_010003.1	PICK1 protein interacting with PRKCA 1	GLGGGRSPSPAPCGRSHCPR	NP_036539.1,	XP_01152	2783	TGAgtgccccgcggctgtggtgccgggggcagggtgcgtgggaggacggagcctgggagcggggcgggccgccgcgcaagggggcgacgcataaaggcctgctggcttggggcgcctgcctccctgctcctctgtcctcgcacagcgaacctgggctcctgcccaggacaggcaccaggtcatg	0.28	0.257
RT_023912.1	PLAC1 placenta specific 1	SSGLGSPEDAISR	NP_068568.1	XP_01152	1924	TGAtcctcaggtttggggtctcctgaagatgctatttctagaattagtatatag	0.131	0.103
RT_006100.1	PLCB4 phospholipase C, beta 4	THSQTSEHKLHG	NP_000924.3,	XP_00526	5813	TGAagcagcaaacccacaaagcatcaaaagactcactcacaaacttctgaacacaaactccatggatga	0.127	0.211
RT_023238.1	PLCZ1 phospholipase C, zeta 1	QLMINDISLAMHRNK	NP_149114.2,	XP_00525	1169	TAAcagctaatgataaatgacatatcattagctatgcatcgcaataaaacagccaaaatgaatgtctttatgttttctttttaaacataaagaaaaataattactcataa	0.028	0.152
RT_009701.1	PLD5 phospholipase D family, member 5	GLEERKNTLICLFF	NP_689879.2,	XP_01154	2529	TAAcatgatgaagaaactgacaggacagctctgtatttcatatttatacataaaggacttgaggagagaaaaaacacttt aatatgtctcttttttag	0.334	0.184
RT_008256.1	PMPCA peptidase (mitochondrial processing) alpha	RSEFPETAK		XP_00526	2176	TAAagagcactcaagttagtaggcgagaagggctcagtagaggactgctacattgtacgtggagtagcagtggctcggaatgccgctgtaccgttgctggctctcgggcaggagtctcagccccaggtttccggggcccccatgagtgaccttaggaggtctgaatttcctgaaactgccaagttgtatgt	0.075	0.259
RT_023570.1	PNPLA7 patatin-like phospholipase domain containing 7	SPDAASSVGLSPR	NP_689499.4,	XP_00671	2907	TAGaggcctctgctaaagagcccggatgcagcgtcttccgtgggactgtccccaaggctgaggctcctgccaagtcctag gggcctctgtacctgccctgctggaagccctgacttccccggggccccaggctgtgtagggttctctgggcctcttctt tgtaccagcagccctgcatacagggccctgtgagcccccctgcagtcctgtga	0.063	-0.102
RT_009079.1	POU2F3 POU class 2 homeobox 3	ISTINEPR	NP_001231611	XP_01154	4268	TGAgaccaaaaagtttctcctactccagctggccctgtattccccctggaaggaagggaatcatgccttctatatacaga cagattgccttcagaagagtggaagaaaatctccactatcaatgaacccagactcttgtcttcttcaagagcaagggcct ccggagatccaaactgtgattga	-0.045	0.055
RT_020178.1	PPP1R12B protein phosphatase 1, regulatory subunit 12B	LASSISPP		XP_01150	97	TGActtgctagtagcatctcacctccttga	0.383	0.655
RT_020123.1	PPT2 palmitoyl-protein thioesterase 2	GYIQGSPGTPR	NP_619731.2,		11122	TGAggatatattcaggggtccccaggaactcctcggtccagagaccaagtggtggccttggaaagcagatgtcaggcttt ggtgtgcctgtga	0.174	0.345
RT_023177.1	PRRC2C proline-rich coiled-coil 2C	SDNAGSQRGK	NP_055987.2	XP_00524	19643	TAAaggctatggtttattgcaggggattgggaggggggcgggaaaacatggagaattaagtcagataatgctggcagcca aaggggcaaaatggcctgtgacattatcctgttcagagcttggagatgtacaagggacataggagcaatttacactgaca cacagctgctgtaccagtga	-0.016	-0.058
RT_027064.1	PTP4A3 protein tyrosine phosphatase type IVA, member 3	HLRALVSEERGAPR	NP_116000.1,	XP_00525	8250	TAGctcaggaccttggctgggcctggtcgtcatgtaggtcaggaccttggctggacctggaggccctgcccagccctgct ctgcccagcccagcaggggctccaggccttggctggccccacatcgccttttcctccccgacacctccgtgcacttgtgtccgaggagcgaggagcccctcgggccctgggtggcctctgggccctttctcctgtctccgccactccctctggcggcgctggccgtggctctgtctctctgaggtgggtcgggcg	0.19	0.491
RT_009826.1	PTPN4 protein tyrosine phosphatase, non-receptor type 4	KNEELK	NP_002821.1,	XP_01150	10201	TAAgaaagcaaaaagatctgggatatgtgttggaaaactgctttcccttatgttcactgtgccataatgctgctcgcagg aaatggcattttacaaaaaaaaaatgaagaactcaaaaaaactttgaaaacttcagcactgttgcactttatgttttaa	0.052	0.103
RT_023418.1	PTPRT protein tyrosine phosphatase, receptor type, T	LNGMGNLPESR	NP_008981.4,	XP_01152	10957	TAGctcaatgggatggggaacctgccggagtccagaggctgctgtgaccaagccccctttttgtgtgaatggcagtaactg ggctcaggagctctga	0.357	0.491
RT_016814.1	PVRL2 poliovirus receptor-related 2 (herpesvirus entry mediator B)	HWSGTLPPTFLGLGGRWNSTLDFS	NP_002847.1,	XP_01152	11516	TGAcctggacacagacagagacagagccaggcccggccctcccgcccccgacctgaccacgccggcctagggttccagactggttggacttgttcgtctggacgacactggagtggaacactgcctcccactttcttgggacttggagggaggtggaaca gcacactggacttctcccgtctctag	0.418	0.373
RT_002300.1	RASAL2 RAS protein activator like 2	ALSVEGDR	NP_733793.2,	XP_01150	7997	TGAcgggctttgtctgtggaaggagacagaaggaaattgacccactctcctatctccagacctttacctagcccctccag gtttacagaatgttgctacttcacaatggcgatgtggtga	0.261	0.394
RT_014669.1	RASSF7 Ras association (RalGDS/AF-6) domain family (N-terminal) m	SQLGTCQAPK	NP_003466.1	XP_00525	869	TGAcagcctagtgagggctgcaagaccatcctgcccggaccacagaaggagagttggcggtcacagagggctcctctgcc aggcagtgggaagccctgggtttggcctcaggagctgggggtgcagtgggggactgccctagtccttgccaggtcgccag caccctggagaagcatggggcgtagccagctcggaacttgccaggccccaaaggccacgactgccttgttggggacaggag atgcatggacagtgtgctcaagctgtgggcatgtgcttgcctgcgggagaggtccttcactgtgtgtacacagcaagagcatgtgtgtgccacttcccctaccccaacgtgaaaacctcaataaactgcccgaagcagcttgagtgtgtgtggaggctgcgctgggcaggtctgaggtcttgaacttgagc	0.289	0.33
RT_013497.1	RBM14 RNA binding motif protein 14	APIMITCGRLR	NP_001185765.1,	NP_00	4196	TAGccgagctctctgattaccgccgtttatcagagtcgcagctttcgttccgccgctcgccgacaaagtcctcgctggattaccgtcgcctgcccgatgcccattccgattacgcacgctattcgggctcctataatgattacctgcgggcggctcagatgcactctggctaccagcgccgcatgtagggccatc	0.152	0.119
RT_024372.1	RFPL3 ret finger protein-like 3	AATAKKNR	NP_006595.1,		7405	TAAgccgccactgcaaaaaaaaacagggtcagaaaattacttgggtgggtagacttaggaattttctacttggtaaaagc attatacagtcataggagaaagatatgggacatttctataatctatattctaatttga	0.076	-0.112

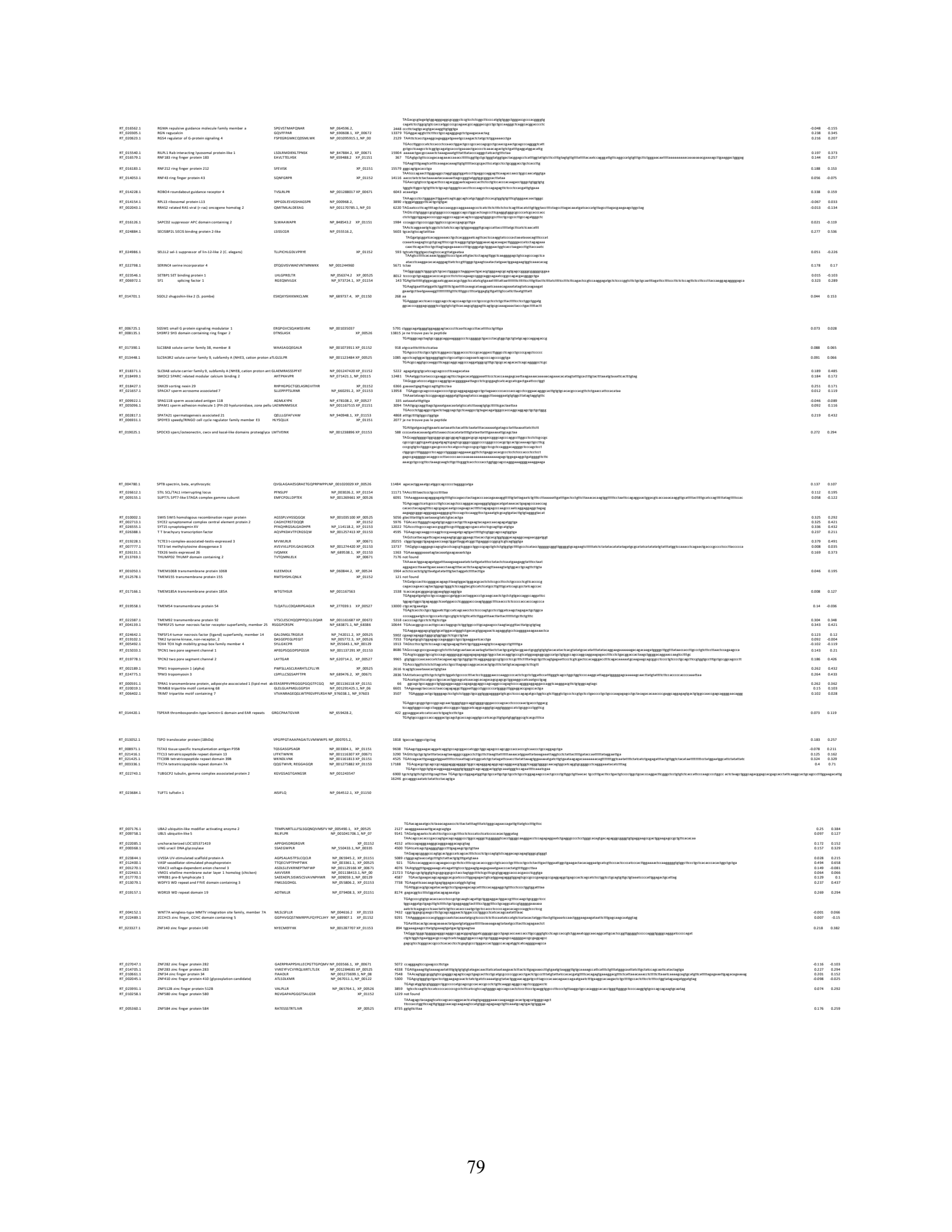

Tableau 5. – Table S4; Raw data

Relative Fluc fold change							
	Condition	**N1**		**N2**		**N3**	
		Norm Fluc/Rluc	**SD**	**Norm Fluc/Rluc**	**SD**	**Norm Fluc/Rluc**	**SD**
UGA Fig 1F	**Vector**	1,0000	0,2409	1	0,2587	1	0,3428
	H-Ras V12-D5	1,0940	0,3269	0,5199	0,2041	0,9202	0,1283
	H-Ras V12-D12	0,5663	0,1330	0,3747	0,1497	0,4701	0,0662
	H-Ras V12-D20	0,4043	0,0241	0,2683	0,1672	0,3423	0,1405
AQP4 Fig 1F	**Vector**	1,0000	0,1645	1	0,1701	1	0,1370
	H-Ras V12-D5	1,7850	0,6203	0,8558	0,1782	1,828	0,3805
	H-Ras V12-D12	0,7813	0,0213	0,3300	0,0806	0,7042	0,1719
	H-Ras V12-D20	0,3594	0,0807	0,2036	0,0492	0,4357	0,1050
UGA Fig 2A	**Vector**	1,0000	0,1771	1	0,1162	1,0000	0,0238
	H-Ras V12	0,4557	0,1307	0,2343	0,1541	0,6687	0,1065
	Vector Gen	1,9220	0,5004	11,3100	1,07700	5,5810	0,0345
	H-Ras V12 Gen	1,1860	0,1066	7,9870	1,61800	4,3510	0,6618
AQP4 Fig 2A	**Vector**	1,0000	0,0864	1	0,2858	1,0950	0,1338
	H-Ras V12	0,3274	0,1348	0,5268	0,0705	0,2753	0,0467
	Vector Gen	2,4020	0,4240	1,5830	0,0189	2,6290	0,6564
	H-Ras V12 Gen	0,9056	0,0795	1,4380	0,3512	0,9912	0,0870
MMuLV Fig2A	**Vector**	0,7927	0,07473	1,0000	0,1428	1,1450	0,2049
	H-Ras V12	1	0,0001726	1,3520	0,000165	1,3150	0,147
	Vector Gen	0,7581	0,07355	1,0250	0,07029	1,1050	0,3146
	H-Ras V12 Gen	1,046	0,1354	1,3480	0,09148	2,0100	0,0386
UGA Fig 2B	**Vector**	1,1310	0,1031	0,8210	0,0169	1,0000	0,1838
	PML-ER	1,0000	0,2771	1,0000	0,1238	0,9085	0,2310
	Vector 4OHT	1,1430	0,1341	0,8441	0,1567	0,9875	0,0128
	PML-ER 4OHT	0,0657	0,1138	0,0000	0,0000	0,9542	0,3150
	Vector Gen	15,9600	4,3580	17,1100	3,2800	17,9200	2,8720
	PML-ER Gen	11,0100	1,1130	17,9700	3,8380	16,8300	2,5950
	Vector 4OHT Gen	14,6700	1,6520	19,1300	4,4710	11,5500	0,3844
	PML-ER 4OHT Gen	2,2040	1,2050	3,9580	0,6262	6,0300	0,6035
AQP4 Fig 2C	**Vector**	1,0000	0,0554	1,0000	0,1457		
	PML-ER	0,8622	0,0583	0,9104	0,1158		
	Vector 4OHT	1,1640	0,2160	1,0570	0,1785		
	PML-ER 4OHT	0,6573	0,0927	0,7367	0,1292		
	Vector Gen	3,7630	0,7502	2,5350	0,2966		
	PML-ER Gen	2,9520	0,3866	2,9780	0,2403		
	Vector 4OHT Gen	2,7590	0,4541	2,4750	0,1161		
	PML-ER 4OHT Gen	1,8230	0,1799	2,0780	0,6261		
AQP4 Fig 2D	**Vector**	1,0000	0,1017	1,0000	0,07772		
	PML-ER	0,8475	0,0784	0,8101	0,1826		
	Vector 4OHT	1,0120	0,1778	1,1320	0,2045		
	PML-ER 4OHT	0,8001	0,1193	0,8046	0,09078		
	Vector Gen	1,4700	0,1510	1,5350	0,4673		
	PML-ER Gen	1,3340	0,0510	1,2730	0,01816		

	Vector 4OHT Gen	1,5010	0,0460	1,4530	0,04499		
	PML-ER 4OHT Gen	0,8767	0,1930	0,9071	0,1145		
UGA Fig 3B	**Vector D12**	1,0532	0,2135	1,0000	0,1817		
	H-Ras V12 D12	0,6578	0,1054	0,7406	0,1223		
	Vector D35	1,0000	0,0579	1,0000	0,0579		
	H-Ras V12 D35	0,9209	0,0639	1,6336	0,1719		
AQP4 Fig 3B	**Vector D12**	1,0000	0,0864	1,0000	0,0479	1,0000	0,2210
	H-Ras V12 D12	0,3274	0,1348	0,5905	0,0455	0,4175	0,1630
	Vector D35	1,0000	0,0537	1,0000	0,1802	1,0000	0,1230
	H-Ras V12 D35	1,5119	0,3644	1,8362	0,2394	1,2496	0,2135
VASP Fig 3B	**Vector D12**	1,0000	0,0120	1,1411	0,3336	1,0000	0,3467
	H-Ras V12 D12	0,7189	0,0187	1,0000	0,2572	0,5411	0,0613
	Vector D35	1,0000	0,2016	1,0000	0,3699	1,0000	0,2288
	H-Ras V12 D35	2,9382	0,3314	2,2841	0,2431	2,9616	0,8335
HPN Fig 3B	**Vector D12**	1,0000	0,0505	1,0000	0,1064	1,0000	0,1580
	H-Ras V12 D12	0,5396	0,1724	0,4845	0,6852	0,8584	0,1746
	Vector D35	1,0000	0,0299	1,2092	0,4646	1,0000	0,3842
	H-Ras V12 D35	3,3707	0,3539	1,6540	0,3531	1,6540	0,3531
UGA Fig 4A	**Vector**	1,0000	0,1751	1,0000	0,0968	1,0000	0,2026
	H-Ras V12	0,3895	0,2037	0,6659	0,1597	0,1657	0,0743
	H-Ras V12/E6	0,4181	0,0877	0,8446	0,1520	0,8052	0,1544
	H-Ras V12/E7	2,3978	0,4075	3,9306	0,4586	3,6125	0,1093
	H-Ras V12/E6/E7	5,8209	1,1219	2,0074	0,0243	1,6591	0,3204
AQP4Fig 4B	**Vector**	1	0,1443	1,045	0,1559	1	0,1168
	H-Ras V12	0,2937	0,076	0,8011	0,07103	0,6803	0,1386
	H-Ras V12/E6	0,3333	0,07278	0,9688	0,0749	0,6761	0,1346
	H-Ras V12/E7	0,5688	0,09934	1,133	0,13	1,147	0,0564
	H-Ras V12/E6/E7	0,9557	0,3249	1,374	0,04987	1,375	0,2305
VASP Fig 4C	**Vector**	1	0,3191	1	0,2039	1	0,1326
	H-Ras V12	0,4874	0,02815	0,4709	0,0702	0,7801	0,0748
	H-Ras V12/E6	0,6765	0,01425	0,4316	0,01853	0,9158	0,0515
	H-Ras V12/E7	1,844	0,3842	0,8383	0,1091	1,342	0,1684
	H-Ras V12/E6/E7	1,536	0,11	1,517	0,0321	1,507	0,242
AQP4 Fig 4D	**Vector**	1	0,1713	1	0,1036	1,045	0,1559
	H-Ras V12	0,3133	0,06554	0,5884	0,05405	0,8011	0,071
	H-Ras V12 /E7	0,5997	0,1068	0,8384	0,0461	1,133	0,13
	H-Ras V12/ E7Δ21-24	0,2692	0,0311	0,3682	0,0506	0,8253	0,085
AQP4 Fig 4E	**Vector**	1	0,06915	1	0,2102	1	0,0437
	H-Ras V12	0,5729	0,07417	0,7011	0,05802	0,66	0,0171
	Vector /CDK4	0,9616	0,2299	1,127	0,3828	1,032	0,139
	H-Ras V12/CDK4	0,9731	0,08102	1,397	0,1968	0,6475	0,1597
UGA Fig 3B	**Vector D12**	1,0532	0,2135	1,0000	0,1817		
	H-Ras V12 D12	0,6578	0,1054	0,7406	0,1223		
	Vector D35	1,0000	0,0579	1,0000	0,0579		
	H-Ras V12 D35	0,9209	0,0639	1,6336	0,1719		
AQP4 Fig 3B	**Vector D12**	1,0000	0,0864	1,0000	0,0479	1,0000	0,2210
	H-Ras V12 D12	0,3274	0,1348	0,5905	0,0455	0,4175	0,1630
	Vector D35	1,0000	0,0537	1,0000	0,1802	1,0000	0,1230

	H-Ras V12 D35	1,5119	0,3644	1,8362	0,2394	1,2496	0,2135
VASP Fig 3B	**Vector D12**	1,0000	0,0120	1,1411	0,3336	1,0000	0,3467
	H-Ras V12 D12	0,7189	0,0187	1,0000	0,2572	0,5411	0,0613
	Vector D35	1,0000	0,2016	1,0000	0,3699	1,0000	0,2288
	H-Ras V12 D35	2,9382	0,3314	2,2841	0,2431	2,9616	0,8335
HPN Fig 3B	**Vector D12**	1,0000	0,0505	1,0000	0,1064	1,0000	0,1580
	H-Ras V12 D12	0,5396	0,1724	0,4845	0,6852	0,8584	0,1746
	Vector D35	1,0000	0,0299	1,2092	0,4646	1,0000	0,3842
	H-Ras V12 D35	3,3707	0,3539	1,6540	0,3531	1,6540	0,3531
UGA Fig 4A	**Vector**	1,0000	0,1751	1,0000	0,0968	1,0000	0,2026
	H-Ras V12	0,3895	0,2037	0,6659	0,1597	0,1657	0,0743
	H-Ras V12/E6	0,4181	0,0877	0,8446	0,1520	0,8052	0,1544
	H-Ras V12/E7	2,3978	0,4075	3,9306	0,4586	3,6125	0,1093
	H-Ras V12/E6/E7	5,8209	1,1219	2,0074	0,0243	1,6591	0,3204
AQP4Fig 4B	**Vector**	1	0,1443	1,045	0,1559	1	0,1168
	H-Ras V12	0,2937	0,076	0,8011	0,07103	0,6803	0,1386
	H-Ras V12/E6	0,3333	0,07278	0,9688	0,0749	0,6761	0,1346
	H-Ras V12/E7	0,5688	0,09934	1,133	0,13	1,147	0,0564
	H-Ras V12/E6/E7	0,9557	0,3249	1,374	0,04987	1,375	0,2305
VASP Fig 4C	**Vector**	1	0,3191	1	0,2039	1	0,1326
	H-Ras V12	0,4874	0,02815	0,4709	0,0702	0,7801	0,0748
	H-Ras V12/E6	0,6765	0,01425	0,4316	0,01853	0,9158	0,0515
	H-Ras V12/E7	1,844	0,3842	0,8383	0,1091	1,342	0,1684
	H-Ras V12/E6/E7	1,536	0,11	1,517	0,0321	1,507	0,242
AQP4 Fig 4D	**Vector**	1	0,1713	1	0,1036	1,045	0,1559
	H-Ras V12	0,3133	0,06554	0,5884	0,05405	0,8011	0,071
	H-Ras V12 /E7	0,5997	0,1068	0,8384	0,0461	1,133	0,13
	H-Ras V12/ E7Δ21-24	0,2692	0,0311	0,3682	0,0506	0,8253	0,085
AQP4 Fig 4E	**Vector**	1	0,06915	1	0,2102	1	0,0437
	H-Ras V12	0,5729	0,07417	0,7011	0,05802	0,66	0,0171
	Vector /CDK4	0,9616	0,2299	1,127	0,3828	1,032	0,139
	H-Ras V12/CDK4	0,9731	0,08102	1,397	0,1968	0,6475	0,1597
UGA Fig 5A	**Vector**	1	0,08361	1	0,3002	1,076	0,2082
	Vector Palbo	1,372	0,1402	0,8938	0,1501	0,9886	0,1107
	Vector Gen	20,4	2,396	10,59	1,821	7,828	1,838
	Vector Palbo + Gen	11,23	1,73	1,708	0,1734	5,699	1,172
AQP4 Fig 5B	**Vector**	1,0000	0,1549	1,0000	0,1802	1,0450	0,1230
	Vector Palbo	0,7022	0,0392	0,9950	0,2310	0,7346	0,0666
	Vector Gen	1,5200	0,2612	4,8140	0,5472	3,9550	0,5800
	Vector Palbo + Gen	1,3210	0,1188	5,2490	0,7914	1,8240	0,3738
AQP4 Fig 5C	**Vector D35**	1	0,1425	1	0,123	1	0,2231
	H-Ras V12 D35	1,466	0,1292	1,25	0,2135	1,178	0,147
	Vector D35 Palbo	0,573	0,2292	0,7346	0,06662	0,2108	0,0208
	H-Ras V12 D35 Palbo	0,5395	0,08137	0,7351	0,1591	0,3108	0,0577
UGA Fig 6B	**AQP4/DMSO**	1,0000	0,2395	1,0000	0,2193	1,0000	0,0632
	AQP4/Camptho	0,8528	0,1537	0,7371	0,1926	0,7678	0,1466
	UGA/DMSO	1,0000	0,2901	1,0000	0,2993	1,0000	0,2401

	Condition	N4		N5		
		Norm Fluc/Rluc	SD	Norm Fluc/Rluc	SD	
	AQP4/DMSO	1,0000	0,3089	1,0000	0,2218	
	AQP4/Camptho	0,6795	0,0323	0,7401	0,0501	
	UGA/DMSO	1,0000	0,1709			

	Condition	N1		N2		N3	
		Norm Fluc/Rluc	SD	Norm Fluc/Rluc	SD	Norm Fluc/Rluc	SD
UGA Fig 6C	AQP4/DMSO	1	0,012	1	0,04	1	0,006
	AQP4/Camptho	0,84	0,017	0,72	0,03	0,77	0,019
	UGA/DMSO	1	0,017	1	0,22	1	0,159
	UGA/Camptho	0,58	0,13	0,7	0,23	0,64	0,17
	Control/DMSO	1	0,019	1	0,03	1	0,026
	Control/Camptho	0,89	0,04	0,8	0,19	0,85	0,023
UGA Fig 6D	AQP4/DMSO	1	0,02	1	0,012	1	0,032
	AQP4/Camptho	1,61	0,01	1,299	0,016	1,23	0,028
	UGA/DMSO	1	0,053	1	0,028	1	0,059
	UGA/Camptho	1,75	0,064	1,206	0,029	2,25	0,012
	Control/DMSO	1	0,028	1	0,017	1	0,031
	Control/Camptho	0,9	0,01	1,1	0,038	0,977	0,03
UGA Fig S1D	Vector D5	1,0000	0,2828	1,0820	0,1161		
	Vector D12	0,8620	0,3315	0,9551	0,1077		
	Vector D20	1,0000	0,1937	0,8995	0,2043		
AQP4 FigS1D	Vector D5	0,9991	0,2331	0,931	0,1098		
	Vector D12	0,7887	0,1582	1,004	0,2469		
	Vector D20	0,7829	0,1559	1,066	0,2165		
AQP4 FigS1E	Vector/Starv	1	0,06281	1	0,04788		
	H Ras V12/Starv	0,4751	0,05073	0,5905	0,04545		
	Vector /FBS	0,928	0,2528	0,8961	0,213		
	H Ras V12/FBS	0,5003	0,1221	0,669	0,01713		
Nat. Rth candidates Ctrl Fig S2C	HPN-Vector	1	0,0752508	0,9999999	0,050515	1	0,2531
	HPN-H-Ras V12	0,3838983	0,384538	0,7287598	0,218933	0,5758567	0,0603
	VASP-Vector	0,9999998	0,0084842	0,9999998	0,292373	1	0,0085
	VASP-H-Ras V12	0,7492877	0,0558898	0,8763331	0,225433	0,7188824	0,0187
	ASPH-H-Ras V12	0	0	0	0	0	0
	FBL-Vector	1	0,1787781	0,9999999	0,197851	1	0,1449
	FBL-H-Ras V12	0,6416453	0,1648477	0,8305688	0,006193	0,9574316	0,076
Nat. Rth candidates Gen FigS2D	HPN-H-Ras V12	7,9446	2,6363	2,4933	0,1470		
	VASP-Vector	19,0749	1,8238	4,4482	0,3532		
	VASP-H-Ras V12	8,2412	1,1154	3,1289	1,0182		
	ASPH-Vector	3,6987	0,4123	1,0000	0,4716		
	ASPH-H-Ras V12	2,4933	0,1470	0,1653	0,0323		
	FBL-Vector	3,1437	0,4392	1,8573	0,3116		
AQP4 FigS3A	Vector	1	0,1713	1,045	0,1559	1	0,1168
	Vector /E7	1,204	0,2172	1,121	0,2537	1,147	0,0564
	Vector/ E7Δ21-24	0,8017	0,1072	1,321	0,0621	0,8594	0,0135

CGA Fig S1C	**Vector D5**	0,1513	0,01336	0,1522	0,0328		
	H-Ras V12-D5	0,1915	0,03523	0,1917	0,02881		
	Vector D12	0,177	0,02829	0,2036	0,05782		
	H-Ras V12-D12	0,1877	0,05967	0,1653	0,01256		
	Vector D20	0,1976	0,01948	0,1937	0,03903		
	H-Ras V12-D20	0,2119	0,02777	0,2063	0,04968		
CGA Fig S2A	**Vector**	0,1586	0,03595	0,1653	0,0114	0,1709	0,0309
	H Ras V12	0,1553	0,007879	0,1812	0,06017	0,1478	0,0295
	Vector Gen	0,1961	0,05043	0,2048	0,04365	0,1997	0,0382
	H Ras V12 Gen	0,229	0,009903	0,2198	0,006688	0,1437	0,006
		Fluc/Rluc	**SD**	**Fluc/Rluc**	**SD**	**Fluc/Rluc**	**SD**
	Vector	1,000	0,066	1,000	0,154	1,000	0,255
	H Ras V12	0,625	0,162	0,748	0,063	0,620	0,034
	Vector CDX5-1	0,973	0,099	1,045	0,094		
	H Ras V12 CDX5-1	0,837	0,178	0,860	0,020		
	Vector Gen	7,038	0,741	5,910	0,425	5,430	1,054
	H Ras V12 Gen	3,702	0,460	3,875	0,442	3,067	1,222
	Vector CDX5-1 + Gen	16,928	3,800	14,750	1,686	14,111	0,822
	H Ras V12 CDX5-1 + Gen	4,896	0,400	6,764	0,990	5,191	0,769

Tableau 6. – Table S5; Real time PCR primer

Gene Name	5' forward primer (5'-3')	3' reverse primer (5'-3')
BRCA1	GGTTGTTGATGTGGAGGGGCAA	CCAGATTCCAGGTAAGGGGTTC
CDKN1A/p21	ACCCTTGTGCCTCGCTCAGG	GCGTTTGGAGTGGTAGAAATCTGT
CDK4	CAGTGCAGTCGGTGGTACCTGA	GGCAGAGATTCGCTTGTGTGG
CENPA	AATGGATTCTGCGATGCTGTCTGG	TTTTCAGGCCTTTGGAACGGTGTT
FANCD2	CCTTAGTAGCCGACTGAAACAGG	TGCAAGTAATGGACGCTCTG
GADD45A	TTGCAATATGACTTTGGAGGAA	CATCCCCCACCTTATCCAT
HMBS	GGCAATGCGGCTGCAA	GGGTACCCACGCGAATCAC
H-RAS	TTGCCATCAACAACACCAAGTC	ATCCGAGTCCTTCACCCGTTTG
KI67	AGAAGACAGTACCGCAGATGA	CGGCTCACTAATTTAACGCTGG
MCM6	ATCCCTCTTGCCAAGGATTT	GAAAAGTTCCGCTCACAAGC
ORC1L	CCCGGCTCAAGCATCYAAAGG	TCGTGCATCTCCAGACAGTCT
TBP	GCTGGCCCATAGTGATCTTTGC	CTTCACACGCCAAGAAACAGTGA
MCM6	ATCCCTCTTGCCAAGGATTT	GAAAAGTTCCGCTCACAAGC
IL-6	CCAGGAGCCCAGCTATGAACTC	AAGGCAGCAGGCAACACCAG
CXCL8/IL-8	GGCACAAACTTTCAGAGACAGCA	GGCAAAACTGCACCTTCACACA

Chapitre 3 : Discussion

Que ce soit par des agents toxiques, dans un contexte de réplication ou de stress oxydatif, les cellules sont perpétuellement exposées à des atteintes cellulaires. L'accumulation de dommages résulant de ces atteintes peut être à l'origine d'instabilité génomique et peut, à long terme, conduire à des pathologies hyperprolifératives telles que le cancer. Afin de favoriser la survie de l'organisme et d'empêcher l'accumulation d'un fardeau tumoral, les cellules ont développé, au fil du temps, différents mécanismes permettant de répondre à ces dommages. Ces voies, appelées voies des gènes suppresseurs de tumeurs, permettent leur prise en charge afin de diminuer leurs possibles impacts délétères. Parmi les réponses cellulaires qu'elles médient, on retrouve le déclenchement de mécanismes de réparation de l'ADN (*Caretakers*), la modulation de l'environnement et de l'interaction avec celui-ci (*landscapers*) et l'arrêt du cycle cellulaire (*Gatekeepers*) (21, 22). Dans l'éventualité d'un préjudice trop important, la cellule enclenche des mécanismes comme l'apoptose et la sénescence pour éviter la propagation de cellules anormales (19, 62). La sénescence est un mécanisme complexe ayant comme conséquence plusieurs phénotypes. On retrouve ainsi le SASP, le SAPD et plus pertinemment le SARD comme caractéristiques de la sénescence induite par l'activation d'oncogène (62, 72, 73). Les ribosomes, à l'aide de divers facteurs de traduction, dirigent la synthèse des protéines. Malgré une fidélité associée à la traduction majoritairement haute, il est possible d'y retrouver certaines incohérences. Les erreurs traditionnelles sont des évènements généralement délétères survenant à des fréquences variables. Certains organismes ont cependant, au cours de l'évolution, développé des mécanismes permettant de réguler la survenue des erreurs de traduction et d'en tirer avantage.

Dans ce mémoire, nous nous sommes intéressés au manque de fidélité de terminaison de la traduction, connue sous le nom de translecture du codon d'arrêt, dans une situation de sénescence cellulaire. Les résultats présentés mettent de l'avant la présence d'un nouveau rôle de la sénescence dans le contrôle du *readthrough.* D'une part, l'induction de la sénescence par divers mécanismes génère une diminution significative de la translecture traductionnelle du ribosome. La sénescence induit même une réduction de l'activité pro-readthrough de composés chimiques régulièrement utilisés pour induire le phénomène. D'autre part, la voie RB semble essentielle dans la limitation du TR, suggérant un nouveau rôle *caretaker* de cette voie. En outre, nous avons observé que le contournement de la sénescence, concomitant à une transformation maligne, induit plutôt une

augmentation significative de la translecture du ribosome. Finalement, le traitement utilisant un inhibiteur de CDK4 a permis de réintroduire ces cellules en arrêt cellulaire et de mener le TR à un niveau inférieur.

3.1 La sénescence limite la translecture du codon d'arrêt

La sénescence s'impose comme l'une des dernières barrières de défense empêchant la transformation cellulaire (58, 62, 65). Il existe une grande hétérogénéité quant à la réponse en fonction de l'inducteur, du type cellulaire et des antécédents cellulaires (69). Malgré cette présentation hétérogène, les effecteurs de la sénescence visent au blocage des outils moléculaires de la tumorigenèse par une reprogrammation transcriptionnelle de grande envergure. Dans tous les cas, la sénescence se caractérise par un mécanisme antitumoral arrêtant efficacement la progression de cellules malignes en induisant la sortie « permanente » du cycle cellulaire (58, 62, 65). Plus récemment, les recherches ont montré une reprogrammation du protéome par le SAPD, ainsi qu'une perturbation de la ribogenèse (SARD) (72, 73). Concernant la traduction, peu de données sont présentes à ce sujet. Ici, nous avons observé que l'efficacité de la terminaison était améliorée après l'induction de la sénescence, démontrant un tout nouveau phénotype de la sénescence cellulaire.

Nous avons pris un soin particulier à confirmer que la diminution du TR ne dépendait pas du type de sénescence induit. Dans le cas contraire, il aurait pu s'agir d'une conséquence spécifique à l'inducteur et non d'une réponse des effecteurs de la sénescence. Afin d'éliminer tout doute, nous avons confirmé ce phénotype dans plusieurs contextes d'induction de la sénescence notamment par l'activation de l'oncogène RAS, le suppresseur de tumeurs *nuclear body scaffold* (PML), l'inhibition de CDK4 ou la chimiothérapie. Ils ont tous montré une diminution significative du TR. Parallèlement, nous avons également montré que sa diminution ne dépendait pas du type cellulaire ou encore du contexte génétique puisque deux lignées cellulaires cancéreuses (PC-3 et MDA.MB.231) ont démontré des résultats semblables. De surcroît, nous avons observé que la sénescence parvenait à réduire le TR même en présence d'un traitement d'aminoglycoside stimulant ce dernier.

De plus, comme rapporté dans ce mémoire, le contexte du codon d'arrêt est grandement impliqué dans l'efficacité de la terminaison (108, 134, 141, 147, 161). Pour compenser les diverses variations dépendantes du contexte, l'effet de la sénescence a été démontré en utilisant des

rapporteurs doubles luciférases ayant différents contextes de terminaison stimulant ou non le TR. Ainsi, nous démontrons que la translecture d'un contexte commun « UGA » ou d'un contexte de cibles connues (AQP4) (129) ou identifiées comme stimulant le TR (p. ex.VASP) (tableau 4) est réduite en sénescence cellulaire. L'utilisation de constructions artificielles telle que les doubles essais luciférase, implique toujours un risque quant à la possible transposition du concept présenté à des conditions endogènes. Afin d'établir plus éloquemment le lien entre la sénescence et une diminution de TR, nous avons montré de manière endogène que la sénescence était en mesure de réduire l'expression d'AGO1x, l'isoforme d'AGO1 généré par TR (143).

Il est communément admis que les dommages à l'ADN et les mutations en découlant résultent en l'initiation de la tumorigenèse ainsi qu'à la propagation des tumeurs (162). Cependant, les dernières recherches ont supposé que le cancer pourrait tirer avantage d'une plasticité traductionnelle lors de sa progression et dans l'acquisition de résistances (155). De manière semblable à ce qui a été observé chez certains organismes, le TR pourrait apporter un avantage dans l'évolution maligne des tumeurs (131). Dans cet ordre d'idée et en accord avec les résultats présentés, nous proposons que la diminution de TR observée en contexte de sénescence soit un nouveau mécanisme antitumoral. Une terminaison plus efficace diminuerait la possibilité de produire des isoformes ayant une localisation inusuelle ou des fonctions oncogéniques. L'exemple d'AGO1x en est un, montrant qu'une diminution de TR résulterait en la diminution de la prolifération cancéreuse, comme il a été démontré lors de la délétion spécifique d'AGO1x (143).

Très peu d'informations sont connues quant aux gènes pouvant acquérir des propriétés oncogènes lors de leur élongation en C-terminal. Dans cet ouvrage (article 1), nous présentons une liste de cibles potentielles du TR ayant été identifiées par analyses bio-informatiques (tableau 4). Il a pu être observé que certaines d'entre elles sont surexprimées en contexte de cancer, notamment *Vasodilator-Stimulated Phosphoprotein* (VASP), Aspartate β-hydroxylase (ASPH) et Hepsin (HPN) (163-165). La présence d'isoformes allongés en C-terminal nécessite cependant d'être confirmée, mais pourrait révéler de nouvelles protéines oncogènes.

Au niveau moléculaire, l'évolution d'un organisme se fait au sein d'une population ayant acquis un nouveau trait favorisant sa survie dans l'environnement (118, 166). Ces nouveaux traits sont générés de manière aléatoire par des mutations qui s'avèreront bénéfiques. Afin de générer un nouveau groupe fonctionnel, tel qu'un pont disulfure, un gène nécessitera de multiples mutations.

Le mécanisme de « Look-ahead » propose donc que les erreurs de transcription et de traduction puissent permettre l'introduction de mutations en deux temps (166). Une première mutation non bénéfique pourrait survenir en C-terminal où le faible taux de TR permettrait à celle-ci de rester silencieuse et de se propager dans la population. Cela se produirait jusqu'à la survenue plus tardive d'une deuxième mutation complémentaire, apportant un nouveau trait bénéfique, menant à la solidification des deux mutations dans le génome. Dans un contexte de cancer, où les cellules ont une instabilité génomique favorisant l'apparition de mutations, ce genre de mécanisme évolutif pourrait s'effectuer de manière accélérée forçant l'apparition de nouveaux traits adaptatifs.

3.2 La voie RB régule majoritairement la réduction du TR en sénescence

Lors de l'induction de la sénescence, un large éventail d'effecteurs est induit afin de médier le phénotype de sénescence. Il est cependant connu que dans la majorité des cas, les voies des gènes suppresseurs de tumeurs p53 et RB sont activées et orchestrent de manière directe ou indirecte les corollaires de la sénescence (58, 62, 65). La littérature a déjà révélé l'implication de p53 dans le contrôle de la fidélité traductionnelle dans les cancers (167). De plus, la transformation cellulaire médiée par SV40, encodant pour de larges antigènes T ciblant RB et p53 (168), résulte en un niveau d'erreurs traductionnelles plus élevé (169).

Contrairement aux expériences de Marcel et ses collègues (167), l'inhibition de p53 seul par E6 a démontré peu de résultats quant à la capacité de TR, mais a mis en évidence un faible effet lorsque couplé à l'inhibition de RB par E7. La réduction de TR lors de l'induction de la sénescence par chimiothérapie dans des cellules PC-3, ayant p53 muté, a confirmé le faible rôle de p53 dans la réduction du TR dans nos conditions expérimentales. Ultérieurement, nous avons cherché à confirmer l'implication de RB en utilisant plusieurs modalités ciblant cette voie (figure 11 J). Les résultats ont convergé de manière à proposer la voie RB comme régulateur majeur, suggérant un nouveau rôle *caretaker* de cette voie suppresseur de tumeurs.

Le mécanisme par lequel RB modulerait le TR reste toutefois à découvrir. Il a été observé que RB pourrait réprimer l'expression de l'ARN pol III, résultant en une diminution de l'expression des ARNt (170). Conséquemment, la diminution d'ARNt pourrait induire moins de

compétition entre les nc-ARNt et l'eRF1/eRF3, stimulant ainsi une meilleure efficacité de terminaison.

D'autres mécanismes, associés ou non à RB, peuvent être proposés. Par exemple, d'une manière semblable à l'ARN pol III, RB pourrait réprimer directement ou indirectement d'autres gènes associés au TR. En effet, comme mentionnés au chapitre 1, les facteurs de traduction peuvent avoir un effet sur la fidélité traductionnelle. En outre, les facteurs eEF1Bβ et eEF1Bα sont tous les deux surexprimés lors de cancer alors qu'ils sont réprimés en sénescence (171). La mutation d'EF-1β (eEF1B) a quant à elle montré une fidélité de traduction augmentée notamment à la terminaison (172). D'un autre côté, les études montrent qu'eIF3k, une sous-unité d'eIF3, et probablement eIF4E ainsi que d'autres facteurs de traduction peuvent être séquestrés au sein des corps PML. Ces corps nucléaires composés de la protéine *promyelocytic leukemia* (PML) sont notamment impliqués dans la réponse antivirale, le DDR et l'apoptose médiée par p53 (173). Comme mentionné plus haut, eIF3 semble promouvoir le TR et sa séquestration pourrait limiter sa compétition avec la terminaison (113).De plus, notre laboratoire a précédemment montré que les corps PML séquestraient E2F lié à RB (174). Une synergie entre ces séquestrations pourrait d'ailleurs expliquer la forte réduction de TR observé lors de la sénescence induite par PML (figure 8).

Finalement, il a été brièvement discuté dans ce mémoire que la composition protéique et les modifications ribosomales peuvent moduler l'activité du ribosome (98). Récemment, Ruggero et ses collègues ont démontré que la perte de SNORA24, un snoARN médiant la pseudouridylation de l'ARNr, en sénescence induite par RAS menait à une perturbation de la sélection d'AA-ARNt causant une faible fidélité traductionnelle et un TR augmenté (175). Le SARD observé en sénescence pourrait aussi contribuer à l'élaboration de ribosomes «antitumoraux» favorisant une fidélité traductionnelle (72). Bien que cela n'explique pas la diminution de TR dans notre modèle expérimental, de manière générale en sénescence, l'implication de p53 dans le transport des composantes ribosomales ainsi que dans la traduction des ARNr pourrait aider à la génération de ribosomes plus fidèles (81, 82).

3.3 Le contournement de la sénescence induit une fréquence augmentée de translecture traductionnelle

La sénescence se caractérise comme étant un arrêt permanent et irréversible de la prolifération (58, 62, 65). Cependant, certaines cellules par des mécanismes encore peu compris parviennent à sortir de la sénescence. Les cellules cancéreuses ou précancéreuses y parvenant, bénéficieraient de la reprogrammation associée à la sénescence, ce qui leur permettrait d'acquérir un potentiel d'agressivité plus élevé qu'initialement (176).

De manière similaire, nos travaux montrent qu'à la suite du contournement de la sénescence, l'efficacité de terminaison est réduite par rapport à celle d'une cellule normale. En d'autres termes, non seulement l'inhibition du TR induite par la sénescence n'est plus présente, mais la machinerie traductionnelle de la cellule à nouveau prolifération a davantage de chance d'ignorer le codon d'arrêt et de poursuivre la traduction dans la région 3'UTR. Par conséquent, si notre proposition s'avère exacte, ce TR augmenté pourrait expliquer en partie les traits agressifs des cellules cancéreuses ayant contourné la sénescence en contribuant à l'expansion du protéome cellulaire.

Inversement, le traitement avec un inhibiteur de CDK4, le palbociblib, a permis de réinduire un arrêt du cycle cellulaire chez les cellules ayant échappé à la sénescence et de rétablir un niveau de translecture inférieur. Si la plasticité conférée par le *readthrough* favorise la progression tumorale, ce résultat propose une utilité thérapeutique des agents réduisant le TR via la voie RB.

Comme mentionné, les mécanismes médiant le *by-pass* de la sénescence ne sont pas encore totalement compris. Nonobstant, il serait possible qu'une plasticité traductionnelle puisse favoriser ce phénomène et que le TR augmenté en soit, du moins partiellement, la cause. Supportant cette hypothèse, l'expression des ARNt ligases, responsables de $ARNt^{Leu\text{-}CAA}$ et $ARNt^{Tyr\text{-}GTA}$, ce dernier étant associé à l'induction de TR (150), était nécessaire à l'échappement de la sénescence (177). Pour confirmer que l'augmentation du TR puisse favoriser la sortie de la sénescence, nous avons tenté de traiter des populations sénescentes avec un aminoglycoside (gentamicine) afin de tester l'éventualité d'une possible augmentation de la capacité d'échappement de ces cellules. Les résultats ont été, cependant, peu concluants [résultats non présentés dans ce mémoire]. Certes, la gentamicine est un outil utile pour l'étude du TR, néanmoins, elle a aussi été montrée comme ayant

des effets cytotoxiques et induisant un stress sur le réticulum endoplasmique (178). Dans le contexte où il est souhaité de favoriser la sortie d'un mécanisme réagissant au stress cellulaire, un traitement ciblant uniquement le TR serait probablement plus approprié.

Chapitre 4 : Conclusion

La recherche présentée dans ce mémoire de maitrise contribue à approfondir nos connaissances sur les mécanismes effecteurs de la sénescence contribuant à limiter la progression tumorale. Plus précisément, nous nous sommes attardés au phénomène de régulation de la fidélité traductionnelle qui, si mal régulée, pourrait avantager la tumorigenèse.

Ici, nous avons décrit un tout nouveau rôle de la sénescence dans la régulation du TR. En effet, nous avons montré que l'induction de la sénescence par différentes causes et dans plusieurs lignées cellulaires, transformées ou non, entraine une réduction significative du TR. Par ailleurs, cette réduction a été démontrée dans divers contextes de terminaison artificiels ainsi qu'endogènes. De plus, ce phénomène parvient aussi à réduire le TR induit par des agents le stimulant. Inversement, nous avons mis de l'avant que l'échappement de la sénescence était associé avec une augmentation du TR et que, suivant un traitement d'inhibiteur de CDK4, nous étions en mesure de rétablir la sénescence et une haute-fidélité de terminaison. En s'intéressant au mécanisme, nous avons montré que l'inhibition de la voie RB supprime l'effet observé. En outre, nos résultats suggèrent que ce phénomène est indépendant de p53. En somme, nous proposons que la sénescence limite la translecture traductionnelle par un mécanisme majoritairement médié par la voie du gène suppresseur de tumeurs RB.

En définitive, l'étude de la sénescence et de ses effecteurs est indispensable, puisque les mécanismes cellulaires ciblés par ce phénomène sont souvent impliqués dans la carcinogenèse. Jusqu'à présent, il y a peu d'informations disponibles sur l'implication des erreurs traductionnelles dans le développement des tumeurs. Une meilleure compréhension de ces phénomènes permettra dans un premier temps de prévenir l'apparition d'anomalies et dans un deuxième temps d'élaborer des traitements pharmacologiques ciblant ces derniers.

Chapitre 5: Références bibliographiques

1. Sender R, Fuchs S, Milo R. Revised Estimates for the Number of Human and Bacteria Cells in the Body. PLOS Biology. 2016;14(8):e1002533.
2. Vermeulen K, Van Bockstaele DR, Berneman ZN. The cell cycle: a review of regulation, deregulation and therapeutic targets in cancer. Cell Proliferation. 2003;36(3):131-49.
3. Terzi MY, Izmirli M, Gogebakan B. The cell fate: senescence or quiescence. Molecular Biology Reports. 2016;43(11):1213-20.
4. Blagosklonny MV. Cell cycle arrest is not senescence. Aging. 2011;3(2):94-101.
5. Whitfield ML, Sherlock G, Saldanha AJ, Murray JI, Ball CA, Alexander KE, et al. Identification of Genes Periodically Expressed in the Human Cell Cycle and Their Expression in Tumors. Molecular Biology of the Cell. 2002;13(6):1977-2000.
6. Otto T, Sicinski P. Cell cycle proteins as promising targets in cancer therapy. Nature Reviews Cancer. 2017;17(2):93-115.
7. Hochegger H, Takeda S, Hunt T. Cyclin-dependent kinases and cell-cycle transitions: does one fit all? Nature Reviews Molecular Cell Biology. 2008;9(11):910-6.
8. Bertoli C, Skotheim JM, De Bruin RAM. Control of cell cycle transcription during G1 and S phases. Nature Reviews Molecular Cell Biology. 2013;14(8):518-28.
9. Cuddihy AR, O'Connell MJ. Cell-cycle responses to DNA damage in G2. Int Rev Cytol. 2003;222:99-140.
10. Peters J-M. The anaphase promoting complex/cyclosome: a machine designed to destroy. Nature Reviews Molecular Cell Biology. 2006;7(9):644-56.
11. Sherr CJ, Roberts JM. CDK inhibitors: positive and negative regulators of G1-phase progression. Genes & Development. 1999;13(12):1501-12.
12. Harper JW, Elledge SJ, Keyomarsi K, Dynlacht B, Tsai LH, Zhang P, et al. Inhibition of cyclin-dependent kinases by p21. Molecular Biology of the Cell. 1995;6(4):387-400.
13. Toyoshima H, Hunter T. p27, a novel inhibitor of G1 cyclin-Cdk protein kinase activity, is related to p21. Cell. 1994;78(1):67-74.
14. Lacy ER, Wang Y, Post J, Nourse A, Webb W, Mapelli M, et al. Molecular Basis for the Specificity of p27 Toward Cyclin-dependent Kinases that Regulate Cell Division. Journal of Molecular Biology. 2005;349(4):764-73.
15. Nan. p57: A multifunctional protein in cancer (Review). International Journal of Oncology. 2010;36(6).
16. Gladyshev VN. On the cause of aging and control of lifespan. BioEssays. 2012;34(11):925-9.
17. Gladyshev VN. Aging: progressive decline in fitness due to the rising deleteriome adjusted by genetic, environmental, and stochastic processes. Aging Cell. 2016;15(4):594-602.
18. Hanahan D, Robert. Hallmarks of Cancer: The Next Generation. Cell. 2011;144(5):646-74.
19. Kontomanolis EN, Koutras A, Syllaios A, Schizas D, Mastoraki A, Garmpis N, et al. Role of Oncogenes and Tumor-suppressor Genes in Carcinogenesis: A Review. Anticancer Research. 2020;40(11):6009-15.

20. Vogelstein B, Kinzler KW. Cancer genes and the pathways they control. Nature Medicine. 2004;10(8):789-99.
21. Kinzler KW, Vogelstein B. Gatekeepers and caretakers. Nature. 1997;386(6627):761-3.
22. Macleod K. Tumor suppressor genes. Curr Opin Genet Dev. 2000;10(1):81-93.
23. Kinzler KW, Vogelstein B. Landscaping the cancer terrain. Science (New York, NY). 1998;280(5366):1036-7.
24. Bissell MJ, Radisky D. Putting tumours in context. Nature Reviews Cancer. 2001;1(1):46-54.
25. Galicia VA, He L, Dang H, Kanel G, Vendryes C, French BA, et al. Expansion of Hepatic Tumor Progenitor Cells in Pten-Null Mice Requires Liver Injury and Is Reversed by Loss of AKT2. Gastroenterology. 2010;139(6):2170-82.
26. Luo X, Liao R, Hanley KL, Zhu HH, Malo KN, Hernandez C, et al. Dual Shp2 and Pten Deficiencies Promote Non-alcoholic Steatohepatitis and Genesis of Liver Tumor-Initiating Cells. Cell Rep. 2016;17(11):2979-93.
27. Perl A-K, Wilgenbus P, Dahl U, Semb H, Christofori G. A causal role for E-cadherin in the transition from adenoma to carcinoma. Nature. 1998;392(6672):190-3.
28. Levitt NC, Hickson ID. Caretaker tumour suppressor genes that defend genome integrity. Trends in Molecular Medicine. 2002;8(4):179-86.
29. Weber AM, Ryan AJ. ATM and ATR as therapeutic targets in cancer. Pharmacology & Therapeutics. 2015;149:124-38.
30. Teng L-S, Zheng Y, Wang H-H. BRCA1/2 associated hereditary breast cancer. Journal of Zhejiang University SCIENCE B. 2008;9(2):85-9.
31. Dowty J, Win A, Buchanan D, Macinnis R, Lindor N, Thibodeau S, et al. Substantial unexplained variation in cancer risks for MLH1 and MSH2 mutation carriers. Hereditary Cancer in Clinical Practice. 2012;10(S2).
32. Kinzler KW, Vogelstein B. Lessons from Hereditary Colorectal Cancer. Cell. 1996;87(2):159-70.
33. Brady CA, Attardi LD. p53 at a glance. Journal of Cell Science. 2010;123(15):2527-32.
34. Nag S, Qin J, Srivenugopal KS, Wang M, Zhang R. The MDM2-p53 pathway revisited. J Biomed Res. 2013;27(4):254-71.
35. Lakin ND, Jackson SP. Regulation of p53 in response to DNA damage. Oncogene. 1999;18(53):7644-55.
36. Chen J. The Cell-Cycle Arrest and Apoptotic Functions of p53 in Tumor Initiation and Progression. Cold Spring Harb Perspect Med. 2016;6(3):a026104.
37. Orlic-Milacic M. TP53 Regulates Transcription of DNA Repair Genes. Reactome - a curated knowledgebase of biological pathways. 2015;55.
38. Liu J, Zhang C, Hu W, Feng Z. Tumor suppressor p53 and metabolism. Journal of Molecular Cell Biology. 2019;11(4):284-92.
39. White E. Autophagy and p53. Cold Spring Harbor Perspectives in Medicine. 2016;6(4):a026120.
40. Dick FA, Rubin SM. Molecular mechanisms underlying RB protein function. Nature Reviews Molecular Cell Biology. 2013;14(5):297-306.
41. Munro S, Khaire N, Inche A, Carr S, La Thangue NB. Lysine methylation regulates the pRb tumour suppressor protein. Oncogene. 2010;29(16):2357-67.

42. Markham D, Munro S, Soloway J, O'Connor DP, La Thangue NB. DNA-damage-responsive acetylation of pRb regulates binding to E2F-1. EMBO reports. 2006;7(2):192-8.
43. Inoue Y, Kitagawa M, Taya Y. Phosphorylation of pRB at Ser612 by Chk1/2 leads to a complex between pRB and E2F-1 after DNA damage. The EMBO Journal. 2007;26(8):2083-93.
44. Narita M, Nuñez S, Heard E, Narita M, Lin AW, Hearn SA, et al. Rb-Mediated Heterochromatin Formation and Silencing of E2F Target Genes during Cellular Senescence. Cell. 2003;113(6):703-16.
45. Vélez-Cruz R, Manickavinayaham S, Biswas AK, Clary RW, Premkumar T, Cole F, et al. RB localizes to DNA double-strand breaks and promotes DNA end resection and homologous recombination through the recruitment of BRG1. Genes & Development. 2016;30(22):2500-12.
46. Cook R, Zoumpoulidou G, Luczynski MT, Rieger S, Moquet J, Spanswick VJ, et al. Direct involvement of retinoblastoma family proteins in DNA repair by non-homologous end-joining. Cell Rep. 2015;10(12):2006-18.
47. White RJ. RNA polymerases I and III, growth control and cancer. Nature Reviews Molecular Cell Biology. 2005;6(1):69-78.
48. Chen WS, Alshalalfa M, Zhao SG, Liu Y, Mahal BA, Quigley DA, et al. Novel RB1-Loss Transcriptomic Signature Is Associated with Poor Clinical Outcomes across Cancer Types. Clinical Cancer Research. 2019;25(14):4290-9.
49. Campisi J. Aging, tumor suppression and cancer: high wire-act! Mechanisms of Ageing and Development. 2005;126(1):51-8.
50. Serrano M. Shifting senescence into quiescence by turning up p53. Cell Cycle. 2010;9(21):4256-7.
51. Storer M, Mas A, Robert-Moreno A, Pecoraro M, M, Valeria, et al. Senescence Is a Developmental Mechanism that Contributes to Embryonic Growth and Patterning. Cell. 2013;155(5):1119-30.
52. Muñoz-Espín D, Cañamero M, Maraver A, Gómez-López G, Contreras J, Murillo-Cuesta S, et al. Programmed Cell Senescence during Mammalian Embryonic Development. Cell. 2013;155(5):1104-18.
53. Jun J-I, Lau LF. The matricellular protein CCN1 induces fibroblast senescence and restricts fibrosis in cutaneous wound healing. Nature cell biology. 2010;12(7):676-85.
54. Demaria M, Ohtani N, Sameh, Rodier F, Toussaint W, James, et al. An Essential Role for Senescent Cells in Optimal Wound Healing through Secretion of PDGF-AA. Developmental Cell. 2014;31(6):722-33.
55. Krizhanovsky V, Yon M, Dickins RA, Hearn S, Simon J, Miething C, et al. Senescence of activated stellate cells limits liver fibrosis. Cell. 2008;134(4):657-67.
56. Acosta JC, Gil J. Senescence: a new weapon for cancer therapy. Trends Cell Biol. 2012;22(4):211-9.
57. Collado M, Serrano M. Senescence in tumours: evidence from mice and humans. Nature Reviews Cancer. 2010;10(1):51-7.
58. Collado M, Blasco MA, Serrano M. Cellular Senescence in Cancer and Aging. Cell. 2007;130(2):223-33.
59. Hayflick L, Moorhead PS. The serial cultivation of human diploid cell strains. Experimental Cell Research. 1961;25(3):585-621.

60. Hayflick L. A brief history of the mortality and immortality of cultured cells. Keio J Med. 1998;47(3):174-82.
61. Harley CB, Futcher AB, Greider CW. Telomeres shorten during ageing of human fibroblasts. Nature. 1990;345(6274):458-60.
62. McHugh D, Gil J. Senescence and aging: Causes, consequences, and therapeutic avenues. Journal of Cell Biology. 2018;217(1):65-77.
63. Campisi J, D'Adda Di Fagagna F. Cellular senescence: when bad things happen to good cells. Nature Reviews Molecular Cell Biology. 2007;8(9):729-40.
64. McHugh D, Gil J. Senescence and aging: Causes, consequences, and therapeutic avenues. J Cell Biol. 2018;217(1):65-77.
65. Salama R, Sadaie M, Hoare M, Narita M. Cellular senescence and its effector programs. Genes Dev. 2014;28(2):99-114.
66. Coppé J-P, Patil CK, Rodier F, Sun Y, Muñoz DP, Goldstein J, et al. Senescence-Associated Secretory Phenotypes Reveal Cell-Nonautonomous Functions of Oncogenic RAS and the p53 Tumor Suppressor. PLoS Biology. 2008;6(12):e301.
67. Tchkonia T, Zhu Y, Van Deursen J, Campisi J, Kirkland JL. Cellular senescence and the senescent secretory phenotype: therapeutic opportunities. Journal of Clinical Investigation. 2013;123(3):966-72.
68. Coppé J-P, Desprez P-Y, Krtolica A, Campisi J. The Senescence-Associated Secretory Phenotype: The Dark Side of Tumor Suppression. Annual Review of Pathology: Mechanisms of Disease. 2010;5(1):99-118.
69. Kirschner K, Rattanavirotkul N, Quince MF, Chandra T. Functional heterogeneity in senescence. Biochemical Society Transactions. 2020;48(3):765-73.
70. Shelton DN, Chang E, Whittier PS, Choi D, Funk WD. Microarray analysis of replicative senescence. Curr Biol. 1999;9(17):939-45.
71. Deschênes-Simard X, Lessard F, Gaumont-Leclerc MF, Bardeesy N, Ferbeyre G. Cellular senescence and protein degradation: breaking down cancer. Cell Cycle. 2014;13(12):1840-58.
72. Lessard F, Igelmann S, Trahan C, Huot G, Saint-Germain E, Mignacca L, et al. Senescence-associated ribosome biogenesis defects contributes to cell cycle arrest through the Rb pathway. Nature cell biology. 2018;20(7):789-99.
73. Deschênes-Simard X, Gaumont-Leclerc M-F, Bourdeau V, Lessard F, Moiseeva O, Forest V, et al. Tumor suppressor activity of the ERK/MAPK pathway by promoting selective protein degradation. Genes & Development. 2013;27(8):900-15.
74. D'Adda Di Fagagna F. Living on a break: cellular senescence as a DNA-damage response. Nature Reviews Cancer. 2008;8(7):512-22.
75. Di Micco R, Fumagalli M, Cicalese A, Piccinin S, Gasparini P, Luise C, et al. Oncogene-induced senescence is a DNA damage response triggered by DNA hyper-replication. Nature. 2006;444(7119):638-42.
76. Sulli G, Di Micco R, Di Fagagna FDA. Crosstalk between chromatin state and DNA damage response in cellular senescence and cancer. Nature Reviews Cancer. 2012;12(10):709-20.
77. Burns DM, Richter JD. CPEB regulation of human cellular senescence, energy metabolism, and p53 mRNA translation. Genes Dev. 2008;22(24):3449-60.

78. Ben-Shem A, Garreau de Loubresse N, Melnikov S, Jenner L, Yusupova G, Yusupov M. The structure of the eukaryotic ribosome at 3.0 Å resolution. Science (New York, NY). 2011;334(6062):1524-9.
79. Woolford JL, Jr., Baserga SJ. Ribosome biogenesis in the yeast Saccharomyces cerevisiae. Genetics. 2013;195(3):643-81.
80. Ma L, Chang N, Guo S, Li Q, Zhang Z, Wang W, et al. CSIG Inhibits PTEN Translation in Replicative Senescence. Molecular and Cellular Biology. 2008;28(20):6290-301.
81. Golomb L, Bublik DR, Wilder S, Nevo R, Kiss V, Grabusic K, et al. Importin 7 and exportin 1 link c-Myc and p53 to regulation of ribosomal biogenesis. Mol Cell. 2012;45(2):222-32.
82. Zhai W, Comai L. Repression of RNA Polymerase I Transcription by the Tumor Suppressor p53. Molecular and Cellular Biology. 2000;20(16):5930-8.
83. Payea MJ, Anerillas C, Tharakan R, Gorospe M. Translational Control during Cellular Senescence. Mol Cell Biol. 2021;41(2).
84. Moy TI, Boettner D, Rhodes JC, Silver PA, Askew DS. Identification of a role for Saccharomyces cerevisiae Cgr1p in pre-rRNA processing and 60S ribosome subunit synthesis. Microbiology. 2002;148(4):1081-90.
85. Romanova L, Grand A, Zhang L, Rayner S, Katoku-Kikyo N, Kellner S, et al. Critical role of nucleostemin in pre-rRNA processing. J Biol Chem. 2009;284(8):4968-77.
86. Calo E, Flynn RA, Martin L, Spitale RC, Chang HY, Wysocka J. RNA helicase DDX21 coordinates transcription and ribosomal RNA processing. Nature. 2015;518(7538):249-53.
87. Tafforeau L, Zorbas C, Langhendries J-L, Mullineux S-T, Stamatopoulou V, Mullier R, et al. The Complexity of Human Ribosome Biogenesis Revealed by Systematic Nucleolar Screening of Pre-rRNA Processing Factors. Molecular Cell. 2013;51(4):539-51.
88. Srivastava L, Lapik YR, Wang M, Pestov DG. Mammalian DEAD box protein Ddx51 acts in 3' end maturation of 28S rRNA by promoting the release of U8 snoRNA. Mol Cell Biol. 2010;30(12):2947-56.
89. Abdelmohsen K, Gorospe M. RNA-binding protein nucleolin in disease. RNA Biology. 2012;9(6):799-808.
90. Wu J, Zhang Y, Wang Y, Kong R, Hu L, Schuele R, et al. Transcriptional Repressor NIR Functions in the Ribosome RNA Processing of Both 40S and 60S Subunits. PLoS ONE. 2012;7(2):e31692.
91. Tsai YT, Lin CI, Chen HK, Lee KM, Hsu CY, Yang SJ, et al. Chromatin tethering effects of hNopp140 are involved in the spatial organization of nucleolus and the rRNA gene transcription. J Biomed Sci. 2008;15(4):471-86.
92. Utama B, Kennedy D, Ru K, Mattick JS. Isolation and characterization of a new nucleolar protein, Nrap, that is conserved from yeast to humans. Genes Cells. 2002;7(2):115-32.
93. Lafontaine DL, Tollervey D. Synthesis and assembly of the box C+D small nucleolar RNPs. Mol Cell Biol. 2000;20(8):2650-9.
94. Lindström MS. NPM1/B23: A Multifunctional Chaperone in Ribosome Biogenesis and Chromatin Remodeling. Biochemistry Research International. 2011;2011:1-16.
95. Artero-Castro A, Kondoh H, Fernández-Marcos PJ, Serrano M, Ramón y Cajal S, Lleonart ME. Rplp1 bypasses replicative senescence and contributes to transformation. Exp Cell Res. 2009;315(8):1372-83.

96. Qi Y, Li X, Chang C, Xu F, He Q, Zhao Y, et al. Ribosomal protein L23 negatively regulates cellular apoptosis via the RPL23/Miz-1/c-Myc circuit in higher-risk myelodysplastic syndrome. Scientific Reports. 2017;7(1).
97. Meng L, Yasumoto H, Tsai RYL. Multiple controls regulate nucleostemin partitioning between nucleolus and nucleoplasm. Journal of Cell Science. 2006;119(24):5124-36.
98. Guo H. Specialized ribosomes and the control of translation. Biochem Soc Trans. 2018;46(4):855-69.
99. Buttgereit F, Brand MD. A hierarchy of ATP-consuming processes in mammalian cells. Biochemical Journal. 1995;312(1):163-7.
100. Russell JB, Cook GM. Energetics of bacterial growth: balance of anabolic and catabolic reactions. Microbiol Rev. 1995;59(1):48-62.
101. Brandman O, Hegde RS. Ribosome-associated protein quality control. Nature Structural & Molecular Biology. 2016;23(1):7-15.
102. Gloge F, Becker AH, Kramer G, Bukau B. Co-translational mechanisms of protein maturation. Current Opinion in Structural Biology. 2014;24:24-33.
103. Hellen CUT. Translation Termination and Ribosome Recycling in Eukaryotes. Cold Spring Harbor Perspectives in Biology. 2018;10(10):a032656.
104. Brown A, Shao S, Murray J, Hegde RS, Ramakrishnan V. Structural basis for stop codon recognition in eukaryotes. Nature. 2015;524(7566):493-6.
105. Cheng Z, Saito K, Pisarev AV, Wada M, Pisareva VP, Pestova TV, et al. Structural insights into eRF3 and stop codon recognition by eRF1. Genes & Development. 2009;23(9):1106-18.
106. McCaughan KK, Brown CM, Dalphin ME, Berry MJ, Tate WP. Translational termination efficiency in mammals is influenced by the base following the stop codon. Proceedings of the National Academy of Sciences. 1995;92(12):5431-5.
107. Cridge AG, Crowe-Mcauliffe C, Mathew SF, Tate WP. Eukaryotic translational termination efficiency is influenced by the 3’ nucleotides within the ribosomal mRNA channel. Nucleic Acids Research. 2018;46(4):1927-44.
108. Cassan M, Rousset JP. UAG readthrough in mammalian cells: effect of upstream and downstream stop codon contexts reveal different signals. BMC Mol Biol. 2001;2:3.
109. Tork S. The major 5' determinant in stop codon read-through involves two adjacent adenines. Nucleic Acids Research. 2004;32(2):415-21.
110. Jackson RJ, Hellen CUT, Pestova TV. The mechanism of eukaryotic translation initiation and principles of its regulation. Nature Reviews Molecular Cell Biology. 2010;11(2):113-27.
111. Khoshnevis S, Gross T, Rotte C, Baierlein C, Ficner R, Krebber H. The iron–sulphur protein RNase L inhibitor functions in translation termination. EMBO reports. 2010;11(3):214-9.
112. Annibaldis G, Domanski M, Dreos R, Contu L, Carl S, Kläy N, et al. Readthrough of stop codons under limiting ABCE1 concentration involves frameshifting and inhibits nonsense-mediated mRNA decay. Nucleic Acids Research. 2020;48(18):10259-79.
113. Beznosková P, Wagner S, Jansen ME, Tobias, Valášek LS. Translation initiation factor eIF3 promotes programmed stop codon readthrough. Nucleic Acids Research. 2015;43(10):5099-111.
114. Schuller AP, Wu CC-C, Dever TE, Buskirk AR, Green R. eIF5A Functions Globally in Translation Elongation and Termination. Molecular Cell. 2017;66(2):194-205.e5.

115. Pelechano V, Alepuz P. eIF5A facilitates translation termination globally and promotes the elongation of many non polyproline-specific tripeptide sequences. Nucleic Acids Research. 2017;45(12):7326-38.
116. Mikhailova T, Shuvalova E, Ivanov A, Susorov D, Shuvalov A, Kolosov PM, et al. RNA helicase DDX19 stabilizes ribosomal elongation and termination complexes. Nucleic Acids Research. 2017;45(3):1307-18.
117. Kramer EB, Farabaugh PJ. The frequency of translational misreading errors in E. coli is largely determined by tRNA competition. RNA. 2006;13(1):87-96.
118. Allan Drummond D, Wilke CO. The evolutionary consequences of erroneous protein synthesis. Nature Reviews Genetics. 2009;10(10):715-24.
119. Ibba M, Söll D. Aminoacyl-tRNA Synthesis. Annual Review of Biochemistry. 2000;69(1):617-50.
120. Kohanski MA, Dwyer DJ, Wierzbowski J, Cottarel G, Collins JJ. Mistranslation of membrane proteins and two-component system activation trigger antibiotic-mediated cell death. Cell. 2008;135(4):679-90.
121. Farabaugh PJ. PROGRAMMED TRANSLATIONAL FRAMESHIFTING. Annual Review of Genetics. 1996;30(1):507-28.
122. Blinkowa AL, Walker JR. Programmed ribosomal frameshifting generates theEscherichia coliDNA polymerase III γ subunit from within the τ subunit reading frame. Nucleic Acids Research. 1990;18(7):1725-9.
123. Matsufuji S, Matsufuji T, Miyazaki Y, Murakami Y, Atkins JF, Gesteland RF, et al. Autoregulatory frameshifting in decoding mammalian ornithine decarboxylase antizyme. Cell. 1995;80(1):51-60.
124. Jacks T, Power MD, Masiarz FR, Luciw PA, Barr PJ, Varmus HE. Characterization of ribosomal frameshifting in HIV-1 gag-pol expression. Nature. 1988;331(6153):280-3.
125. Kelly JA, Woodside MT, Dinman JD. Programmed -1 Ribosomal Frameshifting in coronaviruses: A therapeutic target. Virology. 2021;554:75-82.
126. Hofhuis J, Schueren F, Nötzel C, Lingner T, Gärtner J, Jahn O, et al. The functional readthrough extension of malate dehydrogenase reveals a modification of the genetic code. Open Biology. 2016;6(11):160246.
127. Stiebler AC, Freitag J, Schink KO, Stehlik T, Tillmann BAM, Ast J, et al. Ribosomal Readthrough at a Short UGA Stop Codon Context Triggers Dual Localization of Metabolic Enzymes in Fungi and Animals. PLoS Genetics. 2014;10(10):e1004685.
128. Wickner RB, Masison DC, Edskes HK. [PSI] and [URE3] as yeast prions. Yeast. 1995;11(16):1671-85.
129. De Bellis M, Pisani F, Mola MG, Rosito S, Simone L, Buccoliero C, et al. Translational readthrough generates new astrocyte AQP4 isoforms that modulate supramolecular clustering, glial endfeet localization, and water transport. Glia. 2017;65(5):790-803.
130. Tyedmers J, Madariaga ML, Lindquist S. Prion Switching in Response to Environmental Stress. PLoS Biology. 2008;6(11):e294.
131. Fan Y, Evans CR, Barber KW, Banerjee K, Weiss KJ, Margolin W, et al. Heterogeneity of Stop Codon Readthrough in Single Bacterial Cells and Implications for Population Fitness. Molecular Cell. 2017;67(5):826-36.e5.

132. Sharma J, Du M, Wong E, Mutyam V, Li Y, Chen J, et al. A small molecule that induces translational readthrough of CFTR nonsense mutations by eRF1 depletion. Nature Communications. 2021;12(1).
133. Hoffman EP, Bronson A, Levin AA, Takeda SI, Yokota T, Baudy AR, et al. Restoring Dystrophin Expression in Duchenne Muscular Dystrophy Muscle. The American Journal of Pathology. 2011;179(1):12-22.
134. Dabrowski M, Bukowy-Bieryllo Z, Zietkiewicz E. Translational readthrough potential of natural termination codons in eucaryotes – The impact of RNA sequence. RNA Biology. 2015;12(9):950-8.
135. Dunn JG, Foo CK, Belletier NG, Gavis ER, Weissman JS. Ribosome profiling reveals pervasive and regulated stop codon readthrough in Drosophila melanogaster. eLife. 2013;2.
136. Pelham HR. Leaky UAG termination codon in tobacco mosaic virus RNA. Nature. 1978;272(5652):469-71.
137. Wills NM, Gesteland RF, Atkins JF. Evidence that a downstream pseudoknot is required for translational read-through of the Moloney murine leukemia virus gag stop codon. Proceedings of the National Academy of Sciences. 1991;88(16):6991-5.
138. Schueren F, Thoms S. Functional Translational Readthrough: A Systems Biology Perspective. PLOS Genetics. 2016;12(8):e1006196.
139. Freitag J, Ast J, Bölker M. Cryptic peroxisomal targeting via alternative splicing and stop codon read-through in fungi. Nature. 2012;485(7399):522-5.
140. Geoffrey MC. The Cell: A Molecular Approach. 2nd edition. In: Associates S, editor. The Cell: A Molecular Approach 2nd edition. Sunderland (MA)2000.
141. Loughran G, Chou MY, Ivanov IP, Jungreis I, Kellis M, Kiran AM, et al. Evidence of efficient stop codon readthrough in four mammalian genes. Nucleic Acids Res. 2014;42(14):8928-38.
142. Schueren F, Lingner T, George R, Hofhuis J, Dickel C, Gärtner J, et al. Peroxisomal lactate dehydrogenase is generated by translational readthrough in mammals. eLife. 2014;3.
143. Ghosh S, Guimaraes JC, Lanzafame M, Schmidt A, Syed AP, Dimitriades B, et al. Prevention of dsRNA-induced interferon signaling by AGO1x is linked to breast cancer cell proliferation. The EMBO Journal. 2020;39(18).
144. Sandeepa, Alka, William, Fan Y, Vasu K, Lindner D, et al. Programmed Translational Readthrough Generates Antiangiogenic VEGF-Ax. Cell. 2014;157(7):1605-18.
145. Palazzo C, Abbrescia P, Valente O, Nicchia GP, Banitalebi S, Amiry-Moghaddam M, et al. Tissue Distribution of the Readthrough Isoform of AQP4 Reveals a Dual Role of AQP4ex Limited to CNS. International Journal of Molecular Sciences. 2020;21(4):1531.
146. Xin H, Zhong C, Nudleman E, Ferrara N. Evidence for Pro-angiogenic Functions of VEGF-Ax. Cell. 2016;167(1):275-84.e6.
147. Namy O, Hatin I, Rousset JP. Impact of the six nucleotides downstream of the stop codon on translation termination. EMBO Rep. 2001;2(9):787-93.
148. Roy B, Leszyk JD, Mangus DA, Jacobson A. Nonsense suppression by near-cognate tRNAs employs alternative base pairing at codon positions 1 and 3. Proceedings of the National Academy of Sciences. 2015;112(10):3038-43.
149. Blanchet S, Cornu D, Argentini M, Namy O. New insights into the incorporation of natural suppressor tRNAs at stop codons in Saccharomyces cerevisiae. Nucleic Acids Research. 2014;42(15):10061-72.

150. Beznosková P, Pavlíková Z, Zeman J, Colin, Valášek LS. Yeast applied readthrough inducing system (YARIS): an invivo assay for the comprehensive study of translational readthrough. Nucleic Acids Research. 2019;47(12):6339-50.
151. Mort M, Ivanov D, Cooper DN, Chuzhanova NA. A meta-analysis of nonsense mutations causing human genetic disease. Human Mutation. 2008;29(8):1037-47.
152. Chang Y-F, Imam JS, Wilkinson MF. The Nonsense-Mediated Decay RNA Surveillance Pathway. Annual Review of Biochemistry. 2007;76(1):51-74.
153. Jia J, Werkmeister E, Gonzalez-Hilarion S, Leroy C, Gruenert DC, Lafont F, et al. PTC readthrough in human cells occurs in novel cytoplasmic foci and requires UPF proteins. Journal of Cell Science. 2017;130(18):3009-22.
154. Dahabieh MS, Di Pietro E, Jangal M, Goncalves C, Witcher M, Braverman NE, et al. Peroxisomes and cancer: The role of a metabolic specialist in a disease of aberrant metabolism. Biochimica et Biophysica Acta (BBA) - Reviews on Cancer. 2018;1870(1):103-21.
155. Fabbri L, Chakraborty A, Robert C, Vagner S. The plasticity of mRNA translation during cancer progression and therapy resistance. Nature Reviews Cancer. 2021;21(9):558-77.
156. Santos M, Fidalgo A, Varanda AS, Oliveira C, Santos MAS. tRNA Deregulation and Its Consequences in Cancer. Trends in Molecular Medicine. 2019;25(10):853-65.
157. Jia L, Yang T, Gu X, Zhao W, Tang Q, Wang X, et al. Translation elongation factor eEF1Bα is identified as a novel prognostic marker of gastric cancer. International Journal of Biological Macromolecules. 2019;126:345-51.
158. Kampen KR, Sulima SO, De Keersmaecker K. Rise of the specialized onco-ribosomes. Oncotarget. 2018;9(81):35205-6.
159. Sulima SO, Patchett S, Advani VM, De Keersmaecker K, Johnson AW, Dinman JD. Bypass of the pre-60S ribosomal quality control as a pathway to oncogenesis. Proceedings of the National Academy of Sciences. 2014;111(15):5640-5.
160. Del Toro N, Lessard F, Bouchard J, Mobasheri N, Guillon J, Igelmann S, et al. Cellular Senescence limits Translational Readthrough. Biology Open. 2021.
161. Kleppe AS, Bornberg-Bauer E. Robustness by intrinsically disordered C-termini and translational readthrough. Nucleic Acids Research. 2018;46(19):10184-94.
162. Weinberg RA. The Biology of Cancer. 2ed. ed: Garland Science; 2013. 963 p.
163. Gkretsi V, Stylianou A, Stylianopoulos T. Vasodilator-Stimulated Phosphoprotein (VASP) depletion from breast cancer MDA-MB-231 cells inhibits tumor spheroid invasion through downregulation of Migfilin, β-catenin and urokinase-plasminogen activator (uPA). Experimental Cell Research. 2017;352(2):281-92.
164. Kanwal M, Smahel M, Olsen M, Smahelova J, Tachezy R. Aspartate β-hydroxylase as a target for cancer therapy. Journal of Experimental & Clinical Cancer Research. 2020;39(1).
165. Klezovitch O, Chevillet J, Mirosevich J, Roberts RL, Matusik RJ, Vasioukhin V. Hepsin promotes prostate cancer progression and metastasis. Cancer Cell. 2004;6(2):185-95.
166. Whitehead DJ, Wilke CO, Vernazobres D, Bornberg-Bauer E. The look-ahead effect of phenotypic mutations. Biology Direct. 2008;3(1):18.
167. Marcel V, Ghayad SE, Belin S, Therizols G, Morel AP, Solano-Gonzàlez E, et al. p53 acts as a safeguard of translational control by regulating fibrillarin and rRNA methylation in cancer. Cancer Cell. 2013;24(3):318-30.

168. Ahuja D, Sáenz-Robles MT, Pipas JM. SV40 large T antigen targets multiple cellular pathways to elicit cellular transformation. Oncogene. 2005;24(52):7729-45.
169. Pollard JW, Harley CB, Chamberlain JW, Goldstein S, Stanners CP. Is transformation associated with an increased error frequency in mammalian cells? J Biol Chem. 1982;257(11):5977-9.
170. Gjidoda A, Henry RW. RNA polymerase III repression by the retinoblastoma tumor suppressor protein. Biochimica et Biophysica Acta (BBA) - Gene Regulatory Mechanisms. 2013;1829(3-4):385-92.
171. Negrutskii B. Non-translational Connections of eEF1B in the Cytoplasm and Nucleus of Cancer Cells. Frontiers in Molecular Biosciences. 2020;7.
172. Carr-Schmid A, Valente L, Loik VI, Williams T, Starita LM, Kinzy TG. Mutations in Elongation Factor 1β, a Guanine Nucleotide Exchange Factor, Enhance Translational Fidelity. Molecular and Cellular Biology. 1999;19(8):5257-66.
173. Chang HR, Munkhjargal A, Kim M-J, Park SY, Jung E, Ryu J-H, et al. The functional roles of PML nuclear bodies in genome maintenance. Mutation Research/Fundamental and Molecular Mechanisms of Mutagenesis. 2018;809:99-107.
174. Vernier M, Bourdeau V, Gaumont-Leclerc MF, Moiseeva O, Bégin V, Saad F, et al. Regulation of E2Fs and senescence by PML nuclear bodies. Genes Dev. 2011;25(1):41-50.
175. McMahon M, Contreras A, Holm M, Uechi T, Forester CM, Pang X, et al. A single H/ACA small nucleolar RNA mediates tumor suppression downstream of oncogenic RAS. Elife. 2019;8.
176. Milanovic M, Fan DNY, Belenki D, Däbritz JHM, Zhao Z, Yu Y, et al. Senescence-associated reprogramming promotes cancer stemness. Nature. 2018;553(7686):96-100.
177. Guillon J, Coquelet H, Leman G, Toutain B, Petit C, Henry C, et al. tRNA biogenesis and specific aminoacyl-tRNA synthetases regulate senescence stability under the control of mTOR. PLOS Genetics. 2021;17(12):e1009953.
178. Quiros Y, Vicente-Vicente L, Morales AI, Lopez-Novoa JM, Lopez-Hernandez FJ. An Integrative Overview on the Mechanisms Underlying the Renal Tubular Cytotoxicity of Gentamicin. Toxicological Sciences. 2011;119(2):245-56.
179. Igelmann S, Lessard F, Uchenunu O, Bouchard J, Fernandez-Ruiz A, Rowell M-C, et al. A hydride transfer complex reprograms NAD metabolism and bypasses senescence. Molecular Cell. 2021;81(18):3848-65.e19.

Chapitre 6: Annexes

6.1. Annexe 1 : article 2

A hydride transfer complex reprograms NAD metabolism and bypasses senescence(179)

SebastianIgelmann[1 18] ,Frédéric Lessard[18 19] , Oro Uchenunu[23 19], Jacob Bouchard[18 19], Ana Fernandez-Ruiz[1 19], Marie-Camille Rowell[1], Stéphane Lopes-Paciencia[1], David Papadopoli[26], Aurélien Fouillen[4 18], Katia Julissa Ponce[4], Geneviève Huot[18], Lian Mignacca[18], Mehdi Benfdil[18], Paloma Kalegari1[18], Haytham M. Wahba[12,18], Jan Pencik[7, 14, 15], Nhung Vuong1, Jordan Quenneville[9], Jordan Guillon[1], Véronique Bourdeau[18], Laura Hulea[10], Etienne Gagnon[9,13], Lukas Kenner[7,8,16,17], Richard Moriggl[11], Antonio Nanci[4], Michael N. Pollak[2], James G. Omichinski[18], Ivan Topisirovic[2,3,5,6], Gerardo Ferbeyre[1,18, 20]

Affiliations :

[1] CRCHUM, 900 Saint-Denis St, Montréal, QC H2X 0A9, Canada

[2] Lady Davis Institute for Medical Research, Jewish General Hospital, Montréal, QC H3T1E2, Canada

[3] Department of Experimental Medicine, McGill University, Montreal, QC H4A3T2, Canada

[4] Faculté de médecine dentaire, Université de Montréal, Montréal, QC H3C 3J7, Canada

[5] Department of Biochemistry, McGill University, Montreal, QC H4A 3T2, Canada

[6] Gerald Bronfman Department of Oncology, McGill University, Montreal, QC H4A3T2, Canada

[7] Department of Pathology, Medical University of Vienna, Vienna, Austria

[8] Unit of Laboratory Animal Pathology, University of Veterinary Medicine Vienna, Vienna, Austria

[9] Institut de recherche en immunologie et en cancérologie (IRIC), Université de Montréal, Montréal, QC H3C 3J7, Canada

[10] Maisonneuve-Rosemont Hospital Research Centre, Montréal, QC H1T 2M4, Canada, Département de Médecine, Université de Montréal, Montréal, QC H3C 3J7, Canada

[11] Institute of Animal Breeding and Genetics, University of Veterinary Medicine Vienna, 1210 Vienna, Austria

[12] Department of Biochemistry, Faculty of Pharmacy, Beni-Suef University, Beni-Suef 62521, Egypt

[13] Département de Microbiologie, Infectiologie et Immunologie, Université de Montréal, Montréal, QC H3C 3J7, Canada

[14] Molecular and Cell Biology Laboratory, The Salk Institute for Biological Studies, La Jolla, CA 92037, USA

[15] Center for Biomarker Research in Medicine, 8010 Graz, Austria

[16] Christian Doppler Laboratory for Applied Metabolomics, Vienna, Austria

[17] CBmed GmbH - Center for Biomarker Research in Medicine, Graz, Styria, Austria

[18] Département de Biochimie et Médecine Moléculaire, Université de Montréal, Montréal, QC H3C 3J7, Canada

Author contribution:

[19] These authors contributed equally

KEYWORDS : NAD; NADPH; cellular senescence; mitochondrial dysfunction; hypoxia; MDH1; ME1; PC; metabolon; p53

6.2.1 Contribution à l'article 2

Dans le cadre de cet article, j'ai encore une fois participé à la validation et reproduction de données de l'article (figure 4 A-H et Figure S6 A-H) ainsi qu'à l'investigation. Mon implication directe à permit l'élaboration des figures suivante : figure 5 E - J, figure 6 A-G, figure S1 J-N, figure S5 A-J ainsi que la figure S8 B-C et I-R. de plus, j'ai apporté un aide à l'acquisition des données pour la figure 2 I-K et la figure 5 L-M. Finalement, j'ai participé dans le processus de publication de l'article notamment dans la révision de celui-ci. Cet article auquel je suis 3^{e} deuxième auteur est maintenant publié dans la revue *Molecular Cell.*

Molecular Cell

Article

A hydride transfer complex reprograms NAD metabolism and bypasses senescence

Graphical abstract

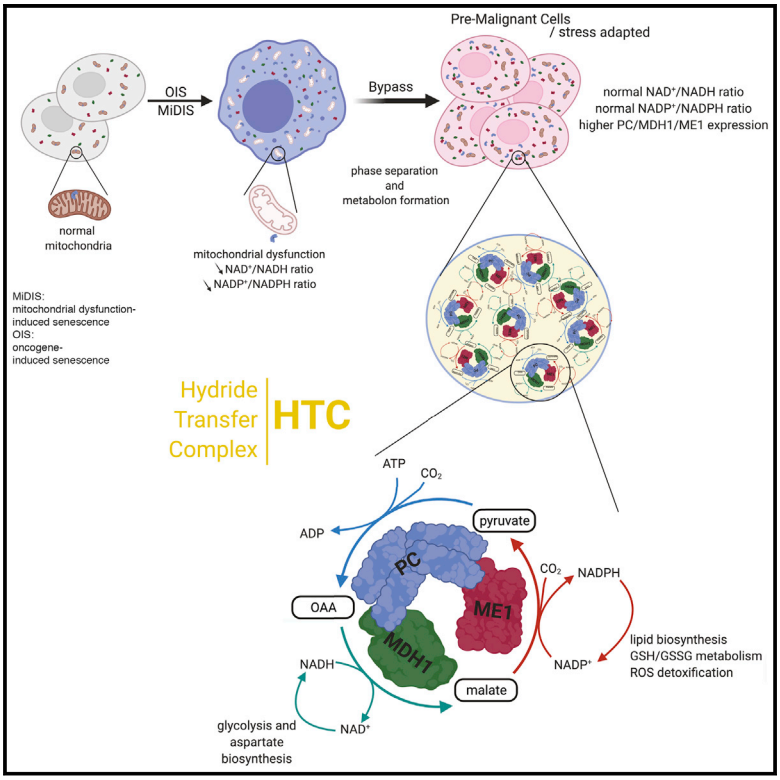

Highlights

- PC, MDH1, and ME1 form a hydride transfer complex (HTC) in the cytoplasm
- HTC transfers reducing equivalents from NADH to $NADP^+$
- HTC promotes tumor formation by bypassing senescence
- HTC confers fitness to cells under hypoxia or mitochondrial dysfunction

Authors

Sebastian Igelmann, Frédéric Lessard, Oro Uchenunu, ..., James G. Omichinski, Ivan Topisirovic, Gerardo Ferbeyre

Correspondence

ivan.topisirovic@mcgill.ca (I.T.), g.ferbeyre@umontreal.ca (G.F.)

In brief

Igelmann et al. identified a hydride transfer complex (HTC) that drives metabolic reprogramming to overcome senescence and induces tumorigenesis. HTC consists of pyruvate carboxylase, malate dehydrogenase 1 and malic enzyme 1 and catalyzes a metabolic cycle whose net effect is to supply NAD^+ and NADPH, which are key cofactors for many essential metabolic reactions.

Igelmann et al., 2021, Molecular Cell *81*, 3848–3865
September 16, 2021
https://doi.org/10.1016/j.molcel.2021.08.028

CellPress

CellPress

Molecular Cell

Article

A hydride transfer complex reprograms NAD metabolism and bypasses senescence

Sebastian Igelmann,[1,18] Frédéric Lessard,[18,19] Oro Uchenunu,[2,3,19] Jacob Bouchard,[18,19] Ana Fernandez-Ruiz,[1,19] Marie-Camille Rowell,[1] Stéphane Lopes-Paciencia,[1] David Papadopoli,[2,6] Aurélien Fouillen,[4,18] Katia Julissa Ponce,[4] Geneviève Huot,[18] Lian Mignacca,[18] Mehdi Benfdil,[18] Paloma Kalegari,[1,18] Haytham M. Wahba,[12,18] Jan Pencik,[7,14,15] Nhung Vuong,[1] Jordan Quenneville,[9] Jordan Guillon,[1] Véronique Bourdeau,[18] Laura Hulea,[10] Etienne Gagnon,[9,13] Lukas Kenner,[7,8,16,17] Richard Moriggl,[11] Antonio Nanci,[4] Michael N. Pollak,[2] James G. Omichinski,[18] Ivan Topisirovic,[2,3,5,6,*] and Gerardo Ferbeyre[1,18,20,*]

[1]CRCHUM, 900 Saint-Denis St, Montréal, QC H2X 0A9, Canada
[2]Lady Davis Institute for Medical Research, Jewish General Hospital, Montréal, QC H3T1E2, Canada
[3]Department of Experimental Medicine, McGill University, Montreal, QC H4A3T2, Canada
[4]Faculté de médecine dentaire, Université de Montréal, Montréal, QC H3C 3J7, Canada
[5]Department of Biochemistry, McGill University, Montreal, QC H4A 3T2, Canada
[6]Gerald Bronfman Department of Oncology, McGill University, Montreal, QC H4A3T2, Canada
[7]Department of Pathology, Medical University of Vienna, Vienna, Austria
[8]Unit of Laboratory Animal Pathology, University of Veterinary Medicine Vienna, Vienna, Austria
[9]Institut de recherche en immunologie et en cancérologie (IRIC), Université de Montréal, Montréal, QC H3C 3J7, Canada
[10]Maisonneuve-Rosemont Hospital Research Centre, Montréal, QC H1T 2M4, Canada, Département de Médecine, Université de Montréal, Montréal, QC H3C 3J7, Canada
[11]Institute of Animal Breeding and Genetics, University of Veterinary Medicine Vienna, 1210 Vienna, Austria
[12]Department of Biochemistry, Faculty of Pharmacy, Beni-Suef University, Beni-Suef 62521, Egypt
[13]Département de Microbiologie, Infectiologie et Immunologie, Université de Montréal, Montréal, QC H3C 3J7, Canada
[14]Molecular and Cell Biology Laboratory, The Salk Institute for Biological Studies, La Jolla, CA 92037, USA
[15]Center for Biomarker Research in Medicine, 8010 Graz, Austria
[16]Christian Doppler Laboratory for Applied Metabolomics, Vienna, Austria
[17]CBmed GmbH - Center for Biomarker Research in Medicine, Graz, Styria, Austria
[18]Département de Biochimie et Médecine Moléculaire, Université de Montréal, Montréal, QC H3C 3J7, Canada
[19]These authors contributed equally
[20]Lead contact
*Correspondence: ivan.topisirovic@mcgill.ca (I.T.), g.ferbeyre@umontreal.ca (G.F.)
https://doi.org/10.1016/j.molcel.2021.08.028

SUMMARY

Metabolic rewiring and redox balance play pivotal roles in cancer. Cellular senescence is a barrier for tumorigenesis circumvented in cancer cells by poorly understood mechanisms. We report a multi-enzymatic complex that reprograms NAD metabolism by transferring reducing equivalents from NADH to $NADP^+$. This hydride transfer complex (HTC) is assembled by malate dehydrogenase 1, malic enzyme 1, and cytosolic pyruvate carboxylase. HTC is found in phase-separated bodies in the cytosol of cancer or hypoxic cells and can be assembled *in vitro* with recombinant proteins. HTC is repressed in senescent cells but induced by p53 inactivation. HTC enzymes are highly expressed in mouse and human prostate cancer models, and their inactivation triggers senescence. Exogenous expression of HTC is sufficient to bypass senescence, rescue cells from complex I inhibitors, and cooperate with oncogenic RAS to transform primary cells. Altogether, we provide evidence for a new multi-enzymatic complex that reprograms metabolism and overcomes cellular senescence.

INTRODUCTION

Senescence is a broadly acting tumor suppressor mechanism wherein cells bearing oncogenic mutations cannot expand due to a chronic state of mitochondrial dysfunction, oxidative stress, DNA damage, and activation of tumor suppressors (Wiley and Campisi, 2016). Dysfunctional mitochondria are a hallmark of senescent cells in response to short telomeres (Passos et al., 2007) or oncogenes (Moiseeva et al., 2009). Mitochondrial dysfunction-associated senescence is characterized by decreased NAD^+ (nicotinamide adenine dinucleotide)/NADH ratio (Wiley et al., 2016), increased reactive oxygen species (ROS), and reduced ATP as compared with non-senescent cells (Moiseeva et al., 2009; Passos et al., 2007). This entices increase in glycolysis to maintain viability (Dörr et al., 2013). Because inhibition of senescence often precedes transformation (Deschênes-Simard et al.,

CellPress

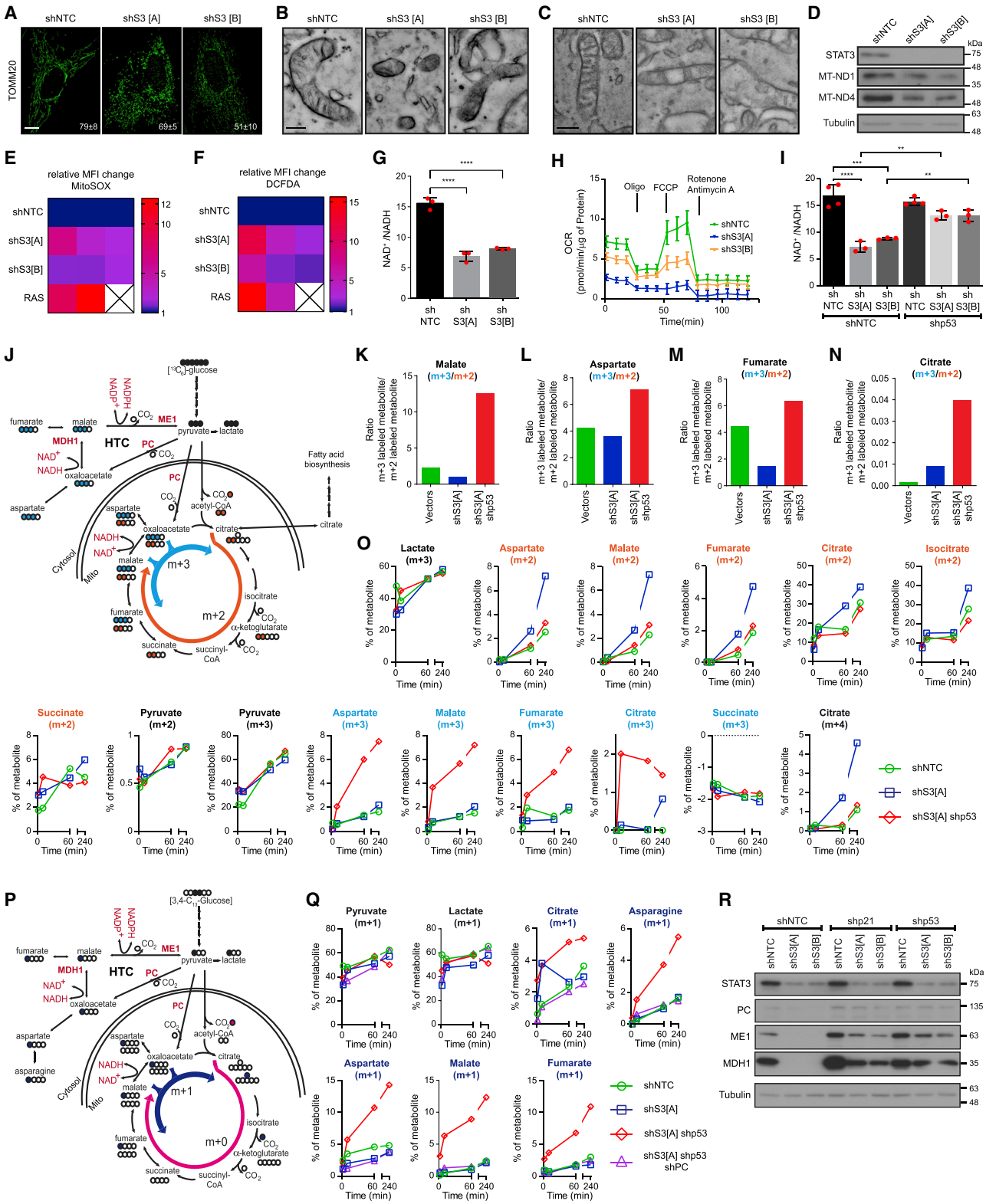

Figure 1. p53 inactivation reprograms the metabolism of senescent cells with mitochondrial dysfunction

(A) Immunofluorescence (IF) using anti-TOMM20 antibody in IMR90 cells expressing shRNAs against STAT3 (shS3[A]) and shS3[B]) or a control non-targeting shRNA (shNTC). Mean % of staining pattern (tubular or puncta) of cells and standard deviation (SD) is shown in the lower right corner; scale, 10 μm.

(legend continued on next page)

2019; Moiseeva et al., 2020; Yu et al., 2018), it is important to understand how cancer cells overcome the barriers to cell proliferation that characterize senescence, including mitochondrial dysfunction.

The origin of mitochondrial dysfunction in senescent cells is not well understood. During oncogene-induced senescence (OIS), several proteins are targeted for degradation affecting a variety of processes required for cell proliferation (Deschênes-Simard et al., 2013; Deschênes-Simard et al., 2014). One of these proteins is signal transducer and activator of transcription 3 (STAT3) (Vallania et al., 2009), which regulates transcription in the nucleus (Kidder et al., 2008) and electron transport and oxidative phosphorylation in mitochondria (Wegrzyn et al., 2009). The mitochondrial functions of STAT3 are required for cellular transformation by oncogenic RAS protein (Gough et al., 2009). Deletion of *STAT3* in hematopoietic stem cells leads to mitochondrial dysfunction, overproduction of ROS, and premature aging of blood cells (Mantel et al., 2012). Collectively, these studies suggest that the mitochondrial functions of STAT3 may be required to prevent senescence.

To discover cellular pathways that compensate for mitochondrial dysfunction and allow tumor cells to circumvent senescence, we used several models of cellular senescence. We found that senescence induced by STAT3 depletion required a decrease in the NAD^+/NADH ratio that was maintained by the actions of the p53 and retinoblastoma protein (RB) tumor suppressors. p53 and RB repress an enzyme complex that catalyzes a metabolic cycle that transfers the hydride anion (H^-) from NADH to $NADP^+$, thus regenerating NAD^+ and supplying NADPH. This hydride transfer complex (HTC) is formed by malic enzyme 1 (ME1), malate dehydrogenase 1 (MDH1), and pyruvate carboxylase (PC) and can be assembled *in vitro* with purified proteins. We also biophysically characterized HTC as well as its ability to compensate for mitochondrial dysfunction and promote tumorigenesis. Strikingly, inhibiting HTC leads to tumor cell senescence even in the absence of p53, revealing the therapeutic potential of targeting this previously unrecognized metabolon.

RESULTS

Depletion of STAT3 induces senescence, mitochondrial dysfunction, and a low NAD^+/NADH ratio

Senescence induced by either oncogenes or short telomeres is accompanied by downregulation of STAT3 (Deschênes-Simard et al., 2013). Since STAT3 is required for mitochondrial functions (Gough et al., 2009; Wegrzyn et al., 2009), we sought to investigate whether disabling STAT3 leads to senescence via mitochondrial dysfunction. We depleted STAT3 from normal human fibroblasts using small hairpin RNAs (shRNAs) and observed a strong decline in proliferation accompanied by increased senescence-associated-β-galactosidase (SA-β-Gal) activity and several senescence biomarkers (Figures S1A–S1H) in line with previous work showing induction of senescence after STAT3 inactivation in some cancer cells (Tkach et al., 2012).

Given the links between STAT3 and mitochondria, (Gough et al., 2009; Wegrzyn et al., 2009) we performed staining for the mitochondria membrane marker TOMM20 (McBride et al., 1996). This revealed that mitochondria in STAT3-depleted cells appear as multiple punctiform structures in contrast to the tubular network of normal human fibroblasts (Figure 1A). Transmission electron microscopy revealed that mitochondria from STAT3-depleted cells are spherical with disrupted cristae (Figures 1B and 1C). It was reported that mitochondrial STAT3 regulates mitochondrial gene expression (Macias et al., 2014), and we found that protein levels of mitochondrial-encoded mt-ND1 and mt-ND4 were reduced in cells with low STAT3 levels

(B and C) Scanning transmission electron microscopy (STEM) micrographs (B) and transmission electron microscopy (TEM) (C) of cells as in (A); scale, 250 nm; n = 2.

(D) Western Blot (WB) of indicated proteins in cells as in (A).

(E and F) Heatmap of relative change over control cells in median fluorescent intensity (MFI) for MitoSOX (E) or DCFDA (F) in cells as in (A) and cells expressing oncogenic RAS. Each column represents a biological replicate with a minimum of 10,000 cells, n = 2–3.

(G) NAD^+/NADH ratio in cells as in (A).

(H) Oxygen consumption rate (OCR) of cells as in (A); n = 4–6, error bars show SEM (standard error of the mean).

(I) Mean NAD^+/NADH ratio in cells expressing a control shRNA (shNTC) or a shRNA against STAT3 (shS3[A], shS3[B]) in combination with an shRNA against p53 (shp53) or non-target control shRNA (shNTC).

(J) Model of regeneration of NAD^+ by MDH1, ME1 and PC plus schematic of metabolite ^{13}C labeling patterns after labeling with $^{13}C_6$-glucose. ^{13}C are noted by filled circles. Orange cycle is the forward direction of TCA cycle giving (m+2) intermediates (orange-filled circles). Light-blue cycle starts with pyruvate carboxylase (PC) and is characterized by (m+3) intermediates (light-blue-filled circles). HTC, hydride transfer complex; mito, mitochondria .

(K–N) Ratio of (m+3)/(m+2) isotopomers for the indicated metabolites in IMR90 cells expressing a control shRNA (shNTC), a shRNA against STAT3 (shS3[A]) alone or in combination with an shRNA against p53 (shp53). Ratios were calculated 10 min post-labeling.

(O) Amount of indicated labeled intermediates over time measured by GC-MS relative to the total amount of each related metabolite for IMR90 cells as in (K). Data show representative experiment.

(P) Model of PC activity labeling pattern with ^{13}C-[3,4]-glucose. ^{13}C-[3,4]-glucose is converted into ^{13}C-[1]-pyruvate. Each intermediate generated via PDH is not labeled (magenta cycle), while in the PC reaction-labeled carbon is maintained (m+1, dark-blue cycle), filled circles show heavy carbon. HTC, hydride transfer complex; mito, mitochondria.

(Q) Amount of indicated labeled intermediates over time measured by GC-MS relative to the total amount of each related metabolite for IMR90 cells expressing a control shRNA (shNTC), a shRNA against STAT3 (shS3[A]) alone or in combination with an shRNA against p53 (shp53), and/or a shRNA against PC (shPC). Data show representative experiment of n = 2.

(R) WB for the indicated proteins in IMR90 cells expressing a control shRNA (shNTC) or shRNAs against STAT3 (shS3[A] and shS3[B]) together with control shRNA (shNTC) or shRNAs against p53 (shp53) or p21 (shp21).

Experiments other than indicated are from n = 3 biological replicates. (A–D, O, Q–R) show representative images. ANOVA with multiple comparison test (G and I). Mean ± SD for (G and I) with red dots as biological values and mean for (K–N). For (K–O), conditions shNTC and shS3[A] are the same as in Figures 4J and 4K. Related to Figures S1–S3.

(Figure 1D). Cells depleted for STAT3 also produced higher levels of ROS (Figures 1E and 1F) and had a dramatically decreased NAD^+/NADH ratio (Figure 1G), which are signs of mitochondrial dysfunction. The decrease in NAD^+/NADH ratio was mainly the result of an increase in NADH because STAT3 depletion did not significantly alter total NAD or NAD^+ (Figure S1I). In support of mitochondrial dysfunction, we found that both basal and maximal respiration were decreased upon STAT3 depletion (Figure 1H).

To confirm that the lack of STAT3 functions in mitochondria leads to mitochondrial dysfunction, we expressed an shRNA-insensitive (i) STAT3 allele with a mitochondrial localization signal in STAT3-depleted cells. This mito-iSTAT3 localized into mitochondria, attenuated senescence, and restored the NAD^+/NADH ratio to the level observed in STAT3-non-depleted control cells (Figures S1J–S1N). We also observed that endogenous STAT3 was reduced in purified mitochondria from cells that undergo OIS (Figure S1O). Furthermore, proximity ligation assay (PLA) revealed that STAT3 interacts with the mitochondrial protein ATAD3A in proliferating cells (Carbognin et al., 2016), whereas in replicative senescent cells or OIS cells, interaction of ATAD3A with STAT3 was lost (Figure S1P–S1U), highlighting the changes of mitochondrial STAT3 levels in response to senescence and aging. By taking advantage of the yeast single subunit complex I NADH dehydrogenase (NDI1) (Birsoy et al., 2014), we next investigated whether mitochondrial complex I inhibition caused by STAT3 depletion is the main cause of the observed decrease in the NAD^+/NADH ratio. We found that NDI1 localized to mitochondria, bypassed senescence, and partially restored the NAD^+/NADH ratio in STAT3-depleted cells (Figures S2A–S2F). Together, these data show that mitochondrial STAT3 plays an important role in preventing senescence.

The NAD^+/NADH ratio can be restored by pyruvate, which, through the action of lactate dehydrogenase (LDH), is converted to lactate while NAD^+ is regenerated from NADH. Alternatively, pyruvate can be metabolized to oxaloacetate, which in turn is reduced to malate, thus converting NADH into NAD^+ (Hanse et al., 2017). Supplementing STAT3-depleted normal human fibroblasts with 2 mM pyruvate rescued cells from growth arrest and senescence while reducing the number of DNA-damage foci and increasing the NAD^+/NADH ratio (Figures S2G–S2L). We also treated STAT3-depleted cells with duroquinone, a compound that is reduced to durohydroquinone by the cytosolic enzyme NQO1(NAD(P)H dehydrogenase [quinone]), which uses NADH as an electron donor and therefore regenerates NAD^+ and decreases the sensitivity to complex I inhibition by biguanides (Gui et al., 2016). We found that this compound increased the NAD^+/NADH ratio without altering the total NAD levels in STAT3-depleted cells, which was paralleled by bypass of senescence (Figures S2M–S2S). Next, we used the NADH-oxidase from *Lactobacillus brevis* (LbNOX) to force an increase in the NAD^+/NADH ratio (Titov et al., 2016). LbNOX expression in the cytosol rescued cells from senescence induced by depletion of STAT3 while increasing the NAD^+/NADH ratio (Figures S2T–S2W). It has been shown that cells with dysfunctional mitochondria and low NAD^+/NADH ratio fail to synthesize sufficient asparagine (Krall et al., 2021) and aspartate (Birsoy et al., 2015; Sullivan et al., 2015), but supplementing STAT3-depleted cells with 20 mM aspartate only moderately rescued the proliferation defects and senescence after STAT3-depletion, and it did not normalize the NAD^+/NADH ratio (Figures S3A–S3G). Together, these data suggest that a failure to reoxidize NADH is implicated in the induction of cellular senescence.

A NAD^+ regeneration metabolic cycle controlled by the p53-RB tumor suppressors

Depletion of STAT3 leads to the activation of both the p53 and RB tumor suppressor pathways, which are mediators of senescence (Mallette et al., 2007). To investigate whether the p53 pathway is required for senescence after STAT3-depletion, we inactivated p53 and p21 with shRNAs. Inactivation of either p53 or p21 prevented the growth arrest and senescence induced by STAT3-depletion (Figures S3H–S3M). Intriguingly, p53 inactivation also restored the NAD^+/NADH ratio in STAT3-depleted cells (Figure 1I). Collectively, the results suggest that p53 and/or p21/RB pathway inactivation in STAT3-depleted cells increases the NAD^+/NADH ratio to sustain the oxidative metabolism of cells that bypass senescence.

To identify NAD^+-regenerating metabolic pathways repressed by p53 and p21/RB, we combined bioinformatics analysis with stable isotope tracing studies. Using CHIP-Atlas, we found that both p53 and RB-binding partner E2F proteins bind to the promoter region for the NAD^+ regenerating cytosolic enzyme MDH1 (Figure S4A). Moreover, MDH1 expression is reduced in senescent cells induced by STAT3-depletion or telomere-shortening (Figures S4B and S4C). MDH1 is a cytosolic enzyme that oxidizes NADH and converts oxaloacetate (OAA) into malate (Hanse et al., 2017). To identify the source of OAA for MDH1, we compared glucose metabolism in senescent cells with cells that bypassed senescence via p53 knockdown, using $^{13}C_6$-glucose tracing. Conversion of pyruvate to OAA via PC can be estimated from the levels of (m+3) malate, fumarate, and citrate relative to the levels of corresponding (m+2) isotopomers generated in the tricarboxylic acid (TCA) cycle from acetyl-CoA (Figure 1J). Because OAA is hard to measure due to its instability, aspartate (m+3) was used as a surrogate marker (Buescher et al., 2015). We found that the pool of pyruvate converted to (m+3) malate, aspartate, fumarate, and citrate is increased in cells that bypass senescence after p53 knockdown (Figures 1K–1O). $^{13}C_6$-glucose may generate (m+3) malate, fumarate, and aspartate through multiple rounds of pyruvate oxidation in the TCA cycle. This was, however, discarded because we failed to detect (m+3) succinate and were only able to detect traces of (m+4) citrate under these conditions (Figure 1O). Hence, $^{13}C_6$-glucose tracing was consistent with PC catalyzed conversion of pyruvate into (m+3) OAA. Labeling cells with [3,4-^{13}C]-glucose provides a more direct assessment of PC activity. [3,4-^{13}C]-glucose is converted to [1-^{13}C]-pyruvate, and the latter is converted to m+1 OAA and its derivatives after the PC reaction while the labeled carbon is lost in the PDH reaction (Cheng et al., 2011). Bypass of senescence after p53 knockdown increased the pool of m+1 metabolites, while depletion of PC with an shRNA abrogated these effects (Figures 1P and 1Q). This indicates that p53 loss bolsters PC activity.

Of note, PC is considered a mitochondrial enzyme in mammals, and this implies that pyruvate enters the mitochondria, is

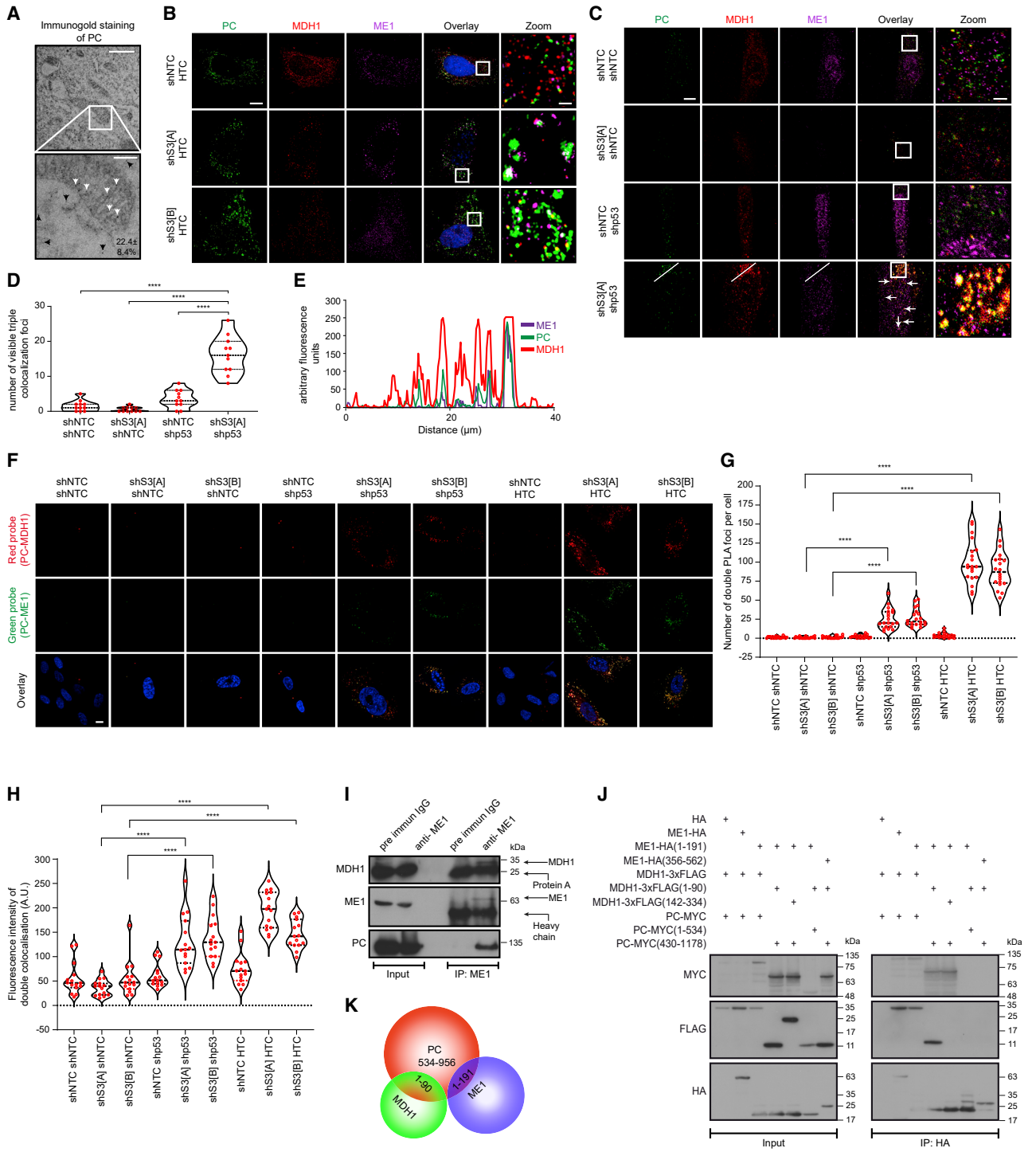

Figure 2. Colocalization and interactions of the enzymes that catalyze the hydride transfer reactions

(A) TEM of PC-3 cells stained with anti-PC antibody followed by immunogold labeling. White arrows: mitochondrial PC. Black arrows: cytosolic PC. Scales: top, 800 nm; bottom, 200 nm. Lower corner shows the percentage of cytosolic PC and SD of a count of 18 representative fields.

(B) IF with super-resolution microscope for the indicated enzymes (MDH1, ME1, and PC) expressed in IMR90 cells depleted for STAT3 (shS3[A], shS3[B]) or STAT3 sufficient cells (shNTC). PC (green), MDH1 (red), and ME1 (magenta), triple colocalization in white. DAPI was used to stain the nucleus. Scale, 10 μm; zoom scale, 1 μm.

(C) Colocalization of endogenous MDH1, ME1, and PC in IMR90 cells expressing shRNAs against STAT3 (shS3[A]) and p53 (shp53) and/or control shRNA (shNTC). Scale, 20 μm; zoom scale, 2 μm. Triple colocalization in white.

(legend continued on next page)

converted to OAA by PC, and then OAA is either exported to the cytosol as aspartate after transamination or as citrate after conjugation to acetyl-CoA. However, adding aspartate did not rescue the NAD^+/NADH ratio, suggesting that the aspartate pathway is not involved (Figure S3C). In yeast and some *Aspergillus* strains, PC is a cytosolic enzyme (Huet et al., 2000), and mammalian PC can re-localize to the cytosol upon viral infection (Cao et al., 2016) or to the nucleus in 2-cell embryos (Nagaraj et al., 2017). We thus anticipated that a change in cellular localization of PC could supply cytosolic OAA for NAD^+ regeneration via MDH1. The concerted action of cytosolic PC and MDH1 is positioned to regenerate NAD^+ in the cytosol to produce (m+3) malate, which is consistent with the m+3 isotopomers that were increased in cells bypassing senescence (Figures 1J–1N). In addition, the cytosolic malic enzyme 1 (ME1) is expected to convert malate back into pyruvate closing a metabolic cycle that would transfer the hydride ion from NADH to $NADP^+$ regenerating NAD^+ and supplying NADPH (Figure 1J). Notably, like MDH1, the PC and ME1 promoters contain p53 and RB/E2F binding sites (Figure S4A) and levels of the corresponding proteins decreased in models of cellular senescence (Figure S4B and S4C). These observations are consistent with reports showing that p53 and/or E2F bind to the promoters of ME1 (Jiang et al., 2013), PC (Li et al., 2016), and MDH1 (Yuan et al., 2019) regulating their expression.

We next investigated whether bypassing senescence by inhibiting either the p53 or RB pathway can restore expression of MDH1, PC, and ME1. We found that both shp53 and shp21 rescued MDH1, PC, and ME1 expresion in STAT3-depleted IMR90 cells to levels comparable to control cells (Figure 1R). Collectively, these data suggest that a metabolic cycle catalyzed by MDH1, ME1, and cytosolic PC regenerates NAD^+ to bypass cellular senescence. Our model predicts that (1) PC localizes to the cytosol in cells that bypass senescence, (2) expression of the enzymes that catalyze the hydride transfer from NADH to $NADP^+$ bypasses senescence, and (3) inactivation of these enzymes should lead to a decreased NAD^+/NADH ratio, REDOX stress, and growth inhibition.

Cytosolic localization of PC and formation of HTC

Although PC is more abundant in the mitochondria, we detected full-length PC as well as lower molecular weight forms in the cytosolic fraction of PC-3 prostate cancer cells, which are devoid of STAT3 due to biallelic deletion of the *STAT3* locus (Figures S4D and S4E). Moreover, we used immunogold staining followed by transmission electron microscopy, which confirmed that a significant proportion of PC localizes to the cytosol in PC-3 cells (Figure 2A). This was further confirmed in IMR90 cells overexpressing PC, where a significant fraction of PC does not colocalize with mitochondria (Figure S4F). Interestingly, overexpression of PC, MDH1, and ME1 in STAT3-depleted IMR90 cells also colocalized in distinctive bodies (Figure 2B) outside mitochondria (Figure S4G). Importantly, we revealed this colocalization pattern with endogenous proteins after inactivation of both STAT3 and p53 in IMR90 cells (Figures 2C–2E). Intriguingly, these foci were dissolved by 1,6-hexanediol, suggesting that they form via liquid-liquid phase separation (Figures S4H and S4I). Additional evidence for the colocalization of HTC enzymes in cytosolic foci was obtained using PLA with antibodies against PC and MDH1 or PC and ME1 (Figures 2F–2H).

The colocalization of PC, MDH1, and ME1 suggested that they interact to form a HTC, and both PC and ME1 co-immunoprecipitated with FLAG-tagged MDH1 in 293T cells. Also, MDH1 and ME1 co-immunoprecipitated with FLAG-tagged PC, and PC and MDH1 co-immunoprecipitated with HA-tagged ME1 (Figures S5A–S5C). Importantly, HTC enzymes co-immunoprecipitated in HuH-7 hepatoma cells that endogenously express high levels of the three enzymes (according to the Cancer Cell Line Encyclopedia, https://sites.broadinstitute.org/ccle/) (Figure 2I) and in PC-3 cells (Figure S5D). PC is a biotinylated enzyme (Xiang and Tong, 2008), and its pull-down with streptavidin from PC-3 cells recovered both MDH1 and ME1, but this was not possible in cells where PC was depleted by a shRNA (Figure S5E). Similar results were obtained in HuH-7 cells (Figure S5F).

Biochemical and biophysical characterization of HTC

To identify the regions required for co-immunoprecipitation of the HTC enzymes, we used a series of deletions mutants. In addition to the full-length PC, it was determined that the fragments from positions 430–1,178 and 1–956 formed a complex with both MDH1 and ME1. However, amino acids 1–534 of PC failed to do so, indicating that the interacting region comprises residues 534–956 in the pyruvate carboxyltransferase domain (Figures S5G and S5J). Second, we mapped the regions of MDH1 required to co-immunoprecipitate with PC and ME1. The residues 1–90, 1–141, and 1–192 of MDH1 co-immunoprecipitated with both PC and ME1, but residues 141-334 and 105-334 failed,

(D) Quantification of triple colocalization foci (white foci) per cells as in (C), N=11.
(E) Fluorescence intensity of ME1 (magenta), MDH1 (red), and PC (green) in shS3[A]/shp53-expressing cells. Colocalization was measured across the indicated line in (C) and represented as arbitrary fluorescence units for each enzyme.
(F) Proximity ligation assay with two PLA probes to specifically reveal PC interaction with ME1 or with MDH1. PLA probes used are PLA green (ME1 PC) and PLA red (MDH1 PC) on IMR90 infected with either control shRNA (shNTC) or shRNA against STAT3 (shS3[A], shS3[B]) and shRNA against p53 or control shRNA or HTC enzymes (MDH1, ME1, PC). Scale, 10 μm. DAPI was used to stain the nucleus. Colocalization of PLA probe green and red is shown in yellow in overlay, n = 2–3.
(G) Count of PLA foci from cells in (F), N=20.
(H) Fluorescence signal intensity of foci in cells in (F), N=15.
(I) IP of endogenous ME1 from HuH-7 cells followed by WB for all HTC enzymes.
(J) IP with HA beads in 293T cells expressing the indicated variants of PC-MYC, MDH1-3x-FLAG and ME1-HA, or control HA vector. IP was followed by WB against indicated proteins.
(K) Schematic of interaction between regions 1–90 of MDH1 and 1–191 ME1 with 534–956 of PC.
A minimum of 3 biological replicates unless indicated. ANOVA with Tukey (G and H) or Dunnett (D) for multiple comparisons, asterisks represent p values for most important comparisons. Related to Figures S4 and S5.

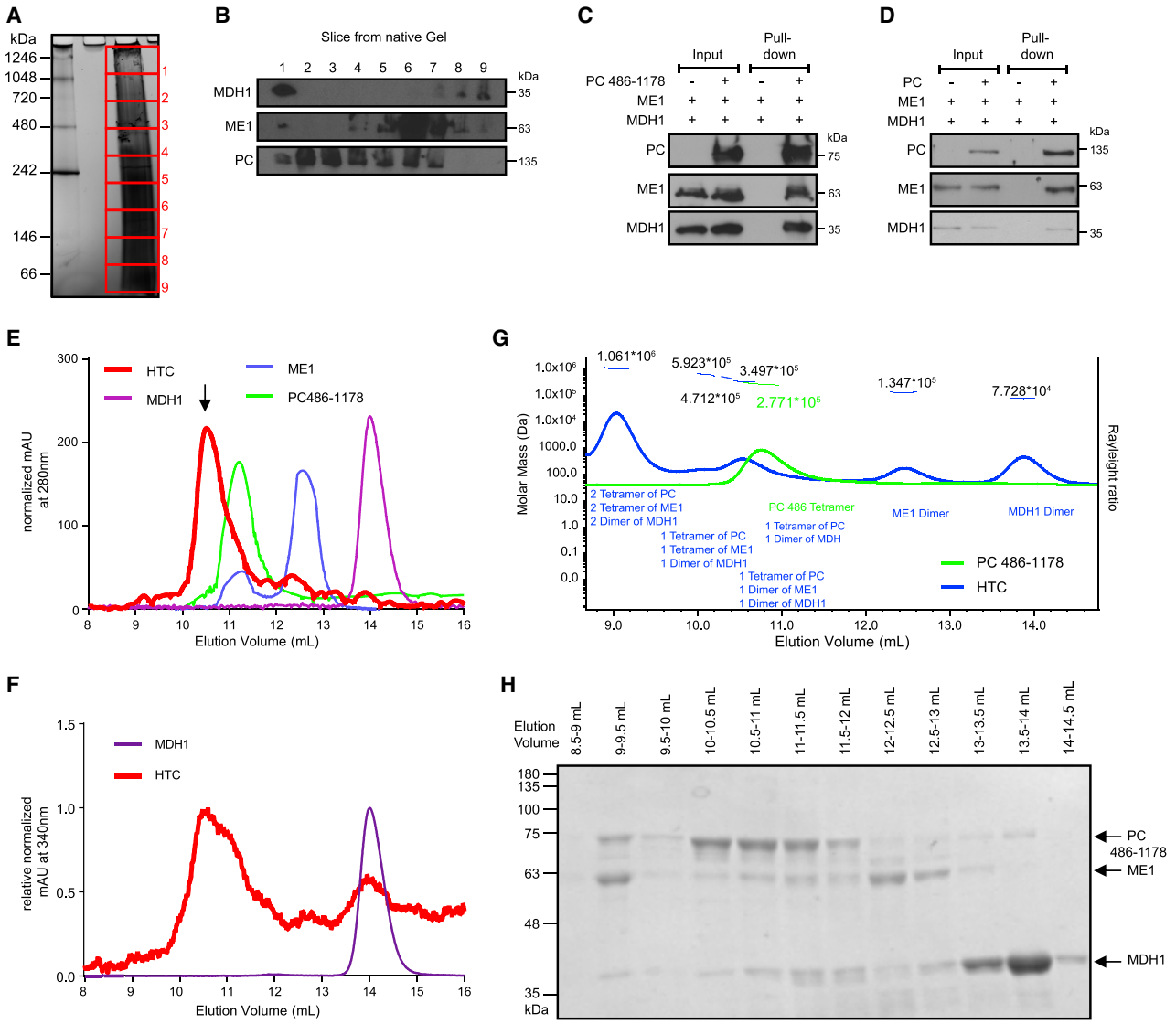

Figure 3. Biophysical characterization of the hydride transfer complex

(A and B) Two-dimensional blue native/SDS gel electrophoresis (2D-BN/SDS-PAGE). Coomassie G-250 staining of BN-PAGE (A) with indicated protein sizes corresponding to collected gel slices (red squares) and immunoblots (B) for the indicated proteins performed on gel slices from (A) migrated on SDS-PAGE.

(C and D) *In vitro* assembly of the hydride transfer complex (HTC) with purified PC(486-1178) (C) or full-length PC (D). Mono-Avidin pull-down of biotinylated PC after *in vitro* assembly followed by immunoblotting against the indicated proteins.

(E) Size-exclusion chromatography (SEC) with either the individual purified proteins or the pre-assembled HTC (fractions 8–12 mL of the assembly run) on a Superdex 200 Increase column. Data show absorbance at 280 nm. Arrow indicates elution peak of assembled complex.

(F) Same SEC experiment as in (E) but with the absorbance at 340 nm (NADH absorbance) normalized relative to either MDH1 or the pre-assembled HTC.

(G) SEC-MALS (multi-angle light scattering) of purified PC (486-1178) (green) or all fraction of previously assembled HTC (blue). The calculated molecular weight is shown above each peak and possible complexes are indicated below.

(H) SDS-PAGE of collected fractions following the SEC-MALS experiment (G) stained with Coomassie Blue to show the purity and assembly of the complexes.

For (A–H) representative images of a minimum of 3 replicates. Related to Figure S5.

concluding that the interacting region is within residues 1–90 (Figures S5H and S5J). Finally, we determined the regions of ME1 required to co-immunoprecipitate PC and MDH1. Full-length ME1 or residues 1–191 immunoprecipitated with both PC and MDH1, but residues 356–562 did not, which suggests that the interacting region is between residues 1–191 (Figures S5I and S5J). The minimal interacting regions ($PC^{430–1,178}$, $MDH1^{1–90}$, and $ME1^{1–191}$) were then confirmed to co-immunoprecipitate (Figure 2J), revealing that the interaction between MDH1 and ME1 requires PC (Figure 2J-K). Together, the data suggest that specific regions of each enzyme mediate HTC formation.

To confirm that HTC occurs endogenously in cells, we used two-dimensional blue native polyacrylamide gel electrophoresis (2D-BN/PAGE) on HuH-7 cell extracts. Proteins were resolved in

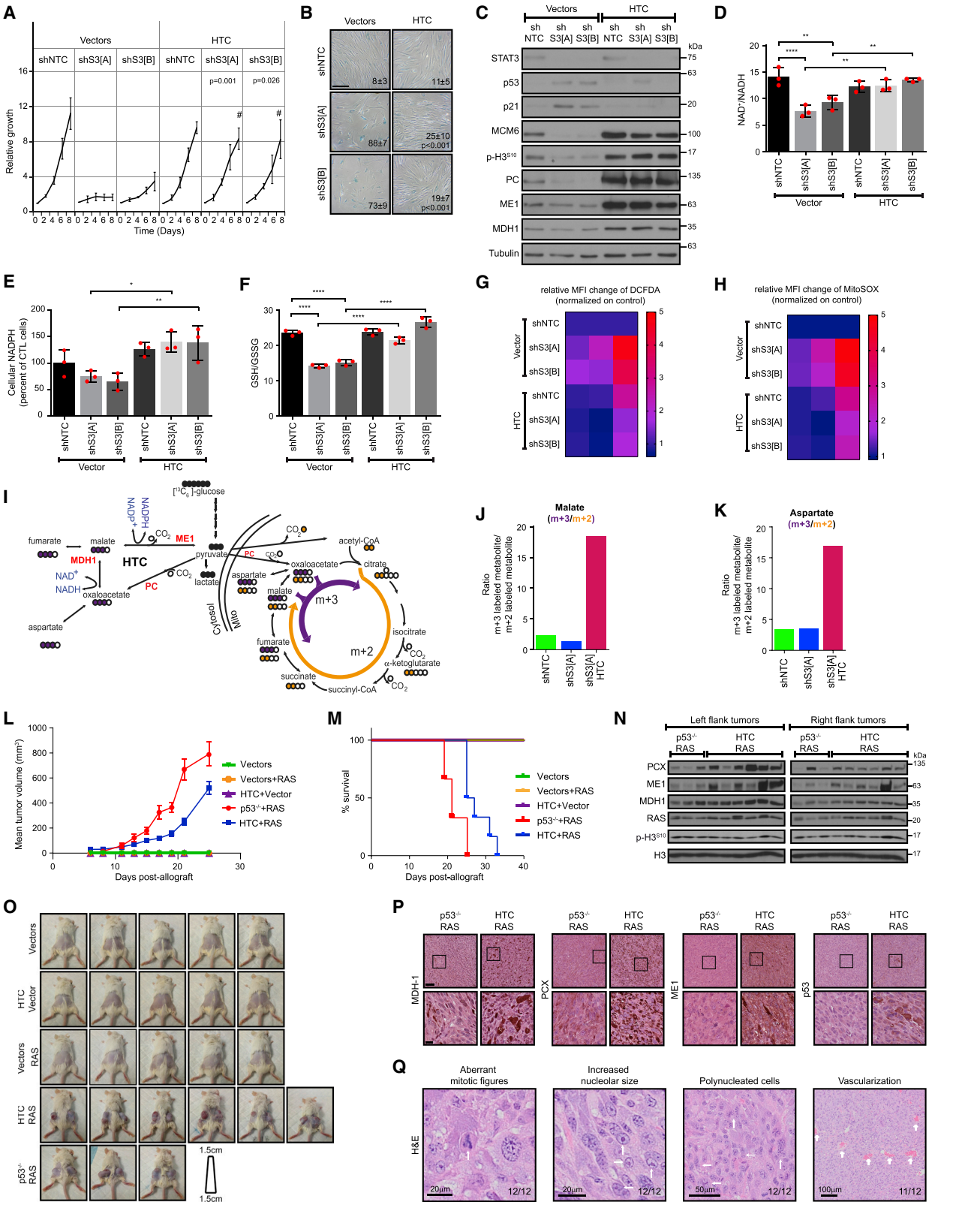

(legend on next page)

a blue native gel in the first dimension followed by SDS-PAGE in the second dimension. This revealed the presence of MDH1 dimers (molecular mass 36.4 kDa); monomers, dimers, and tetramers of ME1 (molecular mass 64.1 kDa); and of PC (molecular mass 129.6 kDa). Importantly, we identified a high molecular weight complex with a mass of ~1 MDa, which contained all three enzymes (Figures 3A and 3B). To determine whether the HTC enzymes interact directly *in vitro*, we expressed and purified each enzyme from bacteria as well as a fragment of PC from residues 486-1,178 because full-length PC form aggregates that affect the identification (Xiang and Tong, 2008).

Size exclusion chromatography with multi-angle light scattering (SEC-MALS) analysis revealed that purified PC forms a tetramer, whereas purified ME1 forms dimers and tetramers while purified MDH1 forms a dimer (Figures S5K–S5M). Then, mono-avidin was used to perform pull-downs of either PC(486–1,178) or full-length PC, which are biotinylated, recovering both MDH1 and ME1 (Figures 3C and 3D). Next, we characterized the biophysical properties of the HTC. We loaded purified PC(486–1,178), MDH1, ME1 alone, or a pre-assembled 1:1:1 mixture of the proteins on a Superdex 200 Increase gel filtration column. Whereas the three individual enzymes eluted as described above, the preassembled complex eluted in higher molecular weight fractions, suggesting the formation of a ternary complex (Figure 3E; see arrow). The presence of MDH1 in the complex was identified by measuring NADH absorbance at 340 nm (Figure 3F). Further proof of the formation of HTC was obtained using SEC-MALS analysis of the PC, ME1, and MDH1 mixture. We resolved several complexes of calculated molecular mass of 1MDa, 590 kDa, and 471 kDa, which correspond to the molecular mass of either: two tetramers of PC, two tetramers of ME1, and two dimers of MDH1 (1 MDa); or one tetramer of PC, one tetramer of ME1, and one dimer of MDH1 (590 kDa); or one tetramer of PC, one dimer of ME1, and one dimer of MDH1 (471 kDa), respectively (Figures 3G and 3H).

HTC enzymes suppress senescence

To investigate whether HTC enzymes bypass the senescence response to STAT3 inactivation, we co-expressed PC, MDH1, and ME1 in IMR90 cells where STAT3 was depleted by shRNA. Strikingly, forced expression of HTC enzymes restored proliferation in cells depleted of STAT3 to the level observed in cells expressing a control non-targeting shRNA, while significantly reducing the percentage of SA-β−Gal positive cells (Figures 4A and 4B). Expression of HTC enzymes in STAT3-depleted cells reduced the expression of p53, p21, DNA damage response markers, and PML bodies while increasing the mitosis marker phospho-$H3^{Ser10}$ and MCM6 (Figures 4C, S6A, and S6B). This was paralleled by restoration of the NAD^+/NADH ratio, increased cellular NADPH levels, elevated GSH/GSSG ratio, and decreased ROS relative to the control (Figures 4D–4H and S6C–S6H). Consistent with these results, the generation of NADPH by ME1 and ME2 was previously linked to ROS detoxification (Jiang et al., 2013). Together, these data suggest that HTC enzymes lead to metabolic reprogramming in STAT3-depleted cells to restore NAD^+ levels and increase NADPH, which is paralleled by the suppression of senescent phenotype.

To monitor the effects of HTC enzymes overexpression on senescent cells metabolism, we performed $^{13}C_6$-glucose tracing. $^{13}C_6$-glucose flux into (m+3) pyruvate or (m+3) lactate was comparable between the cell lines, but HTC enzymes overexpression significantly increased the conversion of pyruvate into OAA via PC as estimated from the (m+3)/(m+2) ratio of malate and

Figure 4. Expression of the hydride transfer complex enzymes bypasses senescence and promotes transformation

(A) Relative proliferation of IMR90 expressing shSTAT3 (shS3[A] and shS3[B]) or control shRNA (shNTC) with co-expression of control vectors or the HTC enzymes MDH1, ME1, and PC. # indicates time point used for statistical test.

(B–H) Analysis of cells as in (A).

(B) SA-β-Gal staining: percent positive cells ± SD is shown in lower corner; scale bar, 250 μm.

(C) WB for the indicated proteins.

(D) NAD^+/NADH ratio.

(E) Total NADPH.

(F) Ratio of GSH/GSSG. Individual levels of NAD, NADH, NADP, GSSG, and GSH can be found in Figure S6.

(G and H) Heat maps of flow cytometry data measuring DCFDA (G) or MitoSOX (H). Data show relative change of median fluorescence intensity (MFI) over control cells. Each column represents a biological replicate with a minimum of 10,000 cells.

(I) Scheme of metabolite ^{13}C labeling patterns after incubation with $^{13}C_6$-glucose. Orange cycle is normal direction of tricarboxylic acid (TCA) giving (m+2) intermediates (orange-filled circles). Violet cycle represents the PC pathway giving (m+3) intermediates (violet-filled circles). HTC, hydride transfer complex; mito, mitochondria.

(J and K) Ratio of (m+3)/(m+2) isotopomers for the indicated metabolites from IMR90 cells expressing a control shRNA with control vectors (shNTC), or expressing a shRNA against STAT3 with either control vectors (shS3[A]) or with vectors expressing HTC enzymes (shS3[A]/HTC). Conditions shNTC and shS3[A] are the same as in Figures 1K–1O.

(L) Mean tumor volume from NRG mice after allograft injection of 1×10^6 MEFs into both flanks expressing either controls (Vectors), HTC enzymes (HTC), or RAS alone or with HTC overexpression (RAS + HTC). MEFs *p53*$^{-/-}$ overexpressing RAS were used as a positive control (RAS + p53$^{-/-}$), n = 3–6. Data are shown until mice bearing tumors from RAS + p53$^{-/-}$ MEFs were all sacrificed.

(M) Survival of NRG mice as in (L), n = 3–6.

(N) WB against indicated proteins from tumors shown in (L).

(O) Images of all mice the day of sacrifice after injection of MEFs as in (L).

(P) Immunohistochemistry with indicated antibodies on tumors from (L); scale, 100 μm and zoom scale, 20 μm.

(Q) Representative H&E images of indicated aberrations in tumors from MEFs expressing RAS and HTC. The numbers represent the frequency of observations.

All experiments other than indicated have been repeated a minimum of 3 times. Mean ± SD for (A, B, and D–F). Mean ± SEM for (L), red dots represent biological value of each replicate (D–F). Two-tailed Student's t test (A) or ANOVA (B and D–F) with Šídák's multiple comparisons test was performed and p value is indicated. Related to Figures S6–S8.

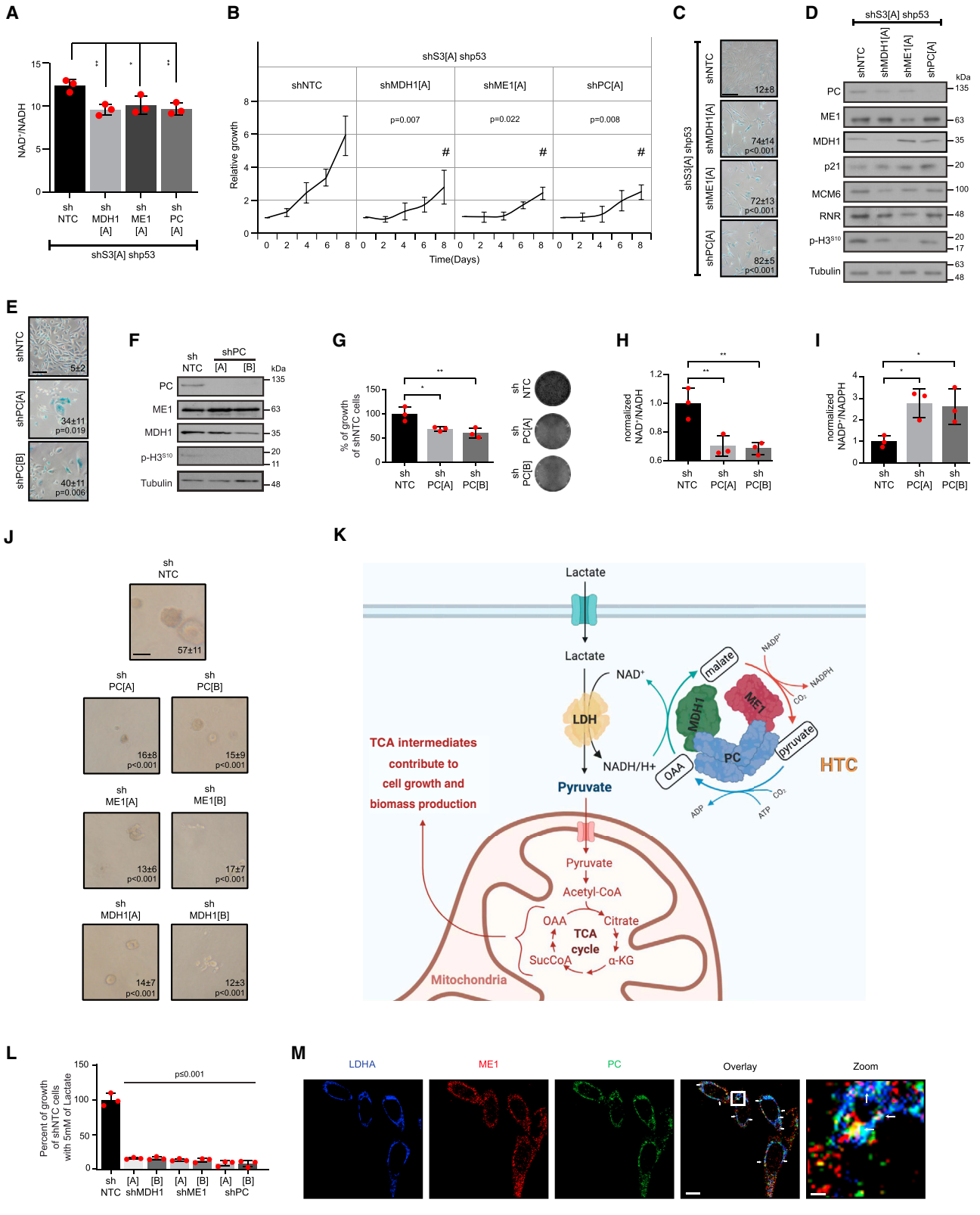

(legend on next page)

aspartate (Figures 4I–4K, S6I, and S6J). This interpretation was further validated by the absence of an increase in succinate (m+3) (Figure S6J), ruling out that (m+3) isotopomers are generated by multiple rounds of the TCA cycle from (m+2) acetyl-CoA. In turn, the levels of citrate (m+2) were reduced in cells expressing the HTC enzymes, which is consistent with a decrease in the contribution of pyruvate to acetyl-CoA, as compared with its utilization by PC (Figure S6J). Tracing using 3-^{13}C-glucose confirmed an increase in m+1 metabolites in cells expressing HTC consistent with conversion of pyruvate into m+1 OAA and its derivatives (Figures S6K and S6L). Collectively, these findings suggest that pyruvate in HTC-overexpressing cells is preferentially converted to OAA via PC, which is subsequently used to replenish the TCA cycle and NAD^+ regeneration via MDH1. Together, these results show that the metabolic program of HTC-overexpressing cells is comparable with that observed in p53-disabled cells.

To determine the contribution of NADPH production by HTC to reduce ROS and bypass senescence, we expressed ME1 in STAT3-depleted cells supplemented with malate. ME1/malate did not rescue these cells from senescence but was sufficient to decrease ROS levels (Figures S7A–S7D). In contrast, duroquinone prevented senescence after STAT3 depletion (Figure S7E), whereby ROS levels remain reduced upon combination of malate and duroquinone (Figures S7F and S7G). Finally, to determine whether the ability of HTC to form was important for the bypass of senescence, we took advantage of the PC residues 1–534 that do not interact with MDH1 or ME1 (Figures 2J and 2K). This PC fragment failed to bypass senescence in STAT3-depleted cells when combined with ME1 and MDH1 (Figures S7H–S7J). Together, these results show that HTC enzymes act in a complex that catalyzes NAD^+ regeneration and NADPH production to reduce oxidative stress and bypass senescence.

HTC enzymes are essential to prevent senescence in transformed cells

OIS protects normal cells from oncogenic stress (Serrano et al., 1997). In murine embryonic fibroblasts (MEFs), expression of HTC enzymes in combination with oncogenic RAS prevented senescence allowing colony formation despite maintaining an intact p53 pathway (Figures S8A–S8D). Also, HTC cooperated with RAS to induce tumor formation in mice (Figures 4L–4O and S8E–S8G). Hematoxylin and eosin staining of tumor sections in conjunction with immunohistochemistry using specific antibodies revealed that HTC- and RAS-induced tumors are similar to RAS-induced tumors in p53 null MEFs. This included abundant mitotic figures, increased nucleoli, more polynucleated cells and vascularisation (Figures 4P, 4Q, and S8H).

It was reported that MDH1 inactivation decreased the NAD^+/NADH ratio leading to senescence (Lee et al., 2012). To determine whether other HTC enzymes also prevent senescence, we knocked down each HTC enzymes in IMR90 STAT3/p53-depleted cells. We found that reducing the expression of any HTC enzyme decreases the NAD^+/NADH ratio inducing proliferation arrest and senescence (Figures 5A–5D). Knockdown of HTC enzymes also induced senescence (Figures 5E–5I and S8I–S8R) and significantly reduced proliferation in a clonogenic assay (Figure 5J) in PC-3 cells. Interestingly, cells using glucose as a carbon and energy source can use the LDH reaction to supply part of the NAD^+ required for glycolysis. However, many tumor cells use lactate as a carbon source (Faubert et al., 2017; Pértega-Gomes et al., 2014) and cannot use the LDH reaction to regenerate NAD^+ (Figure 5K). Consistent with this idea, inactivation of HTC enzymes greatly suppressed proliferation of PC-3 cells grown on lactate (Figure 5L). Interestingly, LDH colocalizes with HTC in PC-3 cells grown on lactate (Figure 5M), a situation that facilitates NAD^+ transfer from HTC to LDH. Together, these results indicate that HTC enzymes prevent senescence and contribute to malignant transformation.

HTC enzymes are highly expressed in prostate cancer

Inactivation of *Stat3* and *Pten* in the prostate leads to tumorigenesis in mice (Pencik et al., 2015). This suggested that elevated expression of HTC enzymes may allow prostate epithelial cells to override senescence caused by STAT3 ablation. Therefore, we measured HTC enzymes in prostate samples from 19-weeks-old wild-type (WT), *Stat3*$^{-/-}$, Phosphatase and tensin homolog (*Pten*$^{-/-}$), or *Stat3*$^{-/-}$*Pten*$^{-/-}$ mice. Each of the three HTC enzymes was significantly upregulated in the *Stat3*$^{-/-}$*Pten*$^{-/-}$ prostate tumors (Figures 6A–6G). Interestingly, in *Pten*$^{-/-}$ tumors, the expression of the enzymes was also higher, but this was mostly confined to KI67 positive cells, which likely already bypassed the senescence response to *Pten* abrogation (Figures

Figure 5. Inhibition of the HTC triggers senescence

(A) Mean NAD^+/NADH ratio in IMR90 cells expressing shRNAs against STAT3 and p53 (shS3[A] shp53) and either a control shRNA (shNTC) or shRNAs against MDH1 (shMDH1[A]), ME1 (shME1[A]), or PC (shPC[A]).

(B–D) Analysis of cells as in (A).

(B) Relative proliferation, # indicates timepoint used for statistical test.

(C) SA-β-Gal staining; scale, 250 μm, and mean percentage ± SD of SA-β-gal positive cells.

(D) WB of indicated proteins.

(E–I), Inactivation of HTC by shRNAs against PC in PC3 cells. SA-β-Gal staining, scale, 100 μm (E); WB (F); normalized proliferation on shNTC cells with an image of a representative well (G); normalized NAD^+/NADH ratio (H); and normalized $NADP^+$/NADPH ratio (I) of PC-3 cells expressing either a control shRNA (shNTC) or shRNAs against (PC: shPC[A] and shPC[B]). The shNTC control is the same as in Figures S8L–S8R.

(J) Images of clonogenic collagen assays on cells as in (E–I); scale, 200 μm.

(K) Schematic representation of NAD requirements for cells growing on lactate.

(L) PC-3 cells with indicated shRNA were grown on 5 mM Lactate and proliferation was normalized on proliferation of control shNTC cells.

(M) IF of PC-3 cells grown in 5 mM lactate showing triple colocalization indicated in white by white arrows of LDHA (blue), PC (green), and ME1 (red). Scale, 10 μm and zoom scale, 1 μm; representative image from 20 cells analyzed from same biological replicate.

All experiments are of 3 biological replicates. Significance was assessed with ANOVA with Dunnett's test. Related to Figure S8.

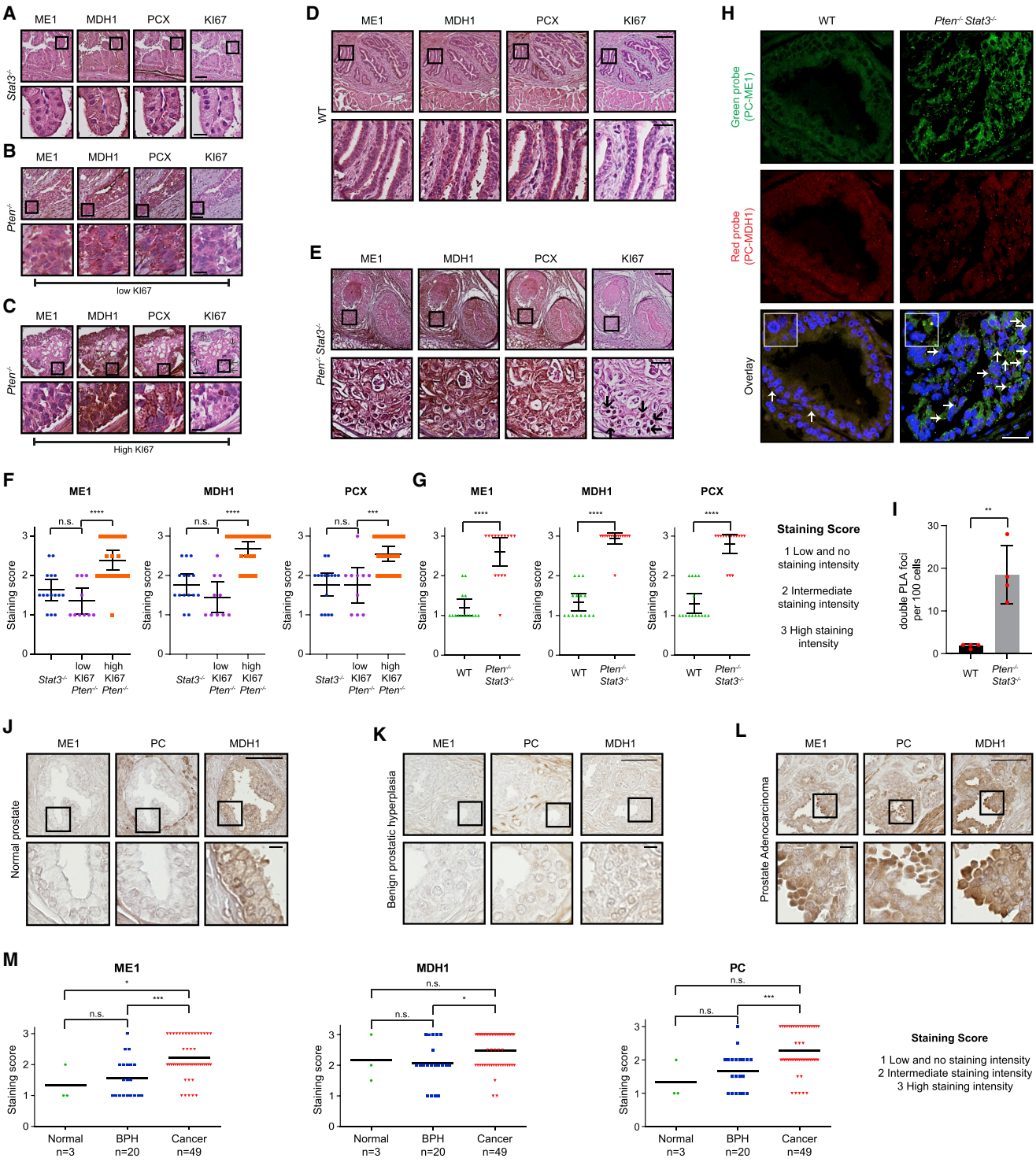

Figure 6. HTC enzymes are overexpressed in prostate cancer

(A-E) Immunohistochemistry (IHC) images detecting HTC enzymes (ME1, MDH1 and PCX) from mouse prostate samples. Samples are from animals with *Stat3*$^{-/-}$ (A), *Pten* $^{-/-}$ displaying areas of prostate tissue with low KI67 staining (B), *Pten*$^{-/-}$ displaying areas of prostate tissue with high KI67 staining (C), wild type (WT) (D), or *Pten*$^{-/-}$ *Stat3*$^{-/-}$ (E). All images scale, 100 μm; zoom scale, 20 μm; n = 5–7 mice.

(F and G) Quantification of (A–C) (F) and quantification of (D and E) (G) according to the scoring key of levels of ME1, MDH1, and PCX from three regions per animal. Colored symbols represent different quantifications and mean, and 95% confidence interval is shown in black bars.

(legend continued on next page)

6B and 6C). PLA with PC and ME1 or PC and MDH1 antibodies confirmed colocalization of HTC enzymes in *Stat3*$^{-/-}$ *Pten*$^{-/-}$ tumors (Figures 6H and 6I). We also found high intensity staining for each of the HTC enzymes in more than 60% of human prostate adenocarcinomas, but low staining in normal prostates or prostates with benign prostatic hyperplasia (BPH) (Figure 6J–6M). Together, these results suggest that HTC enzymes play a pivotal role in prostate cancer.

HTC suppresses both OIS and replicative senescence in fibroblasts and rescues cells treated with complex I inhibitors

We previously reported mitochondrial dysfunction (Moiseeva et al., 2009) and STAT3 reduction (Deschênes-Simard et al., 2013) upon OIS. Overexpression of HTC enzymes counteracted RAS-induced senescence in IMR90 cells (Figures S9A and S9B). Of note, these effects required simultaneous overexpression of all three HTC enzymes (Figures S9A and S9B). Moreover, deleting the mitochondrial localization signal from PC did not alter its ability to bypass OIS in combination with MDH1 and ME1 (Figures S9C–S9F), nor the capacity to restore NAD^+/NADH ratio (Figure S9G), which is consistent with an anti-senescence role for cytosolic PC. HTC also bypassed OIS in BJ fibroblasts more efficiently than in IMR90 (Figures S9H–S9J).

To investigate whether HTC can rescue cells that are already senescent, we induced OIS in MEFs using oncogenic RAS (Figures S10A–S10D). As expected, RAS-senescent cells are highly sensitive to the senolytic agent ABT-263 (Figure S10E). We infected the senescent cell population and control cells with lentiviral vectors expressing HTC. HTC was able to induce cell proliferation in RAS-senescent cells (Figure S10F). To investigate whether cells that proliferate were senescent and not a minor fraction of non-senescent cells in the population, we treated the cells with ABT-263 after infection. HTC-expressing RAS cells were more sensitive to ABT-263 than controls as evaluated 24 h after treatment, indicating that HTC is not immediately rescuing cells from senescence (Figure S10G). However, after seven days of recovery, RAS cells with HTC escaped from senescence (Figure S10H) while RAS cells with empty vectors remained senescent. Importantly, this escape from senescence was prevented when RAS-senescent cells were treated with ABT-263 (Figure S10H), indicating that HTC acts on senescent cells and not on a subpopulation of non-senescent cells. The expression of RAS and HTC enzymes was confirmed in cell extracts from individual clones that escaped senescence (Figure S10I). We did not succeed at promoting proliferation in cultures of RAS-senescent IMR90 after infection with lentiviral vectors expressing HTC, but we did induce proliferation in RAS-senescent BJ human fibroblasts after infection with the same vectors (Figures S10J–S10N). This result is consistent with findings showing that inactivation of p53 and RB can reverse senescence in BJ but not in other strains of normal fibroblasts (Beauséjour et al., 2003).

Although in the context of oncogene expression HTC may favor malignant transformation this complex may play an adaptive role. For example, in normal human fibroblasts, expression of HTC enzymes increased the NAD^+/NADH ratio and delayed replicative senescence (Figures 7A–7F). Also, HTC enzymes rescued proliferation inhibition by complex I inhibitor Piericidin A (Figure 7G), suggesting that HTC may contribute to homeostatic adaptation to mitochondrial dysfunction. This may occur during oxygen deprivation. Hypoxia decreases mitochondrial respiration and rewires metabolism to limit excessive ROS production, inhibiting pyruvate entry into mitochondria and increasing glycolysis (Kim et al., 2006). In such contexts, HTC may contribute to metabolic reprogramming by supplying NAD^+ for glycolysis and NADPH to avoid excessive ROS-mediated toxicity. Consistent with this idea, treatment of normal human fibroblasts with the hypoxia mimetic $CoCl_2$ increased the fraction of PC localized to the cytosol where it can cooperate with MDH1 and ME1 in HTC (Figures 7H and 7I). Furthermore, incubation of IMR90 cells expressing oncogenic RAS in 1% oxygen led to an increase in HTC foci formation together with the induction of several hypoxia-regulated mRNAs compared with IMR90 RAS cells in normoxia (Figures 7J–7L). Hypoxia bypasses Ras-induced senescence (Kilic Eren and Tabor, 2014), but depletion of HTC enzymes blocked this effect (Figures 7M–7O). These results suggest that HTC may contribute to the senescence bypass observed in cells growing in hypoxic conditions (Parrinello et al., 2003).

DISCUSSION

We demonstrate that NAD metabolism alterations secondary to mitochondrial dysfunction can be compensated by a previously unrecognized metabolic cycle that transfers the hydride ion (H^-) from NADH to NADP, regenerating NAD^+, and supplying NADPH for anabolism and redox defenses. This metabolic cycle is catalyzed by an enzyme complex assembled by MDH1, ME1, and PC dubbed HTC. The net stoichiometry of the HTC cycle is: ATP + NADH + $NADP^+$ → ADP + Pi + H^+ + NAD^+ + NADPH. Hence, HTC represents a carbon-saving strategy to regenerate NAD^+ and produce NADPH at the expense of ATP. Interestingly, the reactions catalyzed by HTC seem to be confined in localized phase-separated cytosolic structures. Notwithstanding that MDH1, ME1, and PC co-immunoprecipitate from cells, it is likely that other proteins are also present in these structures. These foci may allow for a localized metabolic recycling of pyruvate, OAA, and malate without affecting the cellular pool of these

(H) Proximity ligation assay with green (ME1-PC) and red (MDH1-PC) PLA probes on mouse prostate samples with either WT genotype or double knockout of *Stat3* and *Pten*. In the overlay, the white arrows indicate double colocalization of PLA probes green and PLA probes red; scale, 25 μm.
(I) Quantification of PLA colocalization. 100 cells were counted and amount of double colocalization is shown; two-tailed t test to assess significance is indicated, n = 4 mice.
(J–L) IHC images of prostate tissue microarray with indicated antibodies. Images are serial images (prostate adenocarcinoma n = 49, normal n = 3, BPH n = 20); scale, 100 μm and zoom scale, 10 μm.
(M) Quantification of (J–L) according to scoring key of levels of ME1, MDH1, and PC from random prostate epithelial regions per sample.
(A–E, H, and J–L) show representative images. Mann-Whitney statistical U test was performed to assess significance for (F–G and M).

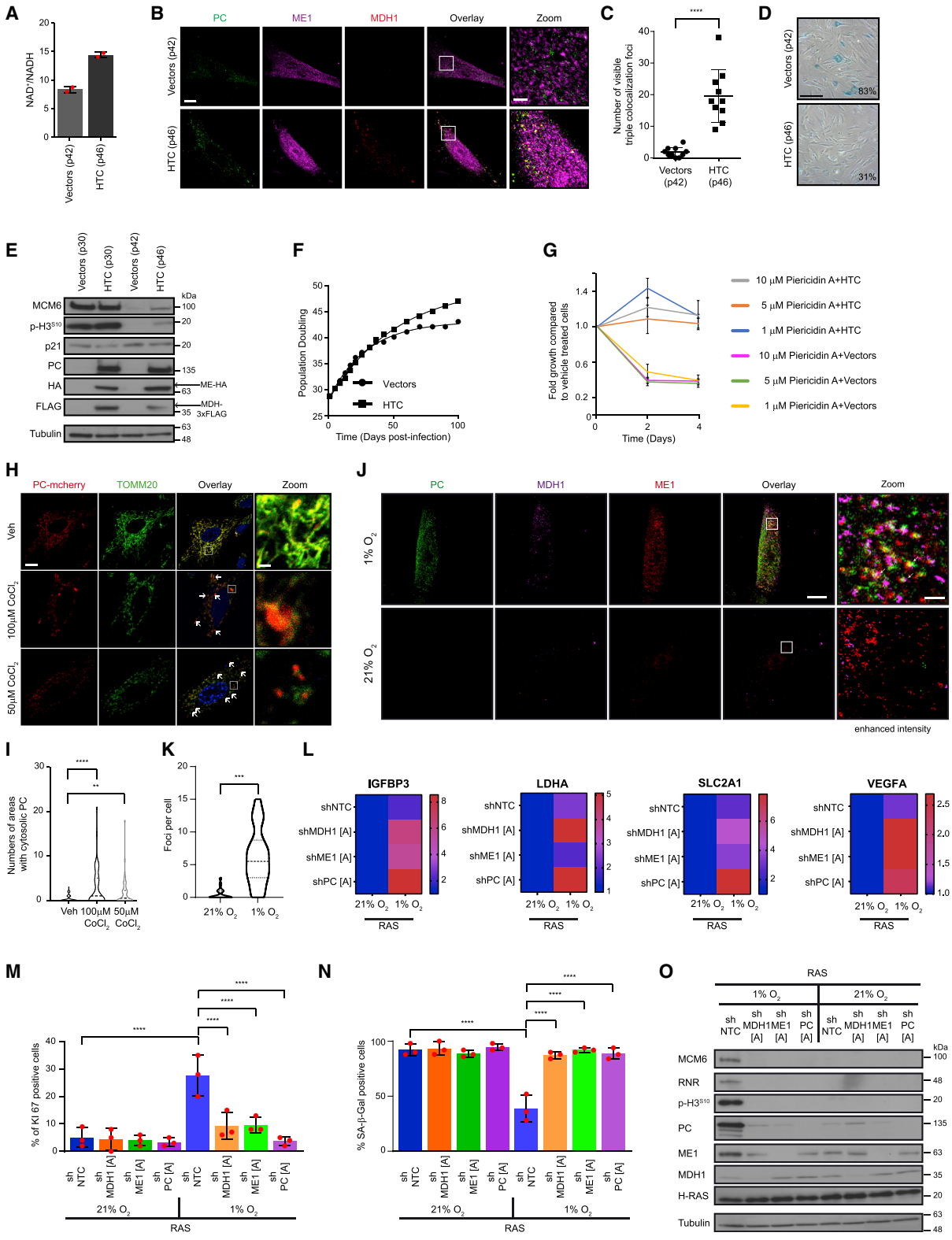

Figure 7. HTC enzymes extend lifespan of normal cells and prevent the action of mitochondrial poisons

(A) Mean NAD^+/NADH ratio in IMR90 cells expressing HTC enzymes (MDH1-3xFLAG, ME1-HA, and PC) or control vectors and grown until replicative senescence for Vector cells (p42). Biological replicate measures are shown in red dots, error bars represent SD.

(legend continued on next page)

metabolites. In addition, the proximity of the active centers for each enzyme in the complex may accelerate metabolic flux by diffusion or the channeling of each substrate (Wheeldon et al., 2016).

Our data demonstrate that HTC plays a role in tumor formation by bypassing or promoting the escape from cellular senescence. Expression of HTC enzymes is sufficient to transform primary mouse fibroblasts in cooperation with oncogenic RAS and is therefore functionally equivalent to a loss of p53. Because HTC enzymes are repressed by p53, our work adds to evidence showing that controlling metabolism is a major tumor suppressor function of p53 (Moon et al., 2019; Morris et al., 2019). Of note, previous work showed that increasing antioxidant capacity by expressing G6PD can transform immortalized but non-tumorigenic fibroblasts (Zhang et al., 2021). HTC provides then two functions for transformation, immortalization dependent on NAD^+ regeneration, and antioxidant activity dependent on NADPH generation. These functions are also important for the survival of cells in hypoxia or for cells growing in lactate that cannot use the LDH reaction to regenerate NAD^+.

We show that the expression of HTC enzymes and their interaction is increased in samples from prostate cancer patients. PC is also highly expressed in metastatic breast cancer (Shinde et al., 2018), non-small cell lung cancer, glioblastoma, renal carcinoma, and gallbladder cancer (Lao-On et al., 2018). MDH1 is amplified in multiple human cancers (Hanse et al., 2017) and MDH1 but not MDH2 is required for cell proliferation of tumor cell lines (Zhang et al., 2017). Moreover, ME1 expression is associated with poor prognosis in gastric cancer (Lu et al., 2018). Finally, analysis of co-expression of HTC enzymes in Oncomine revealed positive correlations between HTC enzyme expression in several cancers including small squamous lung cancer and prostate cancer. Our results therefore suggest that targeting HTC may be exploited to develop anti-cancer treatments.

Limitations of the study

We identified a cytosolic pool of the mitochondrial enzyme PC, but the mechanisms responsible for PC localization to the cytosol upon p53 inactivation remain unknown. Even though, we were able to show evidence of HTC formation *in vitro*, the efficiency of complex assembly is relatively low. This suggests that the recombinant proteins may lack post-translational modifications that help stabilize the HTC complex. We provide evidence that PC, MDH1, and ME1 are the core of the HTC complex, but we could not estimate their precise stoichiometry. Importantly, our data suggest that at least some HTC is contained in complexes larger than 1 MDa, suggesting the presence of additional components. While future work is warranted to answer above questions, our present findings enrich the notion that tumor cells hijack specific metabolic pathways that support proliferation and anabolic reactions while conferring protection to oxidative stress.

STAR★METHODS

Detailed methods are provided in the online version of this paper and include the following:

- KEY RESOURCES TABLE
- RESOURCE AVAILABILITY
  - Lead contact
  - Materials availability
  - Data and code availability
- EXPERIMENTAL MODEL AND SUBJECT DETAILS
  - Mouse Model
  - Cell culture model
- METHODS DETAILS
  - Reagents
  - Plasmids
  - Proliferation analysis and Senescence associated β-galactosidase staining (SA-β-Gal).
  - Retroviral and Lentiviral infections
  - Pyruvate/Aspartate/Duroquinone/ Dimethylmalate/ and $CoCl_2$ supplementation
  - Cell culture with hypoxia
  - MitoTracker staining
  - Hexanediol treatment
  - Immunoblots and Immunoprecipitation
  - Protein purification
  - Native separation of multi-protein complexes
  - Avidin pull down
  - Assembly of ternary complex

(B) IF of cells as in (A) using antibodies for each HTC enzyme as indicated. Scale, 20 μm; zoom scale, 2 μm.
(C) Quantification of foci observed in (B). Number of foci was counted in 10 different cells, and statistics were done using a two-tailed t test.
(D) SA-β-Gal staining on cells as in (A); percent of postive cells is indicated at the bottom right; scale, 250 μm.
(E) WB for the indicated proteins in early or late passage cells expressing HTC or an empty vector, n = 2 for (A, B, D, and E).
(F) Population doubling of cells as in (A). A trendline was added with the linear regression function of Graph Pad, image represents one biological replicate.
(G) Relative fold proliferation of cells expressing HTC enzymes (MDH1, ME1, and PC) or control vectors, treated with indicated concentrations of Piericidin A. Data are normalized to the growth of vehicle-treated cells and show a representative image of n = 3.
(H) IF of IMR90 cells expressing PC-cherry treated with indicated amounts of $CoCl_2$. An anti-TOMM20 (green) antibody was used to reveal mitochondria, n = 2; scale, 10 μm, zoom, 1 μm.
(I) Quantification of PC-cherry signal outside of mitochondria from cells as in (H). A minimum of 25 cells were counted per slide. The violin plot represents the amount of PC-cherry signal outside of mitochondria of two independent immunofluorescent slides. A two-tailed t test was performed.
(J) IF of IMR90 cells expressing RAS cultured in 21% oxygen or 1% oxygen using antibodies for each HTC enzyme as indicated. Scale, 20 μm; zoom scale, 2 μm.
(K) Quantification of HTC foci in cells as in (J). Dashed lines represent median and quartiles. A two-tailed t test was performed.
(L) Heat maps of relative mRNA levels for indicated genes of IMR90 infected with RAS and shRNAs against MDH1, ME1, or PC or control vector (shNTC) followed by either incubation of cells in 21% oxygen or 1% oxygen, n = 2–3.
(M and N) Percent of KI67 positive cells (M) and SA-β-Gal positive cells (N) in cells as (L). Red dots represent biological value of each replicate. Statistical analysis was done with ANOVA with Dunnett's test.
(O) WB for the indicated proteins in cells as in (L).

- SEC-MALS
- Immunofluorescence
- Immunohistochemistry
- STAT3-ATAD3A Proximity ligation assay (PLA)
- PC-MDH1 and PC-ME1 Proximity ligation assay (PLA)
- Electron microscopy and colloidal gold immunocytochemistry
- NAD^+/ NADH, $NADP^+$/ NADPH and glutathione measurements
- qPCR
- MitoSox and DCFDA measurements
- Mitochondrial purification
- Animals
- Stable Isotope Tracer Analysis
- Bioenergetic Analyses
- Nucleotide and nucleoside analysis
- Bioinformatic analysis

- QUANTIFICATION AND STATISTICAL ANALYSIS
- ADDITIONAL RESOURCES

SUPPLEMENTAL INFORMATION

Supplemental information can be found online at https://doi.org/10.1016/j.molcel.2021.08.028.

ACKNOWLEDGMENTS

We thank M. Ali, D. Avizonis, M. Birlea, N. Chandel, P. Chartrand, L. Choinière, N. Cyr, L. G. Dadwhal, P. Dagenais, DesGroseillers, D. Gagné, A. Gosselin, J. Hinsinger, P. Legault, S.W. Lowe, S. Meloche, H. Neubauer, J. Pascal, S. Roy, A. Salvail-Lacoste, N. Stifani, L. Tong, S. Truche, D. Trudel, and M. Vasseur for reagents, comments, and/or technical help. Metabolic analysis was performed at The Rosalind and Morris Goodman Cancer Research Centre's Metabolomics Core Facility. Immunohistochemistry was performed at the IRIC's Histology Core Facility or the Molecular Pathology platform of CR-CHUM. We thank the Platform of microscopy of the Biochemistry and Molecular Medicine Department and the electron microscopy platform of the University of Montreal. A detailed list can be found on Mendeley as well as detailed author contributions. Work was supported by grants from CIHR (MOP11151 and PJT-153217) and CCSRI Innovation 706773 to G.F., CIHR MOP130414 to J.G.O., and TFF Oncometabolism Team Grant 239585 to I.T. and M.P. G.F. is supported by the CIBC chair for breast cancer research. S.I. was supported by NSERC CREATE Trainee program and ICM (Institut du cancer de Montréal) Canderel fellowship. F.L. was supported by FRQS (Fonds de Recherche du Québec-Santé). D.P. is supported by a CIHR Postdoctoral Fellowship (MFE-171312). O.U. was supported from FRQS. J.P. was supported by Max Kade fellowship from the Austrian Academy of Sciences. I.T. is supported by FRQS Senior award. L.H. is supported by FRQS Junior 1 award. A.N. is supported by the Canadian Institutes of Health Research grant (CIHR MOP-110972) and is recipient of a Canada Research Chair in Calcified tissues, Biomaterials and Structural Imaging. E.T. acknowledges funding from CIHR (MOP-133726). L.K was supported by the COMET Competence Center CBmed-Center for Biomarker Research in Medicine (FA791A0906.FFG). The COMET Competence Center CBmed is funded by the Austrian Federal Ministry for Transport, Innovation and Technology (BMVIT); the Austrian Federal Ministry for Digital and Economic Affairs (BMDW); Land Steiermark (Department 12, Business and Innovation); the Styrian Business Promotion Agency (SFG); and the Vienna Business Agency. The COMET program is executed by the FFG. L.K. was in addition funded by the FWF grant P26011 and the Christian Doppler Laboratory for Applied Metabolomics. The financial support by the Austrian Federal Ministry for Transport, Innovation and Technology and the National Foundation for Research, Technology and Development is gratefully acknowledged. R.M. was supported by grants SFB-F4707, SFB-F06107 and EU Transcan-2 consortium ERANET-PLL, all funded via the Austrian Science Funds.

AUTHOR CONTRIBUTIONS

Conceptualization, S.I. and G.F.; validation, F.L., J.B., A.F., G.H., H.M.W., and V.B.; methodology, J.Q., J.G., L.H., A.F., H.M.W., and J.P. ; formal analysis, S.I.; investigation, S.I., F.L., O.U., A.F.-R., J.B., M.-C.R., S.L.-P., J.Q, D.P., A.F., K.J.P., G.H., L.M., M.B., V.B., and L.H.; resources, E.G., L.K., R.M., A.N., J.G.O., I.T., and G.F.; data curation, S.I., O.U., and G.F.; writing – original draft, S.I. and G.F.; writing – review & editing, all authors; visualization, S.I., M.L., P.K., and V.B.; supervision, V.B., A.N., M.N.P, J.G.O., I.T., and G.F.; project administration, V.B. and G.F.; funding acquisition, E.G., R.M., A.N., M.N.P., J.G.O., I.T., and G.F.

DECLARATION OF INTERESTS

The authors declare no competing interests.

INCLUSION AND DIVERSITY

One or more of the authors of this paper self-identifies as an underrepresented ethnic minority in science.

Received: December 14, 2020
Revised: June 25, 2021
Accepted: August 20, 2021
Published: September 16, 2021

SUPPORTING CITATIONS

The following references appear in the supplemental information: Asher et al. (2005); Birts et al. (2020); Chabes et al. (2004).

REFERENCES

Asher, G., Tsvetkov, P., Kahana, C., and Shaul, Y. (2005). A mechanism of ubiquitin-independent proteasomal degradation of the tumor suppressors p53 and p73. Genes Dev. *19*, 316–321.

Audet-Walsh, É., Papadopoli, D.J., Gravel, S.P., Yee, T., Bridon, G., Caron, M., Bourque, G., Giguère, V., and St-Pierre, J. (2016). The PGC-1α/ERRα Axis Represses One-Carbon Metabolism and Promotes Sensitivity to Anti-folate Therapy in Breast Cancer. Cell Rep. *14*, 920–931.

Beauséjour, C.M., Krtolica, A., Galimi, F., Narita, M., Lowe, S.W., Yaswen, P., and Campisi, J. (2003). Reversal of human cellular senescence: roles of the p53 and p16 pathways. EMBO J. *22*, 4212–4222.

Birsoy, K., Possemato, R., Lorbeer, F.K., Bayraktar, E.C., Thiru, P., Yucel, B., Wang, T., Chen, W.W., Clish, C.B., and Sabatini, D.M. (2014). Metabolic determinants of cancer cell sensitivity to glucose limitation and biguanides. Nature *508*, 108–112.

Birsoy, K., Wang, T., Chen, W.W., Freinkman, E., Abu-Remaileh, M., and Sabatini, D.M. (2015). An Essential Role of the Mitochondrial Electron Transport Chain in Cell Proliferation Is to Enable Aspartate Synthesis. Cell *162*, 540–551.

Birts, C.N., Banerjee, A., Darley, M., Dunlop, C.R., Nelson, S., Nijjar, S.K., Parker, R., West, J., Tavassoli, A., Rose-Zerilli, M.J.J., and Blaydes, J.P. (2020). p53 is regulated by aerobic glycolysis in cancer cells by the CtBP family of NADH-dependent transcriptional regulators. Sci. Signal. *13*, eaau9529.

Buescher, J.M., Antoniewicz, M.R., Boros, L.G., Burgess, S.C., Brunengraber, H., Clish, C.B., DeBerardinis, R.J., Feron, O., Frezza, C., Ghesquiere, B., et al. (2015). A roadmap for interpreting (13)C metabolite labeling patterns from cells. Curr. Opin. Biotechnol. *34*, 189–201.

Camacho-Carvajal, M.M., Wollscheid, B., Aebersold, R., Steimle, V., and Schamel, W.W. (2004). Two-dimensional Blue native/SDS gel electrophoresis of multi-protein complexes from whole cellular lysates: a proteomics approach. Mol. Cell. Proteomics *3*, 176–182.

Cao, Z., Zhou, Y., Zhu, S., Feng, J., Chen, X., Liu, S., Peng, N., Yang, X., Xu, G., and Zhu, Y. (2016). Pyruvate Carboxylase Activates the RIG-I-like Receptor-

Mediated Antiviral Immune Response by Targeting the MAVS signalosome. Sci. Rep. *6*, 22002.

Carbognin, E., Betto, R.M., Soriano, M.E., Smith, A.G., and Martello, G. (2016). Stat3 promotes mitochondrial transcription and oxidative respiration during maintenance and induction of naive pluripotency. EMBO J. *35*, 618–634.

Chabes, A.L., Björklund, S., and Thelander, L. (2004). S Phase-specific transcription of the mouse ribonucleotide reductase R2 gene requires both a proximal repressive E2F-binding site and an upstream promoter activating region. J. Biol. Chem. *279*, 10796–10807.

Chen, W.W., Freinkman, E., and Sabatini, D.M. (2017). Rapid immunopurification of mitochondria for metabolite profiling and absolute quantification of matrix metabolites. Nat. Protoc. *12*, 2215–2231.

Cheng, T., Sudderth, J., Yang, C., Mullen, A.R., Jin, E.S., Matés, J.M., and DeBerardinis, R.J. (2011). Pyruvate carboxylase is required for glutamine-independent growth of tumor cells. Proc. Natl. Acad. Sci. USA *108*, 8674–8679.

Consortium, E.P.; ENCODE Project Consortium (2012). An integrated encyclopedia of DNA elements in the human genome. Nature *489*, 57–74.

Davis, C.A., Hitz, B.C., Sloan, C.A., Chan, E.T., Davidson, J.M., Gabdank, I., Hilton, J.A., Jain, K., Baymuradov, U.K., Narayanan, A.K., et al. (2018). The Encyclopedia of DNA elements (ENCODE): data portal update. Nucleic Acids Res. *46* (D1), D794–D801.

Deschênes-Simard, X., Gaumont-Leclerc, M.F., Bourdeau, V., Lessard, F., Moiseeva, O., Forest, V., Igelmann, S., Mallette, F.A., Saba-El-Leil, M.K., Meloche, S., et al. (2013). Tumor suppressor activity of the ERK/MAPK pathway by promoting selective protein degradation. Genes Dev. *27*, 900–915.

Deschênes-Simard, X., Lessard, F., Gaumont-Leclerc, M.F., Bardeesy, N., and Ferbeyre, G. (2014). Cellular senescence and protein degradation: Breaking down cancer. Cell cycle *13*, 1840–1858.

Deschênes-Simard, X., Parisotto, M., Rowell, M.C., Le Calvé, B., Igelmann, S., Moineau-Vallée, K., Saint-Germain, E., Kalegari, P., Bourdeau, V., Kottakis, F., et al. (2019). Circumventing senescence is associated with stem cell properties and metformin sensitivity. Aging Cell *18*, e12889.

Dörr, J.R., Yu, Y., Milanovic, M., Beuster, G., Zasada, C., Däbritz, J.H., Lisec, J., Lenze, D., Gerhardt, A., Schleicher, K., et al. (2013). Synthetic lethal metabolic targeting of cellular senescence in cancer therapy. Nature *501*, 421–425.

Faubert, B., Li, K.Y., Cai, L., Hensley, C.T., Kim, J., Zacharias, L.G., Yang, C., Do, Q.N., Doucette, S., Burguete, D., et al. (2017). Lactate Metabolism in Human Lung Tumors. Cell *171*, 358–371.

Ferbeyre, G., de Stanchina, E., Querido, E., Baptiste, N., Prives, C., and Lowe, S.W. (2000). PML is induced by oncogenic ras and promotes premature senescence. Genes Dev. *14*, 2015–2027.

Fishilevich, S., Nudel, R., Rappaport, N., Hadar, R., Plaschkes, I., Iny Stein, T., Rosen, N., Kohn, A., Twik, M., Safran, M., et al. (2017). GeneHancer: genome-wide integration of enhancers and target genes in GeneCards. Database (Oxford) *2017*, bax028.

Fouillen, A., Dos Santos Neves, J., Mary, C., Castonguay, J.D., Moffatt, P., Baron, C., and Nanci, A. (2017). Interactions of AMTN, ODAM and SCPPPQ1 proteins of a specialized basal lamina that attaches epithelial cells to tooth mineral. Sci. Rep. *7*, 46683.

Ghandi, M., Huang, F.W., Jané-Valbuena, J., Kryukov, G.V., Lo, C.C., McDonald, E.R., 3rd, Barretina, J., Gelfand, E.T., Bielski, C.M., Li, H., et al. (2019). Next-generation characterization of the Cancer Cell Line Encyclopedia. Nature *569*, 503–508.

Gillies, R.J., Didier, N., and Denton, M. (1986). Determination of cell number in monolayer cultures. Anal. Biochem. *159*, 109–113.

Gough, D.J., Corlett, A., Schlessinger, K., Wegrzyn, J., Larner, A.C., and Levy, D.E. (2009). Mitochondrial STAT3 supports Ras-dependent oncogenic transformation. Science *324*, 1713–1716.

Gravel, S.P., Avizonis, D., and St-Pierre, J. (2016). Metabolomics Analyses of Cancer Cells in Controlled Microenvironments. Methods Mol. Biol. *1458*, 273–290.

Gui, D.Y., Sullivan, L.B., Luengo, A., Hosios, A.M., Bush, L.N., Gitego, N., Davidson, S.M., Freinkman, E., Thomas, C.J., and Vander Heiden, M.G. (2016). Environment Dictates Dependence on Mitochondrial Complex I for NAD+ and Aspartate Production and Determines Cancer Cell Sensitivity to Metformin. Cell Metab. *24*, 716–727.

Hanse, E.A., Ruan, C., Kachman, M., Wang, D., Lowman, X.H., and Kelekar, A. (2017). Cytosolic malate dehydrogenase activity helps support glycolysis in actively proliferating cells and cancer. Oncogene *36*, 3915–3924.

Huet, C., Menendez, J., Gancedo, C., and François, J.M. (2000). Regulation of pyc1 encoding pyruvate carboxylase isozyme I by nitrogen sources in Saccharomyces cerevisiae. Eur. J. Biochem. *267*, 6817–6823.

Jiang, P., Du, W., Mancuso, A., Wellen, K.E., and Yang, X. (2013). Reciprocal regulation of p53 and malic enzymes modulates metabolism and senescence. Nature *493*, 689–693.

Kidder, B.L., Yang, J., and Palmer, S. (2008). Stat3 and c-Myc genome-wide promoter occupancy in embryonic stem cells. PLoS ONE *3*, e3932.

Kilic Eren, M., and Tabor, V. (2014). The role of hypoxia inducible factor-1 alpha in bypassing oncogene-induced senescence. PLoS ONE *9*, e101064.

Kim, J.W., Tchernyshyov, I., Semenza, G.L., and Dang, C.V. (2006). HIF-1-mediated expression of pyruvate dehydrogenase kinase: a metabolic switch required for cellular adaptation to hypoxia. Cell Metab. *3*, 177–185.

Krall, A.S., Mullen, P.J., Surjono, F., Momcilovic, M., Schmid, E.W., Halbrook, C.J., Thambundit, A., Mittelman, S.D., Lyssiotis, C.A., Shackelford, D.B., et al. (2021). Asparagine couples mitochondrial respiration to ATF4 activity and tumor growth. Cell Metab. *33*, 1013–1026.

Lao-On, U., Attwood, P.V., and Jitrapakdee, S. (2018). Roles of pyruvate carboxylase in human diseases: from diabetes to cancers and infection. J. Mol. Med. (Berl.) *96*, 237–247.

Lee, S.M., Dho, S.H., Ju, S.K., Maeng, J.S., Kim, J.Y., and Kwon, K.S. (2012). Cytosolic malate dehydrogenase regulates senescence in human fibroblasts. Biogerontology *13*, 525–536.

Lessard, F., Igelmann, S., Trahan, C., Huot, G., Saint-Germain, E., Mignacca, L., Del Toro, N., Lopes-Paciencia, S., Le Calvé, B., Montero, M., et al. (2018). Senescence-associated ribosome biogenesis defects contributes to cell cycle arrest through the Rb pathway. Nat. Cell Biol. *20*, 789–799.

Li, X., Cheng, K.K.Y., Liu, Z., Yang, J.K., Wang, B., Jiang, X., Zhou, Y., Hallenborg, P., Hoo, R.L.C., Lam, K.S.L., et al. (2016). The MDM2-p53-pyruvate carboxylase signalling axis couples mitochondrial metabolism to glucose-stimulated insulin secretion in pancreatic β-cells. Nat. Commun. *7*, 11740.

Lu, Y.X., Ju, H.Q., Liu, Z.X., Chen, D.L., Wang, Y., Zhao, Q., Wu, Q.N., Zeng, Z.L., Qiu, H.B., Hu, P.S., et al. (2018). ME1 Regulates NADPH Homeostasis to Promote Gastric Cancer Growth and Metastasis. Cancer Res. *78*, 1972–1985.

Macias, E., Rao, D., Carbajal, S., Kiguchi, K., and DiGiovanni, J. (2014). Stat3 binds to mtDNA and regulates mitochondrial gene expression in keratinocytes. J. Invest. Dermatol. *134*, 1971–1980.

Mallette, F.A., Gaumont-Leclerc, M.F., and Ferbeyre, G. (2007). The DNA damage signaling pathway is a critical mediator of oncogene-induced senescence. Genes Dev. *21*, 43–48.

Mantel, C., Messina-Graham, S., Moh, A., Cooper, S., Hangoc, G., Fu, X.Y., and Broxmeyer, H.E. (2012). Mouse hematopoietic cell-targeted STAT3 deletion: stem/progenitor cell defects, mitochondrial dysfunction, ROS overproduction, and a rapid aging-like phenotype. Blood *120*, 2589–2599.

Mascle, X.H., Gagnon, C., Wahba, H.M., Lussier-Price, M., Cappadocia, L., Sakaguchi, K., and Omichinski, J.G. (2020). Acetylation of SUMO1 Alters Interactions with the SIMs of PML and Daxx in a Protein-Specific Manner. Structure *28*, 157–168.

McBride, H.M., Goping, I.S., and Shore, G.C. (1996). The human mitochondrial import receptor, hTom20p, prevents a cryptic matrix targeting sequence from gaining access to the protein translocation machinery. J. Cell Biol. *134*, 307–313.

McGuirk, S., Gravel, S.P., Deblois, G., Papadopoli, D.J., Faubert, B., Wegner, A., Hiller, K., Avizonis, D., Akavia, U.D., Jones, R.G., et al. (2013). PGC-1α

supports glutamine metabolism in breast cancer. Cancer Metab. *1*. https://doi.org/10.1186/2049-3002-1-22.

Moiseeva, O., Bourdeau, V., Roux, A., Deschênes-Simard, X., and Ferbeyre, G. (2009). Mitochondrial dysfunction contributes to oncogene-induced senescence. Mol. Cell. Biol. *29*, 4495–4507.

Moiseeva, O., Bourdeau, V., Vernier, M., Dabauvalle, M.C., and Ferbeyre, G. (2011). Retinoblastoma-independent regulation of cell proliferation and senescence by the p53-p21 axis in lamin A /C-depleted cells. Aging Cell *10*, 789–797.

Moiseeva, O., Guillon, J., and Ferbeyre, G. (2020). Senescence: A program in the road to cell elimination and cancer. In Seminars in cancer biology (Academic Press).

Moon, S.H., Huang, C.H., Houlihan, S.L., Regunath, K., Freed-Pastor, W.A., Morris, J.P.t., Tschaharganeh, D.F., Kastenhuber, E.R., Barsotti, A.M., Culp-Hill, R., et al. (2019). p53 Represses the Mevalonate Pathway to Mediate Tumor Suppression. Cell *176*, 564–580.

Morris, J.P., 4th, Yashinskie, J.J., Koche, R., Chandwani, R., Tian, S., Chen, C.C., Baslan, T., Marinkovic, Z.S., Sánchez-Rivera, F.J., Leach, S.D., et al. (2019). α-Ketoglutarate links p53 to cell fate during tumour suppression. Nature *573*, 595–599.

Nagaraj, R., Sharpley, M.S., Chi, F., Braas, D., Zhou, Y., Kim, R., Clark, A.T., and Banerjee, U. (2017). Nuclear Localization of Mitochondrial TCA Cycle Enzymes as a Critical Step in Mammalian Zygotic Genome Activation. Cell *168*, 210–223.

Nguyen, T.T., Grimm, S.A., Bushel, P.R., Li, J., Li, Y., Bennett, B.D., Lavender, C.A., Ward, J.M., Fargo, D.C., Anderson, C.W., et al. (2018). Revealing a human p53 universe. Nucleic Acids Res. *46*, 8153–8167.

Oki, S., Ohta, T., Shioi, G., Hatanaka, H., Ogasawara, O., Okuda, Y., Kawaji, H., Nakaki, R., Sese, J., and Meno, C. (2018). ChIP-Atlas: a data-mining suite powered by full integration of public ChIP-seq data. EMBO Rep. *19*, e46255.

Parrinello, S., Samper, E., Krtolica, A., Goldstein, J., Melov, S., and Campisi, J. (2003). Oxygen sensitivity severely limits the replicative lifespan of murine fibroblasts. Nat. Cell Biol. *5*, 741–747.

Passos, J.F., Saretzki, G., Ahmed, S., Nelson, G., Richter, T., Peters, H., Wappler, I., Birket, M.J., Harold, G., Schaeuble, K., et al. (2007). Mitochondrial dysfunction accounts for the stochastic heterogeneity in telomere-dependent senescence. PLoS Biol. *5*, e110.

Pencik, J., Schlederer, M., Gruber, W., Unger, C., Walker, S.M., Chalaris, A., Marié, I.J., Hassler, M.R., Javaheri, T., Aksoy, O., et al. (2015). STAT3 regulated ARF expression suppresses prostate cancer metastasis. Nat. Commun. *6*, 7736.

Pértega-Gomes, N., Vizcaíno, J.R., Attig, J., Jurmeister, S., Lopes, C., and Baltazar, F. (2014). A lactate shuttle system between tumour and stromal cells is associated with poor prognosis in prostate cancer. BMC Cancer *14*, 352.

Serrano, M., Lin, A.W., McCurrach, M.E., Beach, D., and Lowe, S.W. (1997). Oncogenic ras provokes premature cell senescence associated with accumulation of p53 and p16INK4a. Cell *88*, 593–602.

Shinde, A., Wilmanski, T., Chen, H., Teegarden, D., and Wendt, M.K. (2018). Pyruvate carboxylase supports the pulmonary tropism of metastatic breast cancer. Breast Cancer Res. *20*, 76.

Stelzer, G., Rosen, N., Plaschkes, I., Zimmerman, S., Twik, M., Fishilevich, S., Stein, T.I., Nudel, R., Lieder, I., Mazor, Y., et al. (2016). The GeneCards Suite: From Gene Data Mining to Disease Genome Sequence Analyses. Curr Protoc Bioinformatics *54*, 1.30.1–1.30.33.

Stewart, S.A., Dykxhoorn, D.M., Palliser, D., Mizuno, H., Yu, E.Y., An, D.S., Sabatini, D.M., Chen, I.S.Y., Hahn, W.C., Sharp, P.A., et al. (2003). Lentivirus-delivered stable gene silencing by RNAi in primary cells. RNA *9*, 493–501.

Sullivan, L.B., Gui, D.Y., Hosios, A.M., Bush, L.N., Freinkman, E., and Vander Heiden, M.G. (2015). Supporting Aspartate Biosynthesis Is an Essential Function of Respiration in Proliferating Cells. Cell *162*, 552–563.

Tao, X., Yang, Z., and Tong, L. (2003). Crystal structures of substrate complexes of malic enzyme and insights into the catalytic mechanism. Structure *11*, 1141–1150.

Titov, D.V., Cracan, V., Goodman, R.P., Peng, J., Grabarek, Z., and Mootha, V.K. (2016). Complementation of mitochondrial electron transport chain by manipulation of the NAD+/NADH ratio. Science *352*, 231–235.

Tkach, M., Coria, L., Rosemblit, C., Rivas, M.A., Proietti, C.J., Díaz Flaqué, M.C., Beguelin, W., Frahm, I., Charreau, E.H., Cassataro, J., et al. (2012). Targeting Stat3 induces senescence in tumor cells and elicits prophylactic and therapeutic immune responses against breast cancer growth mediated by NK cells and CD4+ T cells. J. Immunol. *189*, 1162–1172.

Vallania, F., Schiavone, D., Dewilde, S., Pupo, E., Garbay, S., Calogero, R., Pontoglio, M., Provero, P., and Poli, V. (2009). Genome-wide discovery of functional transcription factor binding sites by comparative genomics: the case of Stat3. Proc. Natl. Acad. Sci. USA *106*, 5117–5122.

Voorhoeve, P.M., and Agami, R. (2003). The tumor-suppressive functions of the human INK4A locus. Cancer Cell. *4*, 311–319.

Wegrzyn, J., Potla, R., Chwae, Y.J., Sepuri, N.B., Zhang, Q., Koeck, T., Derecka, M., Szczepanek, K., Szelag, M., Gornicka, A., et al. (2009). Function of mitochondrial Stat3 in cellular respiration. Science *323*, 793–797.

Wheeldon, I., Minteer, S.D., Banta, S., Barton, S.C., Atanassov, P., and Sigman, M. (2016). Substrate channelling as an approach to cascade reactions. Nat. Chem. *8*, 299–309.

Wiley, C.D., and Campisi, J. (2016). From Ancient Pathways to Aging Cells-Connecting Metabolism and Cellular Senescence. Cell Metab. *23*, 1013–1021.

Wiley, C.D., Velarde, M.C., Lecot, P., Liu, S., Sarnoski, E.A., Freund, A., Shirakawa, K., Lim, H.W., Davis, S.S., Ramanathan, A., et al. (2016). Mitochondrial Dysfunction Induces Senescence with a Distinct Secretory Phenotype. Cell Metab. *23*, 303–314.

Xiang, S., and Tong, L. (2008). Crystal structures of human and Staphylococcus aureus pyruvate carboxylase and molecular insights into the carboxyltransfer reaction. Nat. Struct. Mol. Biol. *15*, 295–302.

Yu, Y., Schleich, K., Yue, B., Ji, S., Lohneis, P., Kemper, K., Silvis, M.R., Qutob, N., van Rooijen, E., Werner-Klein, M., et al. (2018). Targeting the Senescence-Overriding Cooperative Activity of Structurally Unrelated H3K9 Demethylases in Melanoma. Cancer Cell. *33*, 322–336.

Yuan, R., Liu, Q., Segeren, H.A., Yuniati, L., Guardavaccaro, D., Lebbink, R.J., Westendorp, B., and de Bruin, A. (2019). Cyclin F-dependent degradation of E2F7 is critical for DNA repair and G2-phase progression. EMBO J. *38*, e101430.

Zhang, B., Tornmalm, J., Widengren, J., Vakifahmetoglu-Norberg, H., and Norberg, E. (2017). Characterization of the Role of the Malate Dehydrogenases to Lung Tumor Cell Survival. J. Cancer *8*, 2088–2096.

Zhang, Y., Xu, Y., Lu, W., Ghergurovich, J.M., Guo, L., Blair, I.A., Rabinowitz, J.D., and Yang, X. (2021). Upregulation of Antioxidant Capacity and Nucleotide Precursor Availability Suffices for Oncogenic Transformation. Cell Metab. *33*, 94–109.

STAR★METHODS

KEY RESOURCES TABLE

REAGENT or RESOURCE	SOURCE	IDENTIFIER
Antibodies		
anti-PC mouse monoclonal	Santa Cruz Biotechnology	Cat# sc 365673; RRID:AB_10842023
anti-ME1 rabbit polyclonal	GeneTex	Cat# GTX104122; RRID:AB_1950905
anti p53 mouse monoclonal	Santa Cruz Biotechnology	Cat# sc98; RRID:AB_628085
anti-KI67 rabbit monoclonal	Thermo Fisher Scientific	Cat# RM9106; RRID:AB_2335745
anti-53BP1 rabbit polyclonal	Calbiochem	Cat# PC712; RRID:AB_564982
anti-phospho-γ-H2A.X ^{S139} mouse monoclonal	Millipore	Cat# 05-636-I; RRID:AB_2755003
anti-PML rabbit polyclonal	Bethyl Laboratories	Cat# A301-167A; RRID:AB_873108
anti-TOMM20 rabbit polyclonal	Santa Cruz Biotechnology	Cat# FL-145; RRID:AB_2207533
anti-FLAG rabbit monoclonal	Cell Signaling	Cat# 14793; RRID:AB_2572291
anti-MYC tag mouse monoclonal	Sigma-Aldrich	Cat# M4439; RRID:AB_439694
donkey anti-mouse IgG (H+L) conjugated to Alexa Fluor 405	Abcam	Cat# ab175658; RRID:AB_2687445
donkey anti-rabbit IgG (H+L) conjugated to Alexa Fluor 488	Life Technologies/ Molecular Probes/ Invitrogen/Thermo Fisher Scientific	Cat# A21206; RRID:AB_2535792
donkey anti mouse IgG (H+L) conjugated to Alexa Fluor 488	Life Technologies/ Molecular Probes/ Invitrogen/Thermo Fisher Scientific	Cat# A21202; RRID:AB_141607
goat anti-mouse IgG (H+L) conjugated to Alexa Fluor 488	Life Technologies/ Molecular Probes/ Invitrogen/Thermo Fisher Scientific	Cat# A11029; RRID:AB_138404
donkey anti-goat IgG (H+L) conjugated to Alexa Fluor 488	Life Technologies/ Molecular Probes/ Invitrogen/Thermo Fisher Scientific	Cat# A11055; RRID:AB_2534102
goat anti-rabbit IgG (H+L) conjugated to Alexa Fluor 488	Life Technologies/ Molecular Probes/ Invitrogen/Thermo Fisher Scientific	Cat# A11008; RRID:AB_143165
goat anti-rabbit IgG (H+L) conjugated to Alexa Fluor 568	Life Technologies/ Molecular Probes/ Invitrogen/Thermo Fisher Scientific	Cat# A11036; RRID:AB_10563566
goat anti-mouse IgG (H+L) conjugated to Alexa Fluor 568	Life Technologies/ Molecular Probes/ Invitrogen/Thermo Fisher Scientific	Cat# A11031; RRID:AB_144696
donkey anti-rabbit IgG (H+L) conjugated to Alexa Fluor 568	Life Technologies/ Molecular Probes/ Invitrogen/Thermo Fisher Scientific	Cat# A10042; RRID:AB_2534017
donkey anti-goat IgG (H+L) conjugated to Alexa Fluor 647	Life Technologies/ Molecular Probes/ Invitrogen/Thermo Fisher Scientific	Cat# A21447; RRID:AB_141844
donkey anti-mouse IgG (H+L) conjugated to Alexa Fluor 647	Life Technologies/ Molecular Probes/ Invitrogen/Thermo Fisher Scientific	Cat# A31571; RRID:AB_162542
donkey anti-rabbit IgG (H+L) conjugated to Alexa Fluor 647	Life Technologies/ Molecular Probes/ Invitrogen/Thermo Fisher Scientific	Cat# A31573; RRID:AB_2536183
normal rabbit IgG	Cell Signaling	Cat# 2729S; RRID:AB_1031062
anti-HA mouse monoclonal magnetic beads	Pierce /ThermoFisher	Cat# 88836; RRID:AB_2749815
anti-FLAG mouse monoclonal Affinity Gel	Sigma-Aldrich	Cat# A2220-5ML; RRID:AB_10063035
Dynabeads® Protein G	Invitrogen/ThermoFisher Scientific	Cat# 100.04D; RRID:SCR_008452
Dynabeads® Protein A	Invitrogen/ThermoFisher Scientific	Cat# 10002D; RRID:SCR_008452
anti-H-RAS mouse monoclonal	Santa Cruz Biotechnology	Cat# Sc-29; RRID:AB_627750
anti-p21 mouse monoclonal	BD PharMingen	Cat# 556431; RRID:AB_396415
anti-phospho-H3S10 rabbit polyclonal	Millipore	Cat# 06-570; RRID:AB_310177
anti-PC goat polyclonal	Santa Cruz Biotechnology	Cat# sc46228; RRID:AB_653879
anti-mt-nd1 rabbit polyclonal	Elabscience	Cat# E-AB-32173

(*Continued on next page*)

Continued

REAGENT or RESOURCE	SOURCE	IDENTIFIER
anti-mt-nd4 rabbit polyclonal	Novus Biologicals	Cat# NBP2-47365
anti-MCM6 rabbit polyclonal	Bethyl Laboratories	Cat# A300-194A; RRID:AB_162727
anti-p53 mouse monoclonal	Santa Cruz Biotechnology	Cat# Sc-126; RRID:AB_628082
anti-phospho-p53^{S15} rabbit polyclonal	Cell Signaling	Cat# 9284; RRID:AB_331464
anti-FLAG mouse monoclonal	Sigma-Aldrich	Cat# F1804; RRID:AB_262044
anti-MYC tag rabbit polyclonal	Santa Cruz Biotechnology	Cat# sc-789: RRID:AB_631274
anti-H3 rabbit polyclonal	Abcam	Cat# ab1791; RRID:AB_302613
anti-RNR mouse monoclonal	Santa Cruz Biotechnology	Cat# sc-398294
anti-α-Tubulin mouse monoclonal	Sigma-Aldrich	Cat# T6074: RRID:AB_477582
anti-phospho-RBS^{795} rabbit polyclonal	Cell Signaling	Cat# 9301; RRID:AB_330013
anti-RB mouse monoclonal	BD PharMingen	Cat# 554136 ; RRID:AB_395259
anti-HA tag goat polyclonal	Abcam	Cat# ab9134: RRID:AB_307035
anti-HA tag rabbit polyclonal	Cell Signaling	Cat# 3724 RRID:AB_1549585
anti-HA tag 12CA5 mouse monoclonal	University of Montreal Department of Biochemistry	n/a
anti-MDH1 mouse monoclonal	Santa Cruz Biotechnology	Cat# sc 166880; RRID:AB_10609512
Protein A- Gold 10 nm	Cell Microscopy Core, Department of Cell Biology University Medical Center Utrecht	Cat# PAG 10 nm
goat anti-rabbit IgG (H-L) conjugated to HRP	Bio-Rad	Cat# 170-6515 RRID:AB_11125142
goat anti-mouse IgG (H-L) conjugated to HRP	Bio-Rad	Cat# 170-6516 RRID:AB_11125547
mouse anti-goat IgG HRP	Santa Cruz Biotechnology	Cat# sc-2354; RRID:AB_628490
donkey anti-goat IgG HRP	Santa Cruz Biotechnology	Cat# sc 2020; RRID:AB_631728
mouse anti-rabbit IgG conformation specific HRP L27A9	Cell Signaling	Cat# #3678; RRID:AB_1549606
Rat mAB to Ms IgG HRP confirmation specfic	Abcam	Cat# ab131368
anti-KI67 mouse monoclonal	DAKO	RRID;AB_2631211
anti-LDH mouse monoclonal	Santa Cruz Biotechnology	Cat# sc-133123; RRID:AB_2134964
anti-ATAD3A rabbit polyclonal	Novus Biologicals	Cat# NBP1-76586; RRID:AB_11025339
anti-PC rabbit polyclonal	Novus Biologicals	Cat# NBP1-49536; RRID:AB_10011589
anti-MDH1 rabbit polyclonal	Novus Biologicals	Cat# NBP1-89515; RRID:AB_11036600
Biological samples		
Tissue Micro Array (TMA) of prostate cancer samples	US Biomax Rockville, MD	Cat# PR807c
Chemicals, peptides, and recombinant proteins		
MDH1 recombinant protein	This study	N/A
PC 486-1178 recombinant protein	This study	N/A
PC 21 −1178 recombinant protein	This study	N/A
ME1 recombinant protein	This study	N/A
Crystal Violet	Bioshop	Cat # CRY 422.100
X-Gal	Wisent Bioproducts	Cat # 800-145-UG
Sodium pyruvate	Sigma-Aldrich	Cat # P8574
DAPI (4',6-Diamidino-2-Phenylindole, Dihydrochloride)	Invitrogen/ Thermo Fisher Scientific	Cat # D1306
Duroquinone	Sigma-Aldrich	Cat # D223204
L-Aspartic acid	Sigma-Aldrich	Cat # A6683
Methanol for LC-MS	Sigma-Aldrich	Cat # 34885-1L

(*Continued on next page*)

Continued

REAGENT or RESOURCE	SOURCE	IDENTIFIER
1,6-Hexanediol	Sigma-Aldrich	Cat # 240117
NAD free acid	Roche	Cat # 10127965001
NADH disodium salt	Roche	Cat # 10128023001
NADP disodium salt	Roche	Cat # 10128058001
NADPH	Roche	Cat # 10107824001
Adenosine 5′-triphosphate disodium salt hydrate(ATP)	Sigma-Aldrich	Cat # 3377
MG132 (Z-Leu-Leu-al)	Sigma-Aldrich	Cat # C2211
Piericidin A	Santa Cruz Biotechnology	Cat # sc-202287
Potassium hexacyanoferrate(II) trihydrate	Sigma-Aldrich	Cat # P3289
Potassium ferricyanide(III)	Sigma-Aldrich	Cat # 702587
Poly(ethylene glycol)	Sigma-Aldrich	Cat # 81310
PhosStop	Roche	Cat # 04906837001
cOmplete protease inhibitor	Roche	Cat # 37378900
Sodium L-lactate	Sigma-Aldrich	Cat # 71718
Unstained Protein Standard	Thermo Fisher Scientific	Cat # LC0725
Dimethylmalate	Sigma-Aldrich	Cat # 374318
DMEM without pyruvate	Wisent Bioproducts	Cat # 319-015
RPMI	Wisent Bioproducts	Cat# 350-000
RPMI without glucose	Wisent Bioproducts	Cat# 350-060
JumpStart™ Tag DNA Polymerase	Sigma-Aldrich	Cat # D9307
TRIzol™ Reagent	Thermo Fisher Scientific	Cat #15596026
Hygromycin B	Wisent Bioproducts	Cat # 450-141-XL
G418 sulfate	Wisent Bioproducts	Cat# 400-130-UG
Puromycin	Wisent Bioproducts	Cat # 400-160-EM
Blaticidin S. Hydrochloride	Wisent Bioproducts	Cat # 400-190-EM
Paraformaldehyde	BioShop	Cat # PAR070
Osmium tetroxide solution	Sigma-Aldrich	Cat # 75632
Sodium (meta)periodate	Sigma-Aldrich	Cat # S1878
LR White Resin	London Resin Company	Cat # AGR1281
L-Lysine monohydrochloride	Sigma-Aldrich	Cat # L5626
Nutragen® Bovine Type I Collagen mix	Advanced BioMatrix	Cat # 5010
X-treme Gene 9	Roche	Cat # 6365787001
E. coli tRNA	Sigma-Aldrich	Cat #10109541001
Deoxyribonucleicacid, low molecularweight from salmonsperm	Sigma-Aldrich	Cat # 31149
hexamethrine bromide (Polybrene)	Sigma-Aldrich	Cat # 107689
Slide-A-Lyzer	Thermo Fisher Scientific	Cat # 66203
Pierce™ Monomeric Avidin Agarose	Thermo Fisher Scientific	Cat # 20228
Glucose Solution	Wisent Bioproducts	Cat # 609-036-EL
D- Glucose (3,4-$^{13}C_2$)	Cambridge Isotope Laboratories	CLM-6750-PK
D-Glucose(3-^{13}C)	Cambridge Isotope Laboratories	CLM-1393
D-Glucose($^{13}C_6$)	Sigma-Aldrich	Cat # 389374
Sodium butyrate	Sigma-Aldrich	Cat # 303410
DMEM with L-glutamine & phenol red,without D-glucose	Wisent Bioproducts	Cat # 319-061-CL
Biotin	Oakwood Chemicals	Cat # M02926
BioVision 10 kDa Spin Column	BioVision	Cat # 1997

(*Continued on next page*)

Continued

REAGENT or RESOURCE	SOURCE	IDENTIFIER
Ammonium formate	Sigma-Aldrich	Cat # 78314
Dithiothreitol (DTT)	Inalco	Cat #1758-9030
Isopropyl-β-D-thiogalactopyranoside (IPTG)	Inalco	Cat#1758-1400
Tobacco Etch Virus (TEV) protease	Cappadocia et al., 2015a, Cappadocia et al., 2015b	N/A
Glutathione Sepharose 4B	GE Healthcare	Cat # 17-0756-05
Chelating Sepharose Fast Flow	GE Healthcare	Cat # 17-0575-01
Imidazole	Sigma-Aldrich	Cat # I202
N-tert-Butyldimethylsilyl-N-methyltrifluoroacetamide	Sigma Aldrich	Cat # 394882
Tris(2-carboxyethyl)phosphine) (TCEP)	Cayman chemicals	Cat # 14329
4-20% native Polyacrylamide Gel	Bio-Rad	Cat # 4568094
Amicon® Ultra-15 Centrifugal Filter Units with 10KDa cutoff	Millipore	Cat # UFC901024
Amicon® Ultra-4 Centrifugal Filter Units with 10KDacutoff	Millipore	Cat # UFC801024
Amicon Ultra-0.5 mL	Millipore	Cat # UFC500396
Bovine Serum Albumin	BioShop	Cat # ALB001
ABT-263 (Navitoclax)	APExBIO	Cat # AA3007
Acrylamide/Bisacrylamide, 30% Solution, 37.5:1	Bioshop	Cat # ACR010.502
Critical commercial assays		
NAD^+/NADH Kit	BioVision	Cat # K337
$NADP^+$/NADPH Kit	BioVision	Cat # K347
GSH/GSSG Ratio Detection Assay Kit	Abcam	Cat # ab138881
Mitochondria Isolation Kit for Cultured Cells	Abcam	Cat # ab110170
MitoTracker™ Deep Red FM	Invitrogen/Thermo Fisher Scientific	Cat # M22426
H_2DCFDA	Invitrogen/Thermo Fisher Scientific	Cat # D399
MitoSOX™ Red Mitochondrial Superoxide Indicator, for live-cell imaging	Invitrogen/Thermo Fisher Scientific	Cat # M36008
Seahorse MitoStress Kit	Aligent	Cat # 103015-100
RNA*later*®	Sigma-Aldrich	Cat # R0901
5x All in One RT Master Mix	ABM	Cat # G490
Duolink® PLA Multicolor Probemaker Kit Red	Sigma-Aldrich	Cat # DUO96910
Duolink® PLA Multicolor Probemaker Kit Green	Sigma-Aldrich	Cat # DUO96920
Duolink® PLA Multicolor Reagent Pack	Sigma-Aldrich	Cat # DUO96000
Duolink® *In Situ* Green Starter Kit Mouse/Rabbit	Sigma-Aldrich	Cat # DUO92014
Duolink® *In Situ* Wash Buffers, Fluorescence	Sigma-Aldrich	Cat # DUO82049
MicroBCA Prrotein Assay Kit	Thermo Fisher Scientific	Cat # 23235
BCA Protein Assay Kit	Thermo Fisher Scientific	Cat # 23237
Bio-Rad protein assay	Bio Rad	Cat # 5000006
LSAB2 System-HRP	DAKO	Cat # K0675
Di-amine-benzidine (DAB) substrate kit	Vector Labs	Cat # SK-4100
Deposited Data		
Cancer Cell Line Encyclopedia (CCLE)	(Ghandi et al., 2019)	RRID:SCR_013836

(*Continued on next page*)

Continued

REAGENT or RESOURCE	SOURCE	IDENTIFIER
For p53 ChIP seq depth and SISSR peaks dataset	(Nguyen et al., 2018)	N/A
Additional p53 and E2F binding sequences were obtained in ChIP Atlas and positions extracted from UCSC genome Browser using Transcription factor ChIP-Seq Clusters (161 factors) from ENCODE	(Consortium, 2012; Davis et al., 2018) Atlas (Oki et al., 2018)	RRID:SCR_006793
Experimental models: Cell lines		
IMR90 (normal human diploid fibroblasts)	American Type Culture Collection (ATCC, Manassas, VA)	ATCC Cat # CCL-186; RRID:CVCL_0347
IMR90 (normal human diploid fibroblasts)	Coriell Institute for Medical Research (Camden, NJ)	Coriell Cat # I90-83,;RRID:CVCL_0347
PC-3 (prostate cancer)	American Type Culture Collection (ATCC, Manassas, VA)	ATCC Cat # CRL-7934;RRID:CVCL_0035
HEK293T (embryonic kidney)	American Type Culture Collection (ATCC, Manassas, VA)	ATCC Cat # CRL-3216, RRID:CVCL_0063
HuH-7 (liver cancer)		RRID:CVCL_0336
Primary MEFs	S. Meloche (IRIC, Université de Montréal)	N/A
Phoenix Ampho packaging cells	S. W Lowe (MSKCC, New York)	RRID:CVCL_H716
MEF $p53^{-/-}$	S. W Lowe (MSKCC, New York)	N/A
BJ, Human normal foreskin fibroblasts	ATCC	CCRL-2522
Experimental models: Organisms/strains		
Transgenic male mice with prostate-specific deletions of *Stat3*, *Pten* and double *Stat3* and *Pten* deletion	(Pencik et al., 2015)	N/A
mouse for allograftmale NOD.Cg-*Rag1*^{tm1Mom} *Il2rg*^{tm1Wjl}/SzJ (also called NRG)	CRCHUM mouse colony. F.Rodier	RRID:IMSR_JAX:007799
BL21 Star (DE3): F$^-$ompT hsdSB(rB$^-$mB$^-$) gal dcm rne131 (DE3)	Department of Biochemistry, University of Montreal	N/A
Oligonucleotides		
Table S1 for qPCR primer		N/A
Table S1 for shRNA target sequences		N/A
Table S1 for cloning primer		N/A
Recombinant DNA		
pLPC-puromycin −3xFLAG	Ferbeyre Laboratory or are also available on addgene	Acevedo et al. Cancer Res. 2016 Addgene
pBABE with selection marker puromycin, hygromycin or *neomycin*	Ferbeyre Laboratory or are also available on addgene	described in (Lessard et al., 2018) also available from Addgene
pBABE-puromycin-H-RASV12	Ferbeyre Laboratory or are also available on addgene	described in (Lessard et al., 2018) also available from Addgene
pWZL-hygromycin	Ferbeyre Laboratory or are also available on addgene	described in (Lessard et al., 2018) also available from Addgene
pWZL-hygromycin-H-RASV12	Ferbeyre Laboratory or are also available on addgene	described in (Lessard et al., 2018) also available from Addgene
pCMV-VSV-G	Addgene 8454	(Stewart et al., 2003); Addgene 8454
*pCMV-dR.8.2*dvpr	Addgene 8455	(Stewart et al., 2003); Addgene 8455
pLPC-puromycin-binary	S. W Lowe (MSKCC, New York)	N/A
pMLP-shp21 puromycin	S. W Lowe (MSKCC, New York)	N/A
pMLP -shp53 puromycin	Ferbeyre laboratory	Moiseeva et al., 2011
pMLP-shp53-neomycin	Ferbeyre laboratory	Moiseeva et al., 2011

(*Continued on next page*)

Continued

REAGENT or RESOURCE	SOURCE	IDENTIFIER
pMLPX-shNTC-puromycin	Addgene 65232	Described in (Lessard et al., 2018); Addgene 65232
pMLPX-shNTC-neomycin	Addgene 65233	Described in (Lessard et al., 2018); Addgene 65233
Vector expressing *NDI 1*	N. Chandel (Northwestern University, Chicago, IL).	N/A
pBABE-puromycin-NDI-1-FLAG	this study	N/A
pMSCV-puromycin-mCherry	this study	N/A
pMSCV-puromycin-mCherry-NDI-1	this study	N/A
pRetroSuper-shp53-hygromycin	R Agami Division of Tumor Biology, the Netherlands Cancer Institute,	Voorhoeve and Agami, 2003
pRetroSuper-shGFP-hygromycin	R Agami Division of Tumor Biology, the Netherlands Cancer Institute,	Voorhoeve and Agami, 2003
pBABE-puromycin-MDH1	this study	N/A
pLPC-puromycin-binary-MDH1	this study	N/A
pLPC-puromycinbinary-MDH1-3xFLAG	this study	N/A
pcDNA3-MDH1-3xFLAG	this study	N/A
pcDNA3	(Life Technologies, Burlington, ON)	N/A
pBABE-puromycin-ME1	Addgene # 49163	(Jiang et al., 2013) Addgene # 49163
pcDNA3-ME1-HA	this study	N/A
pLPC-puromycin-binary-MDH-1-3xFLAG-ME1-HA	this study	N/A
pBABE-puromycin-ME1-HA	this study	N/A
pBABE-neomycin-PC-MYC	this study	N/A
pcDNA3-PC-MYC	this study	N/A
pcDNA3-3xFLAG	this study	N/A
pcDNA3-MYC-tag	this study	N/A
pcDNA3-HA-tag	this study	N/A
pCDNA3-ME1(1-191)-HA	this study	N/A
pCDNA3-ME1(356-572)-HA	this study	N/A
pcDNA3-MDH1(1-90)-3x-FLAG	this study	N/A
pcDNA3-MDH1(1-141)-3x-FLAG	this study	N/A
pcDNA3-MDH1(105-334)-3x-FLAG	this study	N/A
pcDNA3-MDH1(1-90)-3x-FLAG	this study	N/A
pcDNA3-MDH1(142-334)-3x-FLAG	this study	N/A
pcDNA3-PC(1-956)-MYC	this study	N/A
pcDNA3-PC(1-534)-MYC	this study	N/A
pcDNA3-PC(430-1178)-MYC	this study	N/A
pLPC-puromycin-mito-iSTAT3-3xFLAG	this study	N/A
pLKO-shSTAT3 -A- puromycin	Sigma-Aldrich	TRCN0000020840
pLKO-shSTAT3 -B- puromycin	Sigma-Aldrich	TRCN0000329887
pLKO-shMDH1 -A- puromycin	Sigma-Aldrich	TRCN0000028484
pLKO-shMDH1 -B- puromycin	Sigma-Aldrich	TRCN0000275198
pLKO-shME1 -A- puromycin	Sigma-Aldrich	TRCN0000064728
pLKO-shME1 -B- puromycin	Sigma-Aldrich	TRCN0000064731
pLKO shPC-A-puromycin	Sigma-Aldrich	TRCN0000078453
pLKO-shPC-B-puromycin	Sigma-Aldrich	TRCN0000413496
pMXs-3XHA-EGFP-OMP25	Addgene plasmid # 83356	Addgene plasmid # 83356
pET-28-ME1	Addgene plasmid # 38857	Addgene plasmid # 38857

(*Continued on next page*)

Continued

REAGENT or RESOURCE	SOURCE	IDENTIFIER
BirA (*E. coli* Biotin Protein Ligase),	L. Tong (Columbia Univ., NY).	N/A
SCBPL (*Saccharomyces cerevisiae* Biotin Protein Ligase)	L. Tong (Columbia Univ., NY).	N/A
PC-full	L. Tong (Columbia Univ., NY).	N/A
pHIS-MDH1-HIS	this study	N/A
pHIS-PC-HIS	this study	N/A
pHIS-PC 486-1178-HIS	this study	N/A
pHIS		Mascle et al., 2020
pTEV-ME1-GST	this study	N/A
pTEV-GST		Mascle et al., 2020
pBABE-puromycin-mcherry-PC	this study	N/A
pBABE-hygromycin-PC Δnterm-MYC(PC 21-1178)	this study	N/A
pMSCV with selection marker puromycin, hygromycin or *neomycin*	Ferbeyre Laboratory or are also available on addgene	Lessard et al., 2018
pLPC-puromycin	Ferbeyre Laboratory or is also available on addgene	Lessard et al., 2018
pLKO-shNTC-puromycin	Sigma-Aldrich	Lessard et al., 2018
pLKO-shNTC-hygromycin	this study	N/A
pLKO-shNTC-neomycin	this study	N/A
pLKO-shNTC-blasticidin	this study	N/A
pLKO-shSTAT3-A -hygromycin	this study	N/A
pLKO-shSTAT3 -A- neomycin	this study	N/A
pLKO-shSTAT3 -B- hygromycin	this study	N/A
pLKO-shSTAT3 -B- neomycin	this study	N/A
pLKO-shSTAT3 -A- blasticidin	this study	N/A
pLKO-shSTAT3 -B- blasticidin	this study	N/A
pBabe-hygromycin-MDH1-3-X-FLAG	this study	N/A
pLV-EV1-RFP	N. Chandel (Northwestern University)	Vectorbuilder VB 160708-1059xrd
pLV-EV1-RFP-cyto-LBNOX -3-x-FLAG	N. Chandel (Northwestern University)	Vectorbuilder VB 160708-1059xrd ; Original research paper generating LBNOX PMID 27124460 Addgene # 75285
pUltra	Addgene 24129	RRID: Addgene_24129
pUltra-MDH1-ME1	this study	N/A
pUltra-hot	Addgene 24130	RRID: Addgene_24130
pUltra-hot-PC	this study	N/A
Software and algorithms		
Prism 6-9	https://www.graphpad.com/	RRID: SCR_002798
Imaris	https://imaris.oxinst.com/packages	RRID: SCR_007370
Adobe Illustrator	https://www.adobe.com/products/illustrator.html	RRID: SCR_010279
Agilent Masshunter Quantitative Analysis software	http://www.agilent.com/en-us/products/software-informatics/masshunter-suite/masshunter/masshunter-software	RRID: SCR_015040
Seahorse Wave	http://www.agilent.com/en-us/products/cell-analysis-(seahorse)/software-download-for-wave-desktop	RRID:SCR_014526
Astra	https://www.wyatt.com/products/software/astra.html	RRID:SCR_01625

(*Continued on next page*)

Continued

REAGENT or RESOURCE	SOURCE	IDENTIFIER
ZEN Digital Imaging for Light Microscopy	http://www.zeiss.com/microscopy/en_us/products/microscope-software/zen.html#introduction	RRID:SCR_013672
Olympus Fluoview FV10-ASW	http://www.photonics.com/Product.aspx?PRID=47380	RRID:SCR_014215
Fiji	https://fiji.sc/	RRID: SCR_002285
Image Lab	https://www.bio-rad.com/en-us/sku/1709690-image-lab-software	RRID: SCR_014210
FlowJo	https://www.flowjo.com/solutions/flowjo	(RRID:SCR_008520)
BD FACSDiva Software	http://www.bdbiosciences.com/instruments/software/facsdiva/index.jsp	(RRID:SCR_001456)
LightCycler Software	http://www.roche-applied-science.com/shop/products/absolute-quantification-with-the-lightcycler-carousel-based-system	(RRID:SCR_012155)
NDP.view 2.6.8 (NanoZoomer Digital Pathology.view 2.6.8)	Hamamatsu	N/A
OlyVIA 2.9 Virtual Slide Scanner	Olympus	N/A
Additional information		
Mendeley data		http://doi.org/10.17632/xsxwjfhz8f.1
Immunogold staining protocol	www.me-udem.com	www.me-udem.com
IHC staining protocol	https://www.chumontreal.qc.ca/en/crchum/facilities-and-services	https://www.chumontreal.qc.ca/en/crchum/facilities-and-services
Metabolic tracing analysis	https://www.mcgill.ca/gci/facilities/metabolomics-innovation-resource-mir	https://www.mcgill.ca/gci/facilities/metabolomics-innovation-resource-mir

RESOURCE AVAILABILITY

Lead contact

All reasonable requests for material generated for this study should be addressed to G. Ferbeyre (g.ferbeyre@umontreal.ca).

Materials availability

Materials generated in this study are available from the lead contact.

There are restrictions to the availability of TMA of prostate tissue since its discontinued but similar TMA are available from US Biomax. There are restrictions to the availability of HA antibody but its available from commercial distributor.

There are restrictions to the availability of tissue samples from allograft as only a limited number of tumor were generated. Request for *Stat3*$^{-/-}$ *Pten*$^{-/-}$ knockout tissue should be addressed to Richard Moriggl or Lukas Kenner

There are restrictions to the availability of tissue samples from *Stat3*$^{-/-}$ *Pten*$^{-/-}$ as only a limited number of paraffin embedded slides were generated

There are restrictions to the availability of frozen proteins MDH1, ME1, and PC as limited amount of purified proteins were generated.

Data and code availability

- Quantification data of Immunofluorescence, quantification of SA-β-Gal, ROS analysis, NAD analysis, oxygen consumption, analyzed metabolomics data, unprocessed mitochondrial ultrastructure images, unprocessed allograft images, PLA images and unprocessed SA-β-Gal images were deposited to Mendeley Data and DOI is listed in the key resources table. Link to Mendeley http://doi.org/10.17632/xsxwjfhz8f.1. This paper analyses existing, publicly available data. These accession numbers for the datasets are listed in the key resources table. All source data not on Mendeley Data and all supporting information are either included in the figures or will be made available upon request to the lead author or the first author.
- This paper does not report original code.
- Any additional information required to reanalyse the data reported in this paper is available from the lead contact upon reasonable request.

EXPERIMENTAL MODEL AND SUBJECT DETAILS

Mouse Model

All animal experiments were reviewed and approved by the Austrian ministry authorities (BMWF-66.009/0281-I/3b/2012) and the CIPA (Comité Institutionnel d'expérimentation animale du CHUM), protocol C18046GFs. Transgenic male mice with prostate-specific deletions of *Stat3*, *Pten* and double *Stat3* and *Pten* deletion (Pencik et al., 2015) were used to show levels of HTC enzymes in genetic model of prostate cancer development.

Allografts were performed using 7 weeks old male NOD.Cg-*Rag1*^{tm1Mom} *Il2rg*^{tm1Wjl}/SzJ (also called NRG) mice.

Cell culture model

IMR90 and BJ normal human diploid fibroblasts, PC-3 (prostate cancer), HEK293T (embryonic kidney) and HuH-7 (liver cancer) cells were purchased from American Type Culture Collection (ATCC, Manassas, VA) and Coriell Institute for Medical Research (Camden, NJ). Primary MEFs were supplied by S. Meloche (IRIC, Université de Montréal). Phoenix Ampho packaging cells were a gift from S. W Lowe (MSK, New York). MEF p53$^{-/-}$ were provided by S. Lowe. IMR90, MEF and BJ were cultured in Dulbecco's Modified Eagle Medium (DMEM, Wisent Montreal, QC) without pyruvate, supplemented with 10% high grade fetal bovine serum (FBS, Wisent) and 1% penicillin/streptomycin (Wisent). HEK293T, Huh-7 and Phoenix Ampho packaging cells were cultured in Dulbecco's modified Eagle medium (DMEM, Wisent Montreal, QC) without pyruvate, supplemented with 10% fetal bovine serum (FBS, Wisent), 2 mM L-glutamine (Wisent) and 1% penicillin/streptomycin (Wisent). PC-3 cells were cultured in RPMI medium (Wisent) supplemented with 10% fetal bovine serum 1% penicillin/streptomycin (Wisent) and 2 mM L-glutamine.

METHODS DETAILS

Reagents

Pyruvate, aspartate, lactate, MG132, NADH, NADPH, ATP, NAD^+, $NADP^+$, duroquinone and dimethylmalate were purchased from Sigma-Aldrich (Oakville, ON) and piericidin A from Santa Cruz Biotechnology (Dallas, TX). ABT-263 was purchased from APExBIO (Boston, MA).

Plasmids

Retroviruses, , *pBABE, pBABE-H-RASV12, pWZL and pWZL-H-RASV12* are available today on Addgene, but we obtained them from S. W. Lowe (Memorial Sloan Kettering Cancer Center, New York, NY). *pBABE* (Addgene number #1764*), pBABE-H-RASV12 (Addgene number* #1768*), H-RASV12 was cloned with BamHI and SalI resitriction enzymes into pBABE vector. pBABE-puromycin selection marker can be removed by digestion with HindIII and ClaI and new selection marker can be inserted using compatible restriction enzymes. For this study we used pBABE-puromycin, pBABE-hygromycin and pBABE neomycin. pWZL hygromycin (Addgene number* 18750) and *pWZL-hygro-mycinH-RASV12 (Addgene number* 18749). *pWZL-hygromycin-H-RASV12 was generated by cloning H-RASV12 into BamHI / SalI restriction sites of pWZL-hygromycin vector. pLPC* and *pMSCV* were originally generated by Clontech. *pLPC3XFLAG* has Addgene number 73560 and was generated by cloning *3xFLAG* sequence into BamHI/XhoI restriction site. *pMSCV* was modified by the Ferbeyre lab to generate *pMSCV* with multiple cloning site by inserting in BglII / HpaI of MSCV the following linker gatctggatcccagtgtggtggtacgtagatatccatccactggcggccgcactcgagcaatgcatggtt (Lessard et al., 2018). From modified *pMSCV-puromycin*, the selection marker can be removed by HindIII/ClaI digestion and replaced by neomycin or hygromycin with compatible restriction enzymes (Lessard et al., 2018).

pCMV-VSV-G (Addgene no. 8454) and *pCMV-dR8.2 dvpr* (Addgene no. 8455) were from R. Weinberg's laboratory (Whitehead Institute, Cambridge, MA) (Stewart et al., 2003). *pLPC binary* and *pMLP-shp21* were a gift from S. W. Lowe (Memorial Sloan Kettering Cancer Center, New York, NY). *pRetroSuper-shp53* and *pRetroSuper-shGFP* were described in (Voorhoeve and Agami, 2003). The sequence of shp53 from *pRetroSuper* was also subcloned into miR30 context of *MLP-puromycin* and *neomycin* (Moiseeva et al., 2011). *ShNTC* with *mir30* context was subcloned in BglII/AgeI restriction sites to create retroviral vectors *pMSCV-shNTC* and *pMLPX-shNTC (pMLPX* is *pMLP* without GFP reporter). *NDI1* and *LBNOX-3xFLAG* vectors were a gift from N. Chandel (Northwestern University, Chicago, IL). The LBNOX construct was from Addgene 75285 (Titov et al., 2016). *pBABE-NDI-1-FLAG* was generated by PCR amplification with primers containing 3xFLAG sequence and digested with EcoRI/SalI. *NDI1-Cherry* was generated by PCR amplification with EcoRI/EcoRV overhangs and cloned into *pMSCV-Cherry* with EcoRI/HpaI sites. *MDH1* was PCR amplified and subcloned in BamHI/EcoRI restriction sites to create *pBABE-MDH1* (WT) and *pLPCbinary MDH1*. To create *pLPC binary MDH1-3xFLAG* and *pcDNA3-MDH1-3xFLAG*, MDH1 was PCR amplified with one primer containing the 3xFLAG tag and subcloned in BamHI/EcoRI restriction sites to create *pcDNA3-3xFLAG-MDH1* and *pLPC-binary MDH1-3XFLAG*. *pcDNA3* was from (Life Technologies, Burlington, ON). *ME1* was purchased from Addgene (Addgene # 49163) (Jiang et al., 2013). To generate *pcDNA3 ME1-HA* and *pLPC binary MDH-1-3xFLAG-ME1-HA*, ME1 was PCR amplified with one primer containing the HA tag and subcloned into BamHI/XhoI sites of *pcDNA 3* or *pLPC binary* using compatible overlapping ends generated by digestion of BglII/SalI. *PC* was purchased from OriGene (Rockville, MD 20850, USA). *pBABE-PC-MYC* and *pcDNA3-PC-MYC* were generated by PCR amplification of PC, one of the primers containing the *MYC* tag and subcloned into BamHI/EcoRI sites. To generate *pcDNA3-MDH1-MYC* MDH1 was PCR amplified with one primer containing the MYC tag and subcloned in BamHI/EcoRI restriction

sites to create *pcDNA3-MYC-MDH1.* To generate *pcDNA3-PC-3xFLAG* PC was PCR amplified with one primer containing the 3xFLAG tag and subcloned in BamHI/EcoRI restriction sites to create *pcDNA3-PC-3xFLAG. pcDNA3-3xFLAG, pcDNA3-MYC-tag* and *pcDNA3-HA-tag* were generated by cloning double-stranded oligonucleotides coding for the mentioned tags. All variants of *ME1* used for mapping were PCR amplified and then cloned into BamHI/XhoI sites of *pcDNA3*. For *MDH1* and *PC* variants all fragments were PCR amplified with *3XFLA*G tag or *MYC* tag and cloned BamHI/EcoRI into *pcDNA3*. To construct *mito-iSTAT3* resistant to shSTAT3A we first introduced seven mismatches in the sequence targeted by the shRNA keeping the same protein sequence. The new sequence is: *"atG **TTA** AC**T** AA**T** AA**C** CC**T** A**A**A Aat"*; while the WT sequence is:*"atG CTG ACC AAC AAT CCC AAG Aat," (*modified nucleotides are shown in bold and the capital letters indicate the target sequence of the shRNA). We then added the mitochondrial pre-sequence of Cytochrome *c* oxidase subunit IV from yeast to the N terminus of the mutated STAT3 and a FLAG tag to the C terminus using PCR. The PCR product was subcloned into the HindIII and XhoI sites of *pLPC*. Lentiviral vectors expressing HTC enzymes were generated from *pULTRA* and *pULTRA-hot* from Malcolm Moore (Addgene plasmids # 24129 and # 24130). PC was cloned in *pULTRA-hot* as a PCR XbaI/BamHI fragment. MDH1 and ME1 were cloned into *pULTRA* as a fusion protein separated by an intein cleavage site as follows. First, we generated *pUltra-ME1* from a PCR fragment obtained from *pBabe-ME1* and digested with NheI/SalI. Then the MDH1 ORF without stop codon was PCR amplified adding restriction sites XbaI/BamHI for cloning into *pUltra-ME1.*

All PCR primers used for cloning in this study are in Table S1. Lentiviruses *pLKO* expressing *shSTAT3* (*sh3-A, sh3-B)*, *shMDH1 (shMDH1-A, shMDH1-B), shPC (shPC-A, shPC-B), shME1 (shME1-A, shME1-B)*, and *shNTC* were from Sigma-Aldrich. To generate *shSTAT3* expression vectors with *hygromycin*, *neomycin* and *blasticidin* resistance, each resistance gene was PCR amplified with primers containing BamHI and KpnI restriction sites and subcloned into *pLKO-puroMYCIN* to replace the puro resistance gene. *shRNA* target sequences are described in Table S1.

For protein expression in bacteria, *H. sapiens* ME1 expression vector was a gift from N. Burgess-Brown (Addgene plasmid # 38857). BirA (*E. coli* Biotin Protein Ligase), SCBPL (*Saccharomyces cerevisiae* Biotin Protein Ligase), and PC full length were a gift from L. Tong (Columbia Univ., NY).*MDH1-His* and *PC*-full length and *PC 486-1176* were amplified by PCR and cloned via BamHI/EcoRI sites into *pHIS* that enables the expression of N-terminal 6xHIS fusion proteins or into *pTEV* that enables the expression of N-terminal glutathione-S-transferase (GST) that can be cleaved by the TEV protease (Mascle et al., 2020). *pMXs-3XHA-EGFP-OMP25* for mitochondrial purification was purchased from Addgene (Addgene plasmid # 83356).

Proliferation analysis and Senescence associated β-galactosidase staining (SA-β-Gal).

Growth curves for IMR90 and PC-3 cells were measured using 0.1% crystal violet in PBS (Gillies et al., 1986). Briefly, IMR90 were counted using a hemocytometer and 10,000 cells were plated in a 12-well plate in technical triplicates and a minimum of 4 different plates. Cells were incubated for indicated times and fixed for 10 min using 1% glutaraldehyde solution in PBS. Media was replaced with fresh media every 3 days. Fixed cells were washed twice with PBS and then conserved in PBS with 0.1% NaN_3 until all time points were recovered. Then they were washed twice with PBS followed by staining with 0.1% crystal violet in PBS for 30 min at RT. After staining, cells were washed in tap water until no crystal violet dissolved any longer in water. Colored cells were dried for a minimum of 24 h at RT. To measure growth, crystal violet was extracted with 10% acetic acid in water for 15 min with moderate shaking and OD at 590 nm was measured using photometer. The amount of crystal violet correlates well with cell numbers as we verified experimentally.

For all experiments, the number of biological replicates (n) is indicated and within each biological replicate the mean of three technical replicates was taken. For the experiment done in IMR90 expressing RAS and two of the three HTC enzymes each biological replicate only included technical duplicates. For colony assays with MEFs, 10,000 cells were plated in triplicate into 6 cm plates and incubated for 12 days. Cells were fixed with 1% glutaraldehyde in PBS and then colored with 0.1% crystal violet in PBS. Pictures were taken with a Bio-Rad bio imager.

SA-β-Gal staining was performed as described (Deschênes-Simard et al., 2013). Briefly, cells were plated and fixed 24 h after in 0.5% glutaraldehyde in PBS for 10 min at RT. Then they were washed once with PBS for 5 min and twice for 10 min with PBS pH 6.0 containing 1 mM $MgCl_2$. Staining solution was added to cells and incubated for 1-6 h away from light at 37°C. SA-β-Gal staining solution consisted of PBS pH 6.0, 1 mM $MgCl_2$, 2.5 μM X-Gal, 5 μM potassium ferricyanide and 5 μM potassium ferrocyanide. Solution was filtered using 0.45 μm filter and heated to 37°C. For MEFs, PBS 1 mM $MgCl_2$ was at pH 5.5 and for PC-3 cells pH = 5.75 and cells were incubated overnight. For quantification, a minimum of 50 cells per biological replicate were scored under the light microscope.

Clonogenic assay with PC-3 cells was performed in 48-wells plates (Corning, NY) pre-coated with Nutragen® Bovine Type I Collagen mix, (Advanced BioMatrix, San Diego, CA) diluted at 2 mg/mL in ice-cold growth medium, then warmed at 37°C for 30 min to form the gel. PC-3 cells were trypsinized to generate a single-cell suspension and 2,500 cells were prepared in Nutragen®/media mix and deposited in each well to form the second layer. Plates were incubated at 37°C for 45 min to allow the second layer to jellify. Finally, fresh media was added on top of each well and changed every 3 days. Colony formation was scored 1 week after.

Retroviral and Lentiviral infections

For lentiviral infections, $5x10^6$ HEK293T cells were seeded in 10 cm plates and grown for 16 h. Then, cells were transiently transfected using 3 μg of a lentiviral expression vector, 2 μg of the *pCMV-dR8.2 dvpr* plasmid and 1 μg of the *pCMV-VSV-G* envelope

protein expression plasmid in 900 μL of 1 × Opti-MEM (GIBCO Life Technologies, Burlington, ON). Mixture of DNA with 1 × Opti-MEM was vortexed for 10 s followed by adding 16 μL of X-tremeGENE 9 DNA Transfection reagent (Roche, Laval, QC) at the bottom of the Eppendorf tube. Tubes were inverted 6 times and incubated for 15 min at room temperature and then the mix was added to the cells. After 16 h, 10 mM sodium butyrate (Sigma-Aldrich) was added for a minimum of 6 h, and then the medium was changed. Supernatants from the transfected plates were collected 36 to 60 h after transfection. The viral soups were filtered through a 0.45 μm filter, supplemented with 4 μg/mL polybrene (Sigma) as well as 10% high grade serum and added on target cells. In preliminary test the viral titter produced by one 10 cm dish was sufficient to infect two 10 cm of target cells (Lessard et al., 2018) . For shSTAT3 and shNTC in IMR90 2.5 mL of a 10 mL the lentiviral soup was used to infect cells (depletion of STAT3 with high viral titer induces apoptosis in IMR90 cells). For all other IMR90 and PC-3 cells lentiviral infections, 5 mL of a 10 mL lentiviral soup was used. For IMR90 lentiviral soup was incubated for a minimum of 8 h. For all other cell lines 24 h.

For retroviral infections $5x10^6$ Phoenix-Ampho packaging cells were plated into a 10 cm plates and transfected with 20 μg of retroviral plasmid and 10 μg of 4070A amphotropic envelope protein expression plasmid *pAMPHO* by using calcium phosphate method as described (Ferbeyre et al., 2000). Following transfection, the viral soup from one 10 cm plate was used to infect one 10 cm dish of target cells and incubated for a minimum of 8 h. Fresh media was added to the packaging cells and the targets cells were reinfected 8 h after. To prepare target cells for infection cells were seeded so that on day of infection target cells were 70-80 percent confluent. After a minimum of 12 h post last infection, target cell population was selected using 2.0 μg/mL puromycin (Wisent) and/or 50 μg/mL hygromycin (Wisent) and/or 400 μg/mL G418 and/or 2.5 μg/mL Blasticidin S (Wisent). In case two or more selection agents were used at the same time doses were 1.0 μg/mL puromycin (Wisent) and/or 25 μg/mL hygromycin (Wisent) and/or 300 μg/mL G418 and/or 2.5 μg/mL Blasticidin S. If three or more selection were required selection was done sequentially starting by puromycin and G418 followed by hygromycin and G418. For PC-3 cells selection was maintained for the length of the experiments (Ferbeyre et al., 2000).

For spinfection of senescent BJ cells with HTC expression vectors, BJ cells were plated into 6-well plates so that on day of infection they were 90% confluent. Production of pseudo viral particles was done as described above with the modification that 1/10 of a 10 cm produced viral soup was used per well. For infection, viral soup was added with 4 μg/mL polybrene and 10% high grade serum to BJ cells and cells were spun at 3200 RPM for 3 h at 32°C.

For LBNOX expression, IMR90 cells were infected with either control empty vector with RFP selection or its derivative expressing *LBNOX-3-xF*LAG. After infection, cells were incubated for 7 days then selected by RFP positive cells using BD FACSAria cell sorter at IRIC flow cytometry core platform.

Pyruvate/Aspartate/Duroquinone/ Dimethylmalate/ and $CoCl_2$ supplementation

Pyruvate and aspartate were dissolved in DMEM growth media and replaced every 48 h. For vehicle normal DMEM growth media was used. As pyruvate and aspartate were dissolved in the same vehicle only one vehicle condition for both supplementations was run, resulting in same value for three replicates for control conditions (shNTC+ Veh, shS3[A]+ Veh, shS3[B]+ Veh) for growth curve, SA-β-Gal, NAD+/NADH ratio and immunofluorescence. As growth curve of aspartate showed big variation two more independent n were performed. Supplementation started on the day the cells were infected. For duroquinone and dimethylmalate both were dissolved in high-grade DMSO (Sigma) and replaced every 48 h. For $CoCl_2$ treatment, IMR90 cells expressing PC-cherry were plated on coverslips and treated for 48 h with the $CoCl_2$ (Bioshop). Cells were washed and fixed by 4%PFA and standard immunofluorescent protocol. Images were acquired with LSM 800 confocal microscope and Elyra hyper resolution microscope. For quantification, the filter set 77 of Zeiss was used as such the colocalization appears as yellow color where no colocalization is seen as red or green in the oculars. Areas with no colocalization (Red signal from PC cherry) were counted per cell.

Cell culture with hypoxia

Experiments with 1% oxygen were done as described in (Kilic Eren and Tabor, 2014) IMR90 fibroblast were infected with RAS oncogene and control shRNA (shNTC) or RAS oncogene and shRNA targeting a component of the HTC complex and on day 3 post-infection cells were split into two different plates, one was maintained in 21% oxygen and the other one was transferred into a Xvivo System glove box (BioSperix, Parish NY) hypoxia chamber connected to N_2, CO_2 and O_2 gas. The chamber was set to 37°C, 5% CO_2, and relative humidity of 60%. Oxygen level was adjusted to 5% and monitored using the system's own pre-calibrated oxygen sensors. After 24 h at 5% oxygen the chamber oxygen levels were decreased to 1% for the rest of the experiment. Media of the cells was changed every 48 h and replaced with fresh DMEM media. To avoid residual oxygen in the media trypsin or PBS, the solutions were preincubated for a minimum of 24 h in 1% oxygen prior to use. For immunofluorescence to visualize HTC foci, 150,000 cells were plated on coverslips and incubated for another 24 h, Slides were then processed as described in immunofluorescence.

MitoTracker staining

In order to visualize mitochondria, MitoTracker Deep Red (M22426 Thermofisher) was used according to manufactures instructions. To stain cells 250 nM of freshly dissolved MitoTracker Deep Red was added for 20 min to cells. Cells were washed twice with PBS and processed for immunofluorescence as described below. All steps after staining were carried out avoiding exposure to light.

Hexanediol treatment

For 1,6-hexanediol treatment cells were plated for immunofluorescence on coverslips. Media was replaced with media containing 1% hexanediol (Sigma) and then placed for 10 min in the incubator at 37°C. Media was removed and cells were washed twice with PBS and processed for immunofluorescence as described below.

Immunoblots and Immunoprecipitation

Immunoblots and immunoprecipitation were performed as described previously (Lessard et al., 2018). Cells were washed twice with ice cold PBS followed by aspiration of residual PBS. Cells were lysed in 500 μL to 2 mL of modified Laemmli Buffer (4% SDS, 20% glycerol, 0.125 M Tris-HCl pH 6.8) and recovered using a clean cell scraper. Samples were transferred into tubes and sonicated at lowest intensity for 20 s followed by heating for 5 min at 97.5°C. Samples were cooled to RT and protein were quantified using Nanodrop absorbance at A280. Samples were diluted to 2 mg/mL using modified Laemmli Buffer and 10% 2-mercapthoethanol, 0.1% bromophenol blue was added. Samples were kept at −20°C until use.

Multilayered SDS-Gels were poured as follows. For all gels, we used 0.1% SDS, APS and TEMED. For resolving gels, 375 mM Tris HCl, pH = 8.8 was used. A first layer of higher concentration of Acrylamide-BisAcrylamide(37.5:1) (15% or 12%) was poured, then isopropanol was added on top. Isopropanol was removed after the gel was solidified and a second layer of Acrylamide-BisAcrylamide(37.5:1) (12% or 10%) was dispensed and again layered with isopropanol. Isopropanol was again removed and a third layer of Acrylamide-BisAcrylamide(**37.5:1**) (10% or 8% or 7%) was poured and covered by isopropanol. Finally, after removing the isopropanol, the gel was topped with Acrylamide-BisAcrylamide(37.5:1) (4%, with 0.125 M Tris HCl-pH = 6.8) and wells were made using a comb. Once all gels were solidified, samples were heated to 95°C for 2 min and spun down for 30 s at 16.000 g. 20 to 40 μg of protein was loaded per sample. Gels were run in SDS-PAGE Mini (BioRad) machines with Tris-Glycine SDS buffer according to manufacturer's instruction. SDS-PAGE was transferred onto nitrocellulose (BioRad) or PVDF (Millipore) membrane with Tris-Glycine MeOH buffer according to manufacturer's instructions. Membranes were blocked for 1 h in 5% skim milk diluted in TBS (Tris-buffered saline) and incubated overnight at 4°C or 30 min at RT with primary antibodies (see supplementary table S2 for antibody dilutions). After primary antibody incubation, membranes were washed with 3 times 5 min with TBST (Tris-buffered saline with 0.05% Tween-20). Secondary antibody coupled to HRP were diluted 1:3000 in milk TBS and incubated for 1 h at RT. Membranes were rinsed 3 times followed by 3 washes of 10 min each with TBST. To reveal signal, ECL substrate was added (Perkin Elmer (Western Lightning Plus-ECL, Enhanced Chemiluminescence) or Amersham(Amersham ECL Detection Reagents)) and images were acquired using autoradiography.

For estimation of protein molecular weight FroggaBio BLUelf Prestained Protein ladder was run on each SDS-PAGE. In immunoblots, a minimum of one size mark is shown. Of note membranes were cut into pieces to incubate with different antibodies. In case of experiments were performed on several membranes' representative tubulin blot as loading control is shown. Primary antibodies dilutions are listed in Table S2.

Immunoprecipitation protocol was performed as in the great protocol described here (Lessard et al., 2018). Briefly, to reveal endogenous interactions of the HTC enzymes we grew HuH-7 cells in a 15 cm cell culture dish, washed them twice with ice-cold PBS and scrapped them with 1 mL of IP buffer (50 mM Tris-HCl, pH 7.9, 1 mM EDTA, 0.1 mM EGTA, 12.5 mM $MgCl_2$, 400 mM NaCl, 20% glycerol, 1% Triton X-100, 0.1% SDS and 1x cOmplete-EDTA free protease inhibitor cocktail from Roche Applied Science). Cell lysates were sonicated at lowest intensity for 30 s and then cleared at 16,300 g for 30 s. Immunoprecipitation was done using either 5 μg of anti-ME1 rabbit polyclonal or rabbit pre-immune serum overnight at 4°C. Recovery of immunoprecipitated proteins was performed using a 1:1 mix of Protein-A and -G dynabeads (Invitrogen). Prior to use, Protein A/ Protein G mix was blocked for 30 min in IP Buffer containing 2.5% BSA, 0.16 μg/μL *E. coli* tRNA (Sigma-Aldrich) and 0.16 μg/μl salmon sperm DNA (Sigma-Aldrich). Dynabeads were added to cleared lysates and incubated for 2 h at 4°C. Finally, the mixture was washed 2x 10 min at 4°C in IP Buffer followed by 3x 1 h wash in IP Buffer at 4°C. Total cell lysates and immunoprecipitates were separated by SDS-PAGE and analyzed by western blot.

Immunoprecipitations with FLAG-M2 Sepharose beads (Sigma) or HA magnetic beads (Pierce/ Invitrogen) were done as described above, with the following modifications. For immunoprecipitations with FLAG-M2 Sepharose beads, 20 μL of beads per immunoprecipitation were used. For HA immunoprecipitations, 10 μL of magnetic beads were used for each immunoprecipitation. The amount of plasmid transfected for each experiment is detailed in Table S3. HEK293T cells were transfected with calcium phosphate method as described above incubated for a minimum of 16 h and then washed with 1xHEPES and incubated for another 6 h in cell incubator. Finally, cells were washed with ice cold PBS twice and then lysed in IP buffer (50 mM Tris-HCl, pH 7.9, 1 mM EDTA, 0.1 mM EGTA, 12.5 mM $MgCl_2$, 400 mM NaCl, 20% glycerol, 1% Triton X-100, 0.1% SDS and 1x cOmplete-EDTA free protease inhibitor cocktail from Roche Applied Science). Lysates were sonicated at lowest intensity for 30 s and then cleared at 16,300 g for 30 s. Cleared lysates were incubated for 1 h at 4°C on a rocking platform with corresponding beads. Mixture of beads and immunoprecipitate were washed 2x with IP buffer and then washed 3x for 10 min at 4°C on a rocking platform. For FLAG immunoprecipitations, beads were spun down another time and washed again 2x with IP buffer. Total cell lysates and immunoprecipitates were separated by SDS-PAGE and analyzed by western blot.

For Mapping of the interaction sites of ME1, MDH1 and PC, gene fragments for each of the three proteins were generated by PCR as described above. The amount of plasmid transfected for each experiment can be found in Table S3. For ME1 fragments HEK293T cells were treated for 6 h with 20 μM of MG132 in order to stabilize unstable ME1 fragments.

Protein purification

All proteins were purified in three steps; first by metal affinity chromatography followed by ion-exchange chromatography (IEX) and then size-exclusion chromatography as adapted from (Tao et al., 2003) and references therein. For the purification of ME1, the bacterial expression vector was transformed into the *E. coli BL21* Star expression strain and bacteria were grown at 37°C to an OD_{600nm} of 0.8. Expression of ME1-HIS was induced for 6 h at 30°C with 1 mM isopropyl β-D-1-thiogalactopyranoside (IPTG). Bacterial pellets were resuspended and lysed in Lysis Buffer (30 mM imidazole, 30 mM Tris-HCl pH 8.0, 500 mM NaCl) supplemented with 1x cOmplete protease inhibitor cocktail (Roche) and passed through a French Press. Bacterial lysates were centrifugated at 35,000 rpm in a Beckman 55Ti rotor for 45 min at 4°C. The cleared lysates were loaded on a column of chelating Sepharose Fast Flow immobilized metal affinity chromatography resin (GE Healthcare) charged with nickel and washed with 15 column volumes (CV) of 30 mM imidazole, 30 mM Tris-HCl pH 8.0, 500 mM NaCl and 1x cOmplete protease inhibitor followed by a second wash with 2 CV of 60 mM imidazole, 30 mM Tris-HCl pH 8.0, 500 mM NaCl, and 1x cOmplete protease inhibitor. Proteins were eluted with 5 CV of 250 mM imidazole, 500 mM NaCl, 30 mM Tris-HCl pH 8.0, 10% Glycerol and dialysed with 125 mM NaCl, 30 mM Tris-HCl pH 8.0, 5 mM DTT overnight at 4°C, then loaded into a Q Sepharose FF column (GE Healthcare). After loading, the column was washed with 0.5 CV of Buffer A (30 mM Tris-HCl pH 8.0, 75 mM NaCl, 5 mM DTT) or until UV absorbance returned to baseline. The column was then washed with 2 CV of Mix buffer A and buffer B (30 mM Tris-HCl, 1M NaCl, 5 mM DTT) at conductivity of 20 mS/cm. Gradient of B was set to 50 percent for 60 min.

We used the same protocol to purify MDH1 with the following modifications. For MDH1, expression was induced with IPTG at 30°C, eluted from the nickel column with 300 mM imidazole, 500 mM NaCl, 30 mM Tris-HCl pH 8.0, and the purified protein was dialysed into 25 mM NaCl, 30 mM Tris-HCl pH 8.0, 5 mM DTT overnight at 4°C. IEX on the Q-Sepharose column was then performed with Buffer A (30 mM Tris-HCl pH 8.0, 25 mM NaCl, 5 mM DTT) and Buffer B (30 mM Tris-HCl pH 8.0, 500 mM NaCl, 5 mM DTT). ME1 and MDH1 were then concentrated using Amicon centrifugal tubes with a MW cut-off of 10 kDa (Millipore). Samples were frozen at −80°C in 10% glycerol, 200 mM NaCl, 5 mM DTT until used.

For PC full-length, *BL21 Star* bacteria bearing PC- and BPSCL-expressing plasmids were grown until an OD_{600} of 0.9. Then, 25 mg/L of Biotin and 0.1 mM of $MnCl_2$ were added and incubated for another 45 min. Expression was induced for 16 h with 1 mM IPTG at 18°C. For metal affinity chromatography, cleared lysates were loaded on the nickel column washed with 15 CV of 30 mM imidazole, 30 mM Tris-HCl pH 8.0, 500 mM NaCl and 1x protease inhibitor cocktail, followed by washes with 2 CV of 40 mM imidazole and 1 CV of 60 mM imidazole. Proteins were first eluted with 200 mM imidazole, 30 mM Tris-HCl pH 8.0, 500 mM NaCl and then concentrated using slow dialysis by supplying a saturated solution of 35K PEG (Sigma). Dialysis solution 15% glycerol, 200 mM NaCl, 30 mM Tris-HCl pH 8.0 with saturated PEG 35K. Proteins were then frozen at −80°C until used.

For the PC (486-1178) fragment, *BL21 Star* bacteria bearing PC- and BirA-expressing plasmids were grown until an OD_{600} of 0.9. Then, 25 mg/L of Biotin and 0.1 mM of $MnCl_2$ were added and incubated for another 45 min. Expression was induced for 16 h with 1 mM IPTG at 18°C. For metal affinity chromatography, cleared lysates were loaded on the nickel column washed with 15 CV of 30 mM imidazole, 30 mM Tris-HCl pH 8.0, 500 mM NaCl, protease inhibitor cocktail followed by washes of 2 CV of 40 mM imidazole and 1 CV of 60 mM imidazole. Proteins were eluted with 200 mM imidazole, 30 mM Tris-HCl pH 8.0, 500 mM NaCl and dialysed with 75 mM NaCl, 30 mM Tris-HCl pH 8.0, 10% glycerol, 1 mM (tris(2-carboxyethyl)phosphine) (TCEP), 2 mM $MnCl_2$ overnight at 4°C. IEX on the Q-Sepharose column was then performed with Buffer A (75 mM NaCl, 30 mM Tris-HCl pH 8.0, 10% glycerol, 0.2 mM TCEP, 2 mM $MnCl_2$) and Buffer B (500 mM NaCl, 30 mM Tris-HCl pH 8.0, 10% glycerol, 0.2 mM TCEP, 2 mM $MnCl_2$).

For SEC, all frozen proteins were thawed and dialysed into 10% glycerol, 50 mM NaCl, 20 mM $MgCl_2$, 0.2 mM EDTA, 2 mM $MnCl_2$, 30 mM Tris-HCl, pH 7.55. SEC was performed on either a Superdex 200, a Superdex 200 Increase or Superose 6 columns. In all cases, the running buffer was 10% glycerol, 50 mM NaCl, 20 mM $MgCl_2$, 0.2 mM EDTA, 2 mM $MnCl_2$, 30 mM Tris-HCl pH 7.55 supplemented with 1 mM ATP, 1 mM NADH, 1 mM NADPH and 0.2 mM TCEP.

Native separation of multi-protein complexes

The procedure was previously described (Camacho-Carvajal et al., 2004). In brief, a 10 cm Petri dish of HuH-7 at ∼85% confluence was washed twice with ice-cold PBS. Then, cells were scraped in PBS on ice and centrifuged for 10 min at 1500 rpm (Napco, 2028R) at 4°C. Cells were lysed in 250 μL of cold CSH buffer (50 mM Tris-HCl pH7.5, 25 mM NaCl, 1 mM EDTA, 0.1% Triton X-100) supplemented with 1x PhosSTOP and 1x cOmplete EDTA-free protease inhibitors (Roche), and incubated for 30 min on ice. Lysates were spun down for 20 min at 15 000 g at 4°C and the supernatant was loaded on a BioVision 10 kDa Spin column with 375 μL of cold BN buffer (500 mM 6-aminocaproic acid, 20 mM Bis-Tris pH 7.0, 2 mM EDTA, 12 mM NaCl, 10% glycerol, 0.1% Triton X-100, complete EDTA-free protease inhibitor). The column was centrifuged for 45 min at 15 000 g at 4°C. The flow-through was discarded and 350 μL of cold BN buffer was added to the column. This procedure was repeated, then the column was centrifuged for an additional 90 min or until the column content was concentrated to ∼150 μL. 50 μL per well of this product was separated on a 4%–20% native gel (4568094, Bio-Rad) overnight at 16 mA in a cold-room with the anode buffer (50 mM Bis-Tris pH 7.0) and cathode buffer (50 mM Tricine, 15 mM Bis-Tris pH 7.0, 0.02% Coomassie G-250) and using 7 μL of the ladder Native Mark (ThermoFisher). The following day, half of the gel containing the sample and the ladder was stained with Coomassie R-250 to assess the migration of the blue native gel, and a replicate lane containing the sample was cut in 9 equivalent pieces from top (piece 1) to bottom (piece 9). Each gel piece was denatured for 1 h in 1 mL of 2x Læmmli Buffer (4% SDS, 20% glycerol, 120 mM Tris-Cl pH 6.8, 10% β-mercaptoethanol). Then, each piece was inserted in a well of a second 10-well 4%–20% gradient gel with fresh 2x Læmmli Buffer to avoid bubbles, and the gel

was migrated in a SDS-PAGE running buffer (192 mM Glycine, 25 mM Tris base, 0.1% SDS) with the BlueEye Protein ladder (Froggabio) at 90V until the ladder was well separated.

Avidin pull down

To perform Avidin pull-down experiments, either PC or PC(468- 1178) was mixed with a 5-molar excess of purified MDH1-HIS and ME1. MDH1, PC and PC(468-1178) were purified as described above. For ME1, the protein was obtained by expressing an ME1-GST fusion protein in *E. coli* BL21 cells that were grown at 37°C to an $O.D_{600nm}$ of 0.01. Expression of ME1-GST was induced for 16 h at 20°C with 20 μM isopropyl β-D-1-thiogalactopyranoside (IPTG). Bacterial pellets were resuspended and lysed in Lysis Buffer (30 mM Tris-HCl pH 8.0, 500 mM NaCl, 5% DTT) and passed through a French Press. Lysed cells were centrifugated at 35,000 rpm in a Beckman 55Ti rotor for 45 min at 4°C. The supernatant was incubated 1 h, at 4°C with Glutathione Sepharose 4B (GSH; GE Healthcare) resin. After this, the resin was spun down washed three times with lysis buffer to remove non-specifically bound molecules followed by three washes with TEV buffer (20 mM Tris HCl = pH 7.4, 125 mM NaCl, 5 mM DTT) and incubated twice for 18 h at 4°C with 100 units of TEV protease. After the first 18 h, resin was spun down and supernatant was collected and reserved. New TEV was added and incubated again for 18 h. Both fractions were combined filtered and extensively dialyzed into 20 mM Tris HCl = pH 7.4, 250 mM NaCl, 5% Glycerol.

For control of non-specific binding to Avidin beads, PC or PC (486-1178) was not added to mixture. All of the following steps were performed for both PC, MDH1, ME or MDH1, ME1 alone. A mixture of PC, ME1 and MDH1 was dialyzed for 4 h into 50 mM Tris-HCl, pH 7.9, 1 mM EDTA, 0.1 mM EGTA, 12.5 mM $MgCl_2$, 150 mM NaCl, 20% glycerol, 1% Triton X-100, 0.1% SDS at 4°C with rotation. Samples were recovered, and 1% of the mixture was reserved as input. The remaining portion of the mixture was transferred into an Eppendorf tube containing a 30 μL of slurry of Avidin beads (Pierce/ThermoFisher) prepared as described by the manufacturer. The protein mixture was incubated with the avidin beads for 1 h on a rocking platform at 4°C. The beads were washed three times with wash buffer (50 mM Tris-HCl, pH 7.9, 1 mM EDTA, 0.1 mM EGTA, 12.5 mM $MgCl_2$, 300 mM NaCl, 20% glycerol, 1% Triton X-100, 0.1% SDS). To elute proteins from the beads, 50 μL of 6x SDS-loading buffer (0.5 M Tris-HCl pH 6.8, 30% glycerol, 10% SDS, 1% bromophenol blue and 15% β-mercaptoethanol) was added to the mixture and boiled 3x for 10 min, then loaded on an SDS-PAGE gel and transferred onto nitrocellulose membrane for western blot analysis.

Assembly of ternary complex

For assembly of the ternary complex, equimolar quantities of purified PC, MDH1 and ME1 were incubated together in assembly buffer (10% glycerol, 50 mM NaCl, 20 mM $MgCl_2$, 0.2 mM EDTA, 2 mM $MnCl_2$, 30 mM Tris-HCl, pH 7.55) supplemented with 5 mM ATP, 5 mM NADH, 5 mM NADPH and 0.2 mM TCEP on a rocking platform for 1 h at room temperature. SEC as described above was performed and the proteins eluted between 8 and 12 mL were taken for analysis. The sample was then concentrated using centricon mini tubes with a cut-off of 3 kDa.

SEC-MALS

SEC-MALS was performed using a microAkta (GE Healthcare) in-line with a Dawn HELEOS II (Wyatt Technology) and OptiLab T-rEX (Wyatt Technology). For data acquisition, ASTRA 6.1.6.5 (Wyatt Technology) software was used. Freshly prepared BSA (Sigma) and Aldolase (Sigma) were used as standards to normalize the detectors and align the signals at 280 nm absorbance. A Superdex 200 Increase column was used for the SEC portion of all experiments. The column flow rate was set to 300 μl/min and SEC buffer was as described above for protein purification. The flow from the column was collected in 0.5 mL fractions and protein content verified afterward on an SDS-PAGE gel with Coomassie staining. In addition, experiments containing MDH1 or assembled complexes were monitored for absorbance at both 280 nm and 340 nm. Before each experiment, the column and detector were equilibrated with running buffer overnight. The calibration constant for the Dawn Heleos II was determined for these experiments with 3.8200×10^{-5} 1/(V cm). For the analysis, the data acquired from experiments with proteins of interest were aligned and band broadening and normalization was applied. For Aldolase, the dynamic radius was set to 4.8 nm and for monomeric BSA to 3.3 nm. After normalization, despiking of data was set to heavy and baselines as well as peaks were defined. Peaks were defined as half heights of peaks. For multiple peaks, peaks were manually adjusted. Detectors with low signal, high angle and low angle were disabled until fitting line of K*c/R(θ) to sin^(θ/2) was diagonal. Molecular mass was determined using Zimm modeling. The dynamic radius was obtained by Rh from QLES in Astra with analysis standard parameters. Analysis was verified with the results fitting tool and by moving through the peak and molar mass.

Immunofluorescence

A minimum of 50.000 cells were seeded on 1.5 mm thickness coverslips and incubated for at least 48 h. Cells were washed twice with ice cool PBS and then fixed for 15 min with 4%PFA at RT. Then cells were washed three times for 5 min with 0.1 M glycine in PBS to inactivate PFA and stored in PBS 0.2%NaN_3 at 4°C until use. Cells were washed twice 5 min at RT with PBS to remove azide and then permeabilized with 0.1M glycine and 0.4% Triton X-100 in PBS for 5 min at 4°C. Then, they were incubated 3 times for 15 min with 3% BSA in PBS. Primary antibody was diluted in 3%BSA in PBS and 2% Donkey or 2% Goat serum. For dilutions of primary antibody see supplementary table S2. Primary antibody was added to coverslip and incubated in humidified chamber at 4°C overnight. Next day, the cells were washed 3 times with PBS 3%BSA for 10 min. Secondary antibody was diluted 1:1500 in 3%BSA in PBS and 2% Donkey or 2% Goat serum and incubated for 1 h at RT. Cells were then washed three times with PBS, excess PBS was removed and mounted on glass coverslips in Vectashield with DAPI. Edges were sealed off with nail polish and mounted cells were kept

for a minimum of 24 h at 4°C. On day of confocal imaging coverslips were removed from the fridge at least 1 h prior to imaging and put in microscope box to warm up to RT of the microscope. Images were taken randomly in at least 5 different regions of the coverslip to ensure representation of sample using the Zeiss Axio Imager Z2 upright microscope equipped with a CoolSNAP FX camera (Photometrics) and/or Axiocam camera and ZEN 2 blue and black edition software. Images were analyzed using ImageJ and Fiji. For quantification of DNA damage foci, PML nuclear bodies and mitochondrial fragmentation a minimum of 50 cells was counted and scored on microscope. For co-localization, we used an FV300 Olympus confocal microscope (Richmond Hill, ON) with a PMT first generation and Fluoview V4.2 Software. For super-resolution structured illumination microscopy (SR-SIM), images were taken with Super-Resolution microscope Axio Observer Z1 ZEISS Elyra PS.1, from Zeiss (Carl Zeiss, Oberkochen, Germany). All raw data were acquired with EMCCD Du885K ISO VP461 camera. Images were taken with 5 rotations. To obtain the final image the structured illumination algorithm of ZEN 2.1 was used. For further confocal microscope imaging the Zeiss LSM 800 with spectral analysis detector was used. All images were acquired sequentially. The data was acquired with a maximal airy unit of 1. For colocalization, secondary antibodies were incubated sequentially to avoid cross-reactivity between the antibodies. To quantify the colocalization between HTC enzymes, foci containing signals for the three enzymes were counted in different cells. The background was subtracted, and brightness adjusted to the same level for all images. Pseudocolor was added and an overly image was generated using the merge color function of ImageJ. For this function double co-localization is shown in yellow and triple co-localization is shown in white. Colocalization was expressed as the number of foci with visible white signal. Colocalization was also measured using the Plot profile function of ImageJ. The fluorescent intensity for each pixel was determined across a line drawn as shown in Figure 2.

Immunohistochemistry

For TMA of prostate tissue sequential TMA slides were heated at 55 °C for 1 h followed by steps of sequential incubation in xylene (2 × 6 min), 100% ethanol (1 × 5 min), 95% ethanol (1 × 3 min), 75% ethanol (1 × 3 min) and 40% ethanol (1 × 3 min). Finally, samples were washed in dH2O for 3 min.

Heat antigen retrieval was performed by using a steamer with the following settings, 45 min in 10 mM citrate buffer (pH 6.0). The steamer was started at RT and reached 95 °C in 15-20 min. Slides were then incubated for another 25-30 min. Slides were cooled and washed with PBS containing 0.3% Triton X-100 3 times for 3 min with 1 × TBS/0.3% Triton X-100. To inactivate endogenous peroxidases slides were incubated for 5 min at room temperature in a solution of 3% H_2O_2 followed by 3 washes for 3 min in 1 × TBS/0.3% Triton X-100. To delimit tissues a hydrophobic barrier pen (DAKO) was used. Tissues were blocked 1 h at RT with a protein-blocking serum-free ready-to-use reagent (DAKO, cat. no. X0909, Carpinteria, CA). Excess of blocking was tapped of and tissues were incubated overnight at 4°C with primary antibodies diluted in 5% goat serum in 1 × TBS/0.3% Triton X-100. Antibodies used were: anti-MDH1 (1:2000, Santa Cruz), anti-PC (1:500, Santa Cruz) and anti-ME1(1:500, Genetex). After overnight incubation samples were washed 3 times for 3 min in 1 × TBS/0.3% Triton X-100 followed by primary antibody detection using the LSAB2 System-HRP (DAKO, cat. no. K0675, Carpinteria, CA). Secondary biotinylated antibody (DAKO) was incubated for 30 min followed by washes as above. Finally, samples were incubated for another 30 min with streptavidin-HRP (DAKO) and washed as above. To reveal staining peroxidase with Di-amine-benzidine (DAB) substrate kit (SK-4100, Vector Labs., Burlington, ON) was used. To stop the reaction, slides were washed in tap water when the staining was sufficient; the same incubation time was applied to all samples.

For visualization, counterstaining with hematoxylin (HHS16, Sigma-Aldrich) was used and tissues were rapidly dehydrated by sequential incubation in 40% ethanol (1 × 1 min), 75% ethanol (1 × 1 min), 95% ethanol (1 × 1 min), 100% ethanol (1 × 1 min) and xylene (2 × 5 min). Slides were mounted in Cytoseal (8310-4, Thermo Fisher) mounting media and scanned with NanoZoomer 2.0-HT scanner (Hamamatsu). Images were processed with NDP.view 2.6.8 (NanoZoomer Digital Pathology.view 2.6.8) (Hamamatsu) and ImageJ.

Tissue Micro Arrays were purchased from US Biomax (catalog no. PR807c, Rockville, MD). TMAs from US Biomax were reviewed by two board-certified pathologists. Quantification was done by two independent persons and combined. In case of disagreement, the mean of both intensities was taken. There was no occurrence of disagreement by more than 1 score point. Mouse samples IHC were performed at the Molecular Pathology platform of CR-CHUM following the platform protocol https://www.chumontreal.qc.ca/en/crchum/facilities-and-services. For quantification, three sections were selected blindly by one person based on histology for prostate epithelial tissue. For $Pten^{-/-}$, six sections were selected to better represent diversity of the tissue. It is important to notice that $Pten^{-/-}$ knockout is only present in the prostate epithelial cells and all other cells in the prostate still contain Pten. For one $Pten^{-/-}$ sample, only two sections were selected as there was little prostate epithelial cell regions identified. All selected sections were then scored by two independent persons for KI67, MDH1, ME1 and PCX staining intensity according to a scoring key and scoring was combined. In case of disagreement, the mean of both intensities was taken. There was no occurrence of disagreement by more than 1 score point.

STAT3-ATAD3A Proximity ligation assay (PLA)

PLA was done using Duolink® *In Situ* Green Starter Kit Mouse/Rabbit according to manufacture instructions. To prepare wash buffer A 1 pouch of wash buffer A powder was solubilized in 1L of MilliQ Water. To prepare wash buffer B 1 pouch of wash buffer B was solubilized in 1L of MilliQ Water. Wash buffers were kept at 4°C for no longer than 1 month. Prior to use, wash buffers were warmed to RT.

To prepare cells for PLA, IMR90 fibroblasts were plated on coverslips and incubated for 48 h at 37°C. Cells were fixed using 4% PFA in PBS for 10 min. This followed by a two 5-min wash with PBS 0.1M Glycine. Cells were permeabilized with PBS 0.1M Glycine and 0.4% Triton -X100 for 5 min at 4°C. Cells were then blocked using Duolink blocking buffer for 1 h at 37°C. Primary antibodies were diluted with Duolink antibody dilution and incubated in humidified chamber overnight at 4°C. The cells were washed 3x5 min in 1x Wash Buffer A at room temperature. PLUS and MINUS PLA probes were diluted to 1x in the Duolink® Antibody Diluent and incubated on cells in a humidified chamber for 1 h at 37°C. The cells were washed 3x 5 min in 1x Wash Buffer A at room temperature. Ligase solution was prepared by diluting Duolink® Ligation buffer to 1 x and 1 μL of ligase was added for each 40 μL of 1x ligation buffer. Ligation mixture was added on cells in a pre-heated humidity chamber for 30 min at 37°C followed by 3 washes in 1x Wash Buffer A at room temperature. Amplification solution was prepared by diluting Duolink® Amplification buffer to 1 x and 1 μL of Polymerase was added for each 80 μL of 1x Amplification buffer. Polymerase was incubated for 2 h at 37°C in a pre-heated humidity chamber followed by washes of 3x 10 min in 1x Wash Buffer B at room temperature and a final wash of 0.01x Wash Buffer B for 1 min. Cells on the coverslips were mounted using Vectorshild with DAPI and analyzed no later than 48 after the experiment using the confocal microscope LSM800 as described before. To analyze PLA staining in ImageJ, Circle ROI with a diameter of 5 μm was defined. The background was subtracted and the threshold was set. A binary image was created and analyzed using Analyze Particle with the following settings: Max size of particle 2 μm^2 and circularity of 0.5-1.

PC-MDH1 and PC-ME1 Proximity ligation assay (PLA)

PLA was done using Duolink Multicolor Kit with red and green conjugation kits. Conjugation of primary antibodies to green and red oligos was done according to manufactures instructions and conjugated antibodies were stored at 4°C. PLA on cells was performed according to manufacturer's protocol with the following modifications The conjugated antibodies were further diluted using antibody diluent for PC-MDH1 1/75 and for PC-ME1 1/50 and incubated overnight at 4°C. For ligation the multicolor ligase was diluted 1/20 and incubated for 30 min at 37°C. The amplification step was carried out for 120 min at 37°C and the detection step for 45 min at 37°C.

For PLA on tissue, the following modification to the manufacturer's protocol was done. Preparation of tissue slides was done as described in immunohistochemistry. Briefly, paraffin-embedded tissue samples were heated at 55 °C for 20 min followed by incubation in xylene (3 × 5 min), 100% ethanol (2 × 5 min), 95% ethanol (1 × 5 min), 75% ethanol (1 × 5 min) and 40% ethanol (1 × 3 min). Followed by two wash in ddH_2O. Antigen retrieval was performed by heating in a steamer for 45 min in 10 mM citrate buffer (pH 6.0) with 0.3% Tween 20. The steamer was started at RT and reached 95 °C in 15-20 min. Slides were then incubated for another 25-30 min. Slides were cooled and cells were permeabilized with PBS containing 0.4% Triton X-100 and 0.1M Glycine for 10 min. Slides were washed two times in PBS followed by blocking. For blocking the Duolink block buffer was used and washing times were increased to 10 min and performed 4 times with wash buffer A. Image acquisition was done as described above. For quantification of colocalization of PLA signal (Figure 2 G) the filter set 77 of Zeiss was used as such the colocalization appears as yellow color where no colocalization is seen as red or green in the oculars. For intensity scoring of PLA colocalization signal (Figure 2H) signal intensity of green and red for a given foci is the square root of multiplication of green and red fluorescent intensity. For analysis 15 random foci per condition were chosen.

Electron microscopy and colloidal gold immunocytochemistry

Electron microscopy and colloidal gold immunocytochemistry were performed according to (Fouillen et al., 2017). $1x10^7$ cells were recovered using Trypsin, washed twice with 0.1M Phosphate Buffer (PB) pH 7.3 (Sambrook Cold Spring Laboratory protocols) and fixed for 30 min at 4°C on a rocking platform using freshly prepared PLP (Periodate L/Lysine paraformaldehyde) fixative consisting of 4% PFA, 0.01 M $NaIO_4$ and 0.028125 M L-lysine monochloride (Sigma) in 0.1 M PB, then filtered with 0.45 μM filter to remove residual impurities. After fixation cells were washed 3x with PB pH 7.3. Cells were post-fixed for 1 h with 1% potassium ferrocyanide-reduced osmium tetroxide, dehydrated with graded ethanol and then processed for embedding in LR white resin (London Resin Company; Berkshire, UK) as previously reported (Fouillen et al., 2017). Ultrathin 80–100 nm sections were prepared using a diamond knife and transferred onto Formvar®-coated (polyvinyl formate) 200-mesh nickel grids.

For ultrastructural analysis of mitochondria, some ultrathin sections were stained with uranyl acetate and lead citrate and examined either in a FEI Tecnai 12 (Eindhoven, the Netherlands) transmission electron microscope operating at 120 kV or in a Hitachi Regulus 8220 (Tokyo, Japan) scanning electron microscope operating at 30 kV in Bright STEM mode.

For post-embedding colloidal gold immunocytochemistry, some ultrathin sections were incubated with an aqueous solution of 5% sodium metaperiodate for 45 min and washed with distilled water. The nickel grids were then floated on a drop of blocking solution consisting of 1% Ovalbumin in 0.01 M PB for 15 min to avoid non-specific binding, then transferred onto a drop of primary antibody (anti-PC 1:200) and incubated overnight at 4°C. Grids were then rinsed with PB and placed in blocking solution for 15 min. Antibody-antigen complexes were then revealed by floating the grids on a drop of protein A-10 nm colloidal gold complex for 30 min. Negative controls consisted of incubations with protein A-gold alone. Sections were then stained with uranyl acetate and lead citrate, and examined in a FEI Tecnai 12 (Eindhoven, the Netherlands) transmission electron microscope operating at 120 kV.

NAD^+/ NADH, $NADP^+$/ NADPH and glutathione measurements

For NAD^+/NADH measurements, approx. 50,000 cells were plated for technical triplicates in 6 cm plates and incubated for 48 h and processed by a kit from BioVision. Briefly, cells were sonicated 2x for 15 s and lysates were diluted 5 to 20 times to remain in the linear

range of the kit. For $NADP^+$/NADPH measurements, approx. 1,000,000 cells were seeded in triplicate and incubated for at least 48 h. Cells were lysed by sonication twice for 15 s, spun at 13000 rpm in a 10 kDa Spin column to remove endogenous proteins and lysates were assayed using a $NADP^+$/NADPH quantification kit (BioVision) according to manufactures instructions. For glutathione measurements approx. 5,000,000 cells were plated in technical triplicates, grown for 48 h, harvested in PBS pH 6.0 and 0.1% NP40, lysed by sonication on ice twice for 10 s, spun with a 10k Da Spin column to remove endogenous protein and then analyzed using Abcam Glutathione kit according to manufactures instructions. For all three assays, protein content was determined using a Bradford assay kit (Bio-Rad) according to manufacturer's instructions. All assays were carried out in biological triplicates (cells generated from different infections). For NAD and NADP quantification in Figure 4 and Figure S6 same extracts were used to further compare samples.

qPCR

To analyze mRNA expression, cells were collected in Trizol (#15596018, Invitrogen) and RNA extraction was performed according to the manufacturer's instructions. For cDNA preparation, 2 μg or total RNA were reverse transcribed in a 20 μL reaction using the 5X All-In-One RT kit (G590, ABM, Richmond, BC, Canada) as per the manufacturer protocol. Reverse transcription products were diluted 10 times with pure water prior to real-time quantitative PCR. Reactions for qPCR were performed in technical triplicate using 1 μL of diluted cDNA samples per 10 μL reaction volume also containing: 0.25 μM of each primer (synthetized by Biocorp), 0.2 mM dNTP (DD0056, BioBasic), 0.33X Syber Green I (S7563, Invitrogen), 0.25U Jump Start Taq DNA polymerase (D9307, MilliporeSigma) in 1x reaction buffer (provided with the enzyme) enrich with 2.5 mM more of $MgCl_2$ (M1028, Sigma). The LightCycler 96 Real-Time PCR System (Roche Applied Science) was used to detect the amplification level and was programmed to an initial step of six minutes at 95°C, followed by 50 cycles of 20 s at 95°C, 20 s at 58°C and 20 s at 72°C. A high resolution melting from 60°C to 98°C followed the amplifications. All reactions were run in triplicate and the average values were used for relative quantification of target genes using the ΔΔCT method. Outlier of triplicates were excluded if the value was 1 cq different than average.

Prior to use, primers' efficiency was determined by a minimum of 4 serial dilutions and efficiency of amplification between 1.95 and 2.05 was accepted. Primers were validated to show just one amplification product either by running product on agarose gel after PCR or unique peak in melting curves. Primers were designed to be intron spanning where possible. To test for DNA contamination and other contaminants in qPCR a control with no RT was used and a Cq higher than 35 was considered negative for DNA contamination. For normalization TBP and HMBS were used in IMR90 as both mRNA were previously validated to be good housekeeping genes in this cell line (Lessard et al., 2018). For MEFs TBP, HMBS and β-actin were used as housekeeping genes (Deschênes-Simard et al., 2013). Variation of less than 1 Cq in housekeeping genes between conditions was considered acceptable. qPCR primers are presented in Table S1.

MitoSox and DCFDA measurements

ROS measurements were done as described previously (Moiseeva et al., 2009) at the FACS CORE Facility of IRIC Research Center at the University of Montreal, Canada. Briefly, cells were incubated at 37°C for 30 min with either MitoSox (Molecular Probes, Eugene, OR) or H_2DCFDA (Molecular Probes). Cells were collected using Trypsin and washed twice with PBS. Cells were resuspended in 500 μL of HBSS for sorting in the BD FACSCanto II system ran with DiVa analysis software. Acquired data were further analyzed using FlowJO software.

Mitochondrial purification

For PC localization studies, mitochondria were purified using Mitochondria Isolation Kit for Cultured Cells (Abcam) according to manufacturer's instructions. For mitochondrial STAT3 levels in senescent cells mitochondria were purified by immunoprecipitation according to (Chen et al., 2017). For each experiment, an anti-HA immunoprecipitation was performed on IMR90 cells expressing 3XHA-EGFP-OMP25 and RASV12 or an empty vector. At day 12 post-infection, five 10 cm plates of cells were washed twice with PBS and then scraped into 1 mL chilled KPBS buffer (136 mM KCl, 10 mM KH_2PO_4, pH 7.25). The following steps for mitochondrial isolation and metabolite extraction were performed as described in (Chen et al., 2017), except for the incubation with magnetic beads, in which the supernatants were incubated with 30 μL of prewashed anti-HA magnetic beads (88837; ThermoFisher Scientific) on a vertical-rotating mixer for 20 min. Proteins were eluted by adding 100 μL 6x SDS loading buffer (0.5 M Tris-HCl pH 6.8, 30% glycerol, 10% SDS, 1% bromophenol blue and 15% β-mercaptoethanol) and then analyzed by SDS-PAGE. Immunoprecipitates were run on SDS-PAGE and transferred onto nitrocellulose membrane for western blot analysis. The efficiency of mitochondrial purification was assessed with anti-TOMM20 antibodies and the efficiency of immunoprecipitation was assessed using an immunoblot against HA.

Animals

Transgenic male mice with prostate-specific deletions of Stat3, Pten and double Stat3 and Pten deletion (Pencik et al., 2015) were sacrificed at 19-weeks old and their prostate were collected and frozen in OCT for cryosections or in RNA*later* (Invitrogen) for RNA and protein extraction. For further information on the mouse model please refer to (Pencik et al., 2015). For immunohistochemistry, a piece of tissue treated with RNA*later* was washed with PBS, incubated for 8 h in 15% sucrose in PBS and then 16 h in 30% sucrose in

PBS at 4°C and then fixed in 10% formalin for 24 h at 4°C. After fixation and embedding into paraffin, 4 μm serial sections were cut to perform immunohistochemistry according to CR-CHUM histology core platform. For antibodies see Table S2.

Allografts were performed as described (Deschênes-Simard et al., 2013) using 7 weeks old male NOD.Cg-*Rag1*^{tm1Mom} *Il2rg*^{tm1Wjl}/SzJ (also called NRG) mice injected subcutaneously in both flanks with 100 μL of a premixed solution 1:1 of Matrigel (BD Biosciences) and PBS-resuspended cells at 4°C, containing 1x10^6 MEFs cells expressing the different vectors. Tumor formation was evaluated over a period of 40 days. Tumors volumes were assessed with a caliper every two days as soon as the tumors were palpable, and mice were euthanized before 40 days if tumor volume reached 1.5 cm^3. At endpoint, half of each tumor collected was flash-frozen for RNA and protein purification and the other half was fixed in 10% neutral buffered formalin (Sigma) for at least 72 h before paraffin embedding.

Serial sections of 4 μm of each tumor were then cut at the Molecular Pathology platform of CR-CHUM and immunohistochemistry was performed, as described above. For histopathology analysis, H&E staining was done at the CR-CHUM Molecular Pathology facility and evaluated by the histopathology laboratory of Dr. Trudel. For RNA and protein extractions, tumor pieces were transferred into Eppendorf tubes and immediately flash-frozen in liquid nitrogen and then kept at −80°C until further use. For RNA isolation, Trizol was added to frozen tumor samples and then tumors were homogenized using a POLYTRON® PT 1200 E (Kinematica). For protein extraction, frozen tumor samples were also homogenized, but only in Læmmli 2x buffer (4% SDS, 20% glycerol, 120 mM Tris-HCl pH 6.8) instead. Extracted proteins were quantified using Micro BCA Protein Assay Kit (Pierce) and equal amount of proteins were run in SDS-PAGE. All mice work was approved by the ethics committee of the CR-CHUM. The following formula was used to determine tumor volume considered as an ellipsoid after measuring the diameter in x, y and z axis.

$$V = \frac{4\pi \frac{h}{2}\frac{w}{2}\frac{l}{2}}{3} = \frac{4\pi \frac{hwl}{8}}{3} = \frac{\pi hwl}{6}$$

where, h: height, w: width, l: length. Each measured dimension is divided by two to get the radius of tumors.

Stable Isotope Tracer Analysis

8x10^5 cells were seeded in 10-cm dishes to obtain cells at 80% confluency. The media was removed and replaced with fresh DMEM containing 25 mM glucose without pyruvate to equilibrate the cells for 2 h for experiment with fully labeled glucose. For tracer analysis with 3-^{13}C-glucose or 3-4 ^{13}C2-glucose equilibration media contained 10 mM of Glucose. The equilibration media was replaced with DMEM containing either 25 mM $^{13}C_6$-glucose (389374, Sigma Aldrich, Oakville, ON)-labeled media or 10 mM 3-^{13}C-glucose (CLM-1393, Cambridge Isotope Laboratories, Cambridge, MA)- or 10 mM 3-4 ^{13}C2-glucose (CLM-6750-PK Cambridge Isotope Laboratories) for 2 min, 10 min, 1 h or 4 h.

The media was discarded and cells were washed 3x with 4°C isotonic saline solution on ice and quenched with 600 μL of 80% methanol at < −20°C on dry ice. Cells were scraped from the plates and transferred to prechilled tubes. Cell suspensions were lysed using a sonicator at 4°C for 10 min in cycles of 30 s on, 30 s off, at high setting with Diagenode Bioruptor. Sonication was repeated to ensure complete recovery of metabolites. Cell debris were removed by centrifugation (14000 rpm, 4°C) and supernatants were transferred to prechilled tubes and dried in a cold trap overnight at 4°C. Dried pellets were dissolved in 30 μL of pyridine containing methoxyamine-HCl (10 mg/mL) using a sonicator and vortex. Samples were spun down at 14000 rpm, incubated for 30 min at 70°C and then transferred to GC-MS injection vials containing 70 μL of N-tert-Butyldimethylsilyl-N-methyltrifluoroacetamide (Sigma). The sample mixtures were further incubated at 70°C for 1 h. One μL of each sample was injected for GC–MS analysis. GC–MS instrumentation and software were all from Agilent. GC–MS methods and mass isotopomer distribution analyses are as previously described (Gravel et al., 2016). Briefly, GC/MS analysis was conducted on an Agilent 5975C series GC-MSD with triple-axis HED/EM detector, equipped with DB-5MS + DG capillary column (30 m length, 10 m Duraguard deactivated fused silica tubing, 0.25 mm internal diameter, 0.25 μm film thickness) (Agilent, USA) and a 7890A gas chromatograph, with a 7693 autosampler.

1 μL sample was injected in the GC in splitless mode with inlet temperature at 280°C with helium gas as the carrier at a flow rate at 1.552 mL/min. The quadrupole was set at 150°C and the GC/MS interface at 285°C. The oven program for all metabolite analyses started at 60°C held at 1 min and increased at a rate of 10°C/min up to 320°C. Bake-out was at 320°C for 9 min. All data was collected by electron impact set at 70eV. Sample data were acquired both in scan (1-600 m/z) and selected ion monitoring (SIM) modes.

Metabolites were identified by matching mass spectra and retention times using authentic standards from Sigma. Measurements of metabolite concentrations are taken from the metabolite quantifier integration divided by the internal standard quantifier integration (myristic acid-D_{27}) and normalized to cell count. For stable isotope tracer analysis, the integration values for quantifier (m+0) and all possible isotopomers (m+1, m+2, etc…) are summed up to obtain the total amount of metabolite. The mass isotopomer distribution (MID) vector is obtained by dividing the m+0 and all isotopomer by the total amount of metabolite. The corrected MID is obtained by removing the contribution of naturally occurring stable isotopes (McGuirk et al., 2013). The resulting isotopomers are expressed as fractions of the total metabolite pool. To determine the relative ion abundance, the corrected MID is multiplied by the relative metabolite amount at steady state.

Data analysis was performed using the Agilent Chemstation and MassHunter software (Agilent, Santa Clara, USA). For labeling experiment leading to Figure 1, Figure 4 and Figure S6 experiments control cells (shNTC) and senescent cells (shS3[A]) are the same as all 4 conditions (shNTC, shS3[A], shS3[A]+ shp53, and shS3A+HTC were done together. Biological replicates were performed on independent infections.

Bioenergetic Analyses

Cellular respiration in the Seahorse Analyzer was measured as described previously (Audet-Walsh et al., 2016). Briefly, IMR90 cells (7,500 growing or 5000 senescent) were seeded in 250 μL of culture media in a XFe24 cell culture plate and incubated for 24 h at 37°C. Cells were washed twice and incubated in 525 μL of XF media for 1 h at 37°C in a CO_2-free incubator. Measurements were normalized to μg protein.

Nucleotide and nucleoside analysis

$5x10^6$ cells were washed twice with 150 mM ammonium formate and collected in 80% methanol (LC-MS grade, Sigma) chilled to −80°C. Every step was performed on dry ice. The methanol:cell mixture was transferred into pre-chilled 2 mL Eppendorf tubes containing 1.4 mm ceramic beads, then beaten on bead beater for 2 min at 30 Hz. After this, we added an equal volume of ice-cold dichloromethane and half the volume of ice-cold H_2O. The mixture was vortexed for 1 min at maximum speed and left for 10 min on ice. Samples were spun at 4000 rpm at 1°C and the aqueous phase was transferred into a new pre-chilled Eppendorf tube. Samples were dried overnight in a cold trap (Labconco). Samples were suspended and prepared for LC-MS/MS as described above. Data acquisition was performed on Agilent 6430 Triple Quadrupole LC/MS system.

Bioinformatic analysis

Expression of HTC enzymes to find cell lines with high expression was analyzed from the Cancer Cell Line Encyclopedia (CCLE) (Ghandi et al., 2019).

To generate representation of genes shown in Figure S4 we used UCSC genome Browser with different tools. For p53 ChIP seq depth and SISSR peaks dataset (data are shown in green) the tool p53 ChIP seq depth and SISSR peaks dataset was used. This dataset comes from 41 ChIP-seq data analyzed with a common pipeline. In order to get representation the sequence must be found in at least two independent studies. For further information on the pipeline and analysis parameters see Nguyen et al. (Nguyen et al., 2018). Additional p53 and E2F binding sequences were obtained in ChIP Atlas and positions extracted from UCSC genome Browser using Transcription factor ChIP-Seq Clusters (161 factors) from ENCODE. For further information see ENCODE integrative analysis (Consortium, 2012; Davis et al., 2018) and for CHIP Atlas (Oki et al., 2018). Information on H3K27Ac marks on 7 cell lines (Often Found Near Regulatory Elements shown in red) was extracted from ENCODE (Consortium, 2012; Davis et al., 2018). Promoter regions (shown in pink) were extracted from EPDnewNC human version 001 and GeneCards genes TSS v4.14 (Fishilevich et al., 2017; Stelzer et al., 2016). Data for known or predicted gene enhancer regions were extracted using Interactions between GeneHancer regulatory elements and genes tool (double elite) v4.14 (Fishilevich et al., 2017; Stelzer et al., 2016).

QUANTIFICATION AND STATISTICAL ANALYSIS

For Statistical analysis unpaired two-tailed Student's t test or ANOVA with compensation of multiple comparison with Dunnett, Tukey or Šidák based on Prism 9 recommendations for experimental design was performed unless stated otherwise in the figure legend using Graph Pad Prism 6-9 and Excel. A value of $p < 0.05$ was considered significant. For statistical analysis technical replicates were averaged prior to statistical analysis. In figures, data is shown unless stated otherwise as mean ± SD of data from independent experiments and the p value was indicated with three digits after decimal or $p \leq 0.05$ equal to *, $p \leq 0.01$ equal to **, $p \leq 0.001$ equal to *** and $p \leq 0.0001$ equal to ****. For analysis of immunohistochemistry we used Mann-Whitney non-parametric test, two tailed using Graph Pad Prism 6-9. Details of statistical test were deposited with data on Mendeley: http://doi.org/10.17632/xsxwjfhz8f.1

ADDITIONAL RESOURCES

Further details senescence bypass experiments can be found in additional resources on Mendeley Data

For additional information on immunogold staining www.me-udem.com

For additional information on immunohistochemistry performed by the CR-CHUM core facility https://www.chumontreal.qc.ca/en/crchum/facilities-and-services

For additional information of metabolic tracing analysis https://www.mcgill.ca/gci/facilities/metabolomics-innovation-resource-mir